Steel Plate Shear Walls for Seismic Design and Retrofit of Building Structures

by

Darren Vian and Michel Bruneau
University at Buffalo, State University of New York
Department of Civil, Structural and Environmental Engineering
Ketter Hall
Buffalo, New York 14260

NOTICE

Steel Plate Shear Walls for Seismic Design and Retrofit of Building Structures

by

Darren Vian[1] and Michel Bruneau[2]

1   Graduate Research Assistant, Department of Civil, Structural and Environmental Engineering, University at Buffalo, State University of New York
2   Professor, Department of Civil, Structural and Environmental Engineering, University at Buffalo, State University of New York

Preface

The Multidisciplinary Center for Earthquake Engineering Research (MCEER) is a national center of excellence in advanced technology applications that is dedicated to the reduction of earthquake losses nationwide. Headquartered at the University at Buffalo, State University of New York, the Center was originally established by the National Science Foundation in 1986, as the National Center for Earthquake Engineering Research (NCEER).

Comprising a consortium of researchers from numerous disciplines and institutions throughout the United States, the Center's mission is to reduce earthquake losses through research and the application of advanced technologies that improve engineering, pre-earthquake planning and post-earthquake recovery strategies. Toward this end, the Center coordinates a nationwide program of multidisciplinary team research, education and outreach activities.

MCEER's research is conducted under the sponsorship of two major federal agencies: the National Science Foundation (NSF) and the Federal Highway Administration (FHWA), and the State of New York. Significant support is derived from the Federal Emergency Management Agency (FEMA), other state governments, academic institutions, foreign governments and private industry.

MCEER's NSF-sponsored research objectives are twofold: to increase resilience by developing seismic evaluation and rehabilitation strategies for the post-disaster facilities and systems (hospitals, electrical and water lifelines, and bridges and highways) that society expects to be operational following an earthquake; and to further enhance resilience by developing improved emergency management capabilities to ensure an effective response and recovery following the earthquake (see the figure below).
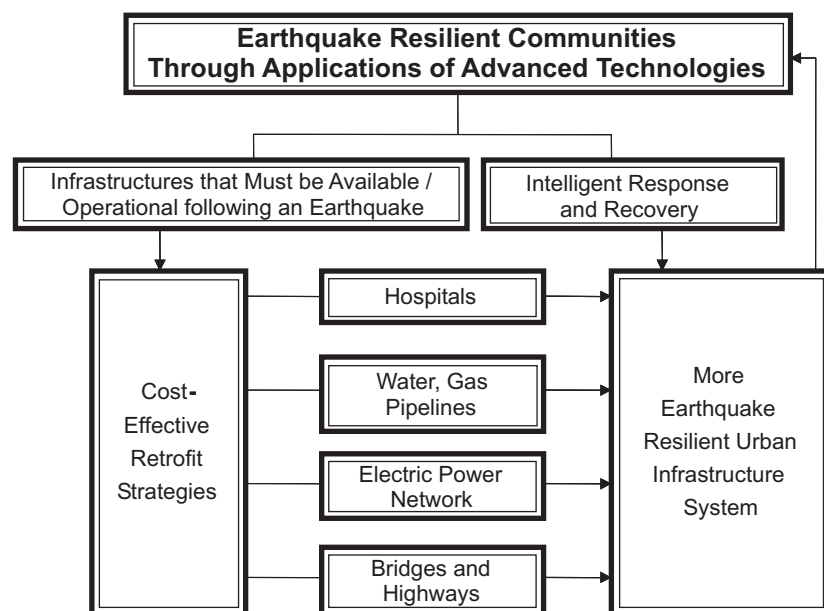
A cross-program activity focuses on the establishment of an effective experimental and analytical network to facilitate the exchange of information between researchers located in various institutions across the country. These are complemented by, and integrated with, other MCEER activities in education, outreach, technology transfer, and industry partner-ships.

This report investigates the use of Steel Plate Shear Walls (SPSW) for use in retrofit and new design as a lateral force resisting system in building structures. An experimental program was conducted using single-story, single-bay SPSW frames. The tested specimens used low yield strength (LYS) steel infill panels and reduced beam sections (RBS) at the beam-ends. Two specimens made allowances for penetration of the panel by utilities, which would exist in a retrofit situation. The first, consisting of multiple holes or perforations in the steel panel, also has the characteristic of further reducing the corresponding solid panel strength (as compared with the use of traditional steel). The second specimen used quarter-circle cutouts in the panel corners, which were reinforced to transfer the panel forces to the adjacent framing. All specimens resisted quasi-static loading from an imposed input history of increasing displacements to a minimum drift of 3%. The perforated panel reduced elastic stiffness and overall strength of the specimen by 15% and 19%, respectively, as compared with the solid panel specimen.

Analytical models using the Finite Element Method (FEM) showed good agreement with the experimental results. Variations of the perforated wall model were analyzed and compared with FEM of simple perforated tension strips to quantify limit states of this system, using material elongation around perforations as the criterion. Recommendations are made for the ductile design of these systems and for the use of RBS connections in SPSW anchor beams.

ABSTRACT

Steel plate shear walls (SPSWs) are investigated in this report, for use in retrofit and new design as a lateral force resisting system in building structures. Limits for sizing (for moment strength) of anchor beams, at the upper and lowermost levels of a multi-story SPSW frame, are introduced and developed. Approximate limits for frame drift at yield are developed for both a bare frame, and including an SPSW, with the intention of designing the infill panel as a "fuse" to yield and dissipate seismic input energy while protecting the surrounding framing.

An experimental program of single-story, single-bay SPSW frames is outlined and some results are presented. The tested specimens utilized low yield strength (LYS) steel infill panels and reduced beam sections (RBS) at the beam-ends. Two specimens make allowances for penetration of the panel by utilities, which would exist in a retrofit situation. The first, consisting of multiple holes, or perforations, in the steel panel, also has the characteristic of further reducing the corresponding solid panel strength (as compared with the use of traditional steel). The second such specimen utilizes quarter-circle cutouts in the panel corners, which are reinforced to transfer the panel forces to the adjacent framing. All specimens resisted quasi-static loading from an imposed input history of increasing displacements to a minimum drift of 3%. The perforated panel reduced elastic stiffness and overall strength of the specimen by 15% and 19%, respectively, as compared with the solid panel specimen.

Analytical models utilizing the Finite Element Method (FEM) are developed to represent the specimens in the experimental program, with good agreement observed between the analytical models and experimental results. Variations of the perforated wall model are analyzed and compared with FEM of simple perforated tension strips to quantify limit states of this system, using material elongation around perforations as the criterion. Recommendations are made for the ductile design of these systems.

Column twisting near the RBS connections during testing is investigated and compared with research on this topic in frame tests without SPSWs. Design recommendations are made for the use of RBS connections in SPSW anchor beams.

Acknowledgements

TABLE OF CONTENTS

TABLE OF CONTENTS (cont'd)

LIST OF FIGURES

LIST OF FIGURES (cont'd)

LIST OF FIGURES (cont'd)

FIGURE   **TITLE**   **PAGE**

LIST OF FIGURES (cont'd)

LIST OF TABLES

NOTATIONS

A_g	gross area of tension member (AISC notation)
A_n	net area of tension member (AISC notation)
a_c	$= \sqrt{E \cdot C_w / G \cdot J}$
b_f	flange width
C_w	warping constant
D	perforation diameter, mm
d	panel depth (Roberts and Sabouri-Ghomi)
DT#	Displacement Transducer channel #
ds	unit panel diagonal width
dx	projection of unit panel diagonal width ds along beam length
E, E_s	Steel modulus of elasticity (MPa)
e_x	eccentricity of beam flange force, F, due to beam LTB
F_H	horizontal reaction on column bending inflection point
F_v	vertical reaction on beam bending inflection point
F_{yab}	yield stress of SPSW anchor beam
F_{yb}	yield stress of steel beam within frame
F_{yc}	yield stress of steel column within frame
F_{yp}	yield stress of SPSW infill panel
f_{ws}	flange warping torsion stress
G	shear modulus of elasticity
H	1. height of frame between beam centerlines
	2. horizontal component of panel tension field force, P
h	column section depth
h_{hinge}	height between centerlines of floor hinge and bottom beam
H_{panel}	height of infill panel between beam flanges
I_b	moment of inertia of beam
I_c	moment of inertia of column
J	torsional constant

K_{panel}	stiffness of SPSW solid infill panel
K_{perf}	stiffness of SPSW perforated infill panel
L	1. length of beam
	2. length of typical perforated tension strip (section 7.2)
L_e	edge distance from perforation center
M_B	beam moment
M_C	column moment
M_L	moment at left end of (anchor) beam
M_n	moment capacity of member (AISC notation)
M_p	plastic moment of column
M_R	moment at right end of (anchor) beam
M_{span}	maximum (anchor) beam interior span moment
M_u	moment demand on member (AISC notation)
N_r	number of rows of perforations
P	($=\sigma{\cdot}t{\cdot}ds$) tension field force in panel unit diagonal width ds
PTM#	three gage strain rosette channel #
PU#	uniaxial strain gage channel #
P_n	axial capacity of member (AISC notation)
P_u	axial force demand on member (AISC notation)
S_{diag}	diagonal spacing between perforations
S_{xb}	beam elastic section modulus
S_{xc}	column elastic section modulus
T	concentrated torque on column due to flange force eccentricity
t	panel thickness, mm
t_f	flange thickness
TMb	bottom beam displacement transducer channel
TMt	top beam displacement transducer channel
V	vertical component of panel tension field force, P
V_{yp}	SPSW inxfill panel yield strength
$V_{yp.perf}$	perforated SPSW infill panel yield strength
w_{avg}	weighted average width of typical diagonal infill panel strip

w_{eff}	effective width of typical diagonal infill panel strip
W_{no}	($= h \cdot b_f/4$) normalized warping function at a point on the column flange
W_{panel}	width of infill panel between column flanges
x	horizontal distance from left end of (anchor) beam
x_{span}	horizontal distance from left end of (anchor) beam to location of maximum interior span moment
Y_t	hole reduction coefficient for tension calculations (AISC notation)
y	vertical distance from bottom of column (at beam centerline)
Z_x	beam section plastic modulus
Δ_b	displacement at column inflection points due to beam bending
Δ_c	displacement at column inflection points due to column bending
Δ_T	total displacement at column inflection points due to beam and column bending
Δ_{yp}	infill panel yield displacement
α	1. angle of inclination of SPSW tension field
	2. location of torsion as a fraction of column height (section 7.3 only)
β	RBS fraction of original section moment strength $M_{p.RBS}/M_p$
δ	axial displacement of quadrant model of typical perforated tension strip
ε_{un}	uniform total elongation of a typical perforated strip in tension
φ	angle of rotation of column
ϕ_n	nominal strength reduction factor
Γ	$= \varphi'' \cdot G \cdot J \cdot a_c / T$
γ_T	($=\Delta_T/H$) total interstory drift between column inflection points (%)
$\gamma_{T.y}$	total interstory drift at frame yield between column inflection points (%)
γ_{yp}	infill panel yield drift
κ	beam moment end condition
λ	distance between centerline of RBS regions as a fraction of total beam length
μ_p	target infill panel ductility
θ	1. orientation angle of SPSW perforations in infill panel
	2. inclined angle of beam flange force (section 7.3 only)

ω_H horizontal component of panel diagonal tension field force distributed over a unit length of beam

ω_{max} maximum infill panel vertical load per length acting on an anchor beam

ω_{ult} ultimate infill panel vertical load per length that can be supported by given anchor beam

ω_V vertical component of panel diagonal tension field force distributed over a unit length of beam

ABBREVIATIONS

AISC   American Institute of Steel Construction

BB   Bottom Beam

BF   Bottom Flange

BRB   Buckling Restrained Brace

EDD   Energy Dissipation Device

FC   Far Column

FEMA   Federal Emergency Management Agency

FF   Far Flange

FLB   Flange Local Buckling

LTB   Lateral-Torsional Buckling

LYS   Low Yield Strength or Low Yield Steel

MCEER   Multidisciplinary Center for Earthquake Engineering Research (Buffalo, NY)

MDOF   multiple-degrees-of-freedom

NCREE   National Center for Research in Earthquake Engineering (Taipei, Taiwan)

NSP   Nonlinear Static Procedure

NTU   National Taiwan University (Taipei, Taiwan)

RBS   Reduced Beam Section

SDOF   single-degree-of-freedom

SPSW   Steel Plate Shear Wall, Steel Panel Shear Wall, Steel Panel Special Wall

TADAS   Triangular Added Damping And Stiffness device

TB   Top Beam

TF   Top Flange

UB   University at Buffalo, *State University of New York*

WC   Wall Column

WF   Wall Flange

WLB   Web Local Buckling

SECTION 1

INTRODUCTION

1.1 General

Steel plate shear walls (SPSWs) are a lateral force resisting system that has seen increased usage in North America and Asia over the last thirty years. Early designs only allowed for elastic behavior, or shear yielding in the post-elastic range, an approach that typically resulted in the selection of relatively thick or heavily-stiffened infill panels. These designs, while resulting in a stiffer structure that would reduce displacement demand as compared to the bare frame structure during a seismic event, would also induce relatively large forces on the surrounding frame members, which must be detailed accordingly to ensure adequately ductile performance.

Researchers on the behavior of SPSWs since the early 1980s (some of this research is discussed in the next chapter) have advocated the use of relatively thinner plates for the infill panels. This approach allows shear buckling to occur in the panels and subsequently develop diagonal tension field action as the method of lateral load resistance and transmission to the boundary frame. More efficient designs resulted, from the perspective of the infill panels themselves, as well as the surrounding frame members, which are typically capacity designed for these panel forces.

Some obstacles still exist impeding more widespread acceptance of this system in the design community. For example, using the yield stress for steel material typically available in North America, the minimum panel thickness available from steel producers may be much thicker than required for a given design situation. In a case such as this, use of the minimum available thickness may result in a large panel force over-strength from those required by design calculations. Attempts at alleviating this problem were recently addressed by the use of light-gauge, cold-formed steel panels, in a new application by Berman and Bruneau (2003a, 2005). Xue and Lu (1994a) suggested additional means of reducing demand on framing adjacent to an SPSW, including the connection of the infill panel to only the beams in a moment frame.

The practical concern of utility placement is another impediment to more widespread acceptance of the SPSW structural system. If the SPSW infill panel occupies an entire frame bay between

1

adjacent beams and columns, then utilities that may have otherwise passed through that location must either be diverted to another bay, or pass through a heavily stiffened opening, as prescribed in current design codes. This would add costs to the project in either additional materials (for the extra stiffening) or in labor (for the re-location of ductwork in a retrofit, for example). Therefore, more work is required to ensure the viability of the SPSW system over a wide range of situations to make it more acceptable to design engineers.

1.2   Scope and Objectives

This report investigates some new methods for the design of SPSWs. The proper and efficient design of SPSW system "anchor" beams, those at the top and bottom levels of a multistory frame, is considered in some detail. The objective of the proposed anchor beam design is to ensure that frame plastic hinging occurs in the beams and not in columns. Limits are proposed to estimate the drift of a frame with and without SPSW panels, at yield, so that the system may be assessed in the context of the structural "fuse" concept, and considered to dissipate input energy through SPSW panel yielding at a drift level less than that causing the frame members to yield (although imperfect a concept in this application).

Two variations on the solid fill panel system that allow for the passage of utilities through the plane of the wall are introduced in the study. One system accomplishes this goal using unstiffened panel perforations, which, it will be shown, in addition to allowing utility pass-through, may be used to reduce the strength and stiffness of a solid panel wall to levels required in a design when thinner plate is unavailable. Another system preserves the general strength and stiffness of a solid SPSW panel, while allowing utility passage through a reinforced cutout that transmits panel forces to the boundary frame.

The design concepts are verified and studied further by means of a series of approximately half-scale test specimens, subjected to quasi-static, displacement controlled, cyclic loading. A typical single story, single bay frame with solid SPSW infill panel is designed and compared with specimens implementing the perforated panel and reinforced cutout design concepts.

Finite element analysis is used to investigate the overall behavior of the tested specimens, and aid in defining design displacement limits for ductile performance of the perforated panel

2

system. Based on the test results and analytical investigation, recommendations are presented for the ductile design of SPSW anchor beams and perforated panel systems.

1.3   Outline of Report

Chapter 2 provides an overview of research related to this structural system for both its overall behavior and specific applications to earthquake resistance.

In Chapter 3, the interaction between an SPSW infill panel and the surrounding steel frame in which it is placed is examined. Guidelines for the design of the bottom and top story "anchor" beams in an SPSW fitted frame are developed. Two concepts to allow for the practical pass-through of utilities through an infill panel are presented and suggested methods for preliminary design of those systems are outlined.

The design of specimens for an experimental program is presented in Chapter 4. The specimens implement some of the concepts described in Chapter 3.

Results of the experimental program are presented in Chapter 5. The establishment of the loading protocol and methods of load application are presented, followed by force versus displacement hysteresis plots, photos of accumulated damage during the inelastic cycling of the each test, and related descriptions.

Chapter 6 describes model development and analytical results of a finite element investigation of the experimental results. Effectiveness of the model results is also discussed.

Various design considerations that were developed in Chapter 3 are studied further in Chapter 7. Design recommendations are made to ensure ductile behavior in perforated panels. The stability of RBS connections in SPSW "anchor" beam locations is studied and a method for checking combined stresses causing column twisting in this application is discussed.

Finally, summary, conclusions, and recommendations for future research in SPSWs are presented in Chapter 8.

SECTION 2

REVIEW OF PAST RESEARCH ON STEEL PLATE SHEAR WALLS

2.1 General

There have been numerous experimental and analytical studies investigating the behavior of SPSWs in the past thirty years. In that time, focus has generally shifted from the use of stiffeners to ensure shear yielding as the energy dissipation mechanism, to the use of thin plates with tension field action as the load carrying mechanism and tension yielding to dissipate input energy. While a number of previous reviews of past research can be found in the literature (i.e. Berman and Bruneau 2003a, Rezai 1999), some work of note is summarized below, including work completed since previous reviews.

2.2 Thorburn, Kulak, and Montgomery (1983)

Thorburn *et al*. (1983) developed a simple analytical model to represent the tension field action of a thin steel wall subjected to shear forces. This model, which replaces the infill panel by a series of inclined tension-only strips, was developed based on the work of Wagner (1931), who first presented a theory for thin webs subjected to shear, utilizing post-buckling strength.

By assuming a thin SPSW infill panel buckling under compressive diagonal load assuming beams and columns rigid in bending and using the principle of least work, as done for aeronautic applications previously by Kuhn *et al*. (1952), the inclination angle for the tension field was derived:

$$\tan^4 \alpha = \left[\frac{1 + \dfrac{L \cdot t}{2 \cdot A_c}}{1 + \dfrac{H \cdot t}{A_b}} \right] \tag{2-1}$$

where H is the frame story height, L is the frame bay width, t is the panel thickness, and A_b and A_c are cross sectional areas of the story beam and column, respectively. The investigation found that ten diagonal tension strips could adequately represent the infill panel for conditions to be studied, and so utilized a tension strip model as shown in figure 2-1, which assumes rigid beams.

This is a reasonable assumption for an interior panel within a multistory structure (i.e. panels not at the top and bottom of the building), since the vertical component of tension field forces from adjacent story panels above and below a beam would oppose each other, and the net vertical beam deflection would be negligible. It was noted that at the top and bottom levels, however, special care must be taken in design to ensure proper anchoring of the tension field at these locations.
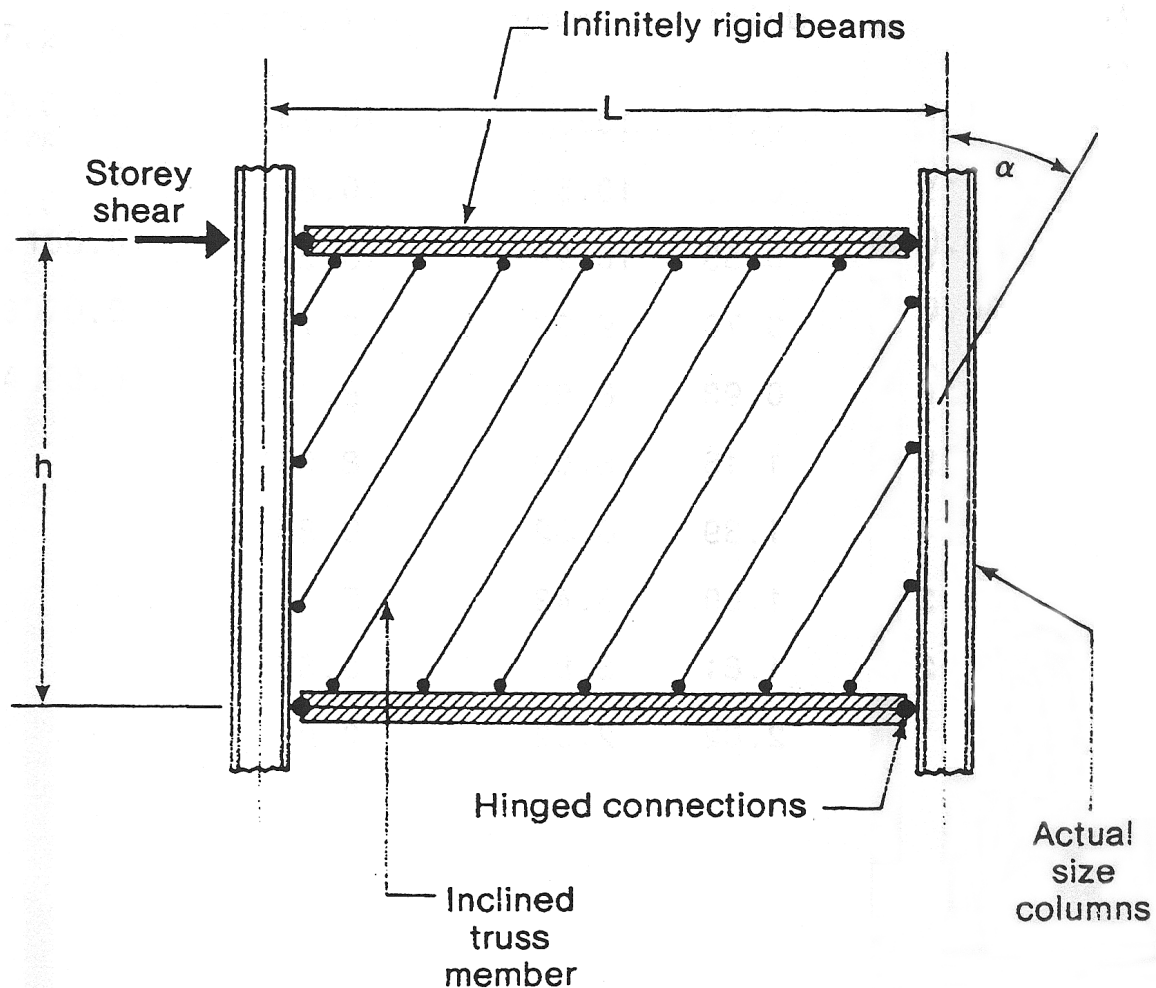
FIGURE 2-1 Schematic of SPSW Strip Model (Thorburn *et al*. 1983)

An equivalent story brace was developed to represent the story stiffness of a panel by a single truss element. In a practical setting, it was assumed that use of the multi-strip model, while convenient for the purpose of research, as described above, would be prohibitively time-consuming. Therefore, the stiffness derived for a panel with rigid boundary frame allowing full development of tension field was equated to the stiffness of an "equivalent story brace" along the

diagonal of the story bay with SPSW infill, and an equation was provided for the area of this equivalent member. This was done for two limiting cases of column stiffness: one in which the columns bounding the panel are infinitely rigid against bending, and the other in which they are completely flexible.

2.3 Timler and Kulak (1983)

Timler and Kulak (1983) performed a test on a single story large scale SPSW specimen to verify the analytical work of Thorburn *et al*. (1983) briefly summarized in the previous section. A specimen consisting of two SPSW panels, with centerline story width of 3750mm by a height of 2500mm, as shown in figure 2-2 was tested under quasi-static cyclic loading to the serviceability limit, followed by loading to failure. Simple beam-to-column connections were used to connect the W460x144 (W18x97) beams to the W310x129 (W12x87) column sections. The 5mm infill panel was connected to the boundary frame by means of a 6mm thick "fish plate". No effective gravity loads were applied to the system.
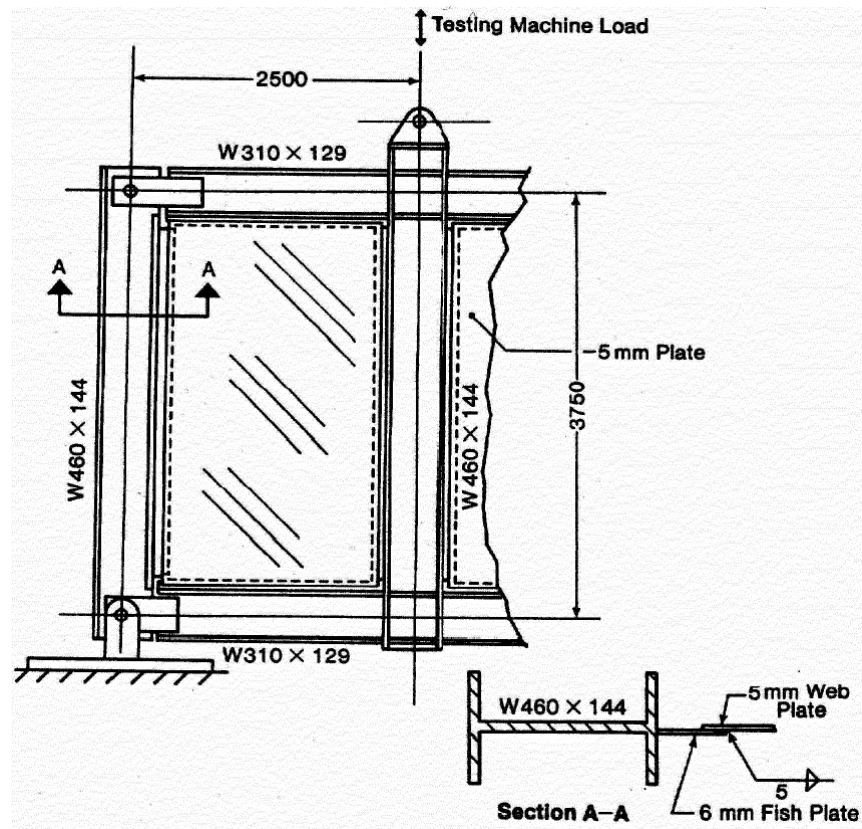
FIGURE 2-2 Schematic of Test Specimen (Timler and Kulak 1983)

On the basis of this work, Timler and Kulak (1983) proposed a slight revision to equation (2-1) for the tension field inclination angle:

$$\tan^4 \alpha = \left[\frac{1 + \dfrac{L \cdot t}{2 \cdot A_c}}{1 + H \cdot t \cdot \left(\dfrac{1}{A_b} + \dfrac{H^3}{360 \cdot I_c \cdot L} \right)} \right] \tag{2-2}$$

where I_c is the boundary column moment of inertia, and all other terms were defined previously. The derivation included the effect of work done by column bending. Both equations appear in the Canadian standard CAN/CSA-S16-01, with (2-1) recommended for preliminary proportioning of beams, columns, and infill plates, and (2-2) utilized in the development of the detailed multi-strip model.

2.4 Roberts and Sabouri-Ghomi (1992)

Roberts and Sabouri-Ghomi (1992) conducted a series of sixteen quasi-static cyclic loading tests on unstiffened steel plate shear panels with centrally placed circular openings. The test setup consisted of a plate clamped between pairs of stiff, pin-ended frame members. Two diagonally opposite pinned corners were connected to the hydraulic grips of a 250kN servo-hydraulic testing machine, which applied the loading.

Specimen panel depth, d, was 300mm for all specimens; panel width, b, was either 300mm or 450mm; panel thickness, h, was either 0.83mm or 1.23mm, with the panels having 0.2% offset yield stress values of 219MPa (32ksi) and 152MPa (22ksi), respectively; and four values were selected for the diameter of the central circular opening, D: 0, 60, 105, and 150mm. A schematic of a specimen and hinge detail are shown in figure 2-3.

They proposed an approximate strength and stiffness reduction factor for a perforated panel:

$$\frac{V_{yp.perf}}{V_{yp}} = \frac{K_{perf}}{K_{panel}} = \left[1 - \frac{D}{d} \right] \tag{2-3}$$

where $V_{yp.perf}/V_{yp}$ and K_{perf}/K_{panel} are the ratios of strength and elastic stiffness, respectively, of a perforated panel specimen to an identical solid panel specimen, and the remaining parameters were described above.
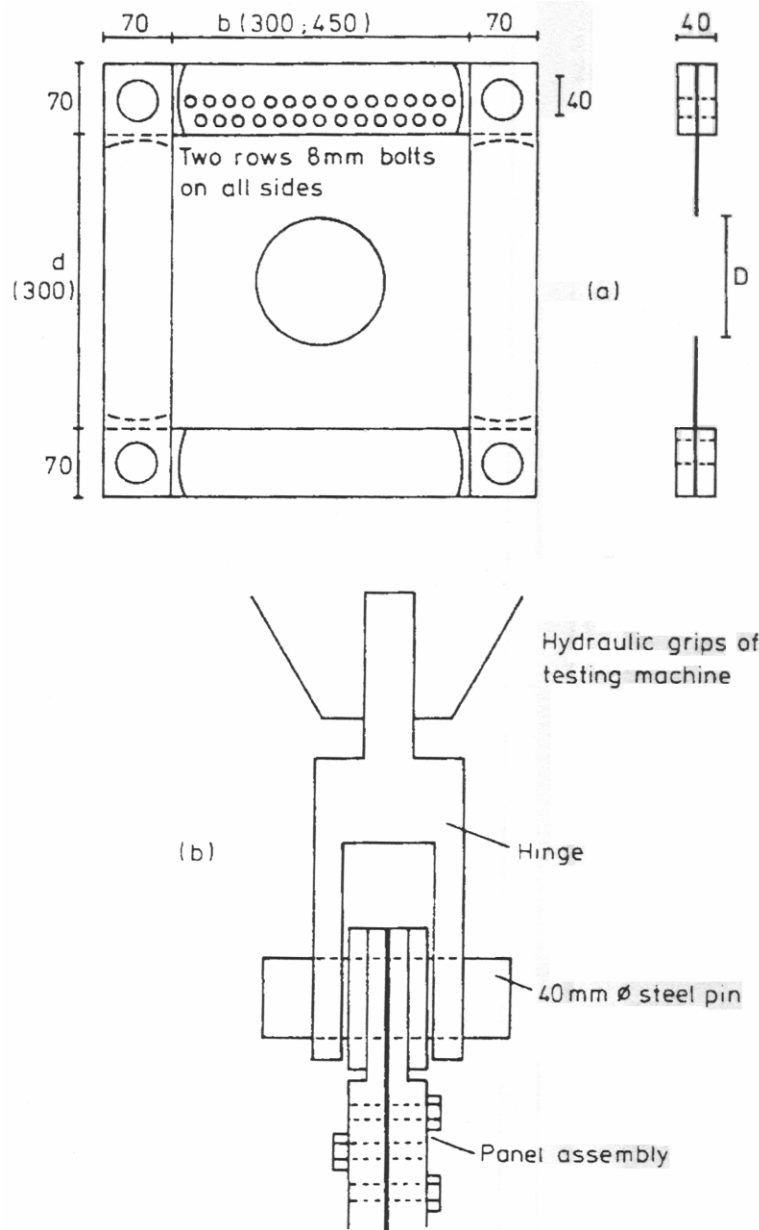
FIGURE 2-3 Schematic of Test Specimen (Roberts and Sabouri-Ghomi 1992a)
(a) Perforated Shear Panel; (b) Hinge

They determined that results for strength and stiffness of a perforated panel can be conservatively approximated by applying the reduction factor of (2-3) to the strength and stiffness of a similar, unperforated panel. In another paper, Roberts and Sabouri-Ghomi (1991)

9

developed a theoretical model for predicting the hysteretic characteristics of unstiffened steel plate shear panels. This model was modified by the linear reduction factor of (2-3) to compare with the test results described above, and was found to give reasonable but conservative values, due to the neglecting of strain hardening and the simply supported plate boundaries, which underestimates the critical load.

2.5 Xue and Lu (1994a, 1994b)

Xue and Lu (1994a) conducted a numerical study of a three-bay, twelve-story frame designed for earthquake loading with the middle bay containing SPSW infill panels. Member internal force distribution and system stiffness was investigated using four different frame configurations having identical frame members in all cases, but differing connection arrangements for each, as follows. Outer bay frame members had full moment connections to one another, while those of the interior bay were either full or simple connections. The panel was either fully connected around its perimeter to both girders and columns ("GC" type system), or only connected to the girders ("G" type).

The researchers selected one system from each group, F-GC and P-G, with full (F) and partial (P) moment connections, respectively, to compare member and system behavior during pushover analysis. Shear panels in the P-G system assumed a larger share of the effective lateral load (compared to the columns) earlier in the loading history as compared to the F-GC panels. However, percentages became closer at high load levels. The SPSW boundary column share of story shear was distributed symmetrically in the P-G system, while one column carried the majority of the total column shear for F-GC.

The F-GC system had a higher lateral stiffness than the P-G system, but its columns were required to resist a substantial portion of the story shear, which was felt may precipitate early damage or failure of critical columns, unacceptable for a well-designed structure. In the less-stiff P-G system, a larger share of the lateral load was resisted by the panels, which would yield and dissipate energy and help avoid early column failure. The reduced stiffness of the P-G system was also seen as potentially beneficial under seismic loads because of the resulting changes in

dynamic response. Based on this and the simpler connection arrangements that may result in fabrication and erection cost advantages, Xue and Lu recommended the P-G system.

Girder internal forces were significantly different based on the system type, with bending moment of the P-G system controlled by infill panel tension field action, as opposed to frame action controlling in the F-GC system (the tension field is essentially equal on both sides, so the moment diagram is close to that of a bare frame). The P-G system peak bending moments were relocated away from the ends (where they are on F-GC), to two inner positions on the girder.

Xue and Lu also examined the overall flexural deformation behavior of the F-GC frame-wall system through the design of a single-bay, twelve-story MRF with wall panels, and analyzed its behavior under lateral loading. This frame had a high height-to-width ratio, and as such, would have substantial flexural deformation. In addition, as a single bay structure, adjacent framing would not contribute to the lateral load resistance or reduce flexural deformations. Therefore, the model behaved initially as a cantilever beam, but following shear buckling of some of the panels, the F-GC system behaved like a bare MRF. Once the interstory drifts, or lateral loads, had exceeded a certain threshold, the force-displacement behavior became similar to the cantilever beam once again, as tension field action developed. It was indicated desirable to prevent or suppress flexural deformations of a frame-wall structure and thereby invoke the panels' tension field action at an early stage of loading. Interaction between the shear and flexural deformations was largely eliminated by not connecting the panels to the columns in the P-G system studied.

In another study, Xue and Lu (1994b) conducted a parametric analytical investigation of shear panel behavior for frame-panel systems subjected to monotonic and cyclic loading, considering the effects of yielding and post-buckling deformation. The parametric study utilized a total of 20 systems, with the panel width-to-thickness ratio (five values) and width-to-height aspect ratio (five values) as the two principal parameters of investigation, subjecting the panels to monotonic shear, and uses three properties (post-buckling stiffness, "significant" yield strength, and post-yield stiffness), with a simple calculation procedure for each, to develop a panel load-deformation relationship.

A single-story, single-bay system was selected for a parametric study, with the P-G connection arrangement (1994a). All lateral loads applied to the system were therefore resisted by the panel only. Column and girder deformations were ignored for the analyses presented in the paper, although their effects were studied.

No significant effect of panel width-to-thickness on stiffness prior to buckling was observed. However, as this ratio increased, the position of the significant yield point was slightly lowered, and the post-yield stiffness slightly reduced, since although the ratio has a crucial influence upon initiation of buckling, it has little affect on the tension field action after buckling. Since shear buckling will occur almost immediately when loading a thin plate, the tension field action determines thin shear panel performance.

2.6   Hitaka and Matsui (2003)

Hitaka and Matsui (2003) conducted static monotonic and cyclic tests on 42 plate wall specimens of roughly one-third scale. The tested system, known as a "slit wall", consisted of an SPSW with vertical slits cut into the plate, causing the plate segments to behave as a series of flexural links. This plate wall system is only connected to the beams of the frame, unlike conventional SPSWs as described in the bulk of the research discussed here. A schematic of a Slit Wall is shown in figure 2-4.

As that time, three buildings incorporating steel Slit Walls had been constructed in Japan, for both commercial and residential usage, ranging from 7 to 19 stories with composite column-steel beam moment resisting frames. In these applications, the Slit Wall was designed to resist approximately 10 to 25% of the seismic base shear, with the remainder resisted by the moment frame.

The research provides an overview of Slit Wall behavior as it relates to slit and stiffener design, verifies the performance of the element, and proposes a method to design the system by specifying the desired strength and stiffness. In the three buildings constructed with this system in Japan, the slit design is varied along the height of the structure according to the strength and stiffness demand.
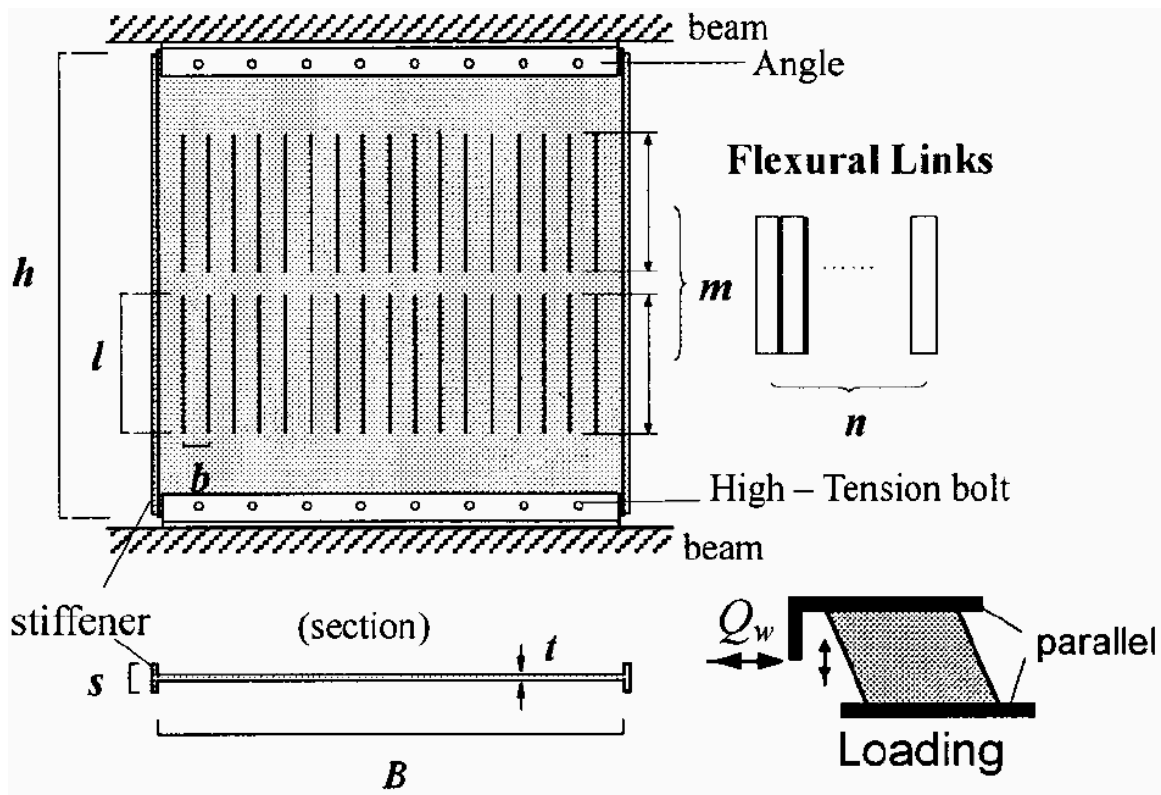
FIGURE 2-4 Schematic of Slit Wall Test Setup – Hitaka and Matsui (2003)

By separating the wall behavior between shear deformation of the entire plate, and flexural link deformation, expressions were developed for panel stiffness and strength as a function of the overall geometry in terms of the number and length of slits. Panel strength and stiffness, according to the developed equations, can be modified independently of one another by adding, say, additional layers of slits while keeping the ratio of slit length to slit spacing constant.

Four series of tests on 42 specimens were conducted to validate the behavior of the new element, as well as examine both the effect of slit configuration on behavior and the effectiveness of supplemental stiffening methods on the wall panel. Stiffening methods considered were steel stiffener strips perpendicular to the plane of the wall welded on each end, and mortar panels, which would constrain the panel laterally, but not contribute to the overall shear strength of the panel. The observed experimental data and subsequent FEM analysis suggest that the steel stiffeners' contribution to stiffness in the initial stage is negligible when calculating system initial stiffness.

The tested specimens displayed generally stable hysteresis behavior during cycling, and, after reaching the peak strength, stable strength degradation caused by transverse plate buckling. In general, the welded edge stiffener specimens demonstrated less degradation and more stable hysteresis behavior when compared with unstiffened panel of similar slit configuration. A few specimens experienced ductile fractures at the end of slits at larger drifts, but generally did not cause significant degradation. Except for a few cases, all tested specimens were pushed to a story drift of greater than 3% without cracks initiating or abrupt drops in strength under monotonic or cyclic loading.

2.7   Berman and Bruneau (2003a, 2003b, and 2005)

Berman and Bruneau (2003a, 2003b) investigated, using the strip model as a basis, the use of plastic analysis as an alternative for the design of steel plate shear walls. Fundamental plastic collapse mechanisms were described for single story and multistory SPSW with either simple or rigid beam-to-column connections, and the ultimate strengths predicted from these mechanisms were compared with experimental results from the literature and used to assess the CAN/CSA S16-01 design procedure.

For a single story SPSW with simple beam-to-column connections, as shown in figure 2-5, the researchers demonstrate, using both the Equilibrium and Kinematic Methods of plastic analysis (Bruneau $et\ al$. 1998), that the assumed collapse mechanism for the diagonal strip model produces an expression for story shear strength, V_{yp}, identical to that of the CAN/CSA S16-01 procedure used in calculating the probable shear resistance of an SPSW panel:

$$V_{yp} = \frac{1}{2} \cdot F_{yp} \cdot t \cdot L \cdot \sin 2\alpha \qquad (2-4)$$

where F_{yp} is the design yield stress of the infill plate and all other parameters have been defined previously. The analysis was extended to a frame with rigid beam-to-column connections, by introducing additional terms into (2-4) for the internal work done by plastic moment hinges in beams and/or columns.
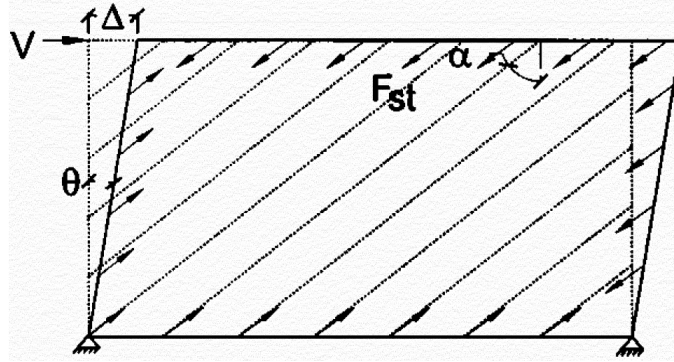
**FIGURE 2-5 Single Story SPSW Kinematic Collapse Mechanism
(Berman and Bruneau 2003a, 2003b)**

Plastic analysis of SPSWs was further extended by the researchers to multistory frames for a few example collapse mechanisms, such as those shown in figure 2-6. These mechanisms and their corresponding ultimate strengths, provide the design engineer simple tools for estimating the ultimate capacity of a multistory SPSW frame, and investigating possible soft story mechanisms. Computerized pushover analysis was further recommended to discern the actual failure mechanisms in a given structure and aid in design as necessary.
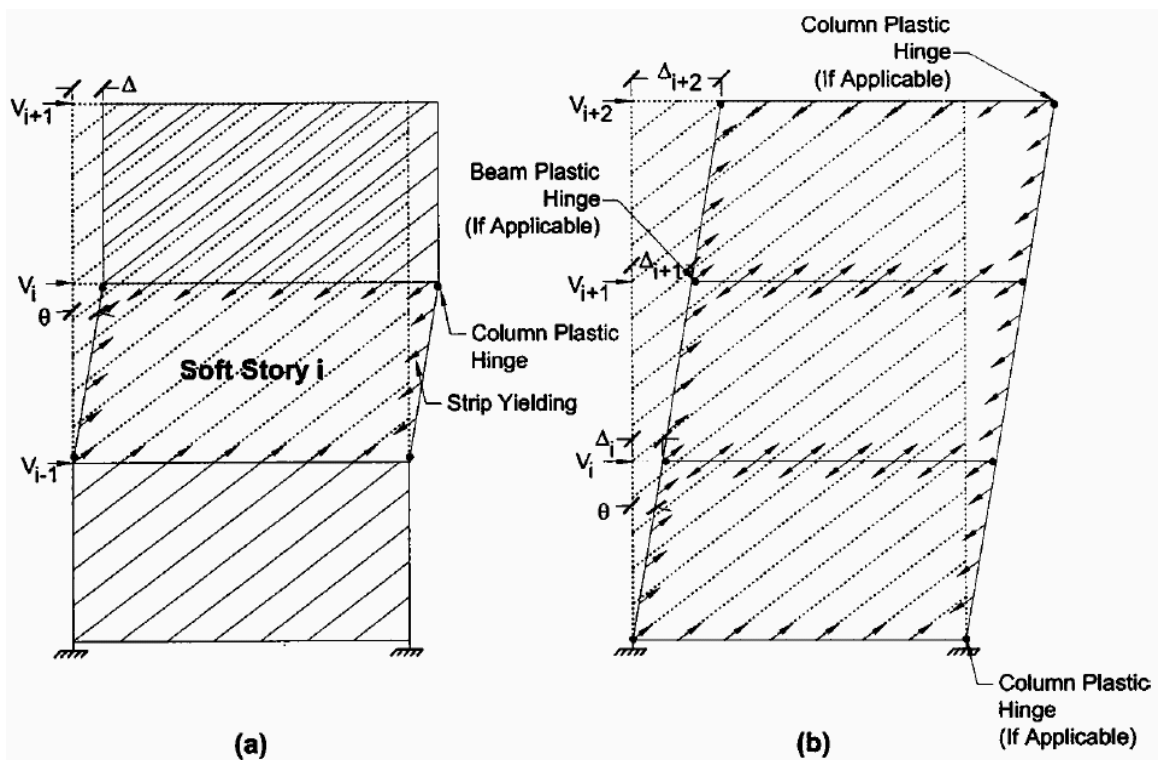
**FIGURE 2-6 Examples of Collapse Mechanisms for Multistory SPSWs
(Berman and Bruneau 2003a, 2003b)**

15

Berman and Bruneau (2003a, 2005) also conducted quasi-static cyclic testing on three SPSW specimens that utilized light gauge, cold-formed steel for the infill panel material. The use of light gauge material was intended to create a system strong enough to resist the required seismic loading, while avoiding heavy reinforcement of the surrounding framing in response to the forces placed on it by the retrofit strategy, since the minimum thickness of plate available is often much greater than that required by lateral force calculations.

Prototype SPSW seismic retrofit options were designed for the MCEER demonstration hospital (Yang and Whittaker 2002), to retrofit frames utilizing simple web-angle beam-to-column connections. Seismic base shear and force reductions factor were calculated from FEMA 302 (FEMA 1997) and the Canadian design provisions CAN/CSA-S16-01 (CSA 2001) for a "limited ductility SPSW". From subsequent SPSW strip model analysis, the minimum required plate thicknesses at the first floor level were calculated to be 22 Gauge (0.75mm) for the corrugated infill plate, and 20 Gauge (1.0mm) for the flat infill plates, assuming a yield stress of 380MPa (55ksi) in both cases. Type B steel deck, as illustrated in figure 2-7, with the corrugations oriented at 45° from the horizontal was assumed in these calculations, using a slightly modified version of the strip model strength design equation to account for the extra material along the arclength of a corrugation versus the projected length, l_p.
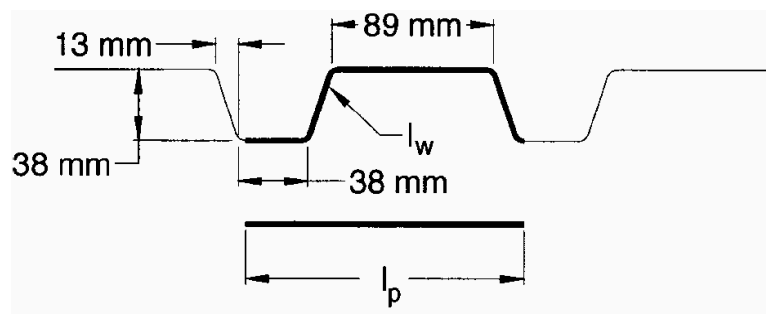
FIGURE 2-7 Corrugation pattern for Type B Steel Deck
(Berman and Bruneau 2003a, 2005)

The specimen frame size was scaled down from the hospital retrofit prototype, since testing would be limited by the maximum force available in the laboratory for quasi-static loading. However, the infill panel thicknesses were identical to the prototype to maintain a practical gauge thickness. Schematics of the testing setup and corrugated infill specimen are shown in figures 2-8 and 2-9, respectively. Strip models were developed for each specimen and used to

16

design the boundary frames members to remain elastic. In two of the three specimens, two-part epoxy was used to connect the infill panel to the fishplates, in lieu of welding, to provide another retrofit option other than welding, which in practice may produce fumes unacceptable to occupants of a building.
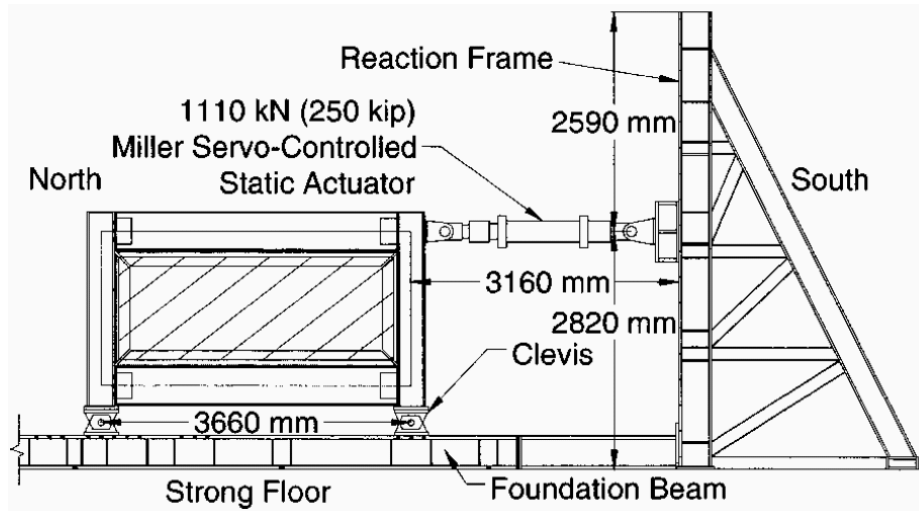
FIGURE 2-8 Schematic of Testing Setup (Berman and Bruneau 2003b)
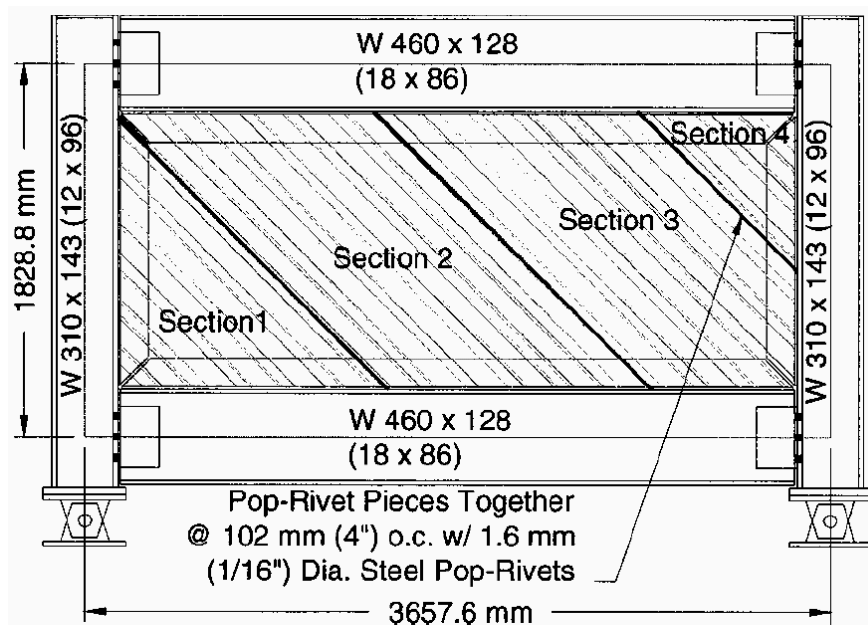
FIGURE 2-9 Schematic of Corrugated Infill Specimen (Berman and Bruneau 2003a, 2005)

The hysteresis curves for corrugated panel specimen C1 and flat panel specimen F2 are shown, along with a pushover analysis of a specimen strip model with measured material properties, in

figures 2-10 and 2-11, respectively. The corrugated infill panel contributed over 90% to the total initial stiffness for specimen C1. This specimen exhibited unsymmetric hysteresis loops since tension field action only developed in the direction of the corrugations, a behavior similar to that of a braced frame with a single slender brace (Bruneau *et al*. 1998). It was recommended that two walls with opposed orientation of corrugations be used in a given structural line to achieve symmetric system behavior.
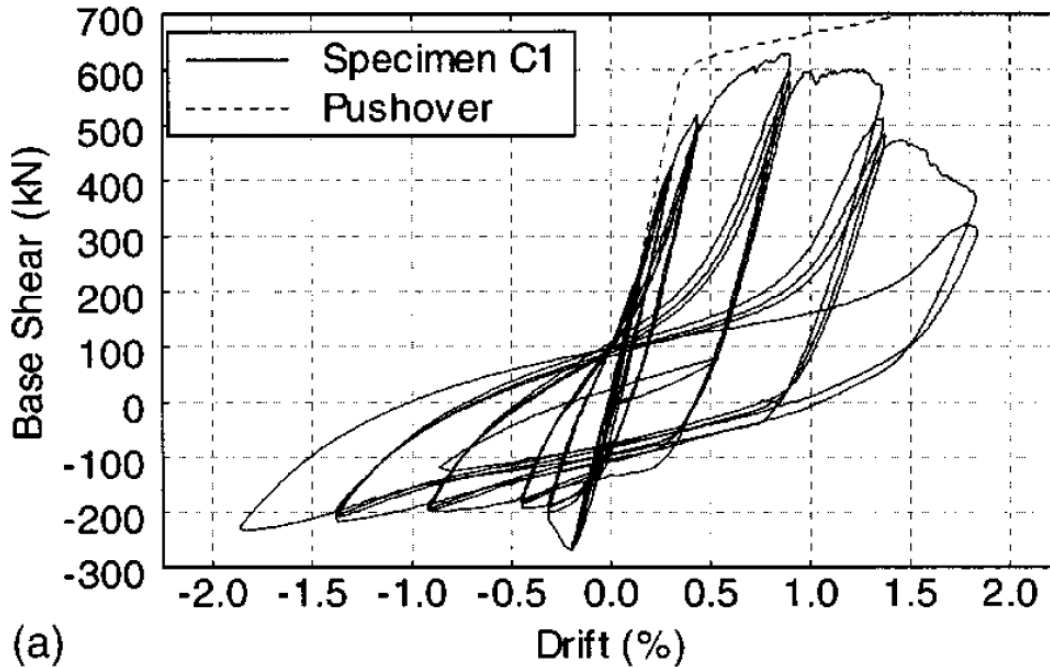
FIGURE 2-10 Specimen Hystereses and Pushover curve: Specimen C1
(Berman and Bruneau 2003a, 2005)

Specimen F2, which reached a ductility ratio of 12 and drift of 3.7%, showed a reasonable agreement in initial stiffness and base shear strength with the monotonic pushover of a strip model, as shown in figure 2-11. The flat infill contributed approximately 90% of the initial stiffness of the system.
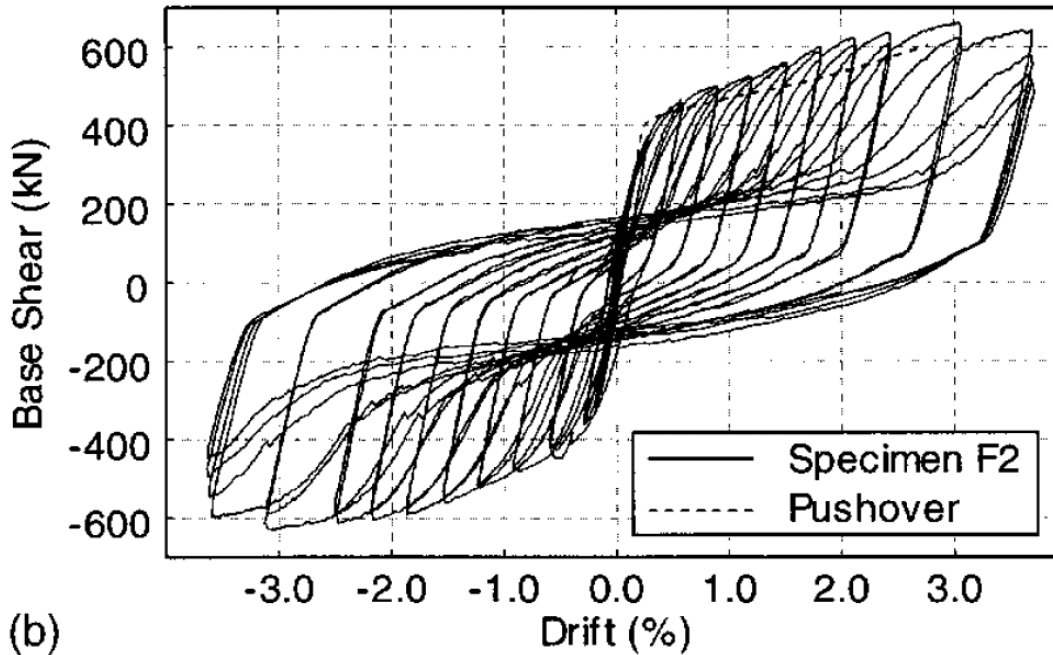
**FIGURE 2-11 Specimen Hystereses and Pushover curve: Specimen F2
(Berman and Bruneau 2003a, 2005)**

2.8 Behbahanifard, Grondin, and Elwi (2003)

Behbahanifard *et al*. (2003) conducted quasi-static lateral cyclic testing, with simulated gravity loads, on a three-story frame structure, consisting of the upper three stories in the four-story SPSW structure tested during an earlier study by Driver *et al*. (1997). Although the infill panel in the second story buckled and underwent plastic deformations during that previous test, there was no significant noticeable permanent damage in the upper three stories. The beam at the top of level 1 was removed and the remainder of the specimen welded to a 90mm thick base plate. This allowed the researchers to add to the database of large-scale SPSW tests and monitor the system's boundary members during testing.

An FEM model was developed based on the nonlinear dynamic explicit formulation, implementing a kinematic hardening material model to simulate the Bauschinger effect, after experiencing convergence problems analyzing the model using the implicit FEM. After validating this model versus the experimental results, it was used within a parametric study to identify parameters affecting the stiffness and capacity of SPSW systems. An interior SPSW

panel was idealized for this analysis by modeling a single SPSW with rigid floor beams and subjected to shear force and constant gravity loading. Dimensional analysis produced ten non-dimensional parameters to investigate, from which, four were investigated in depth: the width-to-height aspect ratio; the ratio between panel and column axial stiffness; a parameter relating column lateral flexibility to that of the panel; and an index related to the initial panel out-of-plane imperfection magnitude.

They found that a decrease in the aspect ratio produced an increase in the capacity and non-dimensional stiffness of SPSWs. However, they note that this increase is negligible within the aspect ratio range of 1.0 to 2.0, but noticeable for aspect ratios less than 1.0.

The axial stiffness ratio was found to have no effect on the strength of the wall, whereas it did have a direct relationship to the non-dimensional lateral stiffness of the system.

As the column flexibility parameter decreased, or in other words, the column lateral stiffness increased relative to the panel stiffness, the shear wall capacity approached the yield capacity. The stiffer column can more effectively anchor the panel tension field forces, therefore allowing a more efficient use of the material composing the system.

The effect of panel out-of-plane imperfections was investigated using the first buckling mode of the infill plate and five different values of the imperfection amplitude, Δ_{imp}. Expressed as a ratio with respect to $(L \cdot h)^{(0.5)}$, where L is the length of the panel between column flanges and h is the panel height, if the imperfection magnitude is less than 1%, the effect on stiffness is negligible. For imperfection sizes larger than 1% of $(L \cdot h)^{(0.5)}$ the stiffness reduction was found to be noticeable and recommended to be accounted for in the design. It was suggested to limit SPSW imperfection size in practice to 1% of $(L \cdot h)^{(0.5)}$ based on this study, a value which seems well within normal fabrication tolerances.

The effect of gravity load and overturning moment on the behavior of SPSW systems was also investigated using data from the parametric study. They found that an increase in either of these factors reduces the elastic stiffness of the shear wall panel. In addition, these factors reduce the overall shear strength of the panel, as well as the drift at which the peak capacity is reached, according to the series of analyses performed.

2.9 Kharrazi, Ventura, Prion, and Sabouri-Ghomi (2004)

Kharrazi *et al.* (2004) investigated the design of SPSW (referred to in the paper as Ductile Steel Plate Walls "DSPW") systems in terms of the separate shear and bending deformations occurring in a multistory frame. The paper presents a model, referred to as the Modified Plate-Frame Interaction (M-PFI) model, for analysis of shear and bending deformations and resulting forces, in SPSWs. The objective was to describe the interaction between those components and characterize the respective contributions to deformations and strength at structural capacity.

A tri-linear shear load displacement diagram is developed by considering the behavior of the panel up to the point of shear buckling (first critical point), then the shear is carried by tension field action, followed by perfectly plastic yielding of the tension field in the plate. Critical strength and displacement values are derived for both shear buckling and tension field yielding, then combined into a bilinear model. It should be noted that, if the critical shear buckling strength is assumed negligible (i.e. a very thin panel), the derived equations for panel strength, stiffness, and yield displacement reduce to those of Thorburn *et al.* (1983).

The bending component of plate wall behavior is also discussed, by considering a horizontal section through a story and comparing the wall to a wide flange shape with the columns as flanges of the section and the infill panel as the web. Moment and displacement expressions were derived for a single story panel at the critical point at which panel buckling occurs, assuming a linear strain distribution across the section.

The procedure then assumes that after panel bucking, the neutral axis will move toward the column in tension, since compressive stresses in the web will be released, similar to the neutral axis migration in a reinforced concrete beam following section cracking on the tension side. Expressions were developed for behavior of the panel after this event. Finally, these individual expressions for shear behavior and bending behavior are combined using interaction equations, to complete the proposed method.

2.10 Eatherton and Johnson (2004)

Eatherton and Johnson (2004) selected an SPSW system for the design of a 7000 square foot (650 m^2) residence in Woodside, California in order to meet certain performance goals. The

walls described were first designed using information in an AISC Steel Tips reference (Asteneh 2001), but the final design was based on the Canadian standard, CAN/CSA S16-01.

The building site is located approximately 1 mile from the San Andreas Fault, and the owner was concerned about the amount of structural damage that would be sustained by the building during an earthquake. The target performance criterion selected for the building called for no significant damage for a seismic design level with a 10% chance of being exceeded in fifty years. This may be the first one and two story low-rise structures with an SPSW. A three-step design approach was reported:

1. "Configure the SPSW to satisfy geometric restraints that have been shown by tests to produce ductile, energy absorbing walls."
2. "Determine the factored shear capacity, ϕV_n, of the shear wall."
3. "Determine the expected shear load, V_{re}, that will cause the plate to yield and using this load to design the columns, beams, and connections."

The SPSWs used throughout the building (with a few exceptions), and sized to also meet architectural requirements, had a typical width of 4'6" (1372mm) and average height of 11'6" (3500mm), resulting in an average width-to-height aspect ratio of 0.47, as shown in figure 2-12. The frame consisted of square HSS columns, with WT sections fully welded at the top and bottom to effectively form a moment frame. One leg of a small angle was welded intermittently to the columns, while the outstanding leg was used as a fishplate for attachment of the infill panel via continuous welding. The majority of the panels in the structure utilized 12 ga. (0.105" or 2.7mm) sheet steel, with the material specified to conform to ASTM A1011 with yield strength of 33ksi (227.5MPa). Coupon tests were used to ensure that the material yield strength did not exceed $R_y F_y = 37$ksi (255.1MPa), with minimum percent elongation of 18%.

Recognizing that the aspect ratio is indirectly limited by CAN/CSA S16-01 by requiring a panel tension field angle of inclination between 38° and 45°, double angle stiffeners were added at approximate third points of the panel height to act as compression struts and ensure that the tension field inclination angle remained within the permissible range, effectively creating a local panel aspect ratio of approximately 1.4. This ratio falls in the range explicitly defined by FEMA 450, for L/h (i.e. between 0.8 and 2.5). Both standards' limits are based on experimental

results found in the literature, some of which have been discussed here or summarized elsewhere (Berman and Bruneau 2003a, Rezai 1999).
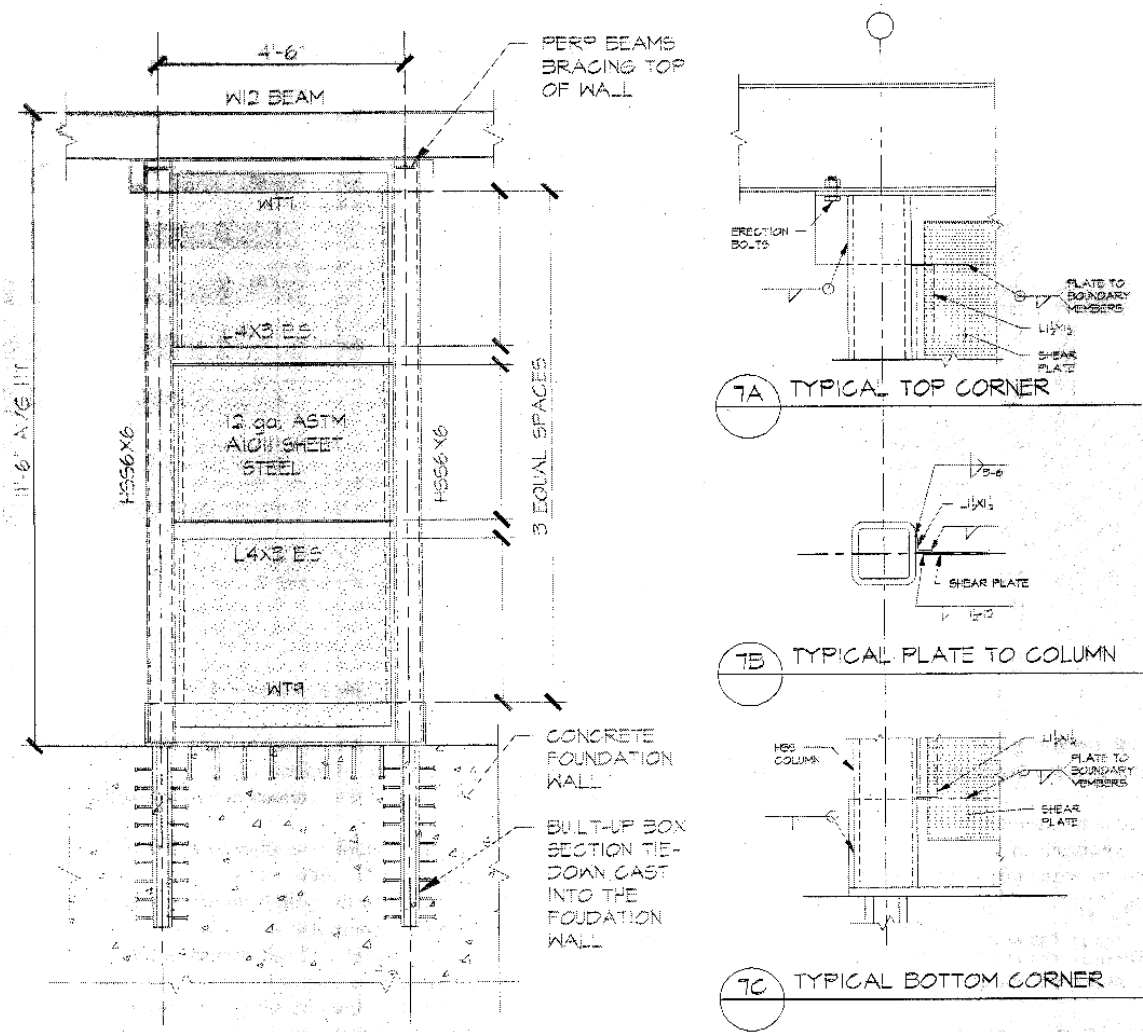
FIGURE 2-12 Details of Typical SPSW used in Woodside, CA Residential Project (Eatherton and Johnson 2004)

SPSWs were found to be well-suited to highly architectural low-rise buildings such as the one described in the paper. The bid from steel fabricators was very close to the project's early estimate made prior to the establishment of the seismic criteria and selection of the lateral resisting system. The ability of the SPSWs to fit into shorter lengths of wall, as well as narrower widths compared with moment framing had distinct architectural advantages. SPSWs in similar applications could be shop fabricated to ensure higher quality and quicker field construction.
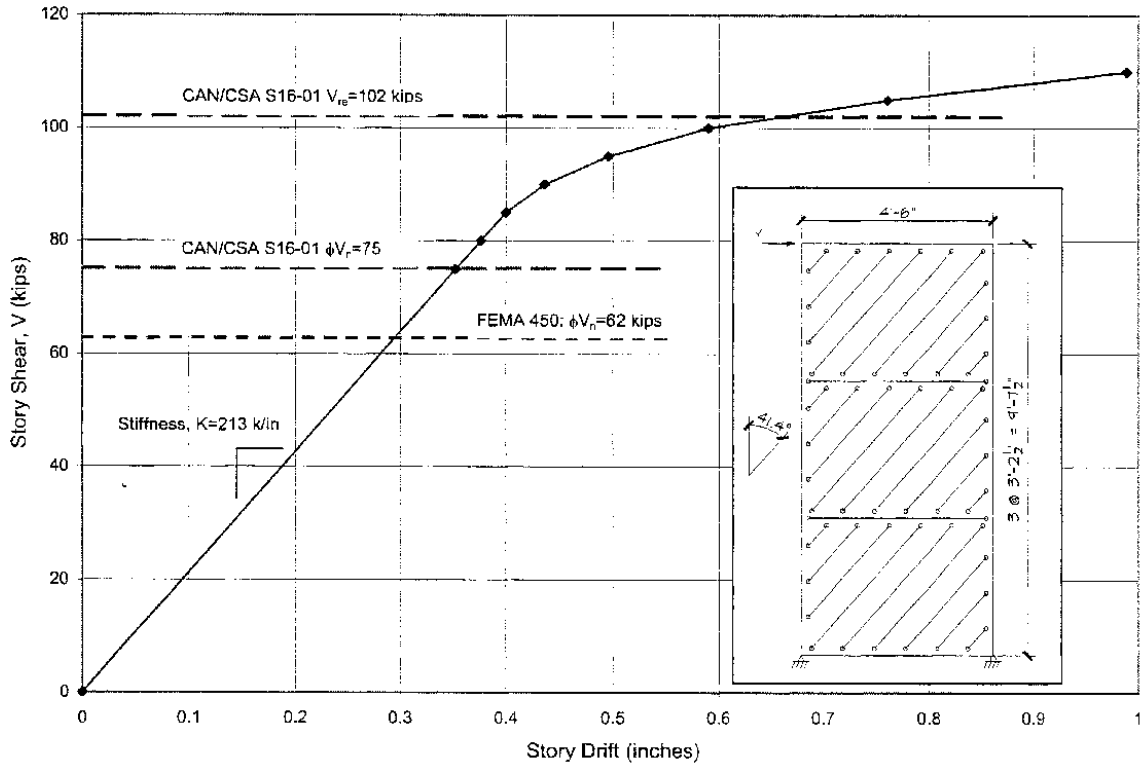
FIGURE 2-13 Pushover Analysis and Model Schematic of Typical SPSW used in Woodside, CA Residential Project (Eatherton and Johnson 2004)

2.11 Lin and Tsai (2004)

Lin and Tsai (2004) conducted quasi-static cyclic tests on SPSWs modeled after the solid panel specimen discussed in chapters 4 and 5 of this report. The researchers added tube-section stiffeners adjacent to the panel to reduce the out-of-plane amplitude of the deformations due to buckling developed by tension field action in the panel. Two specimens of this type were tested: with 2 tubes and 3 tubes, as shown in figures 2-14 and 2-15, respectively. An additional specimen utilized a concrete panel to reduce panel buckling as shown in figure 2-16.

The maximum base shear of these specimens was an average of 4% larger than the unstiffened solid panel specimen; while the elastic stiffness was an average of 15% higher. These approaches therefore provided a marginal improvement to energy dissipation and hysteresis loops exhibited by the unstiffened panel specimen, while simultaneously reducing the out-of-plane panel buckling amplitude.
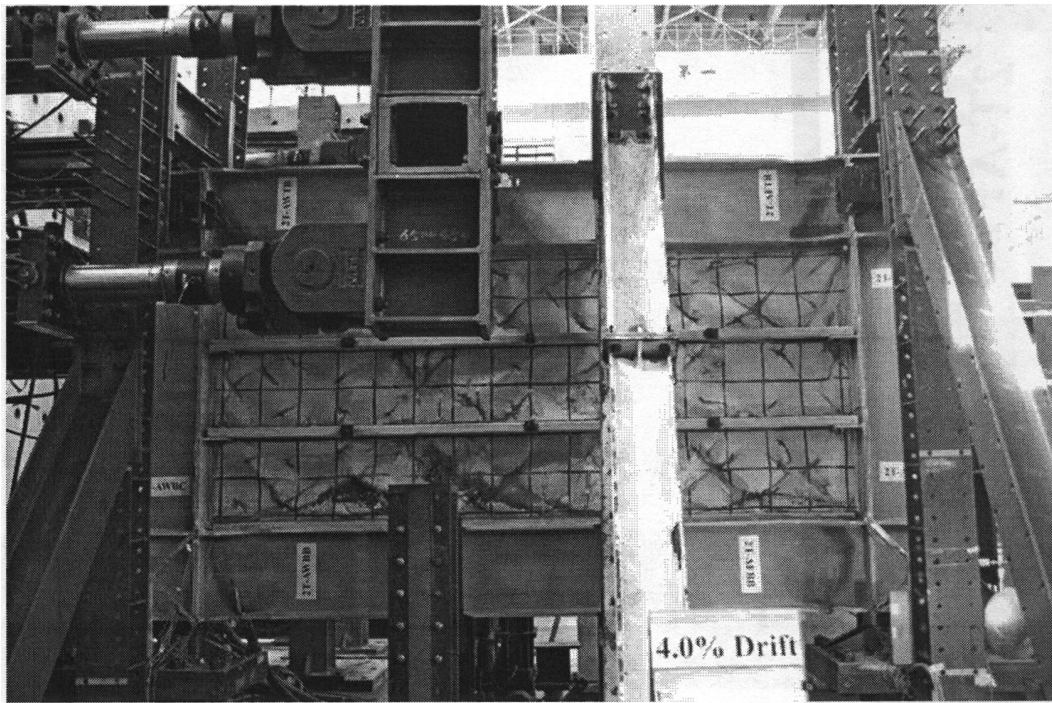
照片 4.76c 試驗結束時之 2T 試體

FIGURE 2-14 Specimen 2T Test at 4% Drift – Lin and Tsai (2004)
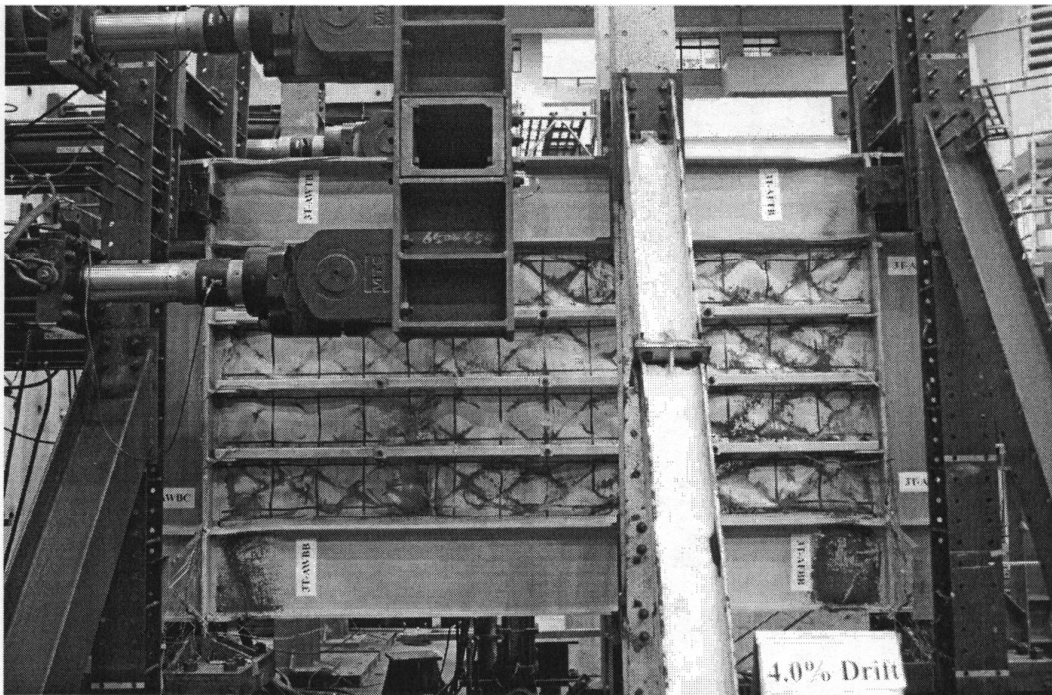
照片 4.92 試驗結束時之 3T 試體

FIGURE 2-15 Specimen 3T Test at 4% Drift – Lin and Tsai (2004)

(a) During Test at 4% Drift

(b) Post-Test with Concrete Removed
FIGURE 2-16 Specimen CP – Lin and Tsai (2004)

SECTION 3

OBSERVATIONS OF SPSW BEHAVIOR,
INTERACTION WITH SURROUNDING FRAME,
AND PRACTICAL CONCERNS FOR IMPLEMENTATION

3.1   General

A key factor affecting the behavior of SPSW is the effect of panel forces on the frame surrounding the infill panels. Unlike damper devices such as a fluid-filled viscous damper or a viscoelastic damper, which exert their resultant reaction forces at discrete locations on the structure (e.g. typically at the frame corners), an SPSW exerts forces along the length of each frame member to which it's attached. With this in mind, developing design strategies to select optimal frame member sizes can be helpful to ensure predictable and ductile behavior.

Furthermore, SPSW infill panels are currently required to be continuous between their boundary elements, which creates an obstacle to the running of utilities within a building and thus limit where these walls can be located. Developing design rules for perforations in an infill panel may increase the adaptability of the SPSW system for a variety of design situations by allowing greater utility access. Two options facilitating access of utilities through an SPSW panel are considered in a later section.

3.2   Top and Bottom Beams

In a multi-story building utilizing an SPSW lateral force resisting system, the basic purpose of the top and bottom beams, at roof and ground (or basement) levels, respectively, is to "anchor" the predominantly vertical SPSW infill panel tension field forces. Therefore, these beams may be referred to as "anchor beams", and their design deserves special attention.

Consider the multi-story building frame pictured in figure 3-1, with SPSW panels in the middle of the three bays. The arrows represent the resultant forces acting on the frame due to the infill panel tension field action that develops during lateral loading of the frame. If there is little or no difference in infill panel thickness on adjacent floors, then, for yielding panels, the forces above and below intermediate beams (non-anchor beams) will result in a negligible or zero net load on

27

these beams. The anchor beams, however, must resist the panel forces from tension field action, in addition to other vertical loads.
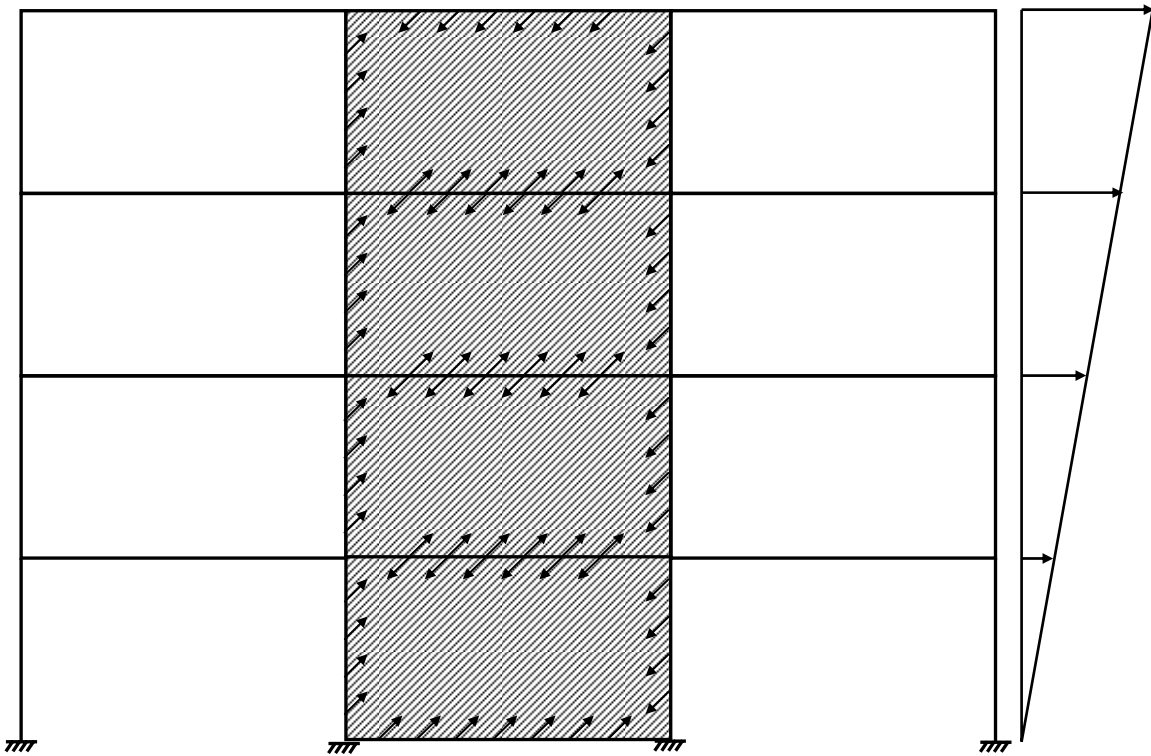
FIGURE 3-1 Moment Resisting Frame with SPSW

To more clearly appreciate the SPSW panel effects on the anchor beam behavior, consider the single bay, single story frame pictured in figure 3-2a, with rigid beam-to-column connections, and column-to-foundation connections free to rotate but restrained against translation. The moment diagram resulting from application of a lateral force is shown below the deformed shape in the same figure. This internal beam moment due to frame sway only (e.g. not considering the tensile force from the infill) varies linearly from one end of the beam to the other. Arrows within the frame of figure 3-2b represent the SPSW panel forces generated during lateral loading of the frame, and the moment diagram corresponding to those tension field action forces only (note that only the component of that force perpendicular to the frame members generate flexural moments). Superposition of these two load cases results in the deformed shape and moment diagram shown in figure 3-2c. At the bottom-right and top-left beam ends, the bare frame moments pictured in (a), are opposed by the panel force-induced moments of (b), while moments at the other ends of each beam are added.
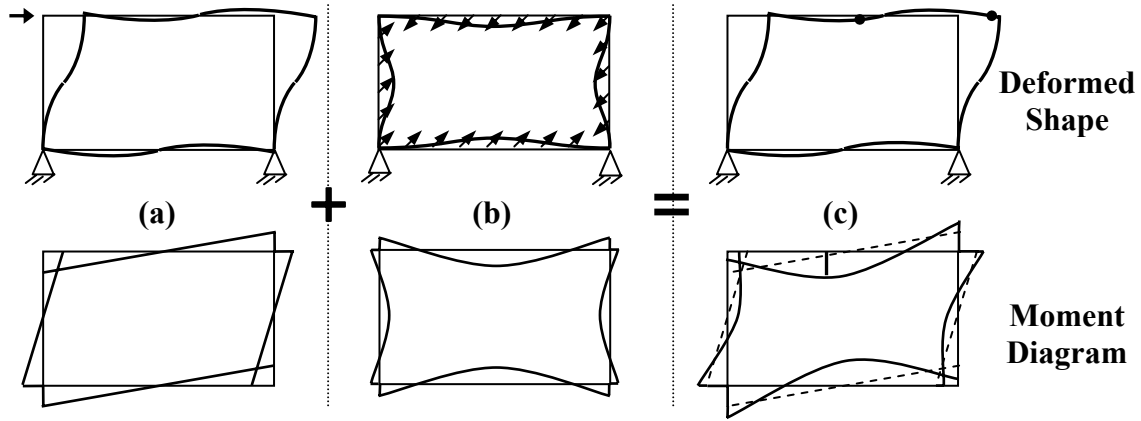
FIGURE 3-2 Deformed Shape, Frame Forces, and Moment Diagrams for:
(a) Frame without Infill Panel; (b) SPSW Infill Panel Forces and;
(c) Combined System

The behavior described above can be investigated quantitatively, prior to beam yielding, by considering the total moment along the beam at a point, x, expressed approximately through the superposition of the linearly varying "sway" moment (i.e. the moment diagram of figure 3-2a), and quadratic-curved moment diagram due to vertical panel forces acting on a fixed end beam (i.e. the moment diagram of figure 3-2b), as given by:

$$M(x) = M_E \cdot \left[\frac{2 \cdot x}{L} - 1 \right] + \left[\frac{\omega}{12} \cdot \left(6 \cdot x^2 + L^2 - 6 \cdot L \cdot x \right) \right] \qquad (3\text{-}1)$$

where M_E is the beam end moment resulting from frame "sway" alone, and the term in the second square bracket is the function defining beam moment over the length, L, due to the vertical component of infill panel forces, ω. It is assumed here that dead and live loads are negligible (but they could otherwise be included in ω). The moment at the left and right beam ends, respectively, is given by:

$$M_L = M(x = 0) = -M_E + \frac{\omega \cdot L^2}{12} \qquad (3\text{-}2a)$$

$$M_R = M(x = L) = M_E + \frac{\omega \cdot L^2}{12} \qquad (3\text{-}2b)$$

Prior to yielding, and depending on the relative values of sway and panel force moments, the values of the end moments may vary greatly.

Note that superposition of these moment diagrams suggests that plastic hinges could develop at a beam end and somewhere near mid-span, depending on the beam and infill panel properties, as described in subsequent sections. This type of mechanism could potentially induce significant plastic deformations of the anchor beams, which would then reduce their effectiveness in anchoring the diagonal tension field forces of the SPSW infill panel, and therefore result in a reduction of system strength. Note that this is illustrated above in figure 3-2c considering an assumed plastic collapse mechanism for a unidirectional lateral load. During a severe earthquake, as the structure oscillates back and forth, hinges may form at both beam ends, in addition to the hinge within the span, which may migrate along the beam during reversing yield excursions. This behavior would result in pinching of hysteresis loops, and reduced energy dissipation.

3.2.1 Design Considerations for Anchor Beams

It has already been established that the resulting moment diagram for an SPSW anchor beam is obtained by superposition of beam end moments due to frame sway and a quadratic "hanging" moment due to the vertical component of infill panel forces. Using the "equilibrium method" for calculating the required beam strength and collapse mechanism (Bruneau *et al.* 1998, Chen and Sohal 1995), an expression for the moment at a distance *x* along the beam from the left support, can be derived by first considering the moment diagram under the applied loading for a statically determinate beam obtained by removing the end fixities, and superposing the moment diagrams obtained for each end moment, M_R and M_L, applied to the same statically determinate beam and corresponding to the degrees of indeterminacy removed in the first step, as shown in figure 3-3. The equation for the resulting moment diagram, *M(x)*, using the sign convention shown in the figure, is:

$$M(x) = \frac{\omega \cdot x}{2} \cdot (L - x) - M_R \cdot \frac{x}{L} + M_L - M_L \cdot \frac{x}{L} \qquad (3\text{-}3)$$

The location of the "maximum moment within the span," x_{span}, is calculated by differentiating *M(x)* with respect to *x*, setting the result equal to zero, and solving:

$$x_{span} = \frac{L}{2} - \left[\frac{M_L + M_R}{\omega \cdot L} \right] \qquad (3\text{-}4)$$

Substituting (3-4) into (3-3) and simplifying:

$$M_{span} = \frac{\omega \cdot L^2}{8} + \frac{[M_L + M_R]^2}{2 \cdot \omega \cdot L^2} + \frac{M_L - M_R}{2} \tag{3-5}$$
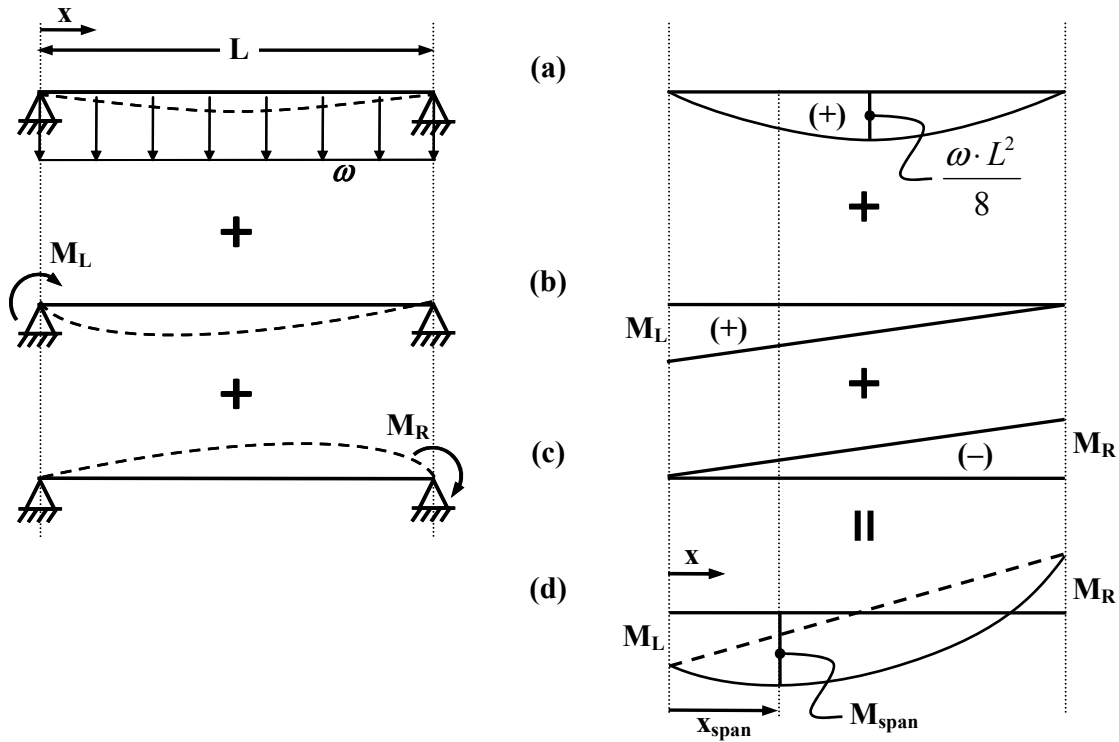
FIGURE 3-3 Deformed Shape, Loading, and Moment Diagrams For Calculating Anchor Beam Collapse Mechanisms Using Equilibrium Method For: (a) Vertical Component Of Infill Panel Forces; (b) Left End Redundant Moment; (c) Right End Redundant Moment; (d) Combined Moment Diagram

By considering various values of the end moment, M_R and M_L, in this expression, anchor beam ultimate behavior can be further examined. Consider possible three cases of ultimate behavior as shown in figure 3-4: (a) $M_L = M_p$ and $M_R = M_p$; (b) $M_L = 0$ and $M_R = M_p$; and

(c) $M_L = -M_p$ and $M_R = M_p$ using the sign conventions/orientations shown in figure 3-3. By substituting these sets of conditions and $M_{span} = M_p$ into (3-5), the equation can be solved for an ultimate load, ω_{ult}, respectively obtained for each case as:

$$\omega_{ult} = \begin{cases} \dfrac{4 \cdot M_p}{L^2} & (a) \\[4mm] \dfrac{2 \cdot \left(3 + \sqrt{8}\right) \cdot M_p}{L^2} = \dfrac{11.657 \cdot M_p}{L^2} & (b) \\[4mm] \dfrac{16 \cdot M_p}{L^2} & (c) \end{cases} \qquad (3\text{-}6)$$

corresponding to x_{span} values (as a fraction of L) of 0, $\left(\sqrt{2} - 1\right) \approx 0.414$, and 0.5 respectively.

Similarly, if the maximum vertical load, ω_{max}, is known from a given infill panel strength and thickness, then the required anchor beam strength can be calculated by substituting the same three sets of moment end conditions into (3-5), and solving for the required M_p:

$$M_p = \begin{cases} \dfrac{\omega_{max} \cdot L^2}{4} & (a) \\[4mm] \dfrac{\left(3 - \sqrt{8}\right) \cdot \omega_{max} \cdot L^2}{2} = \dfrac{\omega_{max} \cdot L^2}{11.657} & (b) \\[4mm] \dfrac{\omega_{max} \cdot L^2}{16} & (c) \end{cases} \qquad (3\text{-}7)$$

For comparative purposes, recall that the required strength of a simply supported anchor beam is:

$$M_p = \dfrac{\omega_{max} \cdot L^2}{8} \qquad (3\text{-}8)$$

This minimum strength is half that required by case (a), but larger than the values of cases (b) and (c). This suggests that simply supported anchor beams could be designed to be smaller than fully fixed-end anchor beams, but these would not provide any contribution to seismic energy dissipation and lateral load resistance.

The location of M_{span} can be constrained to remain within the span:

$$0 \le x_{span} \le L \qquad (3\text{-}9)$$

then, by substituting (3-4) into (3-9), this inequality is solved for the loading conditions satisfying those constraints:

$$|M_L + M_R| \le \frac{\omega \cdot L^2}{2} \qquad (3\text{-}10)$$

Substituting the end moment conditions for the three cases considered above, and solving for the vertical panel load, ω.

$$\omega \ge \begin{cases} \left|\dfrac{4 \cdot M_p}{L^2}\right| & (a) \\[2em] \left|\dfrac{2 \cdot M_p}{L^2}\right| & (b) \\[2em] 0 & (c) \end{cases} \qquad (3\text{-}11)$$

Finally, these conditions can be combined with the ultimate loads calculated in (3-6), providing a range of ω values for which M_{span} is located within the span, and an upper limit for the value of ω, attained when $M_{span} = M_p$ and a mechanism as defined previously, has formed:

$$\frac{4 \cdot M_p}{L^2} \le \omega \le \frac{4 \cdot M_p}{L^2} \qquad (a)$$

$$\frac{2 \cdot M_p}{L^2} \le \omega \le \frac{2 \cdot \left(3 + \sqrt{8}\right) \cdot M_p}{L^2} \qquad (b) \qquad (3\text{-}12)$$

$$0 \le \omega \le \frac{16 \cdot M_p}{L^2} \qquad (c)$$

Note that for case (a), both limits of the inequality in are identical. Therefore, when plastic hinges form at beam-ends in the same manner presented for case (a), $x_{span} = 0$ and the third hinge required to form a beam collapse mechanism is coincident with the left support plastic hinge (corresponding to beam-hinge locations in a sway collapse mechanism).
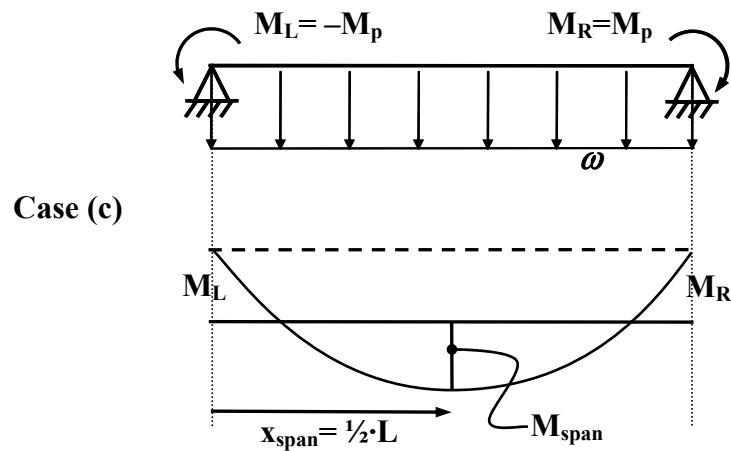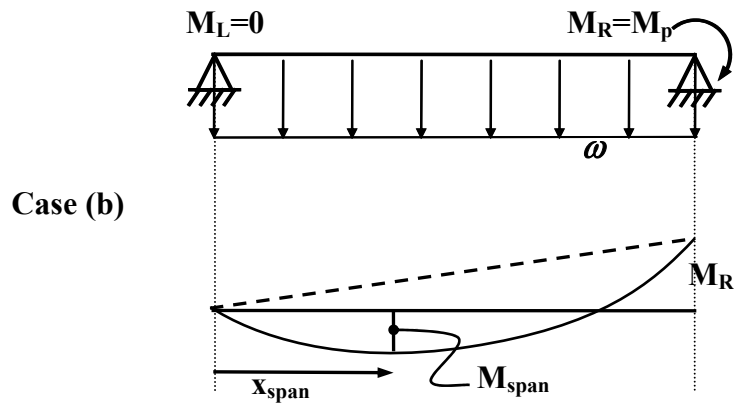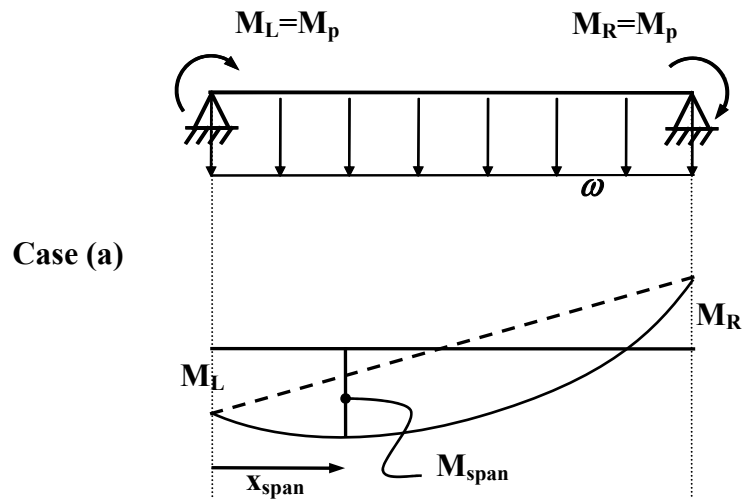
FIGURE 3-4 Anchor Beam Loading and Moment Diagram for:
(a) $M_L = M_p$ and $M_R = M_p$; (b) $M_L = 0$ and $M_R = M_p$; (c) $M_L = -M_p$ and $M_R = M_p$

In figure 3-5, (3-3) is plotted with the conditions: $M_L = M_R = \kappa \cdot \frac{1}{8} \cdot \omega \cdot L^2$, for various values of κ, to demonstrate this trend. The resulting moment diagram, $M(x)$, is normalized by the hanging moment on the vertical axis ($\omega L^2/8$), and plotted versus normalized distance from the left support on the horizontal axis. As the value of the end moment increases, the maximum moment within the span shifts from mid-span, reaching the left support when $M_L = M_R = \frac{1}{4} \cdot \omega \cdot L^2$. This corresponds to $\kappa=2.0$, which is the solution for the case (a) mechanism as listed in (3-7a) when $\omega = \omega_{ult}$ and $M_L = M_R = M_p$. Based on the trends shown in this figure, a method for enhancing beam performance is discussed further in the next section.
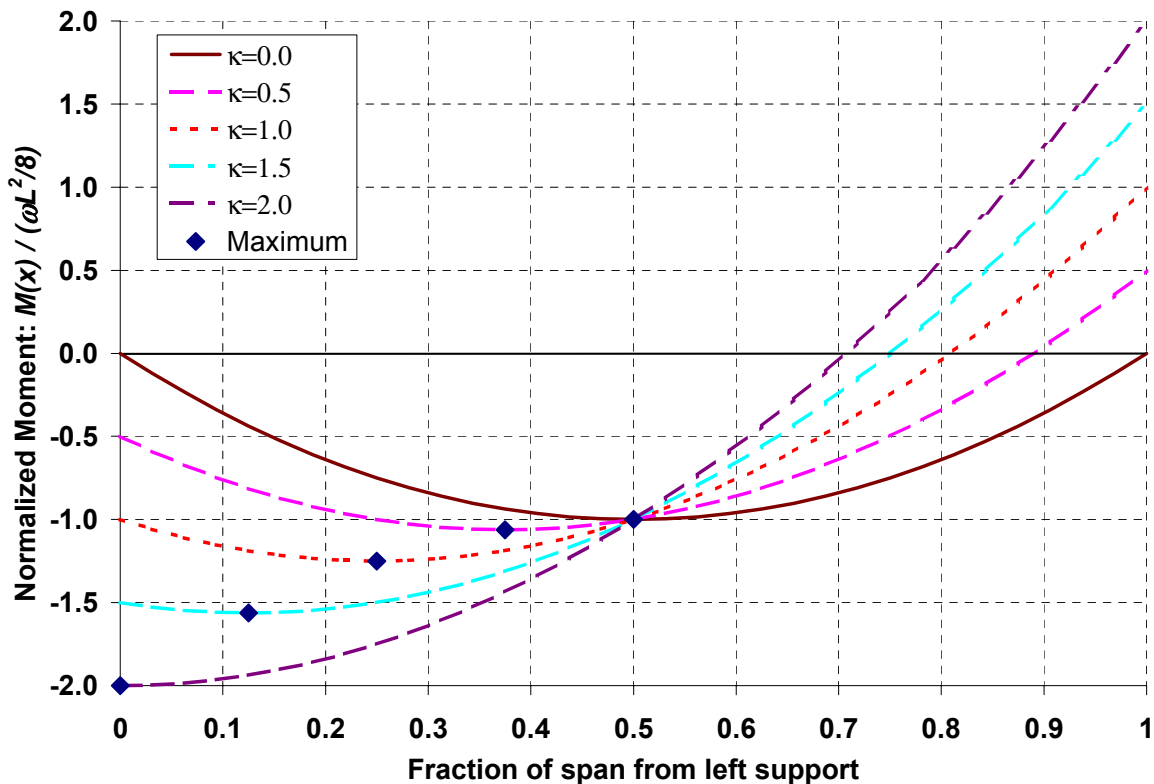
**FIGURE 3-5 Normalized Moment Diagram for End-Moment Values of
0, ½, 1, 1½, and 2 times the Hanging Moment $\omega L^2/8$**

3.2.2 Reduction of Beam End Moments

Considering the possible anchor beam mechanisms and moment diagrams for various end conditions presented in the previous section, a new/innovative method for anchor beam design is proposed below. As noted above, after both end moments have reached M_p, the maximum infill panel load that can be resisted by the anchor beam (without developing a plastic hinge along the

span) is half the load that could be resisted if a simply supported anchor beam was used instead. Conversely, for a given infill panel load, a fully fixed-end anchor beam must have twice the flexural strength of a simply supported anchor beam.

Therefore, to promote the use of fully fixed connections at the end of SPSW anchor beams to resist larger panel forces, while allowing a more optimal design of the anchor beams, it is proposed to design anchor beams by locally reducing the beam end moment strength through the use of reduced beam section (RBS), or "dog-bone," detailing. RBS connections have been introduced for the design of special moment resisting frames and their detailing is fully described in FEMA 350 (2000). The proposed design procedure would reduce anchor beam end moment strength to some fraction of the plastic moment, $\beta \cdot M_p$, where β is the ratio of the plastic modulus at the location of the RBS, Z_{RBS}, to the plastic modulus of the beam section, Z_{xb}. For current purposes, β, referred to here as the "RBS plastic modulus reduction ratio" may vary between a theoretical value of zero (equivalent to a simple support) and one (fully fixed support), through selection of the RBS flange reduction geometry described in FEMA 350.

Therefore, imposing the constraints on (3-5) that $M_{span} \leq M_p$ and $M_L = M_R = \beta \cdot M_p$, an anchor beam at the ultimate load for these conditions must satisfy:

$$M_p = \frac{\omega \cdot L^2}{8} + \frac{2}{\omega}\left(\frac{\beta \cdot M_p}{L}\right)^2 \tag{3-13}$$

This expression can be reorganized as a quadratic equation in either ω or M_p and solved as done in (3-6) and (3-7) above for ultimate panel load and required beam strength:

$$\omega_{ult} = \frac{4 \cdot M_p}{L^2} \cdot \left[1 + \sqrt{1-\beta^2}\right] \tag{3-14}$$

$$M_p = \frac{\omega \cdot L^2}{4} \cdot \left[\frac{1}{1+\sqrt{1-\beta^2}}\right] = \frac{\omega \cdot L^2}{8} \cdot \left[\frac{2}{1+\sqrt{1-\beta^2}}\right] \tag{3-15}$$

Note that as β approaches the limits of zero and one, these solutions approach the simply supported and fixed end cases, respectively, derived in the previous section above (e.g. compare (3-15) using ($\beta=1$) and ($\beta=0$) with (3-8) and (3-7a)).

The vertical component of panel stress can be related to the panel properties by:

$$\omega = F_{yp} \cdot t \cdot \cos^2 \alpha \qquad (3\text{-}16)$$

where t is the panel thickness; F_{yp} is the panel yield stress, assuming elastic perfectly plastic material; and α is the panel tension field angle of orientation with respect to vertical. Substituting this relation into (3-15) and solving for the beam plastic modulus, Z_x:

$$Z_x \geq \frac{L^2 \cdot t \cdot \cos^2 \alpha}{4} \cdot \frac{F_{yp}}{F_{yab}} \cdot \left[\frac{1}{1 + \sqrt{1 - \beta^2}} \right] \qquad (3\text{-}17)$$

where F_{yab} is the yield stress of the anchor beam.

Using this equation to design anchor beams, consider a frame with member yield stress, F_{yab} =345MPa and bay width of 7000mm between column flanges (such as the middle bay of the three bay moment frame of the MCEER demonstration hospital (Yang and Whittaker 2002)). Assume a tension field orientation of $\alpha = 45°$, a value typically chosen for early stages of SPSW design (Driver *et al.* 1997), and, for the sake of this example, assume t =3.25mm (0.125 in). Figure 3-6 shows required beam plastic modulus versus infill panel yield stress for beam-end strength reduction values of 0.5, 0.75, and 0.95, to show trends in behavior as β changes, as well as the simply supported case of $\beta = 0.0$ and fully fixed case, $\beta = 1.0$, discussed above. From this figure, a designer can select a beam section adequate to anchor the tension field forces exerted by the infill panel at the top and bottom of the wall for the given constraints.

The relative reduction in required beam plastic modulus (as a fraction of that needed for end condition case (a) from section 3.2.1) with varying RBS beam end strength reduction is given by the expression in the square brackets of (3-17). This term is plotted versus the RBS plastic modulus reduction ratio for the range $0.0 \leq \beta \leq 1.0$ in figure 3-7, demonstrating the relationship between this relative reduction in required strength for a given infill strength.
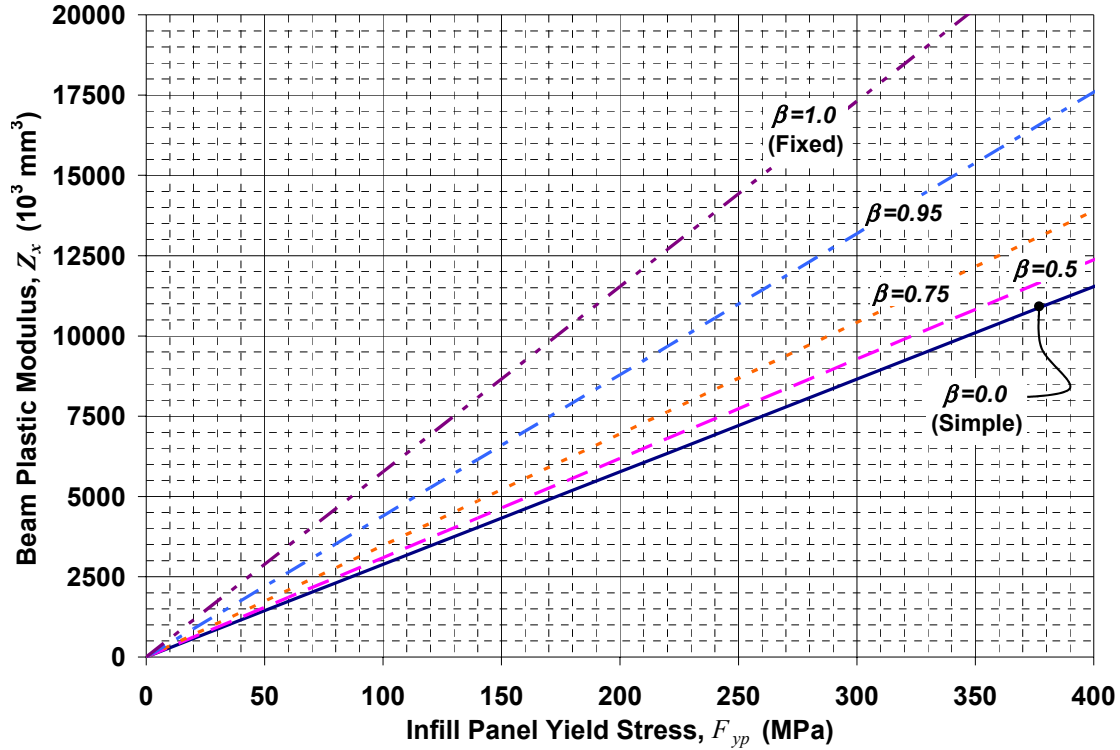
FIGURE 3-6 Required Beam Plastic Modulus as a Function of SPSW Plate Yield Stress for
L=7000mm, t =3.25mm, F_{yab} = 345MPa, **and Various End Conditions,** β.

$$X = \left[\frac{1}{1 + \sqrt{1 - \beta^2}}\right]$$
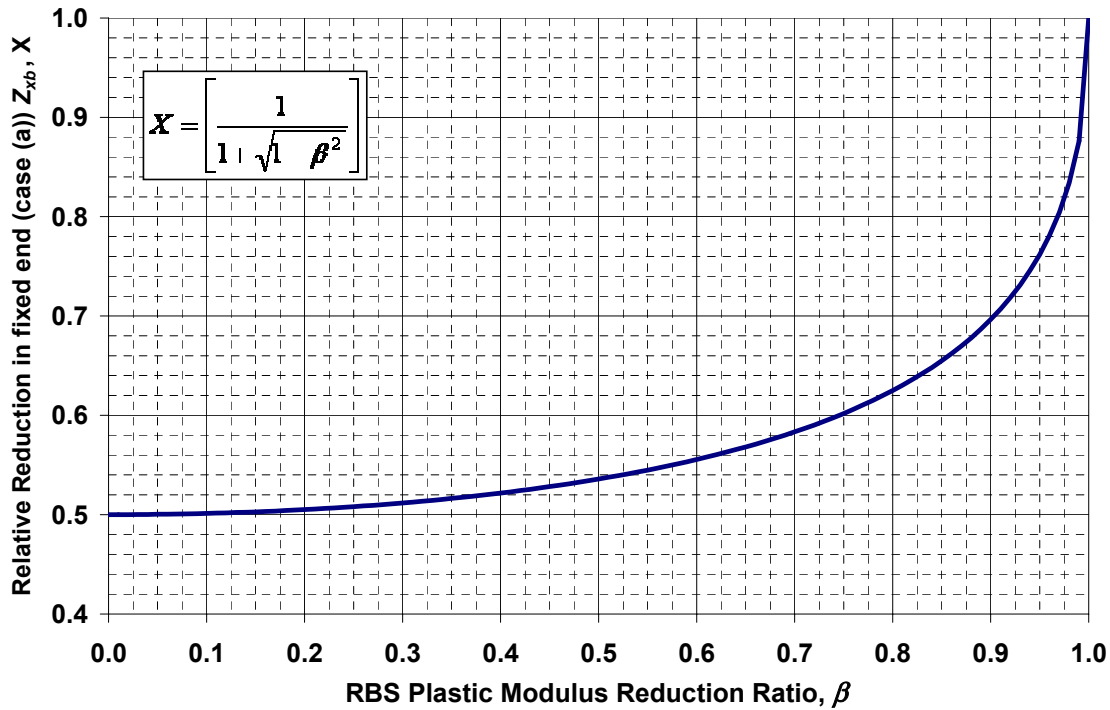
FIGURE 3-7 Relative Reduction in Fixed End Beam Plastic Modulus as a Function of RBS
Plastic Modulus Reduction Ratio

38

3.3 Effects of SPSW on Intermediate Beams and Adjacent Columns

For the purpose of interest here, intermediate beams in a multistory building frame are defined as those beams that do not support the top (roof) or bottom floors. As described elsewhere (Kulak *et al*. 2001), and here in subsequent sections, within a frame bay containing an SPSW, these structural elements will be less affected by the forces of the yielding SPSW panel than the top and bottom beams that "anchor" these forces. For panels of equal or similar thickness above and below an intermediate beam at story *i*, infill panel yielding will have zero or negligible net loading effect on the beam compared with frame action alone (without an SPSW infill). However, due to progressively increasing drift of the SPSW as they resist lateral loads, due to compatibility of deformations, plastic hinges may eventually develop at the ends of the intermediate beams. The following sub sections will outline design limit states to prevent yielding of these members under monotonically increasing lateral loads. Note that in the following, joint panel zone dimensions and deformations, as well as frame member shear and axial deformations, are neglected.

3.3.1 Steel Plate Shear Walls as a "Structural Fuse"

Vargas and Bruneau (2005) have investigated the use of energy dissipation devices (EDD) in the context of a "structural fuse." By this, a yielding device is considered to act as a "fuse," meant to yield hysteretically, or otherwise dissipate the seismic input energy imparted to the system, while the structural frame remains essentially undamaged while deforming within its elastic limits. Therefore, following a seismic event that engaged the EDD, the device can be removed and replaced, analogous to replacement of a burned-out fuse in an overloaded electrical system.

Among many different types of devices developed for this purpose, metallic EDDs commonly used in practice include buckling restrained braces (BRBs) (Uang and Nakashima 2003), Added Damping And Stiffness (ADAS) elements (Whittaker *et al*. 1991), and Triangular Added Damping And Stiffness (TADAS) elements (Tsai *et al*. 1993). These devices are typically implemented within a building frame as, or using, a bracing system similar to a concentrically braced frame (CBF) in an inverted-V configuration, which transmits forces to the frame via connections idealized as single attachment points at the beam mid-span and beam-column intersection locations, as shown in the free body diagrams of figure 3-8. Idealized models such

as those used in this figure are used to perform capacity design checks of the surrounding frame members, i.e. to ensure that they are designed to elastically resist the forces developed by the yielding devices. SPSWs, however, when compared to these other EDDs, present additional challenges for capacity design of the boundary frame. SPSWs are fully connected to each member of the surrounding boundary frame, resulting in essentially uniformly distributed loads along the length of each boundary frame member, as shown in figure 3-1, a fact which complicates the relatively simple check of member limit states described above for other EDD options.

BRB Frame Forces   **ADAS/TADAS Frame Forces**
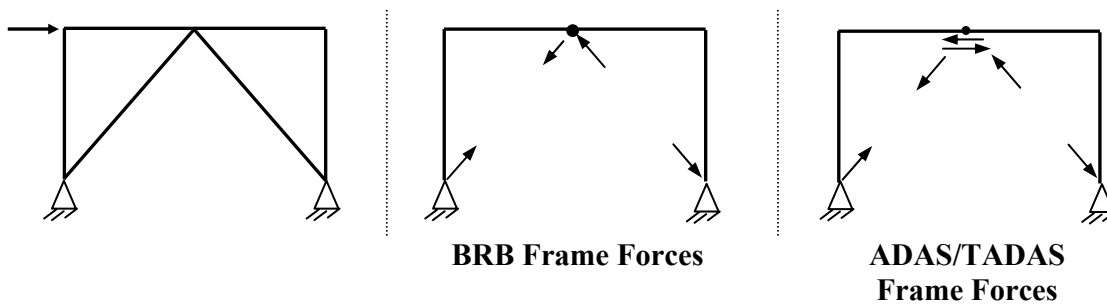
FIGURE 3-8 Schematic of Loading and Frame Forces for
Single Story BRB and ADAS/TADAS frames

The concept of an EDD as a "fuse" relies on the premise that the structure's yield drift (or other suitable performance limit that should not be exceeded) is reasonably predictable, and that the EDD is designed to be effective and dissipate the design earthquake input energy such that the frame does not exceed this performance limit. For the case of an SPSW as discussed below, a structural fuse implementation could be formulated to require that yielding of columns, and intermediate beams, is prevented, i.e. yielding of beams, with the exclusion of top and bottom level "anchor" beams as defined above. While it is debatable whether this should be a desirable performance goal, it is worthwhile to explore, in a preliminary way, what would be required, as a minimum, to achieve it. Incidentally, the following investigation of limits for implementing SPSWs within the structural fuse concept is not used beyond section 3.3, i.e. SPSWs are analyzed, designed, and tested, without any consideration of structural fuse concepts in the rest of this document because it is beyond the primary scope of work.

3.3.1.1 Yield Limits of Frame without SPSW

Yield forces and displacement for a moment resisting frame (MRF), without additional EDDs, subjected to lateral loads only, can be approximated by considering the free body diagram of a cruciform section consisting of a column and beam, from the mid-height and mid-span points, respectively, on either side of a typical interior joint, as in figure 3-9. These locations are usually assumed inflection points, or points of zero moment, for the preliminary design of frames subjected to lateral loads using the portal or cantilever methods of approximate frame analysis (Taranath 1998, Eligator *et al*. 1997). The deformed shape of the interior cruciform is shown in figure 3-10a.
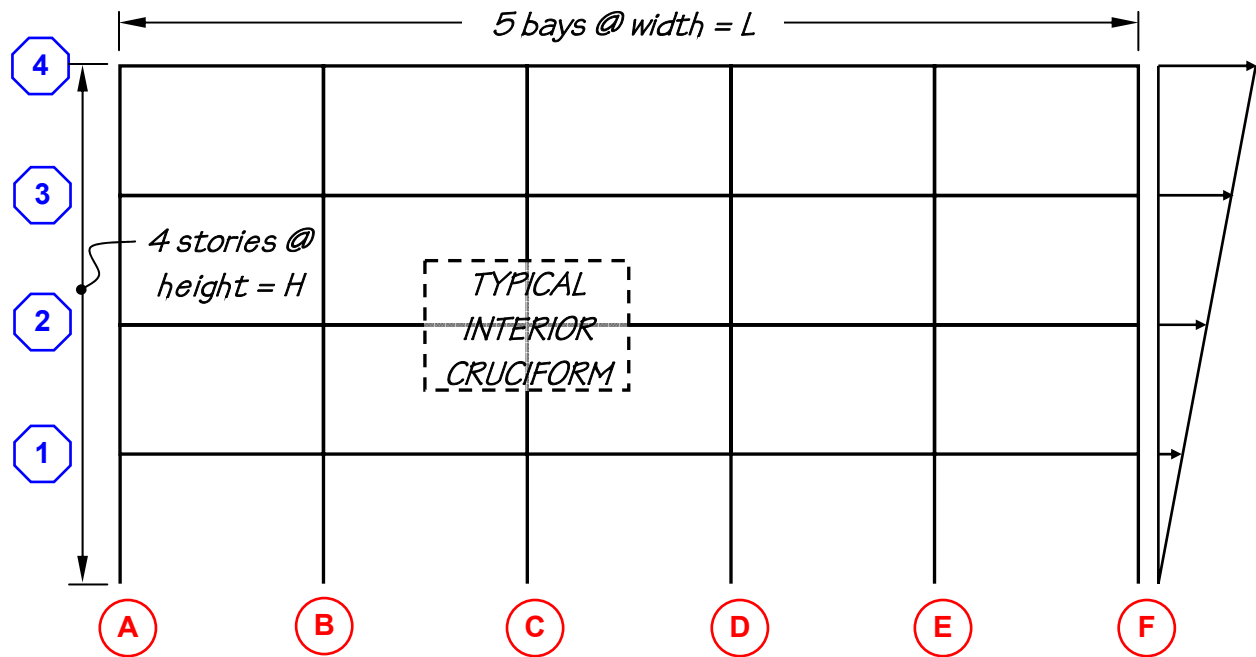
FIGURE 3-9 Moment Resisting Frame without SPSW

From moment equilibrium of the cruciform free body diagram, the shear at the inflection points in the beam and column, F_v and F_H, respectively, are related by:

$$F_v \cdot L = F_H \cdot H \tag{3-18}$$

where H and L are the frame bay height and width between beam and column centerlines, respectively.

41
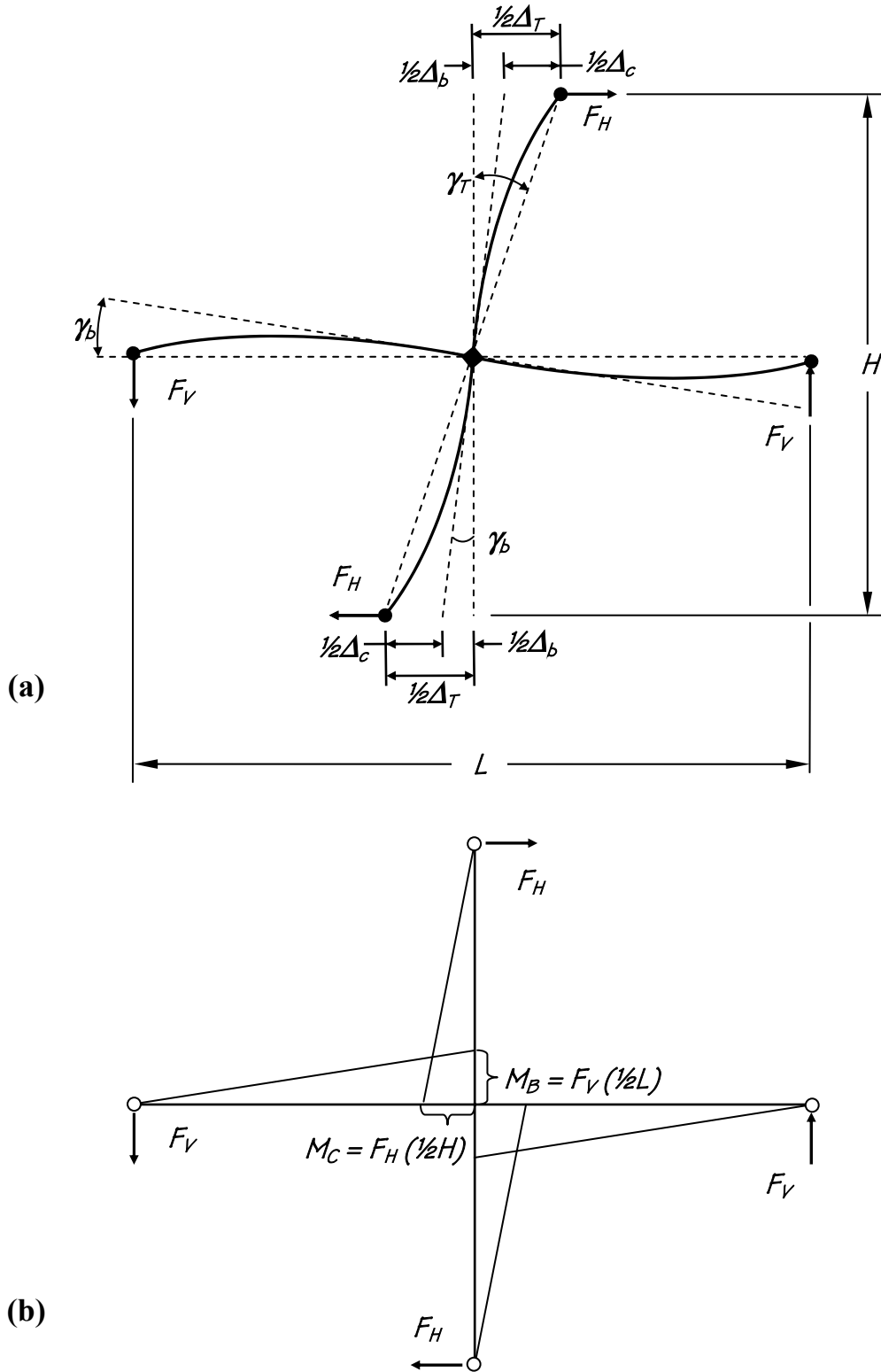
FIGURE 3-10 Cruciform of Frame Interior Joint without Infill Panel: (a) Deformed Shape and (b) Moment Diagram

Total horizontal displacement between column inflection points can be expressed as a summation of the effects from these beam and column shears. Beam bending, and the resulting cruciform joint rotation, produces an elastic horizontal displacement between column inflection points of:

$$\Delta_b = \frac{F_v \cdot H \cdot L^2}{12 \cdot E \cdot I_b} = \frac{F_H \cdot H^2 \cdot L}{12 \cdot E \cdot I_b} \tag{3-19}$$

where E and I_b are the elastic modulus of steel (200GPa) and moment of inertia of the beam, respectively.

Shear forces at the column inflection points cause an additional horizontal displacement of:

$$\Delta_c = \frac{F_H \cdot H^3}{12 \cdot E \cdot I_c} \tag{3-20}$$

where I_c is the moment of inertia of the column.

Therefore, the resulting total horizontal displacement between column inflection points, Δ_T, is:

$$\Delta_T = \frac{F_H \cdot H^3}{12 \cdot E \cdot I_c} + \frac{F_H \cdot H^2 \cdot L}{12 \cdot E \cdot I_b} = \frac{F_H \cdot H^2}{12 \cdot E}\left(\frac{H}{I_c} + \frac{L}{I_b}\right) \tag{3-21}$$

Or expressed as interstory drift:

$$\gamma_T = \frac{\Delta_T}{H} = \frac{F_H \cdot H}{12 \cdot E}\left(\frac{H}{I_c} + \frac{L}{I_b}\right) \tag{3-22}$$

If strong-column/weak-beam behavior is desired, then the column elastic modulus, for the initial yielding limit state, must be greater than that of the beam (e.g. $S_{xc} \geq S_{xb}$). From figure 3-10 and (3-18), the beam moment at the joint, M_B, is equal to:

$$M_B = F_H \cdot \frac{H}{2} \tag{3-23}$$

Setting this beam moment equal to the yield moment M_{yb}, where M_{yb} is equal to $S_{xb} \cdot F_{yb}$, and the shear acting at the column inflection point at beam yield, V_{yb}, is given by:

$$F_H = V_{yb} = \frac{2 \cdot S_{xb} \cdot F_{yb}}{H} \tag{3-24}$$

Substituting (3-24) into (3-22), the drift at beam yield is calculated:

$$\gamma_{T.y} = \frac{S_{xb} \cdot F_{yb}}{6 \cdot E}\left(\frac{H}{I_c} + \frac{L}{I_b}\right) \tag{3-25}$$

This relation can be used to determine an approximate frame yield drift limit for an unretrofitted frame (or incidentally, a frame retrofitted with an EDD other than SPSW).

3.3.1.2 Yield Limits of Frame with SPSW

In order to implement an SPSW-retrofitted moment frame within the context of the "fuse concept," a yield drift limit must be derived to use as a maximum displacement criteria. Consider the frame pictured in figure 3-11, identical to the bare MRF previously considered in figure 3-9, but now with an SPSW panel placed in the middle bay of each story as shown.
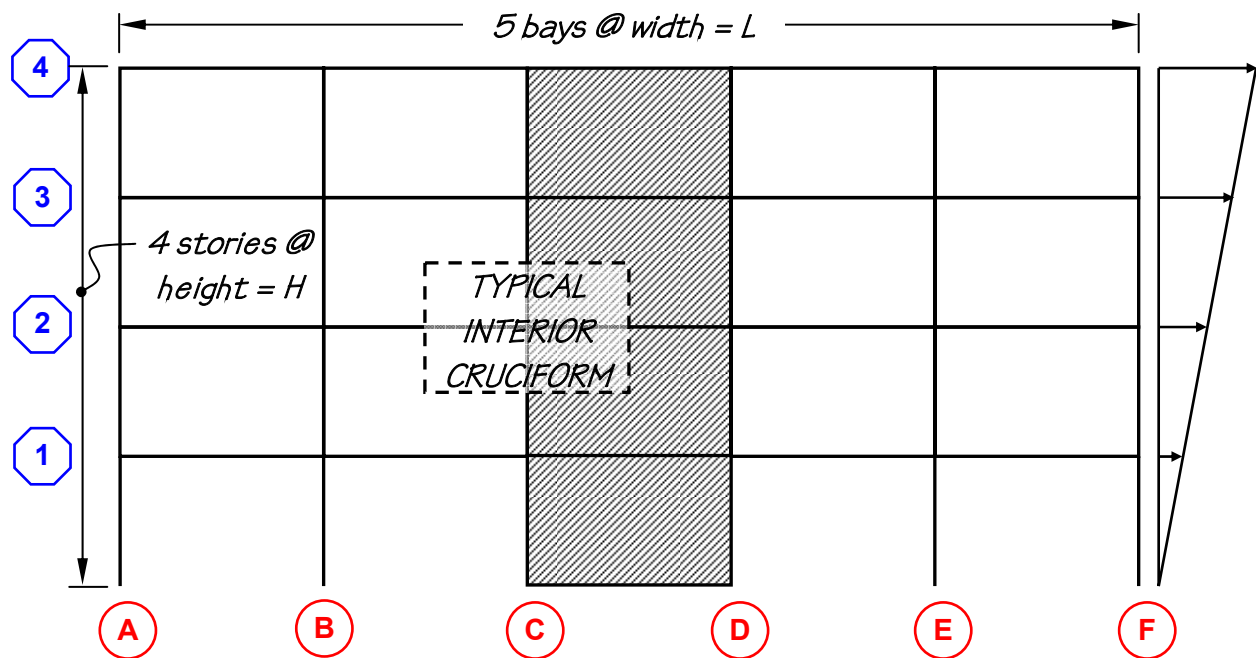
FIGURE 3-11 Moment Resisting Frame with SPSW

If the presence of gravity loads is once again assumed negligible, then the cruciform substructure discussed in the previous section is now subjected to the forces shown in figure 3-12. Considering a free body diagram of the beam section with SPSW forces acting on it, to the right of the column, in which moments and shears caused by the distributed panel yield force on top of the beam, $F_{yp} \cdot t_p$, are equal to those from the story below, therefore, leaving the beam shear

unchanged from the bare frame case. Column shears, however, change with the addition of the panel forces, invalidating the previous assumption of inflection points located at mid-height of columns. A systematic investigation into the significance of the inflection point shift remains to be done. However, based on the simplified calculations shown in Appendix A, the drift between the shifted inflection points on adjacent floors remains unchanged from the bare frame case (prior to frame yielding), for the underlying assumptions described above. With that, the following approximate method for calculating frame drift at yield is described.
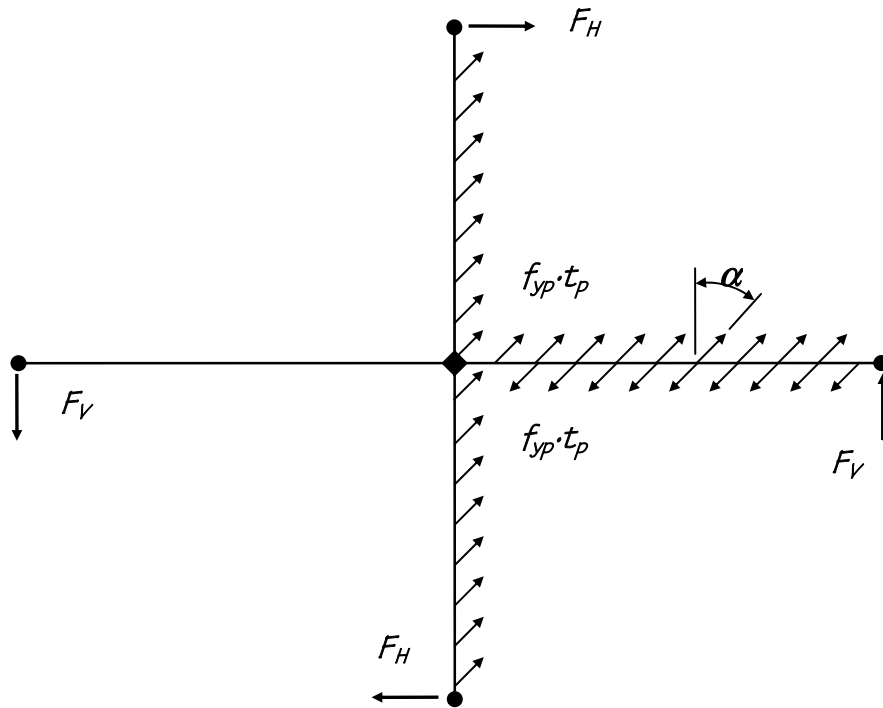
**FIGURE 3-12 Free Body Diagram of Cruciform of Frame Interior Joint
with SPSW Infill Panel Forces**

The resulting column moment diagram may be approximately calculated by considering the free body diagram of an entire column, from beam-to-beam. In figure 3-13, the free body diagrams and moment diagrams for the two superimposed loadings are shown: first, from bare frame action, second, for the distributed load from the component of the panel stress perpendicular to the longitudinal axis of the column assuming fixed-end boundary conditions. The total moment from these two load conditions can then be written as a function of the distance, y, from the column base.

45

$$M_{tot.c}(y) = M_C \cdot \left[1 - \frac{2 \cdot y}{H} \right] + \frac{\omega}{12} \cdot \left[6 \cdot y^2 + H^2 - 6 \cdot H \cdot y \right] \qquad (3\text{-}26)$$

where ω here is the component of panel stress perpendicular to the longitudinal column axis, and with the maximum moment occurring at the ends of the column for columns that are designed to remain elastic. For the direction of lateral load and location of SPSW panel shown in figure 3-13, for example, this would occur at $y=0$, and the maximum moment is:

$$M_{tot.c.\max} = M_C + \frac{\omega \cdot H^2}{12} \qquad (3\text{-}27)$$
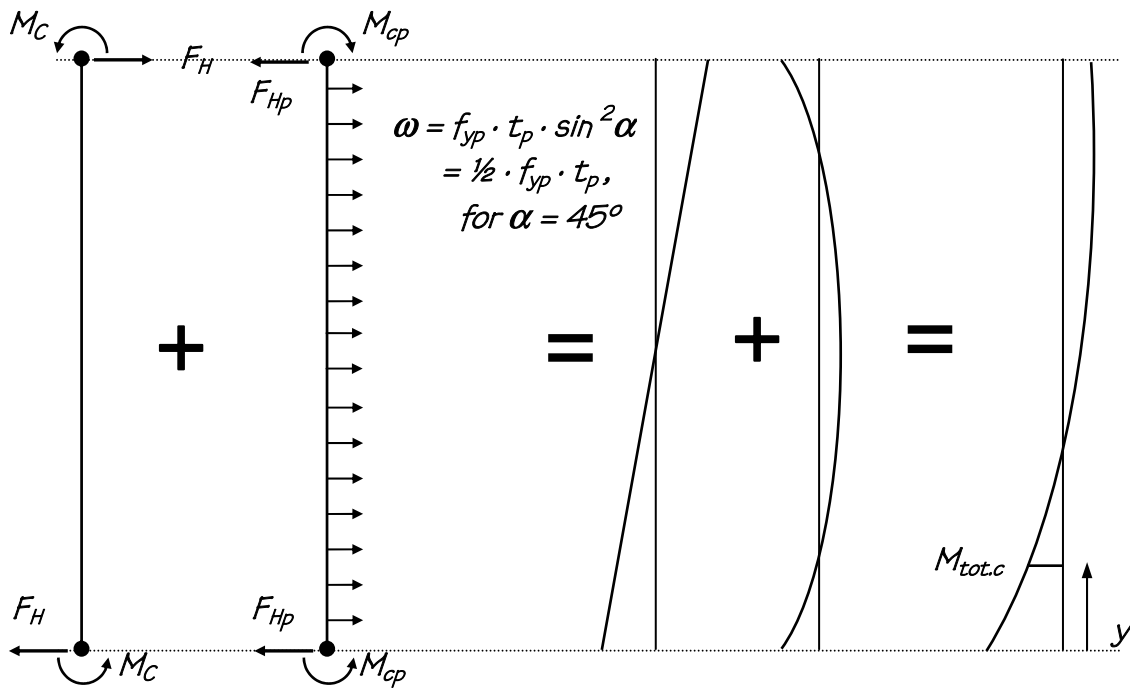
FIGURE 3-13 Forces and Moment Diagrams for Interior Column (Floor-To-Floor) from Frame with SPSW Infill Panel

To satisfy the fuse concept criteria of elastic frame behavior, the beam yield moment strength, M_{yb} (which is equal to $S_{xb} \cdot F_{yb}$), must exceed the beam moment demand, M_B. In addition, from the assumption neglecting panel zone dimensions, the beam and column moments due to frame sway are equal:

$$S_{xb} \cdot F_{yb} \geq M_B = M_C \qquad (3\text{-}28)$$

However, to prevent column yielding, the column moment strength, $S_{xc} \cdot F_{yc}$, must exceed (3-27). Therefore, by utilizing this constraint and setting the frame sway moments equal to the beam strength, $S_{xb} \cdot F_{yb}$, following from (3-28):

$$S_{xc} \cdot F_{yc} \geq S_{xb} \cdot F_{yb} + \frac{\omega \cdot H^2}{12} \tag{3-29}$$

As stated previously, the total drift between column inflection points for the SPSW case is shown in Appendix A to be equal to that of the bare frame case for elastic behavior. Therefore, by solving the inequality of (3-29) for beam strength and substituting this into the bare frame yield drift limit of (3-25), an approximate drift limit for frame yielding with an SPSW infill panel can be written as:

$$\gamma_y \leq \frac{1}{6 \cdot E}\left(\frac{H}{I_c} + \frac{L}{I_b}\right) \cdot \left[S_{xc} \cdot F_{yc} - \frac{\omega \cdot H^2}{12} \right] \tag{3-30}$$

Therefore, considering this inequality, a combined expression for yield drift limit of an MRF frame with SPSW infill panel can be expressed by considering, for a limit state of column yielding, (3-30), and for beam yielding, (3-25), with the frame yield drift, taken as the minimum of those two expressions:

$$\gamma_y = \frac{1}{6 \cdot E}\cdot\left(\frac{H}{I_c} + \frac{L}{I_b}\right)\cdot\left[\min\left\{ \begin{array}{c} \left(S_{xc} \cdot F_{yc} - \frac{1}{12} \cdot F_{yp} \cdot t_p \cdot \sin^2 \alpha \cdot H^2\right) \\ \\ S_{xb} \cdot F_{yb} \end{array} \right\} \right] \tag{3-31}$$

where an expression similar to (3-16), but for the horizontal panel force component normal to the column axis, as shown in figure 3-13, has been substituted for ω.

$$\omega = F_{yp} \cdot t \cdot \sin^2 \alpha \tag{3-32}$$

Considering the underlying assumptions, it appears that the SPSW system can be designed to meet the fuse concept, limiting the drift to less than that specified in (3-31), with the panel designed to yield at a lower drift and dissipate input energy while the frame remains essentially elastic. In Appendix B, such constraints are imposed to develop equations for preliminary design. However, beyond this preliminary assessment, because the panels of SPSWs only yield in tension, it would be important to determine a procedure to also ensure that the panels could

provide the needed energy dissipation throughout the entire cyclic response without exceeding the above limits.   This, however, is beyond the scope of this study.

3.4   SPSWs with Openings

Seismic retrofits must be designed while respecting constraints imposed by as-built conditions, while also accommodating as much as possible existing utility locations (e.g. water pipes, HVAC ducts, electrical conduits). Conversely, in new buildings, placement of such utilities must be accomplished within the building structure such as to not compromise the effectiveness of the lateral force resisting system.

From a practical standpoint, a disadvantage in using SPSWs is that current recommended seismic design provisions (AISC 2005a) require the substantial reinforcement of an infill panel adjacent to any perforation or opening introduced into an infill panel web (i.e. the creation of new boundary elements around openings for utilities). This required strengthening increases the SPSW system fabrication costs, while re-routing utilities around an infill increases project costs in a different manner. Two options for accommodating utility systems through an infill panel with minimal or no stiffeners are proposed here and described below with these concerns in mind.

Note that the intentional reduction of panel strength and stiffness can be an additional reason for using panel perforations such as shown in figure 3-14. Reduction of these SPSW system properties using holes may be an appealing option in practice, when available panel material is thicker or stronger than required for stiffness and strength calculations, respectively (as described in section 3.4.1.2). Some simple relations for approximating strength and stiffness reductions are described below.
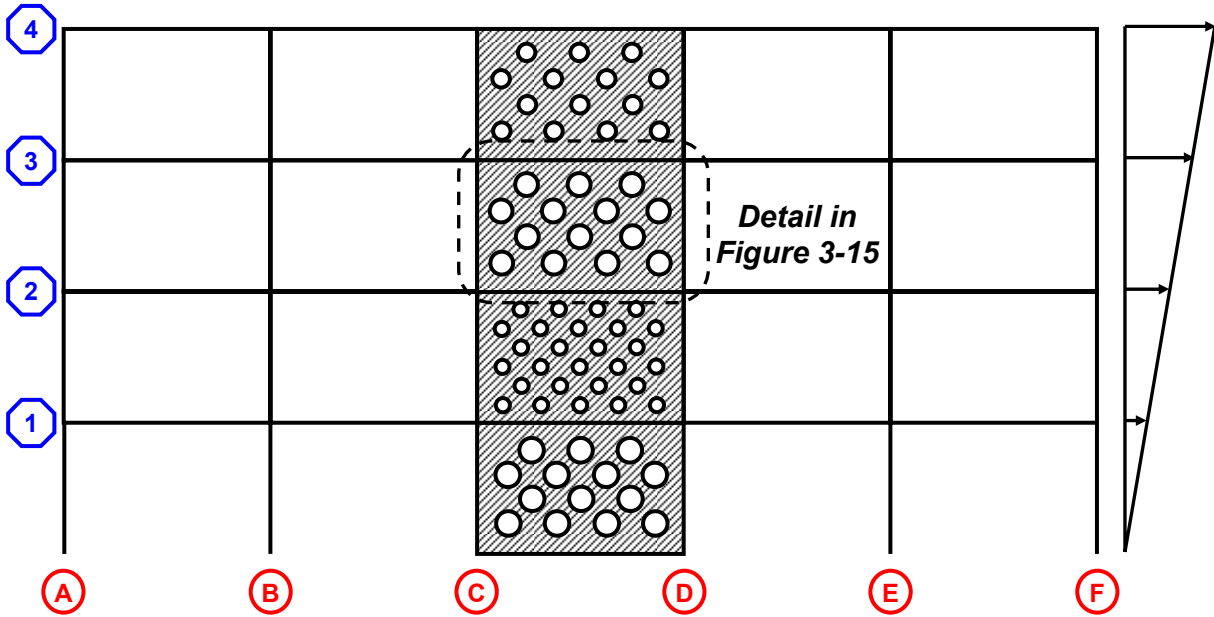
FIGURE 3-14 Schematic Examples of Possible Perforated SPSW Infill Panels in Four Story Building Frame (Arbitrary Configurations to Illustrate Sample Geometry Only)

3.4.1 Perforated Panel SPSWs

Introducing unreinforced perforations into an SPSW infill panel can be a viable option for accommodating the numerous utilities present in buildings such as hospitals. Un-stiffened panel perforations may allow for robust performance during a seismic event.

SPSW panel tension field action is typically oriented at an angle near 45° with respect to surrounding frame members (Driver *et al*. 1997). From this observation, a pattern of multiple perforations may be introduced in a solid panel, and arranged such that the tensile stress field is free to develop at that angle. Therefore, in this proposed concept, horizontal and vertical distances between holes are equal in each direction, and each row is staggered horizontally, resulting in "strips," oriented near 45º, which transfer the load within the panel, as described in further detail below.

3.4.1.1 Panel Stiffness with Single Perforation

Roberts and Sabouri-Ghomi (1992a) investigated the effects of a perforation in a thin steel shear panel. A series of relatively small rectangular and square shear panel specimens (maximum size: 450mm x 300mm), with single center circular perforation of varying diameters (maximum: 150mm), were tested under quasi-static cyclic loading.

49

They proposed a simple reduction factor, for both strength and stiffness, to account for the presence of a single hole, centrally located in a square or rectangular panel loaded in shear:

$$\frac{V_{yp.perf}}{V_{yp}} = \frac{K_{perf}}{K_{panel}} = \left[1 - \frac{D}{d}\right] \tag{3-33}$$

where $V_{yp.perf}/V_{yp}$ and K_{perf}/K_{panel} are the ratios of strength and stiffness, respectively, of a perforated panel specimen to an identical solid panel specimen, D is the perforation diameter, and d is the panel depth. This is equivalent to completely discounting the contribution of the steel along the diagonal strip of width equal to the hole diameter in the development of tension field action. This a conservative assumption, and the strength and stiffness observed experimentally during Roberts and Sabouri-Ghomi's tests were indeed greater than predicted by the equations.

3.4.1.2 Panel Stiffness for Proposed System with Multiple Perforations

The panel perforation layout possibilities schematically shown in figure 3-14 utilize a relatively large number of holes, somewhat evenly distributed throughout the infill panel width and height. Two methods are proposed below to assess the panel stiffness for walls with this configuration of holes.

Consider an arbitrary panel, shown in detail in figure 3-15. Perforations of diameter, D, are evenly spaced at increments of S_{diag}, along parallel lines at the same spacing, oriented diagonally with respect to the beam axis, at an angle, θ (Note that although 45° was mentioned earlier as a logical and convenient angle, technically, θ could be selected as any value). Therefore, a "typical" panel strip is defined as the region within a tributary width of ½S_{diag} on either side of a perforation layout line.
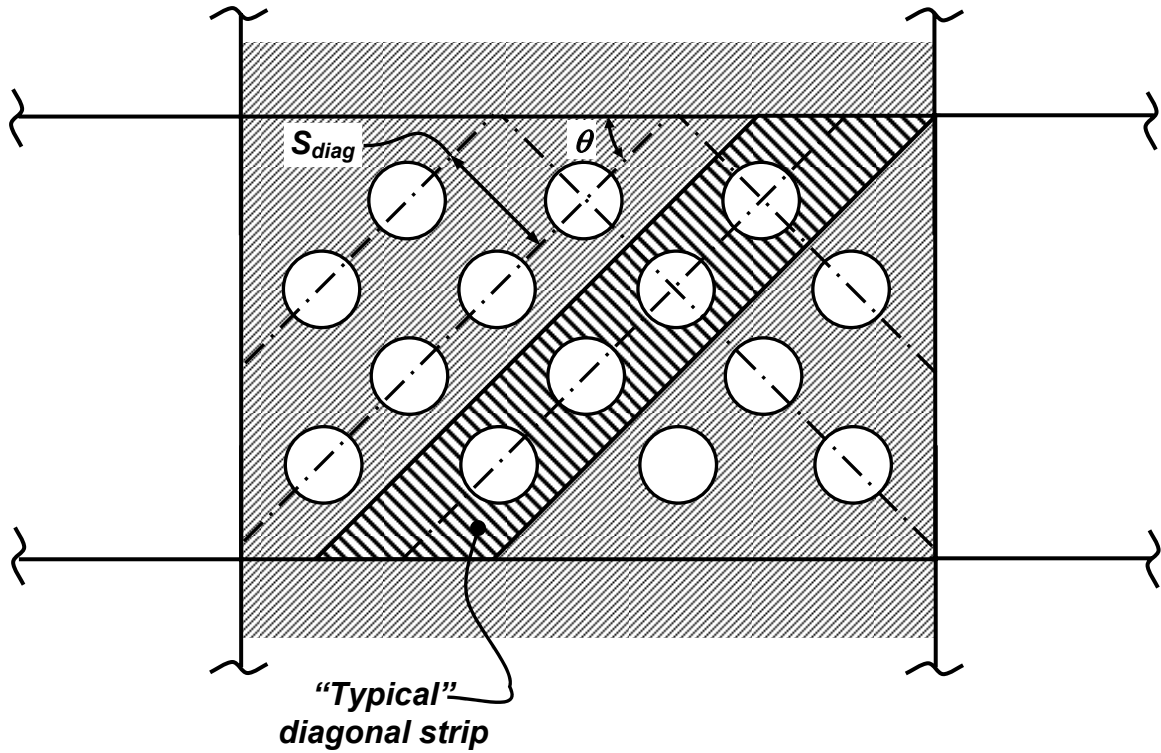
FIGURE 3-15 Schematic Detail of Third Story Panel and "Typical" Diagonal Strip

Similar to the property reduction factor for a shear panel with single perforation, put forth by others and described in the previous section, an empirical equation could be developed by extension, for use in calculating stiffness reduction in a panel with multiple perforations, by calculating a weighted (based on length) "average" strip width as compared to the full solid "typical" panel strip width, S_{diag}. This average width is given by:

$$w_{avg} = \frac{\sum\limits_{i=1}^{N} w_i \cdot L_i}{\sum\limits_{i=1}^{N} L_i} \qquad (3\text{-}34)$$

where L_i and w_i are the longitudinal length and transverse width, respectively, of an arbitrary strip segment "i". For strip segments next to a perforation, $L_i = D$ and $w_i = (S_{diag} - \pi D/4)$ while for strip segments in between perforations, $L_i = (S_{diag} - D)$ and $w_i = S_{diag}$, as shown in figure 3-16.

Un-perforated segment "*i*"
of typical strip

Width: $w_i = S_{diag}$

Length: $L_i = (S_{diag} - D)$
(between perforations)

Top edge
of panel

Perforated segment "*i+1*"
of typical strip

Width: $w_{i+1} = \left(S_{diag} - \frac{\pi \cdot D}{4} \right)$

(both pieces A & B)
Length: $L_{i+1} = D$
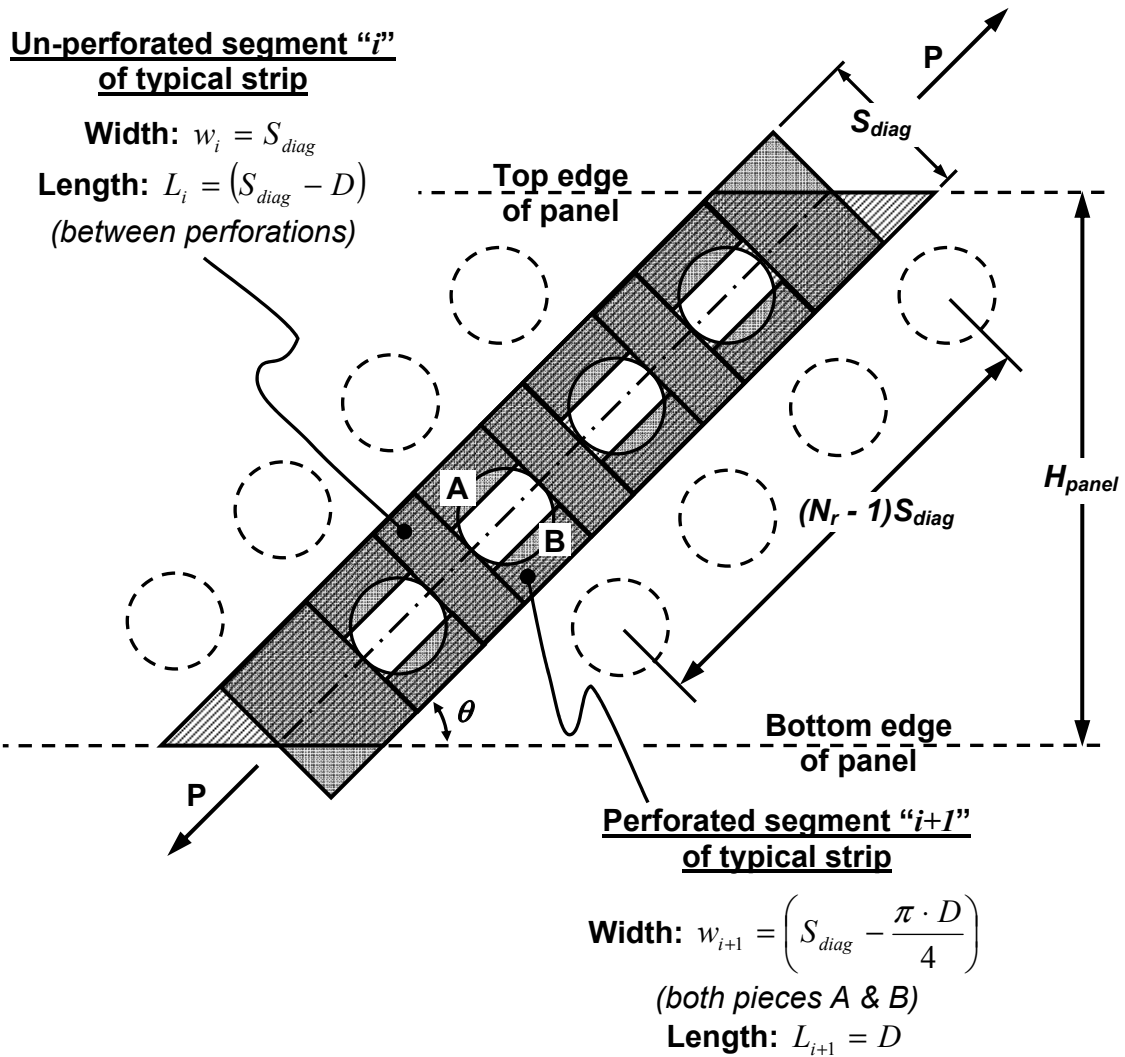
FIGURE 3-16 Details of Typical Diagonal Strip - Segment Lengths and Widths

Substituting the segment widths and lengths into (3-34), and simplifying:

$$w_{avg} = S_{diag} - \frac{N_r \cdot \pi \cdot D^2 \cdot \sin\theta}{4 \cdot H_{panel}}$$ (3-35)

where N_r is the number of rows of perforations along the diagonal (e.g. in figure 3-16, $N_r = 4$) and H_{panel} is the height of the panel between beam flanges. Dividing both sides of this expression by S_{diag} results in a ratio of the "average" strip width to the solid panel strip width:

$$\frac{w_{avg}}{S_{diag}} = 1 - \left[\frac{N_r \cdot \pi \cdot D^2 \cdot \sin\theta}{S_{diag} \cdot 4 \cdot H_{panel}} \right]$$ (3-36)

By analogy to (3-33), one could postulate that:

$$\frac{K_{perf}}{K_{panel}} = \frac{w_{avg}}{S_{diag}} \tag{3-37}$$

Note that substituting (3-36) into (3-37) gives an expression that differs from (3-33) in that the expression in square brackets is the ratio of the areas removed from the panel by the perforations to the area of the originally solid panel strip, whereas (3-33) contains a ratio of perforated to solid widths.

Alternatively, another method is proposed here for calculating the effect of perforations on the solid panel stiffness, by considering the idealization of a typical diagonal strip, as shown in figure 3-16, as a combination of members in series, axially loaded by a force P. For an arbitrary segment "i", with longitudinal length, L_i, and transverse cross-sectional area, A_i, the corresponding axial displacement due to this force, δ_i, is given by:

$$\delta_i = \frac{P \cdot L_i}{A_i \cdot E} \tag{3-38}$$

The area, A_i, can be replaced with $w_i \cdot t$, where t is the infill panel thickness and w_i is the transverse width of segment "i". Therefore, total axial displacement over the length of a strip is the summation of individual segment displacements:

$$\delta_{total} = \sum_{i=1}^{N} \delta_i = \frac{P}{E \cdot t} \cdot \sum_{i=1}^{N} \left(\frac{L_i}{w_i} \right) \tag{3-39}$$

from which, an expression for the axial stiffness can be calculated:

$$\frac{P}{\delta_{total}} = E \cdot t \cdot \left[\sum_{i=1}^{N} \left(\frac{L_i}{w_i} \right) \right]^{-1} \tag{3-40}$$

This axial stiffness for a typical perforated panel strip of overall strip length, L, can be equated to the axial stiffness of a panel strip with effective cross section, A_{eff}, and a uniform width:

$$\frac{E \cdot A_{eff}}{L} = \frac{E \cdot w_{eff} \cdot t}{L} = E \cdot t \cdot \left[\sum_{i=1}^{N} \left(\frac{L_i}{w_i} \right) \right]^{-1} \tag{3-41}$$

and then solved for the "effective" width, w_{eff}:

$$w_{eff} = L \cdot \left[\sum_{i=1}^{N} \left(\frac{L_i}{w_i} \right) \right]^{-1} \tag{3-42}$$

Terms required for (3-42) can be calculated from figure 3-16, and the summation within the square brackets can be expanded into two terms: one representing the summation of perforated segments and another for the un-perforated segments:

$$\sum_{i=1}^{N} \left(\frac{L_i}{w_i} \right) = \underbrace{\frac{N_r \cdot D}{S_{diag} - \frac{\pi \cdot D}{4}}}_{perforated} + \underbrace{\frac{L - N_r \cdot D}{S_{diag}}}_{un-perforated} \tag{3-43}$$

Substituting (3-43) into (3-42) and simplifying:

$$w_{eff} = \frac{S_{diag} \cdot \left[1 - \frac{\pi}{4} \cdot \left(\frac{D}{S_{diag}} \right) \right]}{1 - \frac{\pi}{4} \cdot \left(\frac{D}{S_{diag}} \right) \cdot \left(1 - \frac{N_r \cdot D}{L} \right)} \tag{3-44}$$

Replacing the overall diagonal strip length, L, with $H_{panel}/\sin\theta$:

$$w_{eff} = \frac{S_{diag} \cdot \left[1 - \frac{\pi}{4} \cdot \left(\frac{D}{S_{diag}} \right) \right]}{1 - \frac{\pi}{4} \cdot \left(\frac{D}{S_{diag}} \right) \cdot \left(1 - \frac{N_r \cdot D \cdot \sin\theta}{H_{panel}} \right)} \tag{3-45}$$

This effective width, divided by the diagonal spacing, S_{diag}, can serve as a stiffness reduction factor for a perforated panel, as (3-36) does using the weighted average width divided by the diagonal spacing:

$$\frac{w_{eff}}{S_{diag}} = \frac{1 - \frac{\pi}{4} \cdot \left(\frac{D}{S_{diag}} \right)}{1 - \frac{\pi}{4} \cdot \left(\frac{D}{S_{diag}} \right) \cdot \left(1 - \frac{N_r \cdot D \cdot \sin\theta}{H_{panel}} \right)} \tag{3-46}$$

Solid panel story stiffness may be obtained using an expression given by Thorburn and Kulak (1983) for a fully developed tension field:

$$K_{panel} = \frac{E \cdot W_{panel} \cdot t}{H_{panel}} \cdot \sin^2 \alpha \cdot \cos^2 \alpha \qquad (3\text{-}47)$$

where W_{panel} is the infill panel width between column flanges, and other terms have been defined previously. Therefore, the ratios given by (3-36) and (3-46) may be used to estimate perforated panel stiffness through reduction of solid panel story stiffness:

$$K_{perf} = \left[\frac{w_{avg}}{S_{diag}} \right] \cdot K_{panel} \qquad (a)$$

$$(3\text{-}48)$$

$$K_{perf} = \left[\frac{w_{eff}}{S_{diag}} \right] \cdot K_{panel} \qquad (b)$$

These expressions will be compared with experimental results and finite element models in the subsequent chapters to confirm if the values provide a reasonable estimate of perforated panel stiffness. But, for now, consider a frame similar to the MCEER demonstration hospital discussed earlier. For illustrative purposes, assume a perforated strip layout angle of $\theta = 45°$, a panel height between beam flanges of $H_{panel} = 3200$mm, and diagonal strip spacing of $S_{diag} = 500$mm. The second proposed stiffness reduction factor (3-46) is plotted in figure 3-17 using these constraints, as a function of perforation diameter for various values of N_r. Note that three bold vertical lines appear on the figure, delineating when the perforation diameter is one third, one half and equal to the perforation spacing. Obviously, for the last case, adjacent perforations are touching one another, which is not a practical option. The other vertical lines can be used to demonstrate the degree of stiffness reduction for a given geometry. It is observed that, for the given geometry, the stiffness reduction at $D/S_{diag} = 0.5$ decreases by approximately 2.5% for each additional row of perforations added to the panel. Note that this illustrative example is only applicable to the specified values of H_{panel} and S_{diag}; a similar design chart to aid in the selection of perforation diameter, D would need to be generated for other values of H_{panel} and S_{diag}.
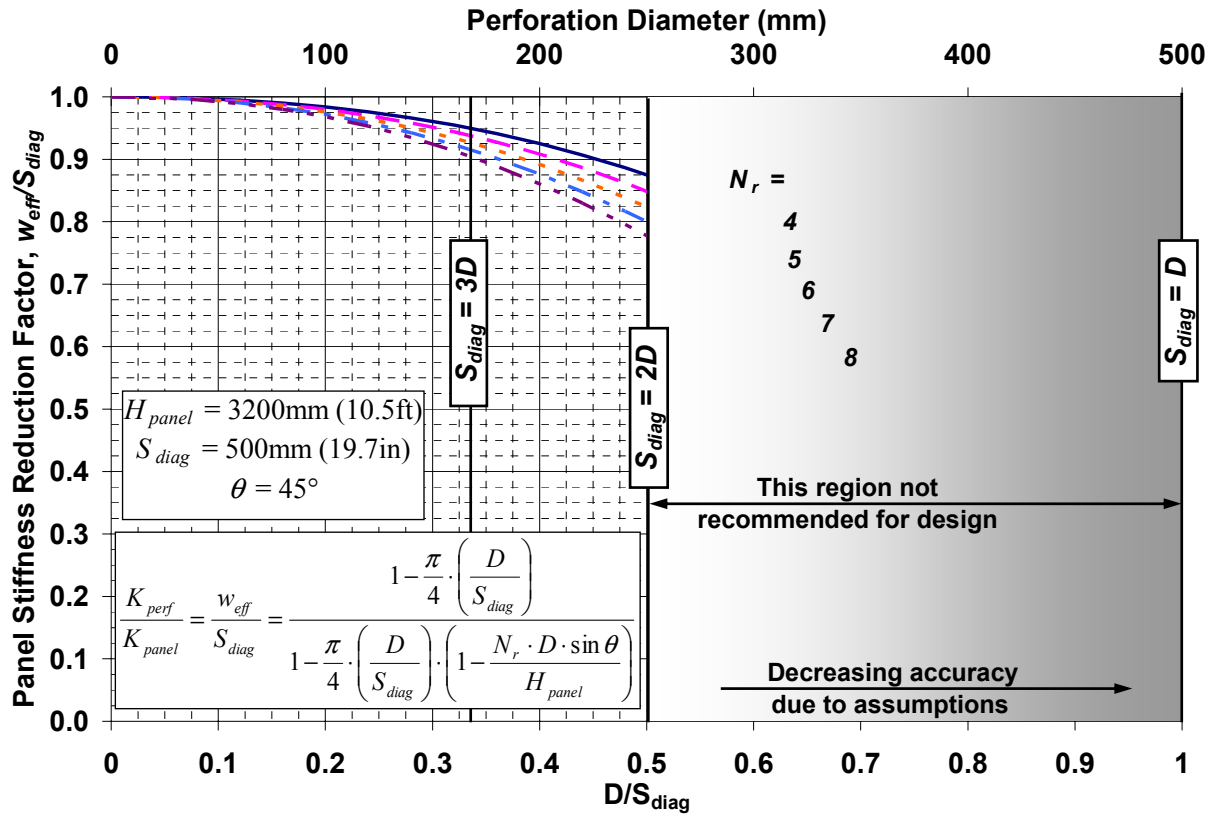
FIGURE 3-17 Stiffness Reduction Factor versus Perforation Diameter

Note that following the selection of a desired perforation diameter using a chart such as the one above, the appropriateness of a particular layout would need to be checked. For example, whereas eight rows of perforations spaced at 500mm could fit within the plate length considered in the above scenario, no constraints were placed on the edge distance, an important consideration in the fabrication of such a system. Some additional geometric constraints are introduced below to further assist in the selection of an appropriate panel perforation layout for a given situation.

Constraining that a desirable vertical distance from the panel edge to the center of the first perforation could be equal to a value of $2D$, the diagonal strip width (or diagonal perforation spacing) for a desired perforated panel layout can be expressed as:

$$S_{diag} = \frac{H_{panel} - 4 \cdot D}{(N_r - 1) \cdot \sin \theta} \tag{3-49}$$

From this expression, additional relations for ratios D/S_{diag} and $D \cdot \sin\theta / H_{panel}$ can be written:

$$\frac{D}{S_{diag}} = (N_r - 1) \cdot \left(\frac{H_{panel}}{D \cdot \sin\theta} - \frac{4}{\sin\theta} \right)^{-1} \tag{3-50}$$

$$\frac{D \cdot \sin\theta}{H_{panel}} = \left[(N_r - 1) \cdot \left(\frac{S_{diag}}{D} \right) + \frac{4}{\sin\theta} \right]^{-1} \tag{3-51}$$

Either of these ratios can be substituted into (3-46), to produce expressions for stiffness reduction as a function of the other ratio. The solid lines of the design chart in figure 3-18 show, for various numbers of rows, N_r, the stiffness reduction factor of (3-46) on the vertical axis versus $N_r \cdot D \cdot \sin\theta / H_{panel}$, a parameter which represents, along the length of the strip, the ratio of the sum of the diameters of perforations, $N_r \cdot D$, to the overall strip length, $H_{panel}/\sin\theta$. In these plots, the ratio D/S_{diag} varies internally as defined by (3-51). However, figure 3-18 also shows (3-46) versus $N_r \cdot D \cdot \sin\theta / H_{panel}$ for various constant values of D/S_{diag}, as represented by the dashed lines.
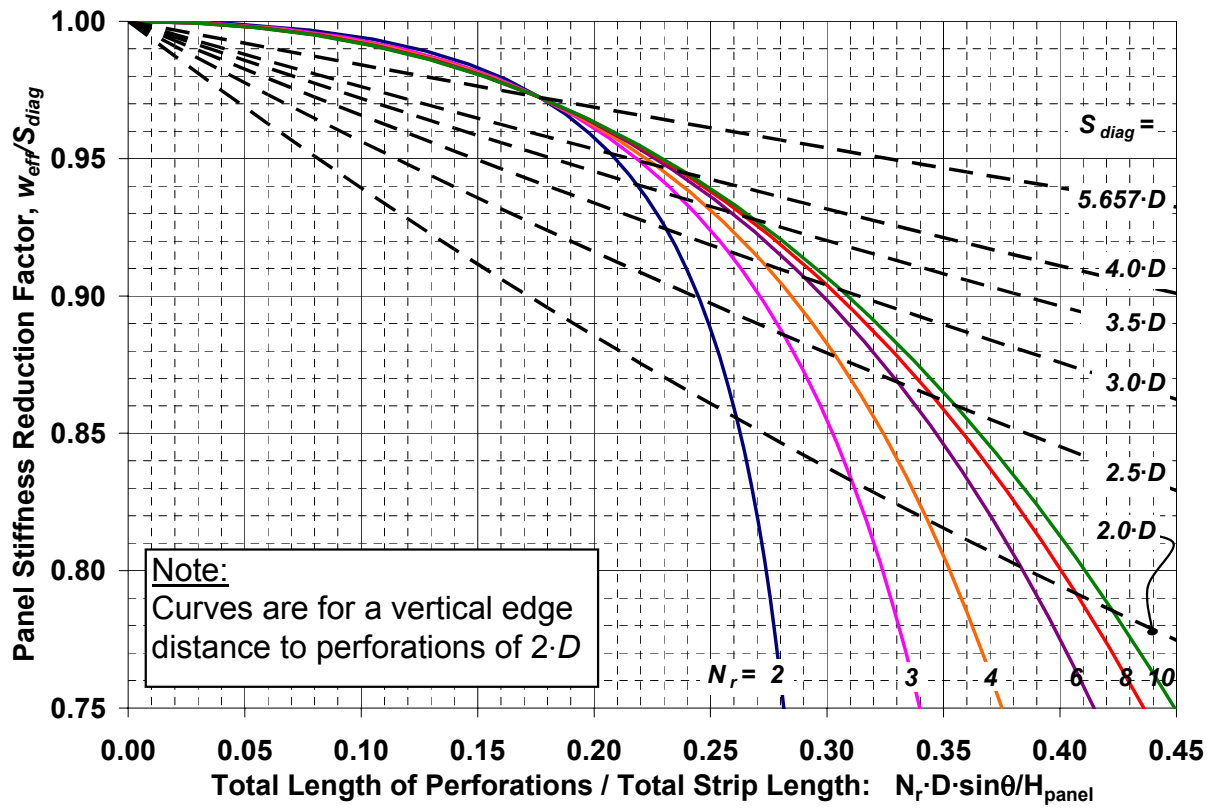
FIGURE 3-18 Stiffness Reduction versus Perforation Layout Parameters

Entering the chart of figure 3-18 with a desired stiffness reduction, K_{perf}/K_{panel}, panel height, H_{panel}, and strip layout angle of θ equal to 45°, a designer could chose a perforation diameter and layout as follows:

1. From the desired K_{perf}/K_{panel} on the vertical axis, read the ratio $N_r \cdot D \cdot \sin\theta / H_{panel}$ on the horizontal axis for various values of N_r.
2. Select a value for N_r and calculate D for the corresponding value of $N_r \cdot D \cdot \sin\theta / H_{panel}$.
3. The selected value of K_{perf}/K_{panel} (vertical axis) and $N_r \cdot D \cdot \sin\theta / H_{panel}$ (horizontal axis) identifies a uniquely defined point located between various curves of S_{diag} as a function of D (equivalent to a D/S_{diag} ratio and expressed by dashed lines). By interpolating between these lines, find the corresponding value of S_{diag} for this system for the value of D calculated in Step 2.

The preceding examples illustrate possible methods for design of the proposed perforated panel system. In the subsequent chapters, such a specimen is designed, constructed and subjected to cyclic testing; the experimentally obtained strength and stiffness are then compared with similar results for a solid panel wall of identical dimension, as well as with results predicted from these analytical equations.

3.4.2 SPSWs with Cut-out Corners

Infill panel corner cutouts, such as the quarter-circle cutouts shown in figure 3-19, are another option for accommodating utility penetrations of large size. This concept may be implemented with or without reinforcement to the cutout edge. However, the former option was judged more likely to perform adequately and is considered below with a discussion of design considerations.

Stiffness and strength of the corner reinforcement are important design concerns for implementation of this option. If, for example, a straight member (and cutout) were used, then the reinforcement member would behave as a "knee brace", with a tendency to "lock up" the corner angle as it opens and closes during frame sways. In addition, the panel forces acting on this member would induce relatively large moment at the ends of the member, which would likely be welded connections. A quarter circle arch shape, however, would provide more flexibility to accommodate angle change at the frame corners during sway, compared to a straight member of the same area, and would possibly have lower end moments.
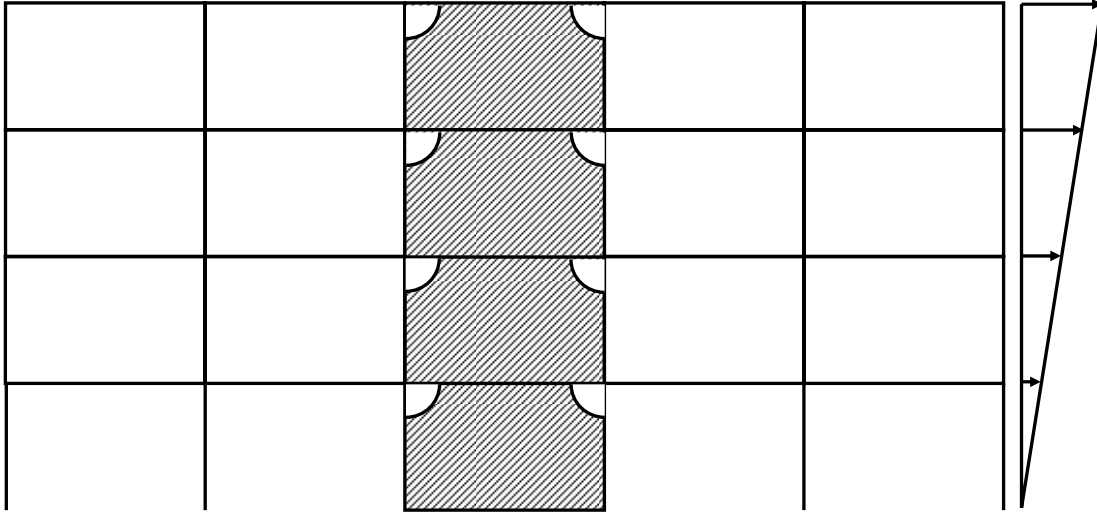
FIGURE 3-19 Cut-Out Corner SPSW for Utility Penetration

To illustrate the above concerns, consider the idealized deformed shape of the frame bay subsection in figure 3-20. Note that this "racking" shape neglects the flexural behavior of frame members and assumes non-moment-resisting beam end connections – a presumably conservative assumption with respect to the change in corner angle with increasing drift, and therefore, with respect to the deformation imposed on the reinforcement arch end and resulting design forces described subsequently.
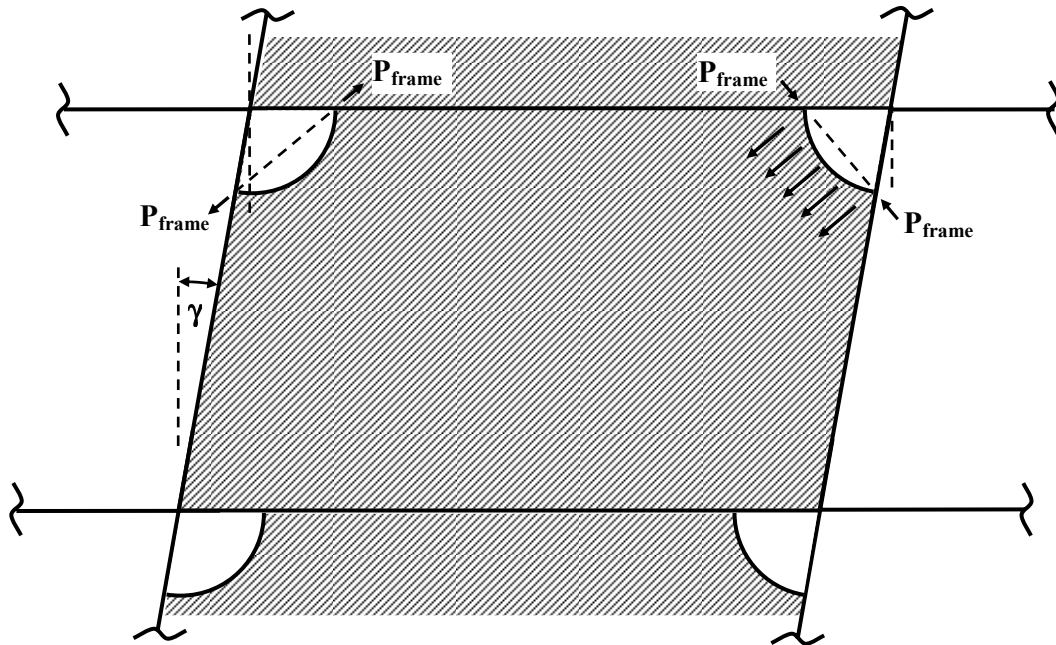
FIGURE 3-20 Arch End Reactions Due to Frame Deformations, and Infill Panel Forces on Arches Due to Tension Field Action on Cut-Out Corner SPSW

Temporarily neglecting the contribution from the infill panel, as the frame drift to the right increases as shown, the left arch is pulled in tension and the right arch compressed, by the force P_{frame}, due to the "opening" and "closing," respectively, of the right angle at each frame corner. For elastic behavior, these end reactions can be estimated using the arch section properties, knowledge that the arch height from the diagonal is $(2 - \sqrt{2}) \cdot R / 2$, and existing and available closed form solutions such as those provided by Leontovich (1959), for a hingeless fixed end arch with a support subjected to a horizontal displacement:

$$P_{frame} = \frac{45 \cdot E \cdot I}{\sqrt{2} \cdot (2 - \sqrt{2})^2 \cdot R^3} \cdot \delta \qquad (3\text{-}52)$$

where, for the case considered here using the right arch schematic shown in figure 3-21, P_{frame} and δ are the force and displacement, respectively, along the diagonal axis between arch ends; I_x is the arch cross section moment of inertia; and R is the arch radius. End moments for the same case are given by:

$$M_{frame.end} = \frac{15 \cdot E \cdot I}{2 \cdot (\sqrt{2} - 1) \cdot R^2} \cdot \delta \qquad (3\text{-}53)$$

From equilibrium, the moment at arch mid-span can be derived from (3-52) and (3-53) as half of the end moment.

For small displacements, the arch diagonal displacement can be related to the story drift by:

$$\delta = \frac{\gamma \cdot R}{\sqrt{2}} \qquad (3\text{-}54)$$

Therefore, the arch end reactions along the diagonal axis (and axial load at the center) can be expressed in terms of story drift:

$$P_{frame} = \frac{45 \cdot E \cdot I}{2 \cdot (2 - \sqrt{2})^2 \cdot R^2} \cdot \gamma \qquad (3\text{-}55)$$

Similarly, the arch end moments can be written as:

$$M_{frame.end} = \frac{15 \cdot E \cdot I}{2 \cdot (2 - \sqrt{2}) \cdot R} \cdot \gamma \qquad (3\text{-}56)$$
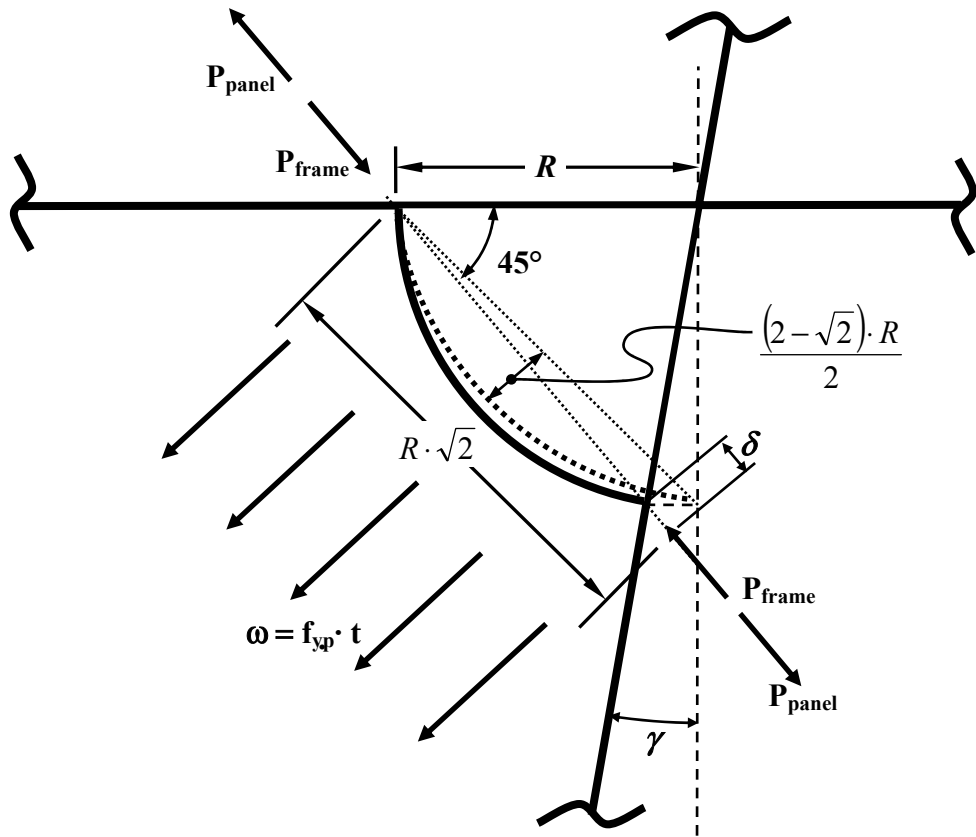
FIGURE 3-21 Deformed Configurations and Forces Acting on Right Arch

The infill panel tension field forces can be superimposed on the frame corner deformation end reactions described above. This can be done considering again a free body diagram of the arch configuration of figure 3-21 for preliminary analysis, and infill panel forces are assumed to act at 45° to the surrounding frame members and therefore as a uniformly distributed loading perpendicular to the arch diagonal axis. Using variables previously defined, this loading at ultimate panel strength is:

$$\omega = F_{yp} \cdot t \qquad (3\text{-}57)$$

Using a closed form solution tabulated by others (e.g. Young 1989, or Leontovich 1959), in this case for an arch with uniformly distributed vertical loading, end reactions along the diagonal axis (and equal to the axial force at the arch center) for this case are given by:

$$P_{panel} = \frac{\omega \cdot R}{4 - 2 \cdot \sqrt{2}} \qquad (3\text{-}58)$$

61

This reaction pulls on the ends of the arch along the diagonal axis, opposing the reaction, P_{frame}, due to the frame corner deformation as described above. Note that as with an arch compressed by a uniform horizontally distributed vertical load, the internal moment along the arc length of the corner cutout reinforcement is minimal. However, also note that tension field action would only act on the "closing" corner, and that arches on the opening corners would be subjected to the forces of (3-55) and (3-56) only. This implies that a reasonable design practice may be design of the arch reinforcement for forces induced via corner opening only (i.e. the left side in figure 3-20), since P_{panel} would reduce the magnitude of P_{frame} in the corner closing case (i.e. the right side in figure 3-20). Note that a comprehensive parametric study to determine relative contribution of frame and panel effects has not yet been performed. However, in some cases (as for design of the specimen described in the next chapter for example), it may be possible to obtain a satisfactory design by using the frame effect to select the thickness of a rectangular arch cross section, and the panel effect to select the width.

The above expressions for axial force and moment at given arch locations due to panel force and frame deformation can be combined and used for design by substitution into an axial force-moment interaction equation:

$$\frac{P}{P_n} + \frac{M}{M_n} \leq 1 \tag{3-59}$$

using the nominal strength values, P_n and M_n, corresponding to the axial and moment yield limit states to design the arch. By considering critical sections at the ends and mid-span of the arch, a designer may select, using these equations, appropriate section dimensions for the first iteration of a design, to be followed by a more rigorous check of section strength using computer analysis.

3.5 Summary

Observations and design considerations were presented for each type of boundary frame member composing an SPSW-infilled steel frame. Top and bottom story anchor beams designed for large drifts must ensure plastic hinging is limited to the beam-ends, to prevent release of tension field forces. The use of reduced beam section connections at the ends was suggested as a possible and effective means of ensuring that performance objective.

The possible use of SPSW infill panels as a "structural fuse" was described. Approximate frame yield drift limits were derived to facilitate design of infill panels that would yield and dissipate energy while avoiding frame yielding. This approach would allow for minimal disruption to a building following a damaging earthquake, by only requiring replacement of the infill panel and possibly the upper and lower anchor beams.

Two options for allowing passage of utilities through an SPSW infill panel were described. The first option uses multiple perforations in the infill panel, a technique that may also be used to strategically weaken a solid panel's strength and stiffness as a design situation may dictate. The second option uses cutout panel corners to allow the pass-through of utilities. A method for designing reinforcement for the cutouts was proposed, to allow transmission of full panel forces to the surrounding framing.

SECTION 4

DESIGN OF EXPERIMENTAL PROGRAM

4.1   General

This chapter describes the design of SPSW specimens for a program of quasi-static cyclic testing. Two specimens incorporate the utility-accommodating features described in the previous chapter. Specimen infill panels were designed and fabricated using low yield strength steel. The layout of instrumentation, the testing facility, and test setup are also described below.

4.2   Design of Test Specimens

Three types of SPSW specimens were selected for the experimental program. A "reference" specimen consists of a single-bay, single-story frame, with rigid beam-to-column connections, and a solid infill panel of LYS steel. The second specimen introduces multiple regularly spaced holes (perforations) into the panel, while the third introduces reinforced quarter-circle cutouts in the upper corners of the panel. The solid panel, perforated, and cutout-reinforced corner specimens are designated as S, P, and CR, respectively, in the following. Note that size and layout of perforations (P specimen) and cutout size (CR specimen) were chosen based on assumed geometry and size of utilities as described later.

Two solid panel specimens, S1 and S2, were built and tested, as will be described subsequently. Specimen S1 was built and tested prior to the fabrication of the remaining three specimens, partly to investigate the fabricator's ability to assemble the LYS infill panel with seam welds joining three pieces into one solid panel, among other things. Specimen behavior observed during testing revealed substantial deficiencies in fabrication and overall quality of workmanship was deemed "inadequate", particularly for the panel seam and beam-to-column welds, both of which sustained adjacent fractures or ruptures during testing, as detailed in Chapter 5. These deficiencies were then corrected for the subsequent specimens.

4.2.1 NCREE Laboratory Facility

The experimental phase of this research project was conducted in collaboration with the National Center for Research on Earthquake Engineering (NCREE) in Taipei, Taiwan. The NCREE laboratory had experience and equipment to perform quasi-static cyclic testing to the desired force level. Testing in the NCREE laboratory also facilitated the use of low yield strength (LYS) steel, which is bcoming more widely available in Asia, for the specimen infill panels.

The NCREE's reinforced concrete reaction wall and strong floor facility for large-scale structural testing, illustrated in figure 4-1 (NCREE 2002), was used for this purpose. The reaction wall consists of two parallel 1200mm thick reinforced and post-tensioned concrete walls, separated by a distance of 2600mm, and tied together by 400mm thick reinforced concrete ribs spaced at 3000mm. Both the 1200mm thick reinforced concrete strong floor, and the reaction wall were built with concrete specified compression strength of 35MPa (5ksi). Four static MTS hydraulic actuators, having maximum force and displacement output of 1000kN and 500mm, respectively, were used to laterally load the specimens.
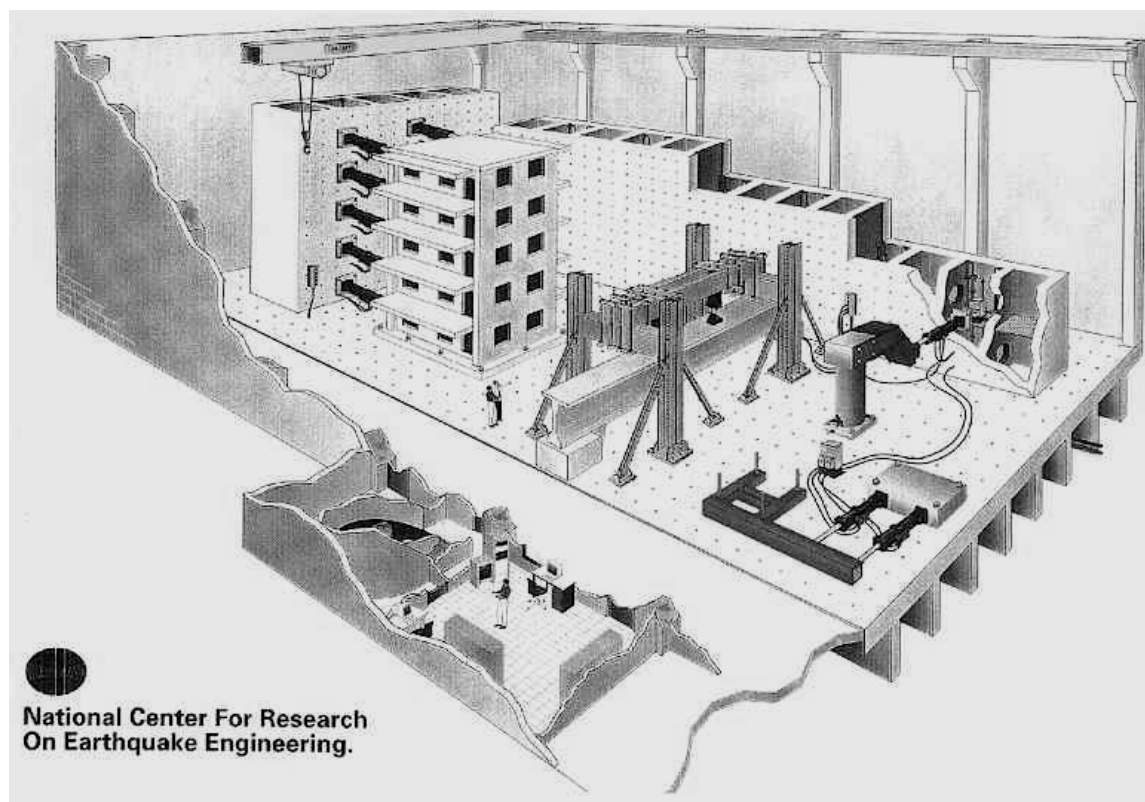
FIGURE 4-1 NCREE Laboratory Reaction Wall and Strong Floor Layout (NCREE 2002)

4.2.2 Overall specimen size

Specimen size was partly dictated by the physical layout of the NCREE laboratory. The horizontal and vertical spacing of anchorage points along the strong floor and reaction wall, respectively, is 1000mm, which constrained the specimen height and width to increments of that value. Maximum stroke and force output of the available actuators were the other main constraints of concern during the design phase.

At the beginning of the design process, it was proposed to adapt an existing frame previously used for the testing of BRBs (Tsai and Huang 2002). The frame's centerline dimensions were 6000mm wide by 2000mm high, and consisted of square box column and I-shaped beam sections. Frame widths of 3000mm, 4000mm, 5000mm and the original 6000mm were considered for the SPSW testing, as part of preliminary design, prior to selecting the final sizes, as discussed below.

Figure 4-2 shows the deformed shape of an SPSW specimen as the top beam is pushed to the right. A few assumptions regarding frame behavior at ultimate displacement were made leading to the selection of specimen member sizes. First, in order to test the "anchor" beams concepts discussed in the previous chapter, all frame yielding was assumed to occur in the form of plastic moment hinges at the beam-ends, with a value of $\beta \cdot M_p$. Second, a uniform infill panel tension field stress, σ, is assumed for simplified calculations for preliminary design (which is equivalent to assuming a boundary frame with rigid members and pin-ended connections). On the basis of that assumption, note that when panel tension field action is discretized into diagonal strips at an angle, α, all strips would have the same strain and stress at any given magnitude of frame sway.
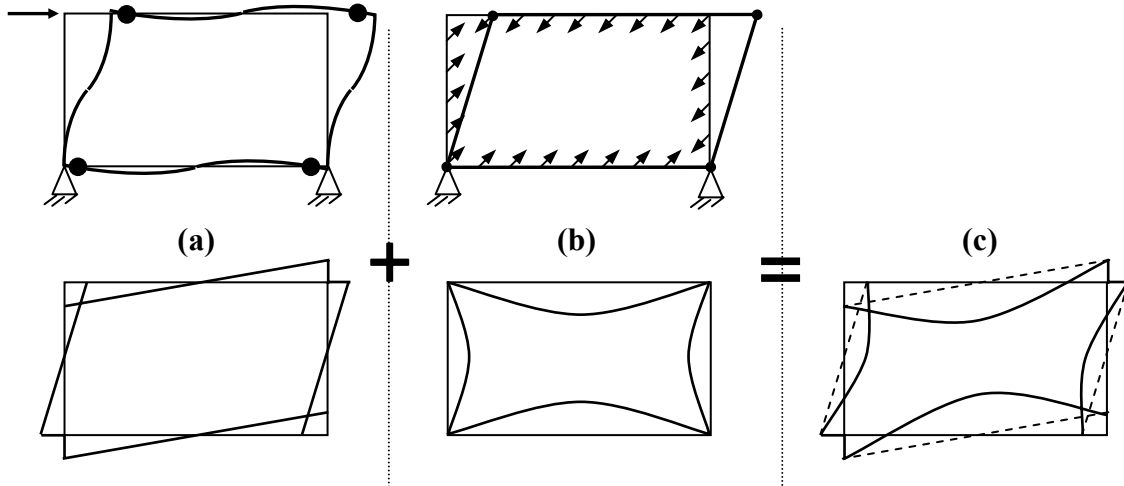
FIGURE 4-2 Force and Moment Diagrams of Frame + Panel forces used in Design (a) frame without infill panel; (b) with SPSW infill panel and rigid, pin-ended frame members; (c) combined system

A free body diagram of the bottom beam is shown in figure 4-3. Considering a length of the bottom beam, and a unit panel width, ds, for a strip oriented at an angle, α, as shown in figure 4-4, the axial force in that strip is given by:

$$P = \sigma \cdot t \cdot ds \qquad (4\text{-}1)$$

where t is the infill panel thickness, and the strip axial stress, σ, is assumed uniform across the panel. The unit length along the beam, dx, is calculated from the projection of ds. The horizontal and vertical components of P, H and V respectively, are resolved from geometry and then used to calculate the distributed loads on the beam, ω_H and ω_V respectively, by distributing those values across the projected unit length, dx:

$$\omega_H = \frac{H}{dx} = \frac{P \cdot \sin\alpha}{dx} = \tfrac{1}{2}\sigma \cdot t \cdot \sin 2\alpha \qquad (4\text{-}2\text{a})$$

$$\omega_V = \frac{V}{dx} = \frac{P \cdot \cos\alpha}{dx} = \sigma \cdot t \cdot \cos^2 \alpha \qquad (4\text{-}2\text{b})$$

If the tension field is oriented at an angle of $\alpha = 45°$, then the horizontal and vertical components are of equal magnitude, and (4-2) can be simplified to:

$$\omega = \omega_H = \omega_V = \frac{\sigma \cdot t}{2} \qquad (4\text{-}3)$$
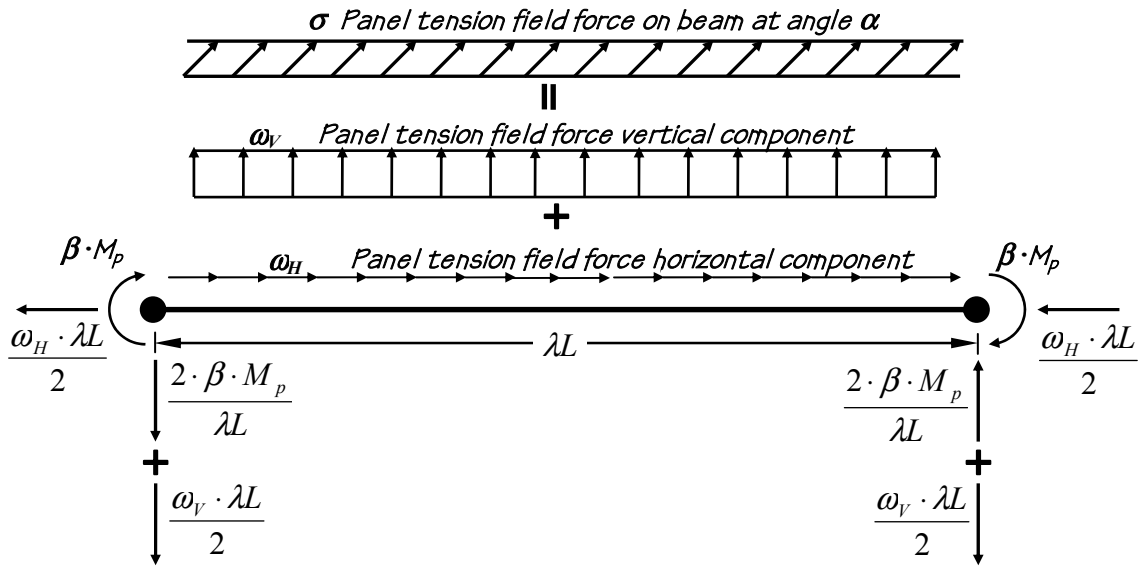
FIGURE 4-3 Bottom beam free body diagram and end reactions
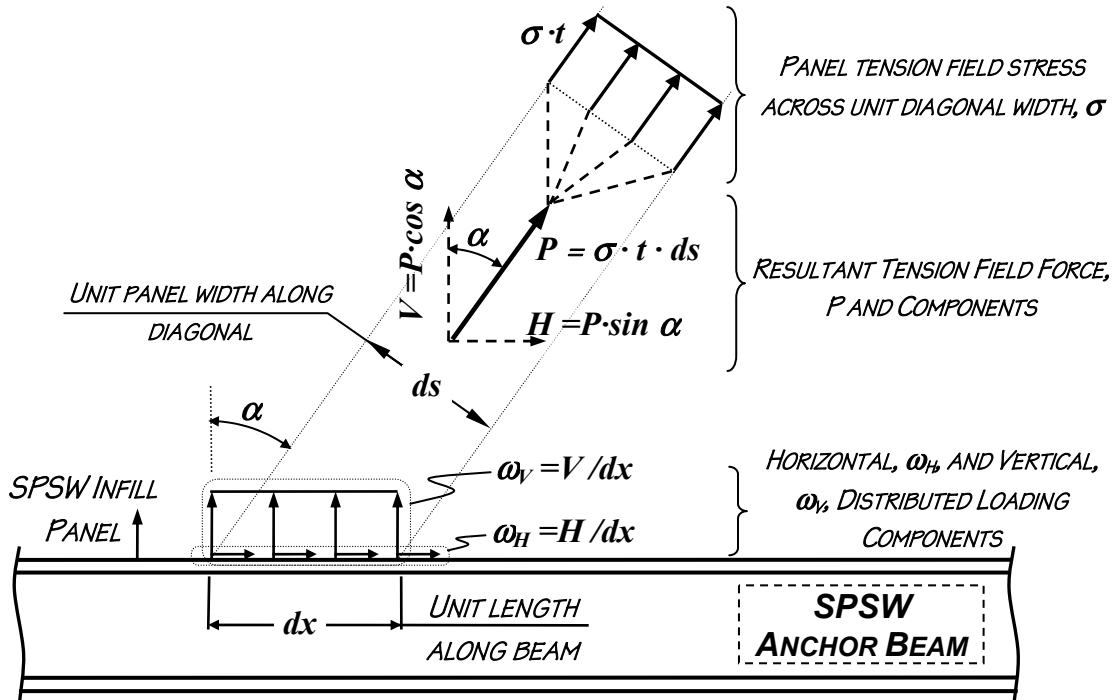
FIGURE 4-4 Horizontal, ω_H, and Vertical, ω_V, Distributed Loading Components of Panel Diagonal Tension Field Force, *P*, per Unit Width, *ds*

The interaction between the shear and axial forces produced by the diagonal panel forces effectively reduces the beam's plastic moment strength at the ends, especially at the end where the shear from panel forces is additive to the shear from beam end moments (i.e. the left end in the case illustrated in figure 4-3). Therefore, this internal force interaction was checked as follows, to ensure that a considered beam section and length, L, would form plastic hinges at the beam ends, but not within the span (desired as a result of the discussion of section 3.2) when loaded by panel forces. This was done as follows:

1. Given beam end plastic moments, $\beta \cdot M_p$, and length between end moment locations, $\lambda \cdot L$, the ultimate panel load that can be resisted by this member, ω_{ult}, is calculated from (3-14), with $\lambda \cdot L$ substituted for L.

2. Using the ultimate panel load from step 2, calculate the beam-end shear and axial reactions as pictured in figure 4-3.

3. Calculate the reduced web strength due to the presence of average shear stress using the Von Mises yield criterion (Bruneau *et al.* 1998).

4. Considering the axial force end reaction, calculate the further reduction in web strength from this effect.

5. Calculate the reduced plastic moment at the beam end, M_{pr}, using the total of reduced web strength from steps 3 and 4.

6. Using M_{pr} in place of M_p, recalculate ω_{ult} as done in step 1.

Note that the value of ω_{ult} recalculated in step 6 increases from that of step 1, due to the reduction in end moments by the shear and axial end reactions calculated in step 2. This allows the panel load-induced hanging moment to increase before the beam ultimate strength is reached (recall section 3.2). Therefore, the ω_{ult} from step 1 was then substituted into (4-3) to calculate the infill panel stress for a given panel thickness, t. Finally, the drift at which the proposed specimen could reach that panel stress was estimated by assuming rigid pin-ended frame members (i.e. assuming a rigid "racking" behavior as shown in figure 4-2(b) for the purpose of panel stress calculations). This deformation imposes a uniform axial strain on the tension field strips, ε, which can be related to interstory drift through compatibility relations:

$$\varepsilon = \frac{\gamma_F \cdot \sin 2\alpha}{2} \qquad (4\text{-}4)$$

Therefore, following the iteration process used to calculate the value of ω, the panel stress, σ, calculated from substitution into (4-3), was compared with the available panel material uniaxial stress-strain data (Maeda *et al*. 2001); the corresponding strain for this condition was substituted into (4-4) to calculate the frame drift, γ_F. Therefore, the drift to which a specimen specific strength is reached was estimated for the various beam lengths considered and a range of panel thicknesses, by generating plots of specimen drift versus plate thickness. This provided useful tools and data for the design of the test specimens.

A 4000mm width was chosen for the design and fabrication of a new frame, with a 2000mm centerline frame height, resulting in a 2:1 width-to-height aspect ratio. These dimensions would allow for comparison with previous experiments by Berman and Bruneau (2003), which utilized specimens with an identical ratio, but slightly smaller dimensions in each direction. Those specimens were dimensioned to approximate the aspect ratio of a bay in the MCEER demonstration hospital (Yang and Whittaker 2002).

4.2.3 Boundary Frames

Following the selection of 4000mm x 2000mm frame size described above, using the existing NCREE BRB test frame as a basis for those calculations, new frame members were designed using the sequence of steps outlined below, assuming LYP100 infill panel material.

1. Assume a maximum tested drift of $\gamma = 4\%$ and tension field angle of 45°, calculate the maximum strain in an axial strip, ε, from (4-4).
2. Use published LYP100 σ–ε curve (Maeda *et al*. 2001) to find panel tension field stress, σ at this strain.
3. Increase σ by a safety factor of 1.5 and calculate resultant distributed loads on beams and columns using (4-3).
4. Design beam and column sections with resistance reduction factors of 1.0, assuming $F_{yf} = 50$ksi (345MPa), using the force resultants from figure 4-3 to calculate V, M, and P and AISC-LRFD beam-column design relations, and beam plastic moments reduced to account for shear and axial forces.

These design steps were preliminarily used to select members assuming simply supported end conditions, then fully moment resistant end conditions, and finally 50% (beam) end moment

71

strength reduction using RBS connections. This latter scenario is the case to be considered via experimental testing. The chosen beam and column sections were W18x65 and W18x71, respectively.

Following this design process, system strength was calculated by superimposing the frame collapse mechanism case with that of a fully yielded panel, exerting a distributed force along the length of each of the surrounding frame members, as detailed below. This provided a means of comparing the overall proposed specimen strength with the maximum force output of the actuators.

Figure 4-5 shows the FBD of frame and infill panel forces. From simple plastic analysis, the strength of the bare frame (without infill panel) is given by:

$$V_{yf} = \frac{4 \cdot \beta \cdot M_p}{\lambda \cdot (H + h_{hinge})} \qquad (4\text{-}5)$$

where λ is a ratio of the distance between centerline of the RBS connections and the centerline of the columns; H is the frame height between beam centerlines; h_{hinge} is the distance from the column base pinned hinge to the bottom beam centerline; and other variables have been defined previously. RBS beam-to-column connection detailing is described in a subsequent section, and provides the desired beam-end moment strength reduction, β.

(a)   **(b)**
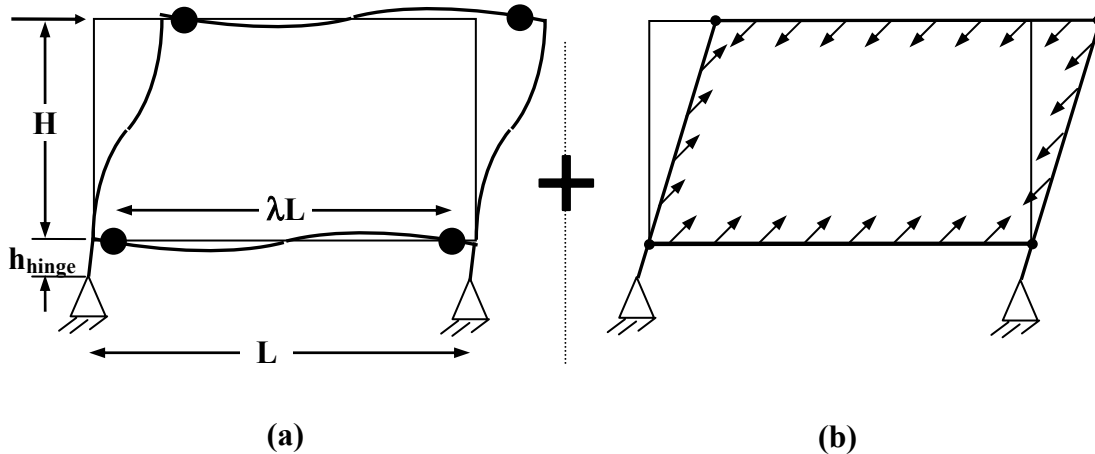
FIGURE 4-5 Force and Moment Diagrams of Frame + Infill Panel forces used in specimen design (a) frame without infill panel (b) with SPSW infill panel and rigid, pin-ended members

From previous work (e.g. Thorburn and Kulak 1983), the panel's contribution to the strength of the system is given by:

$$V_{yp} = \frac{1}{2} \cdot F_{yp} \cdot t \cdot W_{panel} \cdot \sin 2\alpha \qquad (4\text{-}6)$$

However, for the specimens considered, the panel's force contribution to the overall system strength must be modified to account for the presence of the hinged base:

$$V_{yp}' = \frac{H}{\left(H + h_{hinge}\right)} \cdot V_{yp} \qquad (4\text{-}7)$$

Therefore, the total strength of the system is given by the summation of (4-5) and (4-7):

$$V_{y.tot} = V_{yf} + V_{yp}' \qquad (4\text{-}8)$$

Using these relations and the selected sections and geometry with: h_{hinge} = 850mm, a frame material yield strength of F_{yf} = 379.5MPa (345MPa (50ksi) increased by a factor of 1.1 to account for uncertainty), panel thickness and strength of t = 2.6mm and F_{yp} = 230MPa, respectively, the frame and panel contributions to strength are: V_{yf} = 941kN, and V_{yp}' = 741kN, respectively. Total system strength was therefore calculated as 1682kN.

These component and combined strength values were confirmed via nonlinear static pushover analysis conducted using SAP2000 and the LYP material properties for the panel to be tested (as described in the next section). The developed SAP2000 model was a "strip model" representation of the specimen, developed by idealizing the panel as a series of diagonally-oriented "truss elements" (i.e. resisting only axial force effects). This modeling of SPSWs has been accepted for usage, as first proposed by Thorburn *et al*. (1983), discussed in many of the publications reviewed in chapter 2, as well as suggested by the commentaries of various design guidelines (i.e. CSA 2001, FEMA 2004, and AISC 2005a). The force versus interstory displacement of the SAP model is shown in figure 4-6 along with the values of (4-5), (4-7), and (4-8).
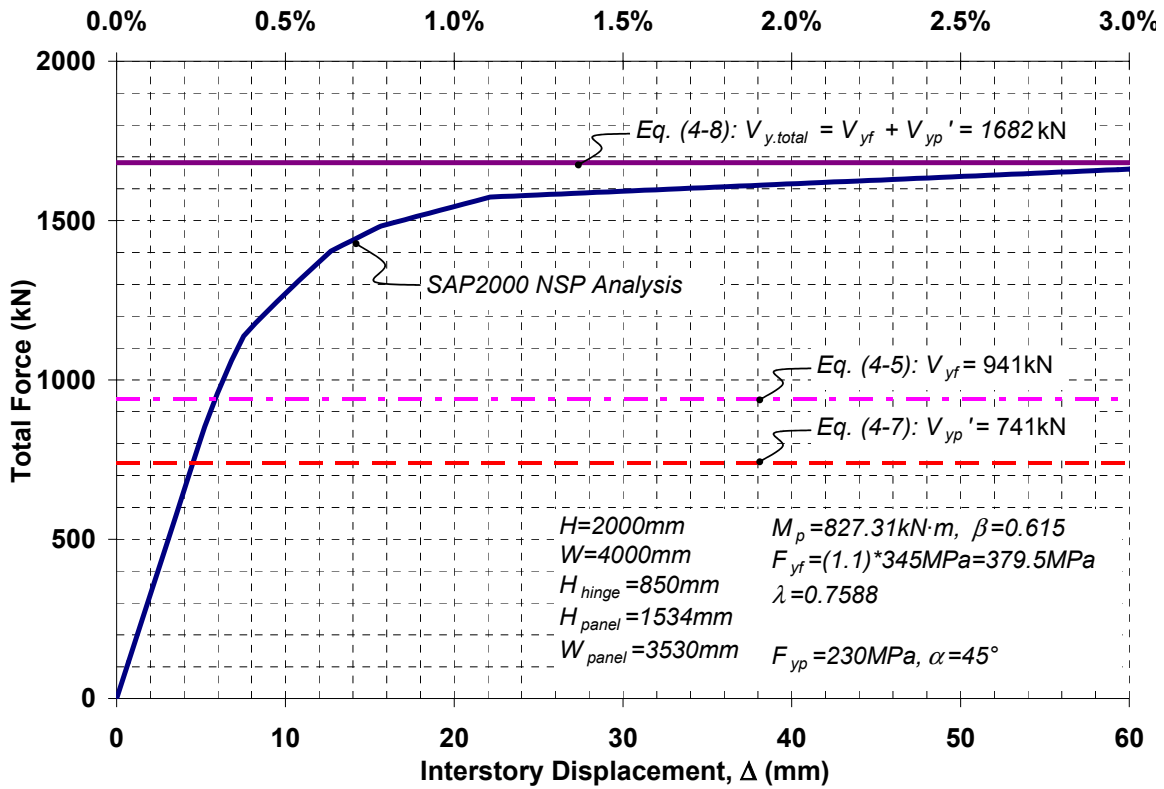
FIGURE 4-6 SAP2000 Pushover Analysis versus Limit Analysis Calculations

To facilitate comparison of the behavior between specimens and quantification of the impact of various infills, all specimens were designed to have the same beams and columns. Frame members were specified to be fabricated from steel equivalent to ASTM A572 with minimum yield strength of 345MPa. These sections sizes were converted to built-up sections with metric measurements, as is the fabrication practice in Taiwan, where the testing occurred. The basic specimen and section details are shown in figure 4-7.
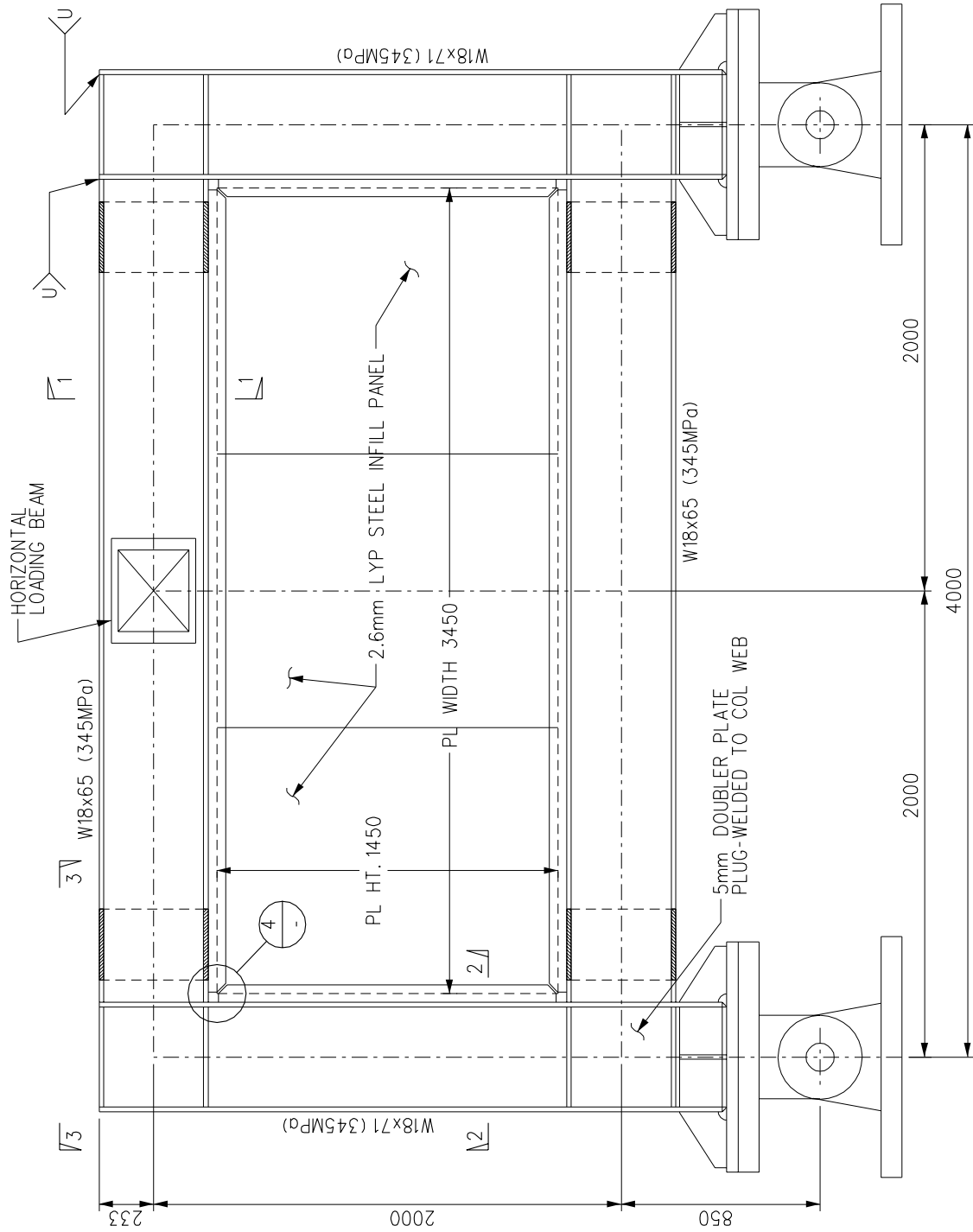
FIGURE 4-7 Basic Specimen Dimensions
(a) Overall Specimen Frame

75

(b)
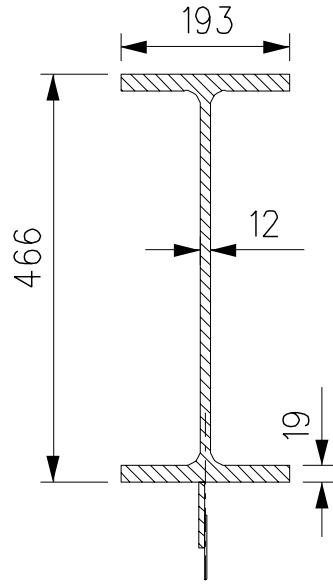
SECT 1 - 1
W18x65 BEAM
(W460x97)
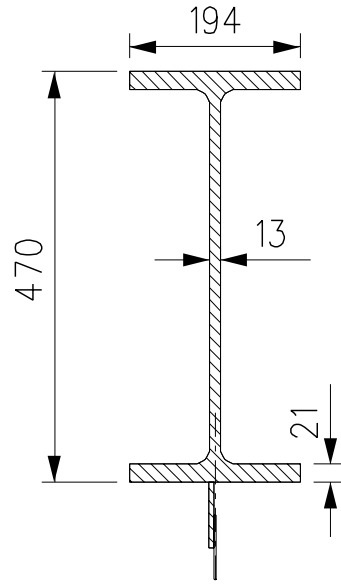
SECT 2 - 2
W18x71 COLUMN
(W460x106)

(c)

6mm
FISH PLATE

2.6mm INFILL PANEL

(d)

45-by-45 mm
Corner Cut-Out
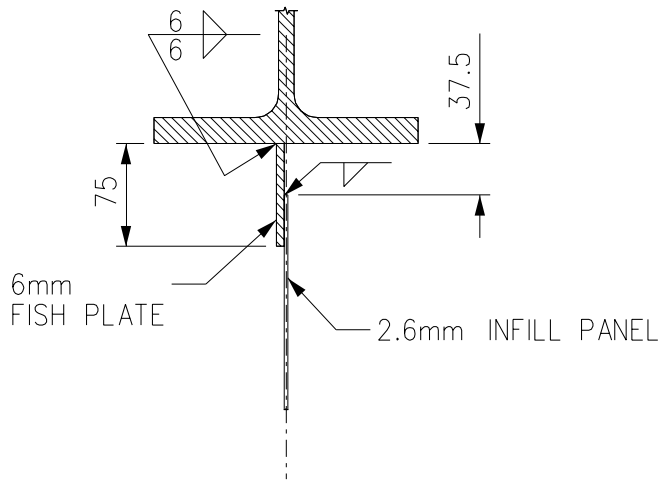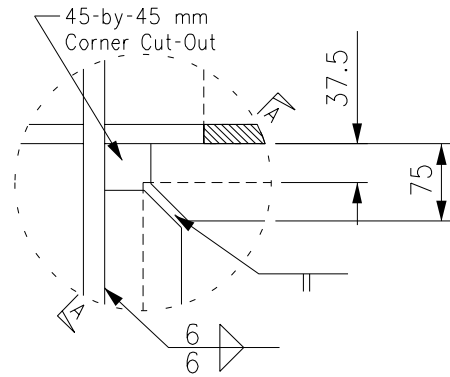
DETAIL 4
FISH PLATE

(e)

FIGURE 4-7 (cont'd) Basic Specimen Dimensions
(b) 1-1: Built-up W18x65 Beam Section; (c) 2-2: Built-up W18x71 Column Section;
(d) Fishplate and Panel Section Detail; (e) 4: Fishplate Corner Detail

4.2.4 Infill Panels LYS Steel

Low Yield Strength (LYS) steel was utilized for the infill panel material for all specimens in the experimental program. The China Steel Company provided LYS panels of 2.6mm thickness, in 2000mm by 1230mm sections, with yield and ultimate stresses of 165MPa and 305MPa, respectively (The intent was to use LYS100 steel, but since this specification does not include such thin plates, this steel was custom produced to be a LYS at the lowest possible yield strength approaching 100MPa, but no less). Results from uniaxial tension tests of four panel coupons are shown in figure 4-8, two each cut transverse (T1 and T2) and longitudinal (L1 and L2) to the direction of rolling. Three panel sections were joined manually by the fabricator with "seam welds" using E7018 electrodes at section interfaces, approximately located at the third points (between column faces) of beam clear span in the completed specimens. This "seam welding" was performed prior to installation in the framing (via the connection detail described in section 4.2.6), to ensure the panel was as flat as possible. Seam welds were ground down on the "trial" specimen tested, but this practice was eliminated in subsequent specimens after fractures occurred at these locations, as described in the section 5.3.1.
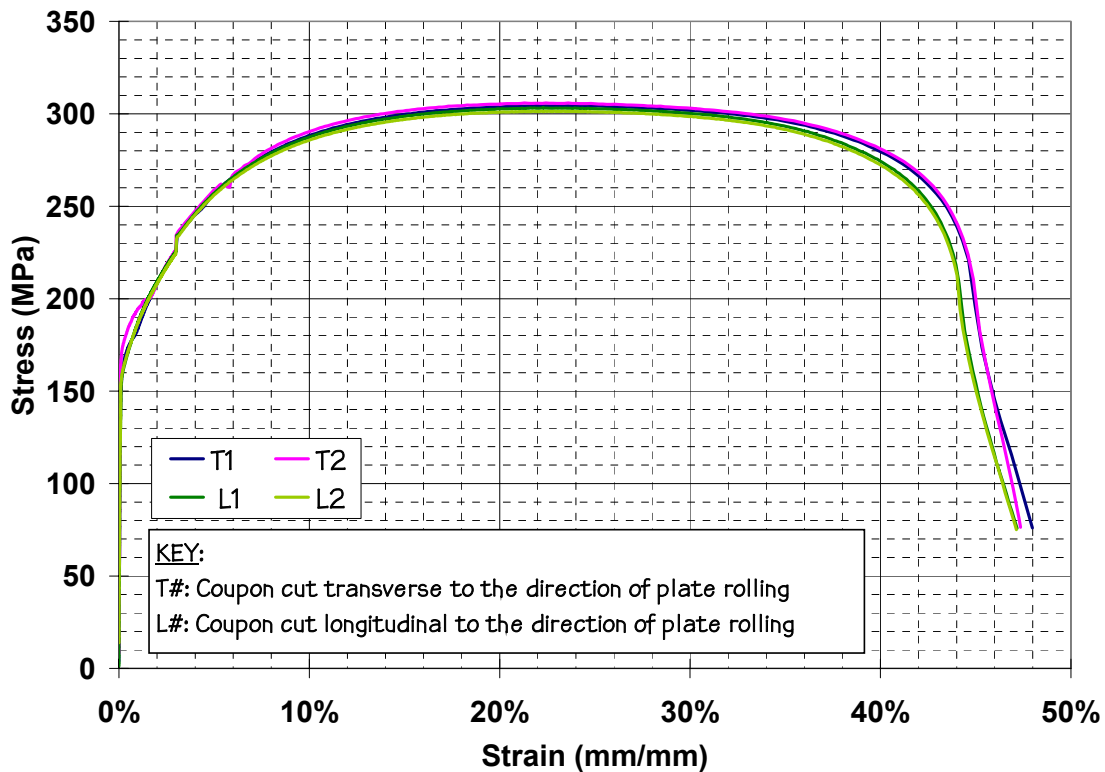
FIGURE 4-8 Low Yield Strength Steel Coupon Tension Test Results

4.2.5 RBS connections

Reduced beam section (RBS) connections were implemented in the specimen design, to physically demonstrate the concepts developed in the previous chapter. While the target moment strength at the RBS was fifty percent of the span value, the SAC project RBS dimensioning criteria suggest a maximum beam flange width reduction of 50 percent (FEMA 2000). Following this specified limit, due to the contribution of the web to flexural strength, the resulting RBS plastic moment (452.6kN·m for specified yield strength) ended up being 60.2 percent of the span plastic moment (752.1kN·m). This resulted in the connection shown in figure 4-9.
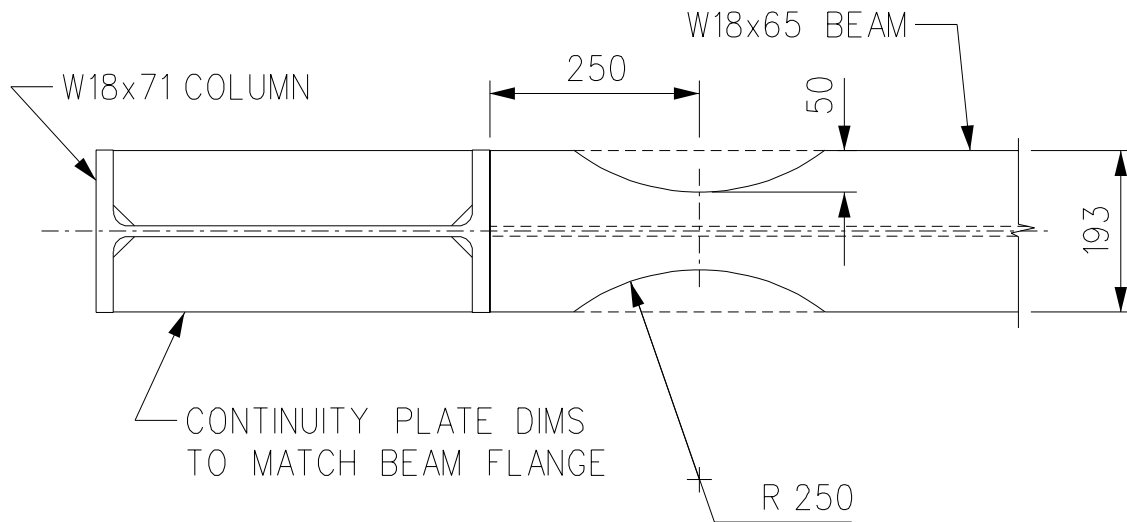
FIGURE 4-9 Reduced Beam Section detailing

4.2.6 Infill Plate-to-boundary frame connections

"Fish plates" connecting the infill panel to the boundary frame were designed using simple capacity design principles. The 7mm thick fish plate consisted of hot-rolled steel that was thicker (and of higher yield strength) than the LYS infill panel material. The plate was attached to beam and column flanges using fillet welds on both sides of the plate as shown in figure 4-7(d). The corner detail chosen was similar to the "Modified Detail B" recommended by Schumacher *et al*. (1999), as shown in figure 4-7(e).

4.2.7 Perforated Panel Specimen (P)

In the previous chapter, an option for allowing the passage of utilities through an SPSW infill panel, via perforations, was presented, as shown in figure 3-14. An equation quantifying panel stiffness reduction due to the presence of perforations was derived, while the strength reduction could be calculated via a relation previously proposed by Roberts and Sabouri-Ghomi (1992a).

As discussed in the previous chapter, tension field action in SPSW panels is typically oriented at an angle near 45° with respect to the surrounding frame (Driver 1997). Therefore, this value was selected as the orientation angle for layout of diagonal strips of perforations in the perforated panel specimen. The next step was to select the number of rows, N_r, diameter, D, and spacing of the perforations, S_{diag}, and then determine the expected effective panel stiffness (using (3-36) and (3-46) for the two approaches presented in the previous chapter) for a panel height, H_{panel}, equal to 1534mm (same as for the solid panel specimen above).

Substituting the relation for S_{diag} (3-49), with H_{panel} =1534mm, into the expressions for w_{avg} (3-35) or w_{eff} (3-45), and θ =45° held constant as selected above, the stiffness reduction factor is expressed into a function of N_r and D. Figure 4-10 shows a plot of (3-35), (3-45), and (3-49), versus perforation diameter, D, for N_r= 2, 3, 4, 5, and 6. For each value of N_r, the linear relationship between S_{diag} and D is shown, as are the reductions by w_{avg} and w_{eff} from S_{diag} for a given D. Note that (3-35) and (3-45) are not valid for the region for which $S_{diag} \leq D$ (outlined and shaded in figure), since in this case, adjacent perforations would be touching one another – for example, $D = 200$mm, $N_r = 6$ is not a possible option. Reading from figure 4-10, for the cases of N_r equal to 2, 3, 4, and 5 rows, for which the diagonal perforation spacing would be 1038, 519, 346, and 260mm, respectively, the corresponding effective stiffness reductions are 3.2%, 10.7%, 23.5%, and 41.4% (considering w_{eff}), or 2.8%, 8.4%, 16.8%, and 27.9% (for w_{avg}).
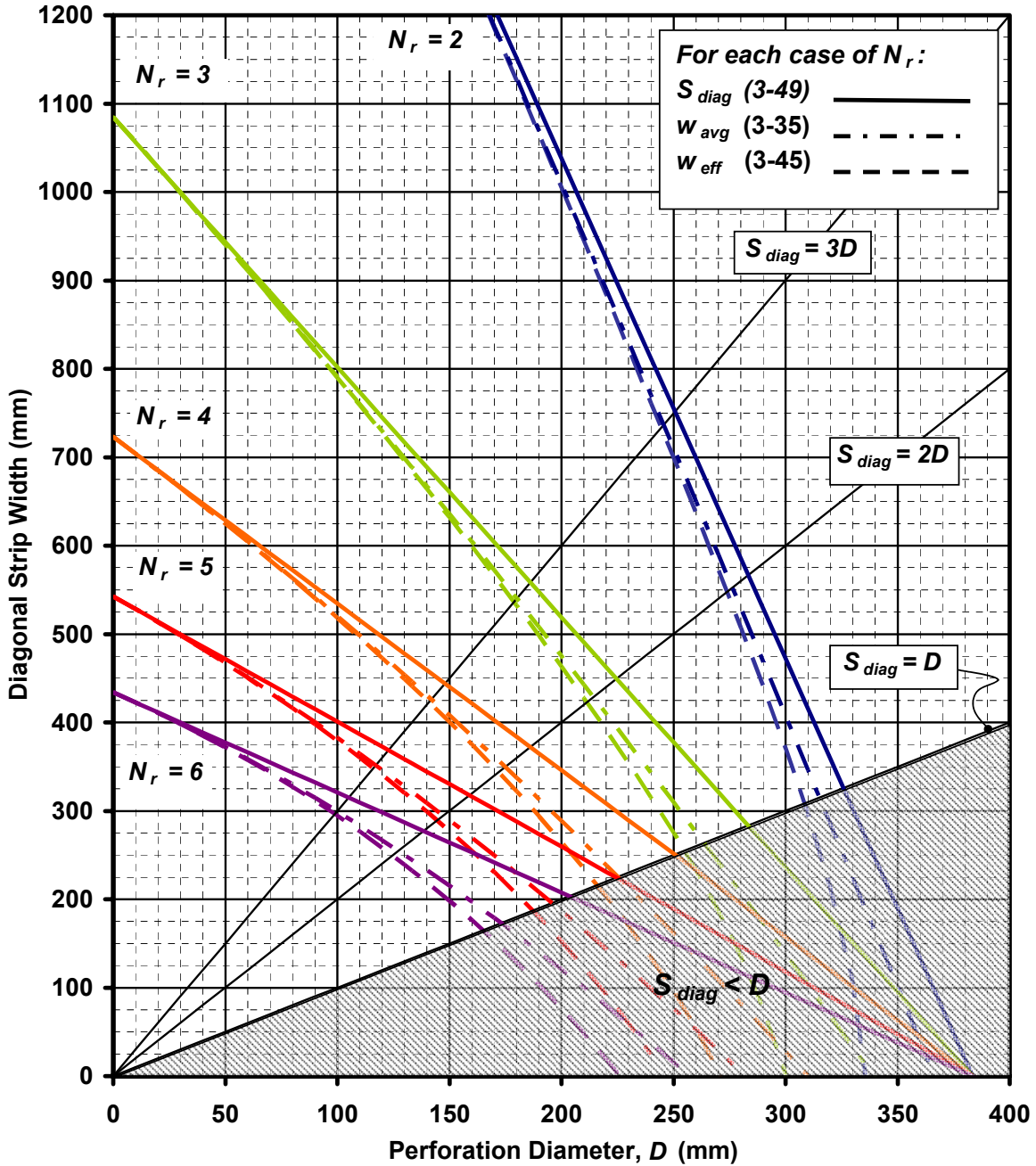
FIGURE 4-10 Diagonal Strip Width versus Perforation Diameter
for H_{panel} = 1354mm, edge distance, L_e=2.0·D, and θ = 45°

As with the plots in the previous chapter, it is useful to express both w_{avg} and w_{eff} as a fraction of S_{diag}, so that the intended reduction in solid panel stiffness can be easily observed graphically for various normalized perforation geometries. Figure 4-11 shows plots of w_{eff}/S_{diag}, as a function of D/S_{diag} for 2, 3, 4, and 5 rows of perforations, N_r, and a specimen panel height, H_{panel}, of 1534mm. For comparison, the single perforation panel reduction factor proposed by others of

(3-33) is plotted in the same figure. Note that, due to the normalization of the variables, the geometry required for a given stiffness reduction will vary greatly. For example, for each of the considered options of N_r, the stiffness reduction factor of (3-46) is equal to 0.9723 when the ratio of D/S_{diag} is equal to 0.1768 (0.25/sinθ). Shown in figure 4-12 are three options for which this condition is satisfied: N_r =3, D=128mm, and S_{diag}=723mm; N_r =4, D=96mm, and S_{diag}=542mm; and N_r =5, D=77mm, and S_{diag}=434mm.

Figure 4-11 also indicates stiffness reduction factor and D/S_{diag} values for layout options considering D =200mm. Specimen options with D =200mm are shown in figure 4-13 for N_r equal to 3, 4, and 5.
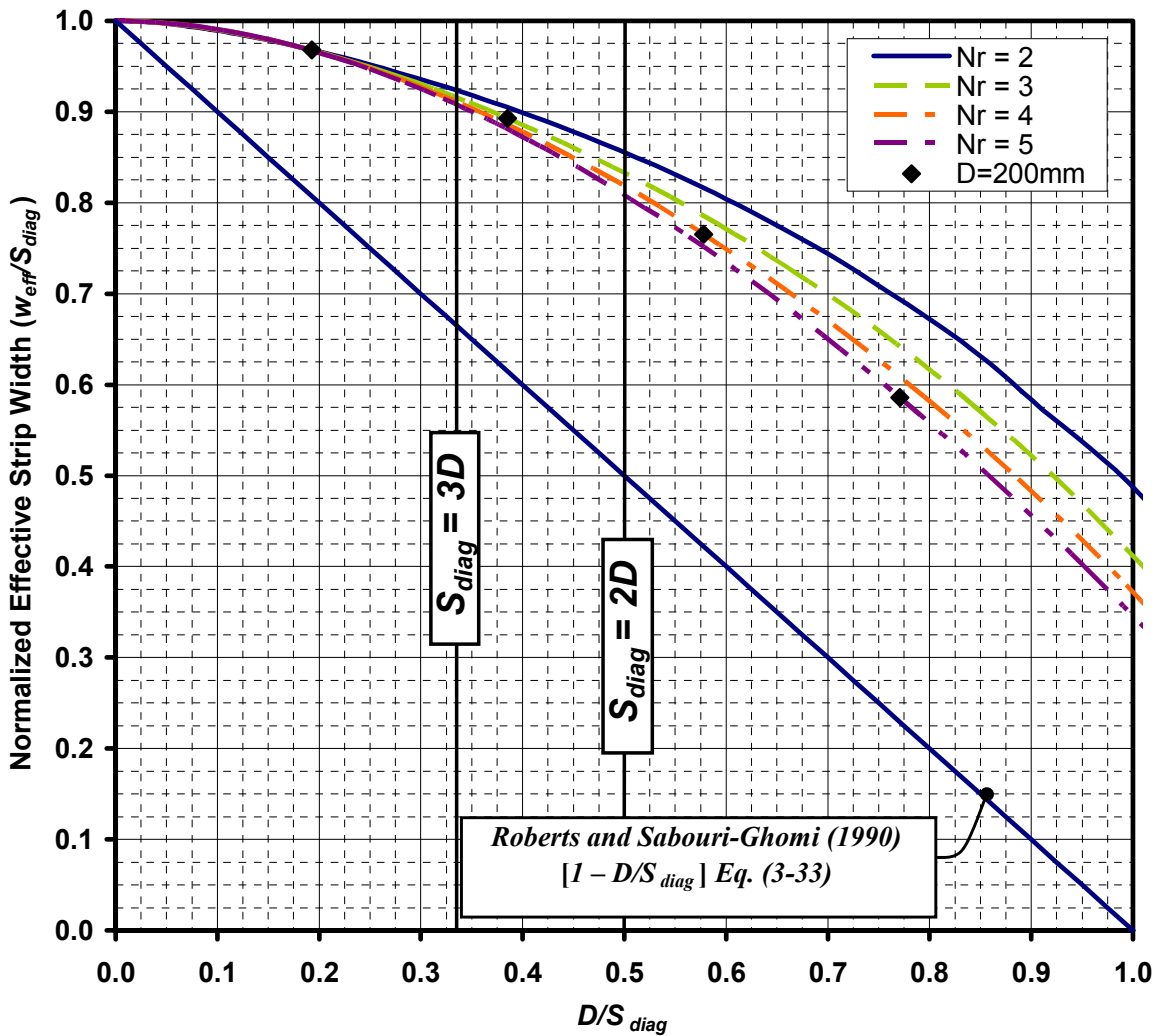
FIGURE 4-11 Normalized Strip widths versus Perforation Diameter
H_{panel} = 1534mm and θ = 45°

(a)
$N_r = 3$
$D = 128$mm
$S_{diag} = 723$mm
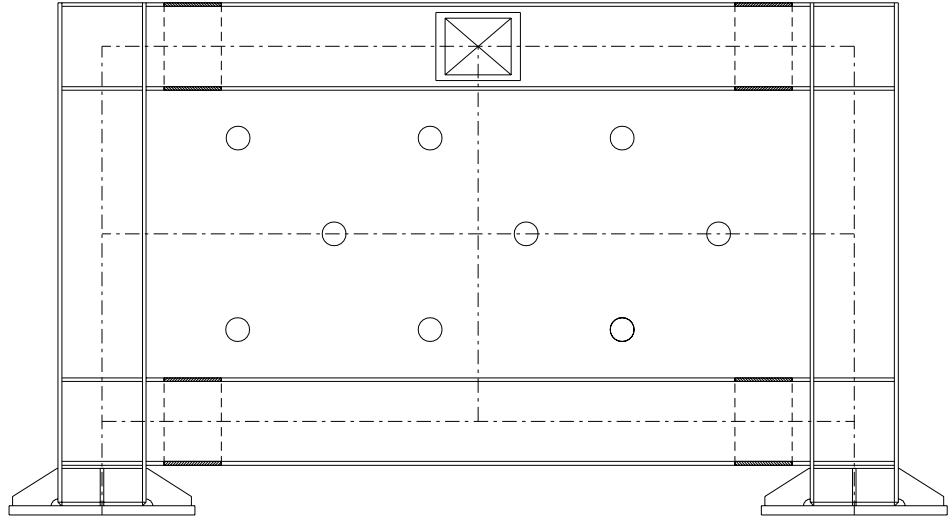
(b)
$N_r = 4$
$D = 96$mm
$S_{diag} = 542$mm
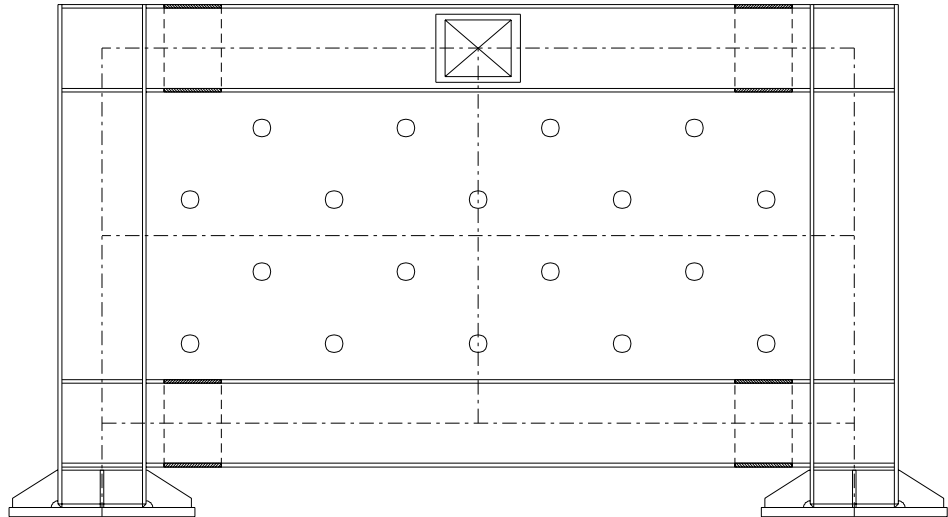
(c)
$N_r = 5$
$D = 77$mm
$S_{diag} = 434$mm
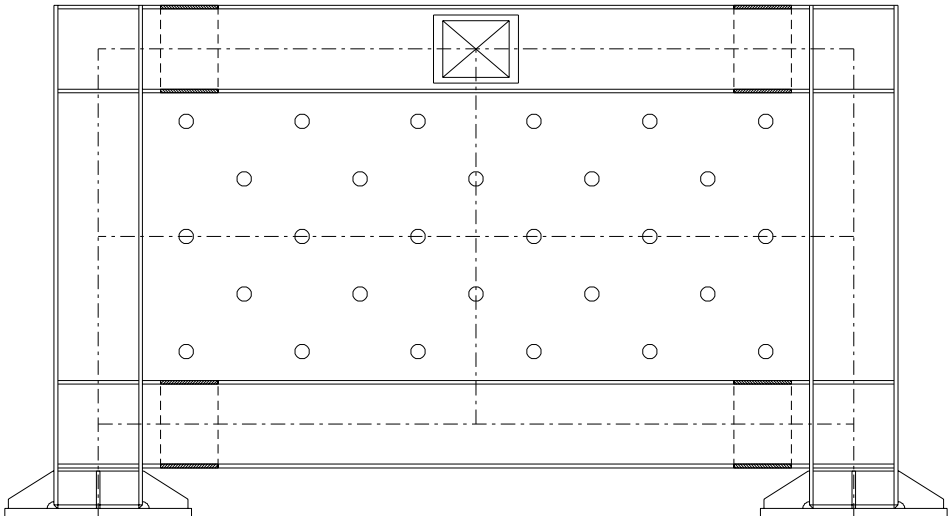
FIGURE 4-12 Perforation Layout Options with D/S_{diag}=0.1768, w_{eff}/S_{diag}=0.9723

(a)
$N_r = 3$
$S_{diag} = 519mm$
$D / S_{diag} = 0.385$
$w_{eff} / S_{diag} = 0.893$
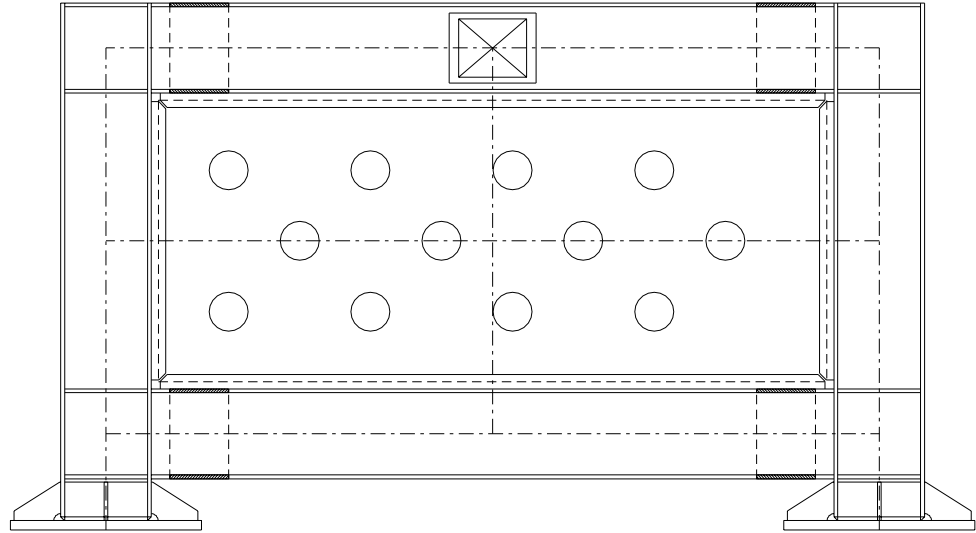
(b)
$N_r = 4$
$S_{diag} = 346mm$
$D / S_{diag} = 0.578$
$w_{eff} / S_{diag} = 0.765$
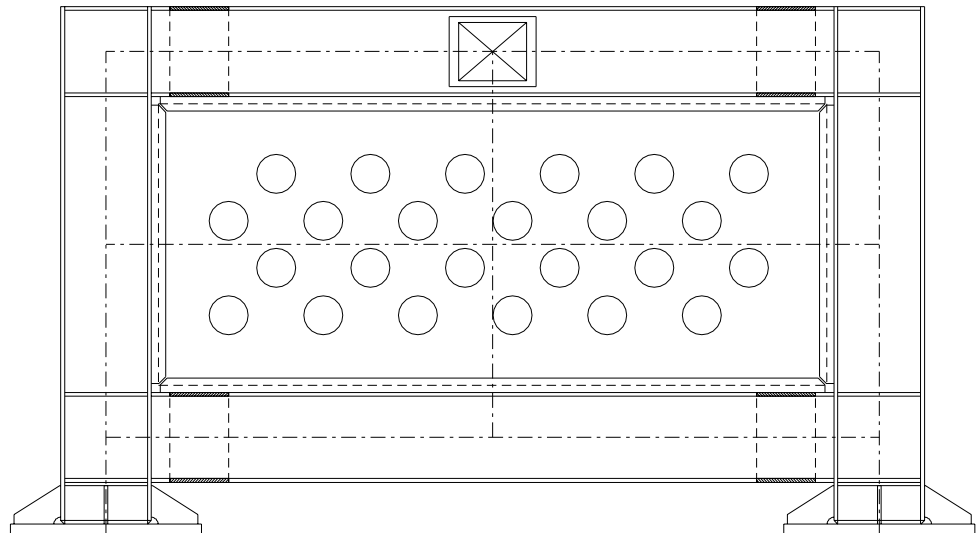
(c)
$N_r = 5$
$S_{diag} = 260mm$
$D / S_{diag} = 0.771$
$w_{eff} / S_{diag} = 0.586$
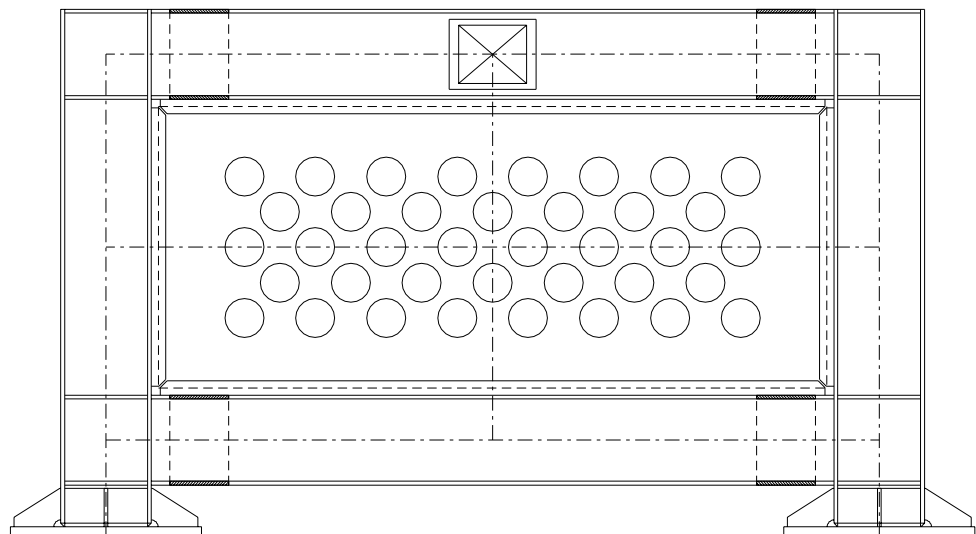
FIGURE 4-13 Perforation Layout Options with *D* =200mm

Since the specimens approximated a one-half size frame bay from the MCEER hospital project, a perforation diameter of 200mm was deemed a suitable half size hole, allowing for pass through, in practice, of a 350mm (14in) diameter water conduit. Therefore, from the options presented with perforations of that diameter, N_r equal to 4 was selected as the basis for a final specimen design. This choice provided a balance in perforation layout concerns, with the diagonal spacing slightly less than twice the perforation diameter, and the layout was estimated to provide a significant amount of stiffness reduction (23.5% less stiff compared with a solid panel) according to the relations developed in the previous chapter. In the final design, shown schematically in figure 4-14, this choice was altered to ease fabrication, providing a horizontal and vertical perforation spacing of 300mm, or S_{diag} of 424.26mm (300/sin45°). This alteration decreased the ratio D/S_{diag} to 0.4714 (and related estimated stiffness reduction of 17.8%) by slightly reducing the edge distance to approximately 1.6D.

In final fabrication of this specimen, the perforations were flame cut from the solid panel (which was, recall, built up from three smaller panels and jointed with a "seam weld"). Therefore, prior to testing, the edge of each perforation was de-burred with a power grinder to remove the small notch left from the initial burn-through from the flame-cutting process. This also smoothed out any additional smaller imperfections in the hole that were less conspicuous.
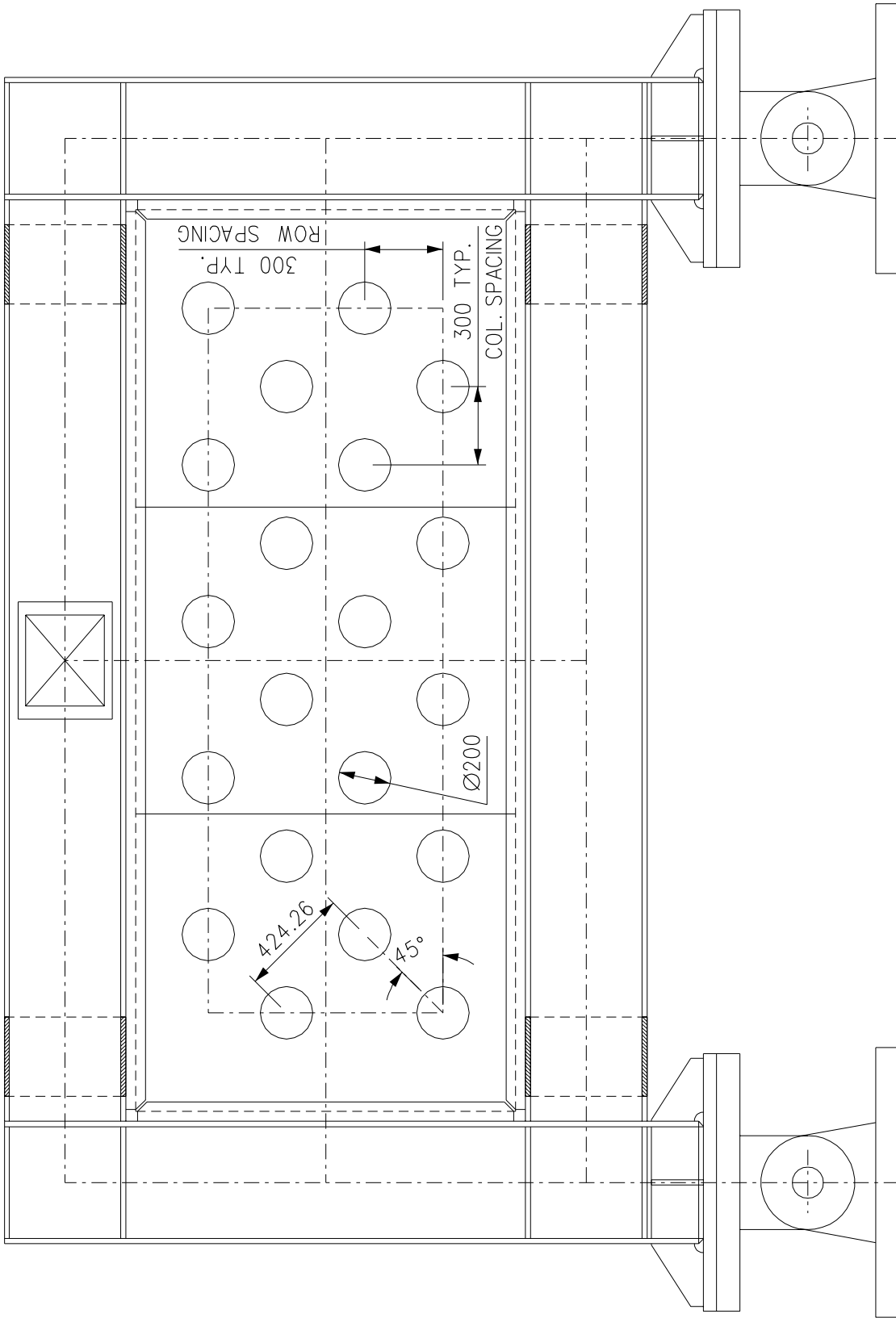
FIGURE 4-14 Specimen P Final Design

4.2.8 Cutout Corner-Reinforced Panel Specimen (CR)

Cutout corner SPSWs were presented as another option for allowing utility passage through an SPSW infill panel in the previous chapter. While providing utility access, this proposed system is expected to provide strength and stiffness similar to a solid panel SPSW system.

Although chapter 3 suggested using a fix-end semi-circular arch for the preliminary design of the cutout corner reinforcement, recognize that:

1. Hinges at arch ends could just as well be actual hinges or plastic moment hinges. Either case will not risk the release of infill panel tension load through arch collapse mechanism formation, until the development of a mid-span plastic hinge.

2. Therefore, tabulated relations (Leontovich 1959) similar to those of chapter 3 (but for the hinged-end case), for axial load and bending moment at the arch midpoint, given by (4-9) and (4-10), respectively, are utilized:

$$P_{frame-pin} = \frac{15 \cdot E \cdot I}{4 \cdot \left(2 - \sqrt{2}\right)^2 \cdot R^2} \cdot \gamma \qquad (4\text{-}9)$$

$$M_{frame.CL} = \frac{15 \cdot E \cdot I}{8 \cdot \left(2 - \sqrt{2}\right) \cdot R} \cdot \gamma \qquad (4\text{-}10)$$

These relations are substituted into the axial-moment interaction equation of (3-59), and the resulting expression can be solved for the maximum arch plate section thickness at mid-span.

3. Then, by choosing a desired drift of 4%, and 345MPa material yield stress, the maximum thickness of the "opening" corner arch (left side of figure 3-20, with no panel stresses assumed to be acting on it) is calculated as 19.5mm.

4. The arch plate width disappears from the solution of the interaction equation in the previous step. However, by considering the axial component of force in the arch due to the panel forces (3-58) at the closing corner (right side of figure 3-20) only (for conservatism), the arch plate width can be selected to resist the applied loading. Since, as described in section 3.4.2, the components of arch forces due to panel forces are opposing those due to frame corner opening, the resultant force will be smaller than the components considered individually.

5. Following the size selections of the previous steps, a fish plate was added to the section to facilitate infill panel attachment to the arch. Recognize that this addition would result in a stiffer arch section, and consequently, due to compatibility of frame corner deformation, it would be possible to yield part of this "T" at 4% drift due to corner opening. However, because the thickness selected in step 2 was considered robust enough to withstand the loads alone, it was assumed that the presence of the stiffer and stronger T section would not be detrimental to system performance.

From the above steps, an arch section 160mm wide by 19mm thick was selected, with a 6mm by 45mm fish plate resulting in the specimen detail shown in figure 4-15.

Following the above design procedure, nonlinear static pushover analysis was performed on a model of the specimen using SAP2000. This analysis was used to confirm that the selected section did not produce the "knee-brace effect" by inhibiting corner deformation expected in typical frame action (or in this case, the deformation required for the intended function of the RBS detail), or precipitate column yielding or beam yielding outside of the RBS region.
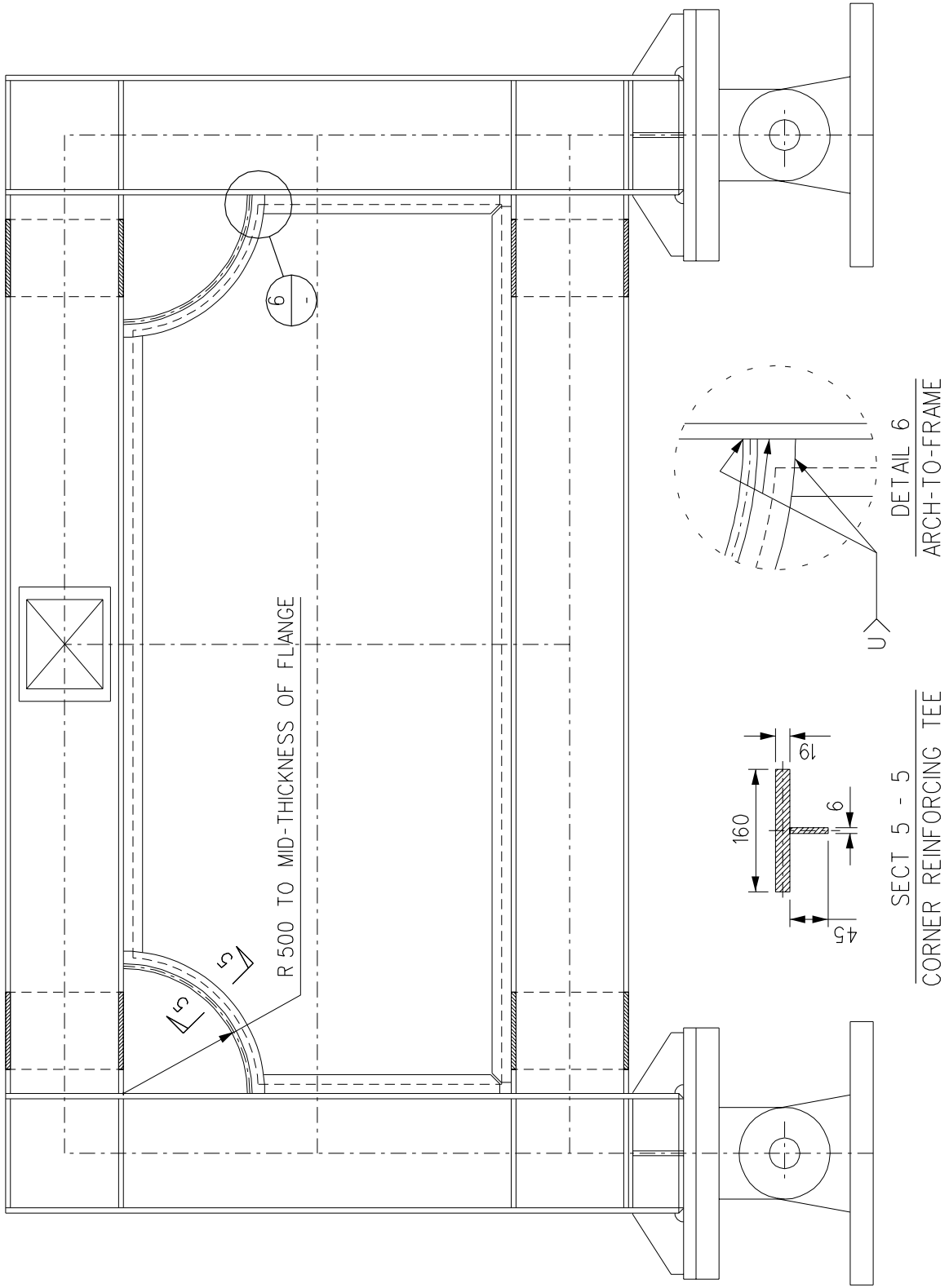
FIGURE 4-15 Specimen CR Final Design

R 500 TO MID-THICKNESS OF FLANGE

DETAIL 6
ARCH-TO-FRAME

SECT 5 - 5
CORNER REINFORCING TEE

160

19

6

45

4.3 Test Setup

Specimens S1, P, CR and S2 are shown prior to testing in figures 4-16, 4-17, 4-18, and 4-19, respectively. These figures show some of the setup details described below. Details of the loading protocol and observations of test results are presented in the next chapter.

4.3.1 Specimen Mounting

The column base hinges, each of 3000kN capacity, previously used for testing of the BRB specimens (by others) were re-used for these tests, fastened to the strong floor of the NCREE laboratory using high strength, post-tensioned rods. Specimen column base plates and spacers were dimensioned such that the hinge axis was 850mm from the centerline of the bottom beam (i.e. the distance h_{hinge} referenced above as shown in figure 4-5 (a)). Base plates were attached to the hinges using eighteen 35mm diameter high strength bolts per hinge, with an identical number attaching the bottom of the hinge to the laboratory strong floor.

4.3.2 Actuator Mounting

Although it was considered to use a loading beam connected to the top of each column using hinges to laterally load the specimen during testing, NCREE had successfully used an H-shaped loading detail in the BRB experiments mentioned previously that was re-used for the SPSW tests. This detail, designed by the NCREE staff, allowed for the attachment of four actuators in parallel for applying the load to the specimen via the center of the top beam. The horizontal box beam of the "H" was fabricated into each specimen welded to the top beam's web and flanges. The two vertical legs of the H were connected to the box beam, using eight high strength bolts per leg, after each specimen was moved into the testing bay and affixed to the column base plates. Actuators were then bolted to the concrete reaction wall and the legs of the H loading detail, as shown in figures 4-16 to 4-19.

FIGURE 4-16 Specimen S1 prior to Testing
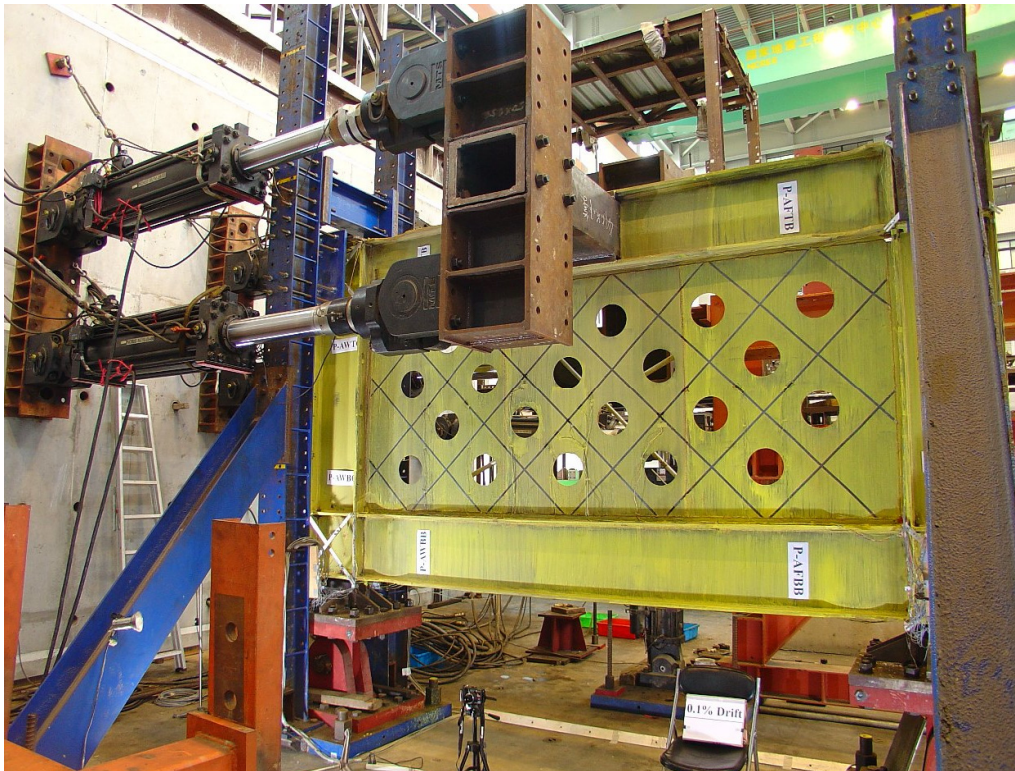
FIGURE 4-17 Specimen P prior to Testing
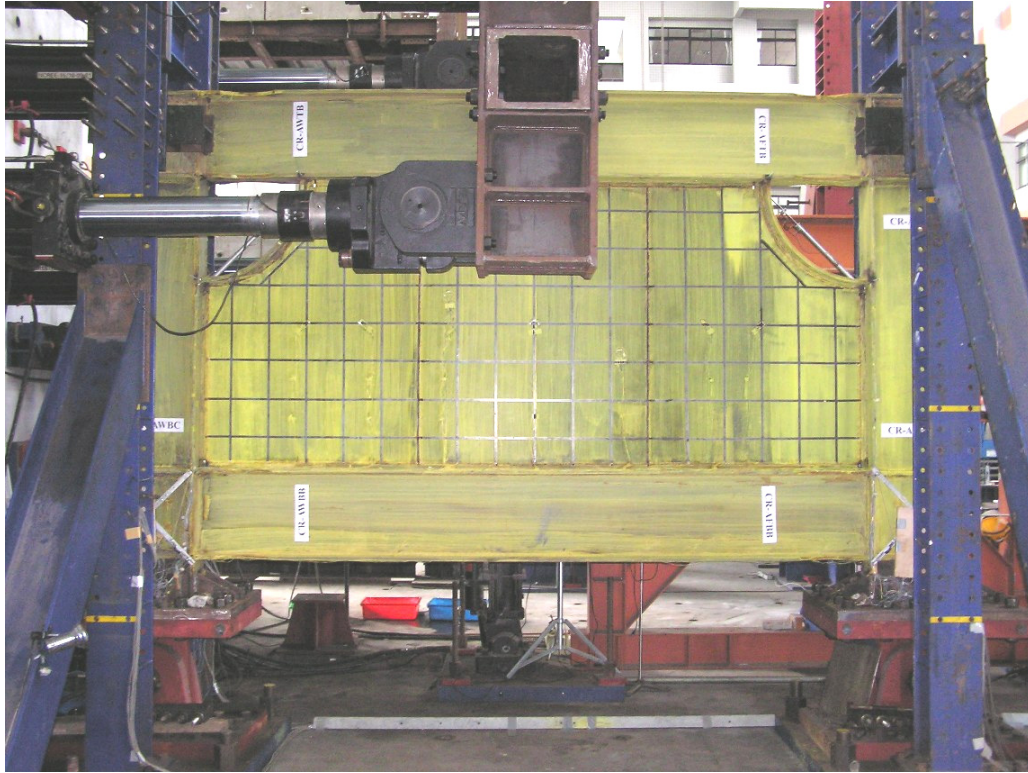
FIGURE 4-18 Specimen CR prior to Testing

FIGURE 4-19 Specimen S2 prior to Testing

4.3.3 Lateral Supports

The specimens were laterally supported at three locations along the top beam. Physical lateral supports typically used by NCREE were provided at each column, while the loading detail itself provided some degree of additional support at the center of the beam, as shown in figures 4-16 to 4-19. In the first two tests, the lateral support detail used at the top of the column consisted of a plate, bolted to the top beam top flange continuity plate, and restrained on the edge by vertical plates parallel to the plane of motion of the specimen, and lubricated with grease to minimize friction between the surfaces. This detail is shown in figure 4-20. The final two tests used a slightly different system, to be described in the next chapter.

FIGURE 4-20 Lateral Support at Top of Column
(Shown for Specimen S1 Prior to Testing)

4.4 Instrumentation

4.4.1 Frame Behavior

Boundary frame behavior during testing was measured in a number of ways. Figure 4-21 is a schematic of instrumentation used for frame behavior measurement. A naming convention was established for specifying channel names and locations on the specimen, for notetaking and photo documentation during the testing. As shown in the figure, with the reaction wall to the left of the specimen, the side in view is denoted side "A", while side "B" is the opposing side of the specimen. Locations on columns are noted by the relation to the reaction wall with the column designation first (WC or FC for "wall column" of "far column"), followed by the detail designation. For example, the flange furthest from the wall on the column closest to the wall is designated "WCFF" for "Wall Column-Far Flange." Beams follow a similar convention, except use top and bottom identifiers, e.g. "TBBF" for "Top Beam-Bottom Flange." Finally, locations along frame members are indexed using numbers, as shown in the figure, increasing along the length of beams with increasing distance from the wall, and increasing along the height of columns as the distance from the top beam increases. Beyond these conventions, the exact meaning of each acronym used is not described here (but could be guessed); the notation described in figure 4-21 was used for all data analysis.

4.4.1.1 Strains in Frame Members

Uniaxial strain gages were used for flange strain measurement along the member axis, at three and four locations on columns and beams, respectively, as designated by the previously described labeling convention. As shown in Sections A-A and B-B in figure 4-21(a), each of the numbered locations on a frame member has four strain gages, two affixed to each flange, at the middle of each flange half width, on either side of the web. Assuming that plane sections remain plane, this arrangement allows for measurement of average axial strains and curvature at a cross section, which can be used to calculate axial load and moment, respectively, at that location.

Uniaxial strain gages were also attached to the cutout corner reinforcing arch, on both sides of the flange, at three cross-sectional locations along the arc length: the center and near each end at a distance of 37.5mm from the face of the nearest boundary frame member flange (half the width of the frame-to-infill fish plate), as indicated in figure 4-21(b). Gages locations were designated

with a naming convention similar to that described above for the frame gages. The first two letters were either WA for "Wall Arch" or FA for "Far Arch", followed by an H or P for "Hole" side or "Panel" side, respectively. Locations along the arch were numbered 1 to 3, from top (closest to the top beam) to bottom (where the arch meets the column). Gages were placed at the middle of the half-flange width as for the frame sections, for a total of 12 gages per arch flange. In addition, one gage was placed at each of the three cross section locations on the arch fish plate (far arch only), at half the depth, and positioned such that each gage was tangential to the arch orientation.

4.4.1.2 Frame/Specimen Displacements

Displacements were measured at a number of locations on the specimen. Channels "TMt" and "TMb" correspond to Temposonics Magnetostrictive Transducers (Temposonics) for measurement of horizontal displacements at the centerline of the top and bottom beams, respectively. Potentiometers were used to measure horizontal displacements at the quarter points of the height of the far column with respect to a fixed reference instrumentation column. These data channels were named DT1, DT2, and DT3, from top to bottom, coinciding with the column strain gage location convention described above and shown in figure 4-21. Potentiometers were used to measure diagonal displacements DT4 and DT5, the relative displacements between opposite frame corners and along a 45° line centered about the vertical centerline of the specimen, respectively.
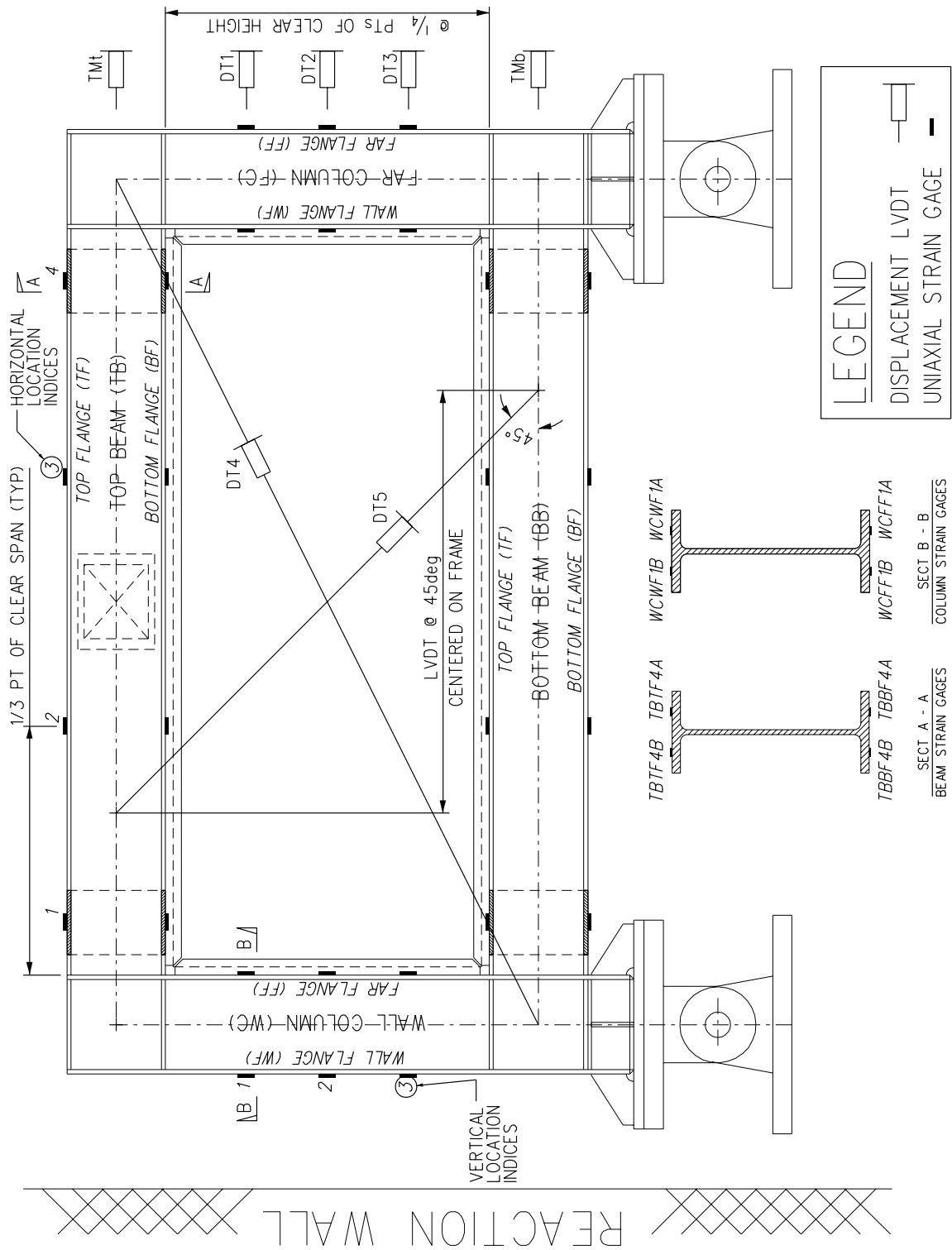
FIGURE 4-21 Specimen Frame Instrumentation Layout and Labeling Convention (a) Channels Typical of all Specimens

95
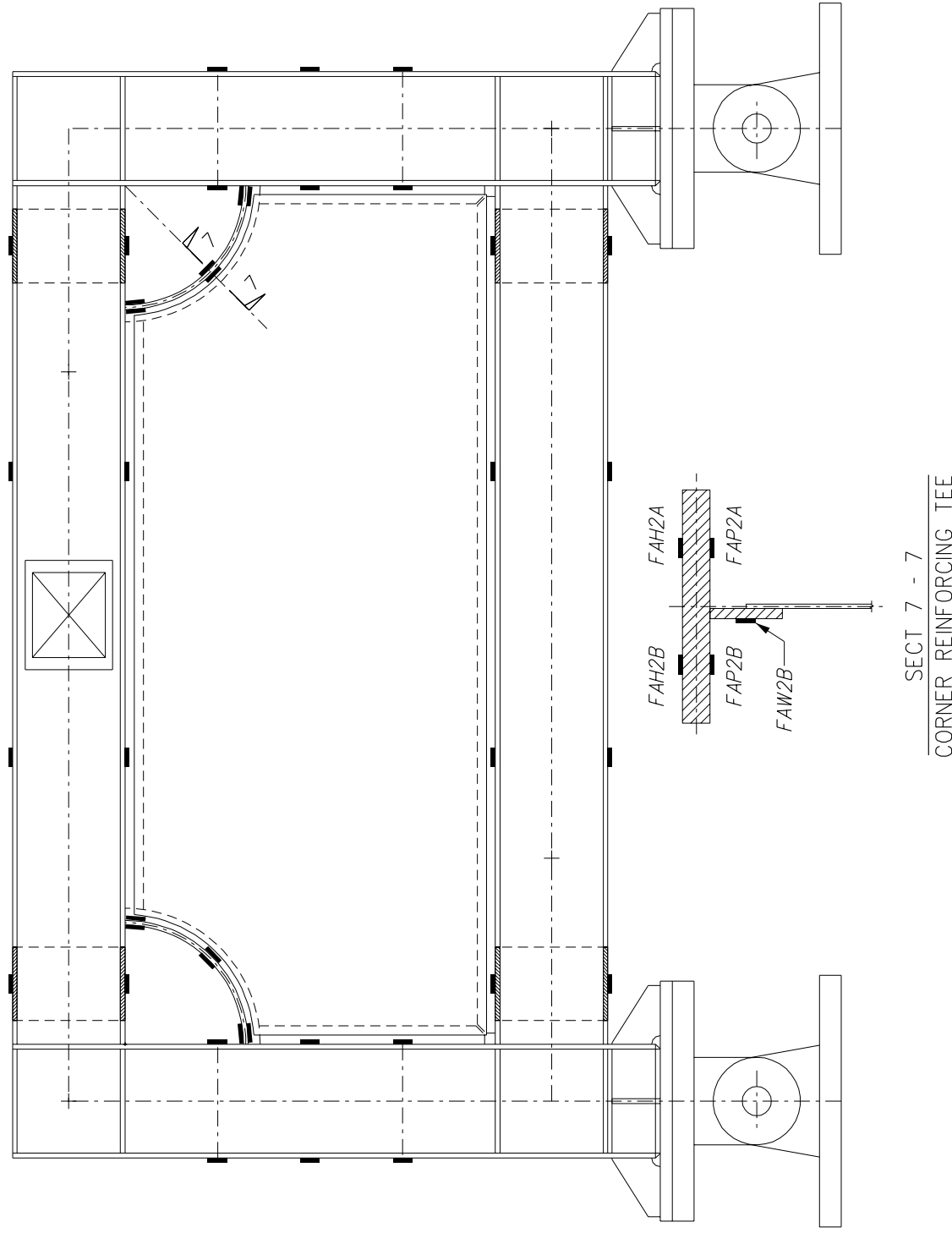
FIGURE 4-21 (cont'd) Specimen Frame Instrumentation Layout and Labeling Convention
(b) Strain Gages and Channel names for Corner Reinforcing Arch – Specimen CR

4.4.1.3   Panel Zone and Arch Deformation Measurements

All specimens (except for the first tested, S1) included "pi" gages for measuring the deformation of the panel zone. Pictured in figure 4-22, a "pi" gage device consists of an aluminum bar, one end pinned at a corner of the panel zone and the other end slotted to allow movement but guidance along the diagonal, while there is a piece of metal, bent in a semi-circular "omega" shape, which measures displacement via a calibrated strain gage, as this omega shape opens or closes. The "pi" gage was also utilized to measure diagonal displacements between the ends of arches in specimen CR as shown in figure 4-23.

FIGURE 4-22 "Pi" gage for Panel Zone Deformation Measurement

FIGURE 4-23 "Pi" gage for Arch Deformation Measurement in Specimen CR

4.4.2 Panel Behavior

Quantitative measurements of panel behavior were made by means of strain gages affixed to the panel. A strain gage layout was developed for the panel to provide uniform measurements for all four specimens, plus additional measurements as each specimen dictated. As with the gages placed on frame members, the panel gages were placed at the same locations on sides "A" and "B", so that both axial and bending strains in the panel could be measured.

Specimen P served as the template for panel gage layout as shown in figure 4-24. Uniaxial gages were positioned at 4 locations (PU1, PU2, PU3, and PU4) to measured strain in the narrow width between holes. This gage orientation was along the 45° diagonal that was the basis for the hole layout. Three-gage rosettes were placed at three locations as shown on the figure, labeled PTM2, PTM3, and PTM4. These rosettes were placed on the panel to allow measurement and calculation of principal strains and therefore the orientation of the panel tension field action.

Panel behavior was also measured qualitatively by means of a visible "grid" on the specimen, produced by applying a masking tape before application of the paint/whitewash coating, and then removing the tape prior to testing. This grid allowed for simple observations of buckling orientation and yielding in the panel during testing. Gridlines were spaced at 200mm horizontally and vertically on specimens CR and S2, while on specimen P, gridlines were centered between diagonal strips of perforations, as shown in figures 4-16 to 4-19.
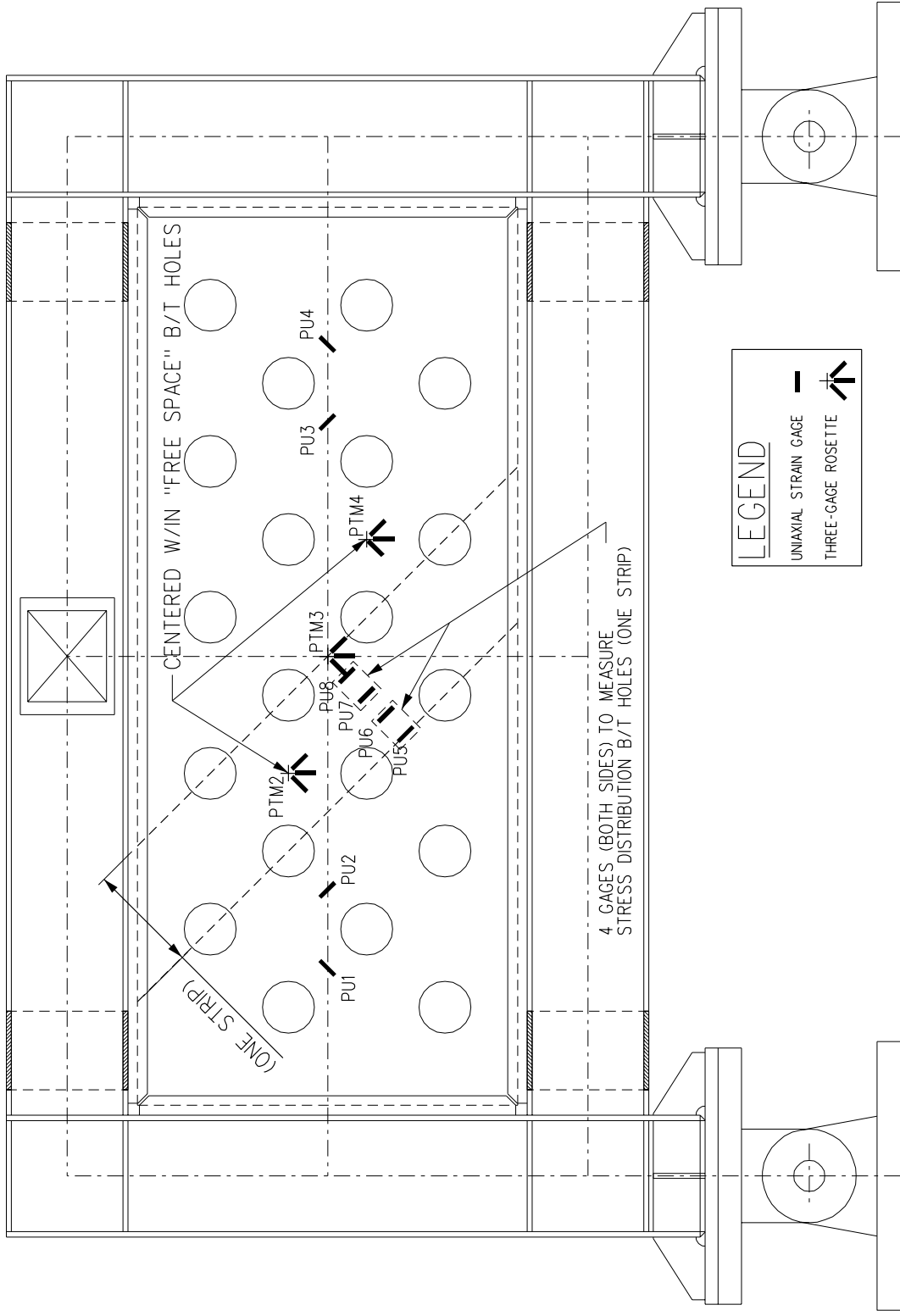
FIGURE 4-24 Specimen P Panel Strain Gage Layout and Labeling Convention

SECTION 5

EXPERIMENTAL PROGRAM RESULTS AND OBSERVATIONS

5.1   General

This chapter describes the loading program and experimental observations for the three LYS SPSW specimens discussed in Section 4. Methods utilized for estimation of yield base shear and displacement values prior to testing are briefly discussed. Development of the loading protocol used in testing, and recorded cyclic displacement histories are presented. Following this discussion, the testing of each specimen is described in detail, and observations of specimen behavior made during testing are given.

5.2   Loading Program/Protocol

Experiments at NCREE conducted using quasi-static cyclic loading typically utilize a displacement-controlled loading history. Therefore, the loading protocol was developed as a hybrid/combination of the ATC-24 (1992) protocol and the AISC Seismic Provisions (2002) requirements for loading sequence in testing of, as described below.

5.2.1   Estimation of Yield Force and Displacement

Estimation of yield force and displacement values was required prior to the establishment of a specimen loading sequence. The structural analysis program SAP2000 (CSI 1998) was utilized for this purpose. An analytical model representing the solid panel specimen was developed, using the strip model representation of the infill panel described previously. Coupon tension test data for the material used in specimen fabrication was input into the SAP2000 models. A nonlinear static pushover analysis was performed on this model, producing the base shear versus top beam displacement relationship, shown in figure 5-1, which was used to aid in the selection process for cycle amplitudes as described below.
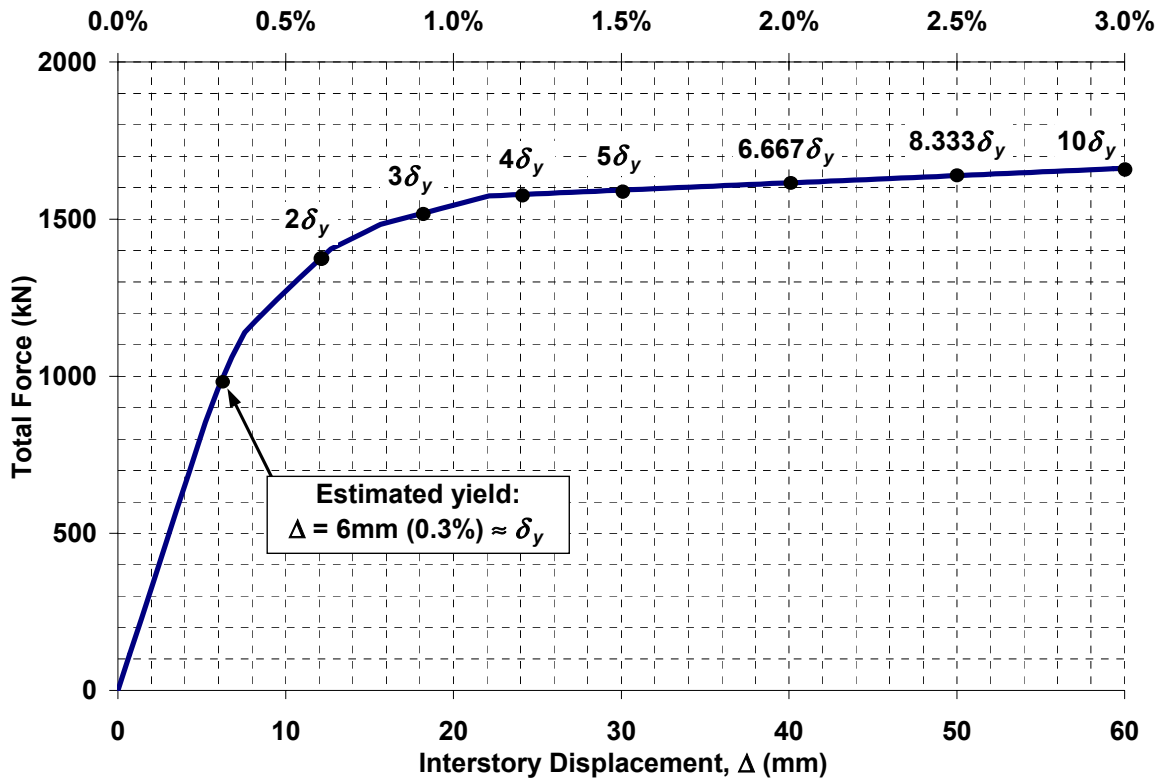
FIGURE 5-1 SAP Strip Model Predicted Pushover Curve

5.2.2 Cyclic Displacement Loading History

In agreement with the typical testing procedure at NCREE, a displacement-controlled loading scheme was selected for the entire experimental program. The same cyclic displacement loading history was developed for actuator control of all the specimens tested. The base shear versus displacement curve generated from the SAP2000 pushover analysis described in the previous section was used to formulate a proposed loading protocol, and estimate the yield displacement. Values of the initial two displacement amplitudes were chosen as 1/3 and 2/3 of the estimated yield displacement to insure observation of multiple elastic cycles prior to the specimen reaching the global inelastic region of behavior. Three cycles were to be performed at each of these amplitudes, in compliance with the ATC 24 loading protocol (1992) recommendation of a minimum of six cycles at amplitudes less than δ_y (although it suggests using force control up to a force level of approximately $0.75Q_y$). Once the three cycles at the estimated yield displacement were completed, maximum displacements were increased by multiples of δ_y until reaching an estimated ductility of three. After this point, the number of cycles at each target displacement was decreased from 3 to 2, and these target values continued to increase by an estimated ductility

102

of one until a ductility of five was reached. This estimated ductility coincided with a 1.5% story drift between the top and bottom beams. Beyond this point, cycle amplitudes were increased by drift increments of 0.5% until reaching 3.0%. After this point, if the specimen could still resist loading, the amplitude would be increased by increments of 1.0% drift. Table 5-1 lists the resulting values for the target loading history, while figure 5-2 presents the same information graphically, showing interstory displacement magnitude on the left vertical axis, and corresponding interstory drift on the right vertical axis.

TABLE 5-1 Cyclic Displacement History

Displacement Step	Number of Cycles	Cumulative Number of Cycles	Estimated Ductility Δ/δ_y	Interstory Displacement (mm)	Interstory Drift (%)
1	3	3	0.33	2.0	0.10
2	3	6	0.67	4.0	0.20
3	3	9	1.00	6.0	0.30
4	3	12	2.00	12.0	0.60
5	3	15	3.00	18.0	0.90
6	2	17	4.00	24.0	1.20
7	2	19	5.00	30.0	1.50
8	2	21	6.67	40.0	2.00
9	2	23	8.33	50.0	2.50
10	2	25	10.00	60.0	3.00
11	2	27	13.33	80.0	4.00
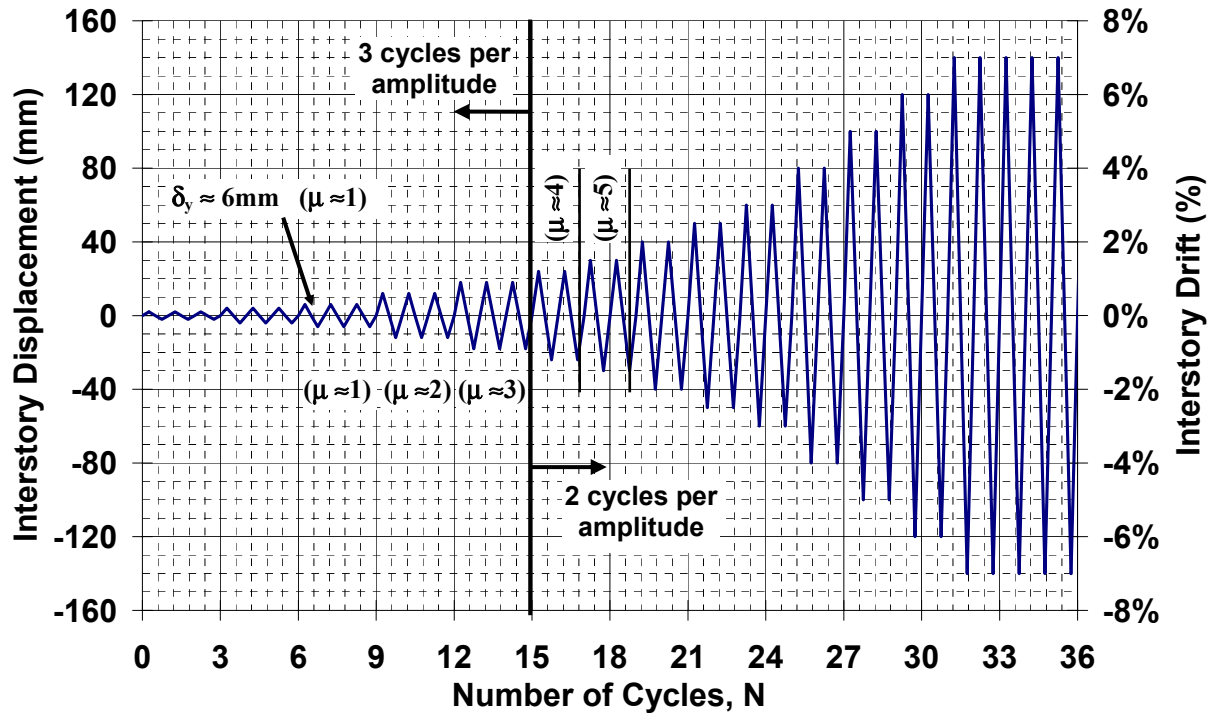
FIGURE 5-2 Loading History

5.2.3 Loading of Specimens (Actuator Control Schemes)

Four actuators were used in loading the specimens by means of the H-shaped loading detail described in chapter 4. Actuators were operated using two different control schemes during the testing program. The primary scheme specified equal forces in each of the four actuators, with one of the top actuators serving as the "master" actuator, matching its displacement to that of the target interstory displacement between the beams, measured by the difference in Temposonics TMt and TMb. The remaining three "slave" actuators would then match the force of the master actuator. The secondary actuator control scheme constrained the top two actuators to the same displacement, which was targeted to the interstory displacement as in the primary scheme. After the top actuators matched the target displacement, the bottom diagonally opposite actuator would match the top actuator force, (e.g. the top, B-side actuator would have the same force has the bottom A-side actuator) with the intention of preventing out-of-plane moments on the top beam. The primary control scheme was used initially, with the secondary scheme implemented as necessary and described in sections below for each specimen.

5.3 Experimental Observations

This section describes in detail the testing of the four low yield strength steel plate shear wall specimens. Qualitative (visual, auditory) and some quantitative observations regarding specimen performance during both linear and nonlinear regions of behavior are presented. It should be noted that in this section, the displacements and drifts are expressed in terms of *relative* or interstory displacements and drifts, i.e. the difference between the readings from top and bottom beam Temposonics, TMt and TMb, respectively, as shown in figure 4-21. Hysteresis plots of specimen base shear versus interstory displacement are shown for specimens S1, P, CR, and S2 in figures 5-3, 5-4, 5-5, and 5-6, respectively.
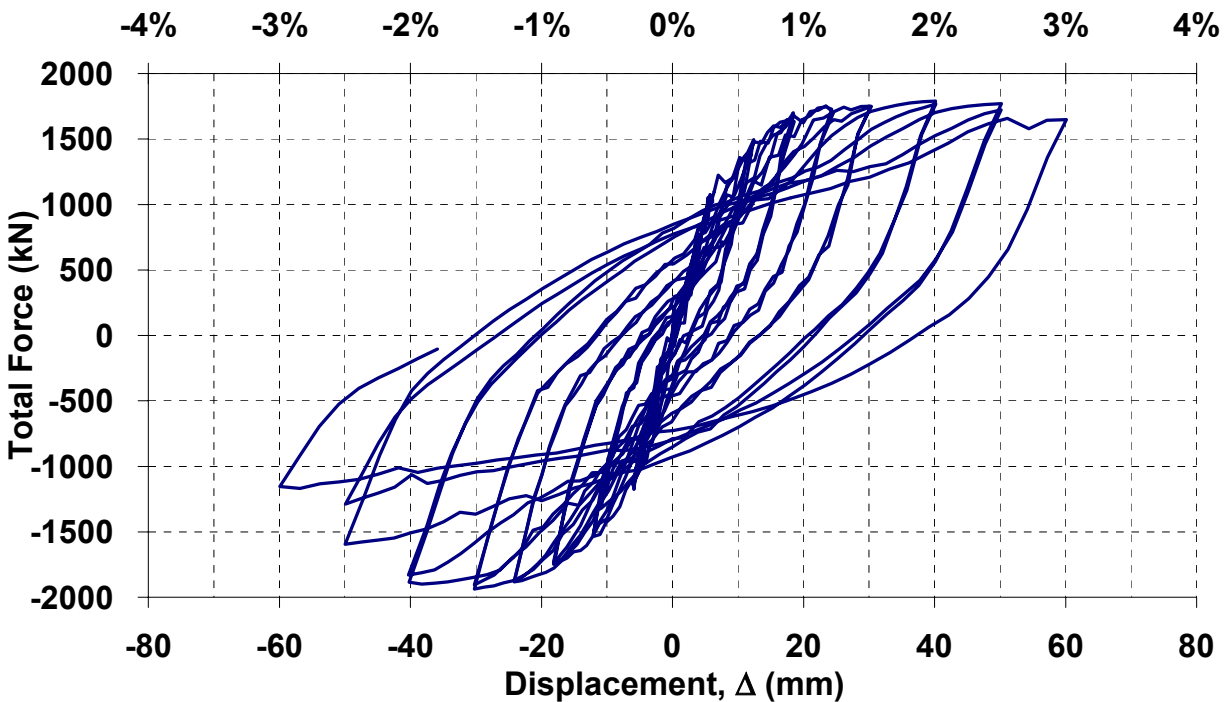
FIGURE 5-3 Specimen S1 Hysteresis
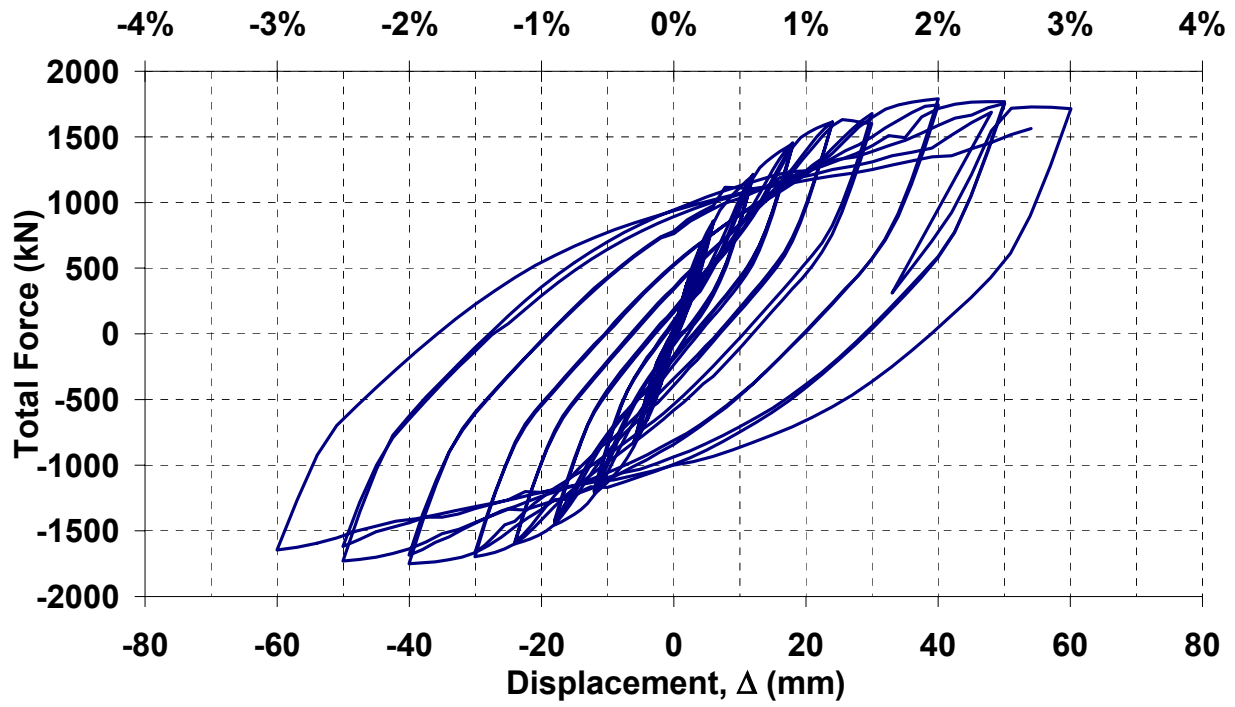
FIGURE 5-4 Specimen P Hysteresis
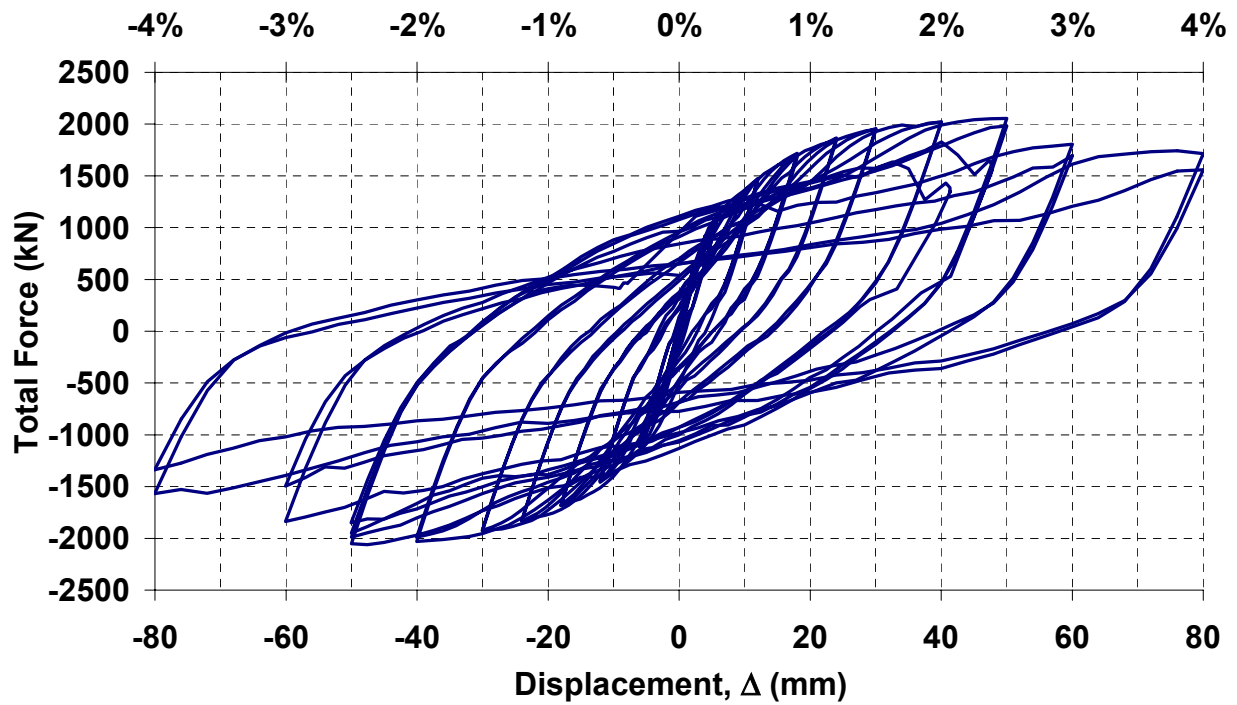
FIGURE 5-5 Specimen CR Hysteresis

106
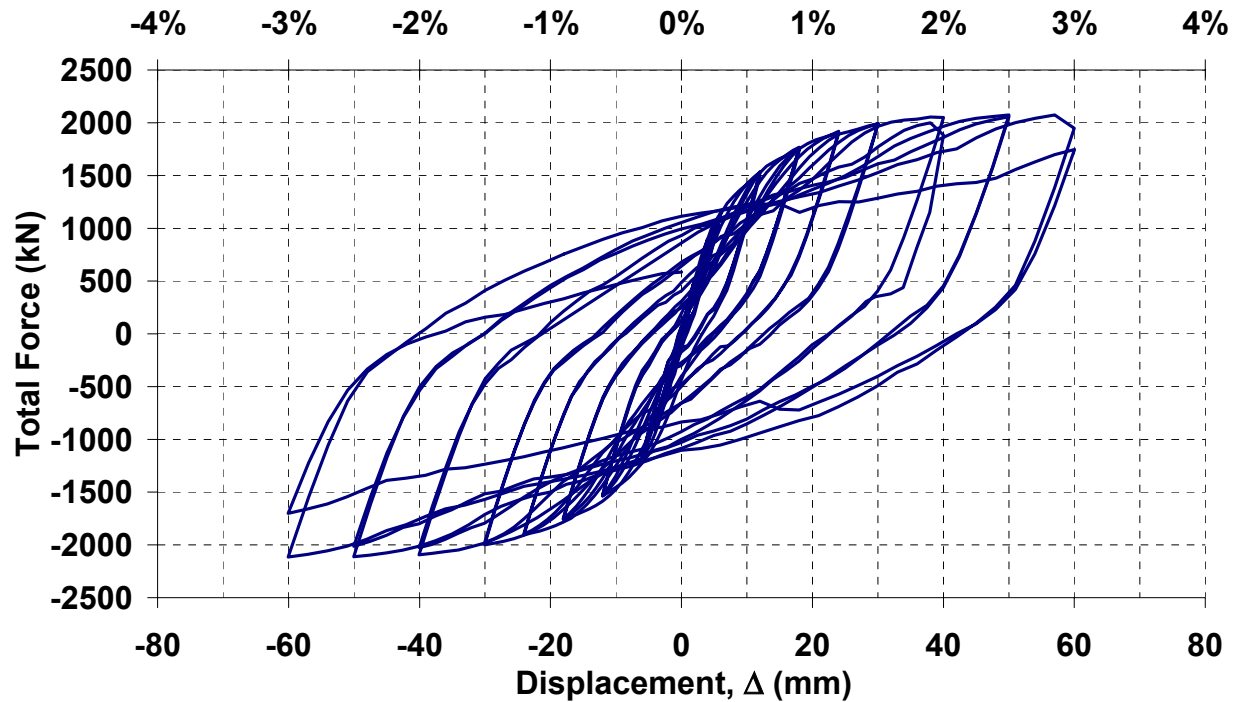
FIGURE 5-6 Specimen S2 Hysteresis

5.3.1 Specimen S1

Recall that, as described in chapter 4, specimen S1 was built as a "trial" specimen, to ensure that proper fabrication of the LYS panel was possible and could be implemented into the specimen as designed, prior to fabricating the remaining specimens in the test program. As described below, the specimen contained a number of fabrication deficiencies that were remedied in subsequent specimens. The test also utilized less instrumentation than the subsequent tests. For these reasons, only a brief summary of the test results is presented below.

Testing was conducted by the NCREE staff using the primary actuator control scheme and the same loading history described in sections 5.2.3 and 5.2.2, respectively. Figure 5-7 shows the specimen A-side following stoppage of the test after reaching 3.0% drift amplitude, due to fracture of the weld of the bottom beam bottom flange to the far column wall flange. Inspection of the flange weld failure surface, shown in figure 5-8, revealed a lack of weld penetration. Smooth un-welded and milled bevels were visible on the flange where the material should have been welded to the column, as shown in (d) of figure 5-8. The partial penetration weld with

107

backing fillet favored by the fabricator was changed for all subsequent tests to a full penetration weld, which was the preferred detail in the design drawings.

Panel fractures occurred at a number of locations due to the fabrication methods used for this specimen: adjacent to the seam welds, and at the locations of the tack welds along the B-side of the fishplate, as shown in figure 5-9. As indicated on (b) of figure 5-9, the fabricators had ground down part of the weld during fabrication of specimen. This was believed to be the cause of the fractures along the seam welds, so this practice was eliminated in the subsequent specimens, as were the B-side tack welds noted in (b) and (c).

In addition to the changes in fabrication described above, doubler-plates were added to the panel zones at each beam-column connection. Although specimen S1 performed well overall prior to the fracture of the beam-column connection weld, since it was only considered for a "trial" run with fewer pieces of instrumentation than subsequent tests, it will not be referenced further in this report.
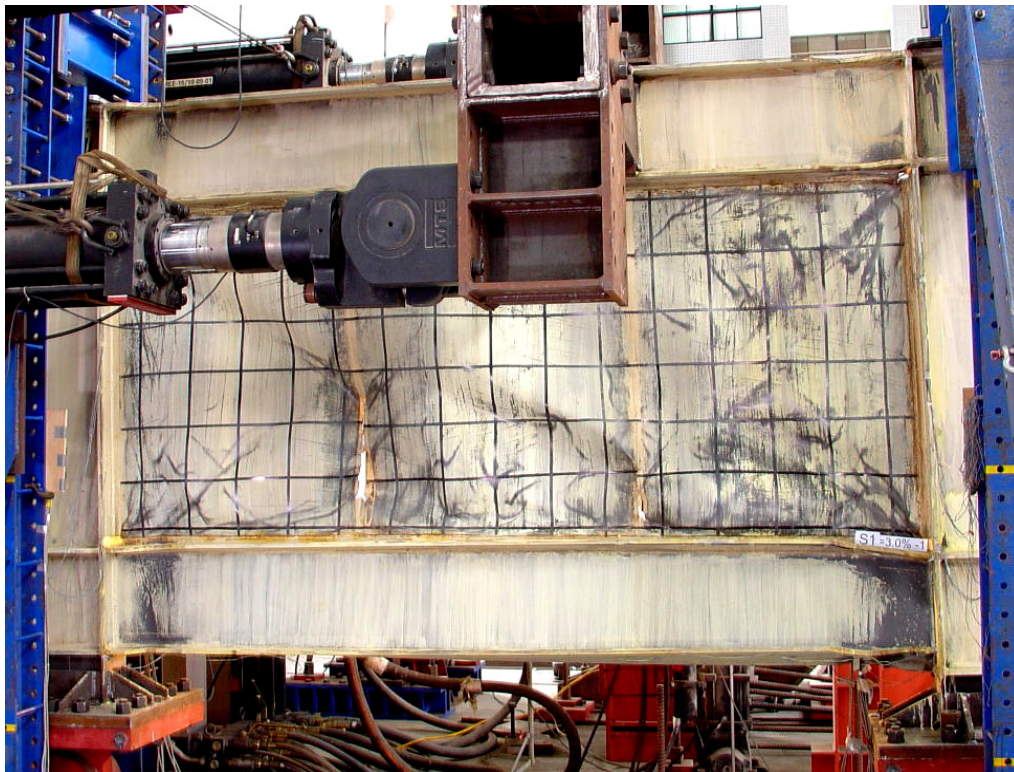
FIGURE 5-7 Specimen S1 following testing (Cycle 24, γ= 3.0% ≈10δ_y)

(a) Failed far beam to column connection from B-side

FIGURE 5-8 Bottom beam far RBS weld fracture (S1: Cycle 24, $\gamma = 3.0\% \approx 10\delta_y$)

(c) Detail of failed weld surface on column

(b) Detail of failed weld surface on beam

FIGURE 5-8 (cont'd) Bottom beam far RBS weld fracture (S1: Cycle 24, γ= 3.0% ≈10δ_y)

110

(d) Lack of weld fusion to beam flange

FIGURE 5-8 (cont'd) Bottom beam far RBS weld fracture
(S1: Cycle 24, γ = 3.0% $\approx$ 10δ_y)

(a) Wall seam weld fractures

FIGURE 5-9 Panel fractures adjacent to seam welds
(S1: Cycle 24, γ= 3.0% ≈10δ_y)
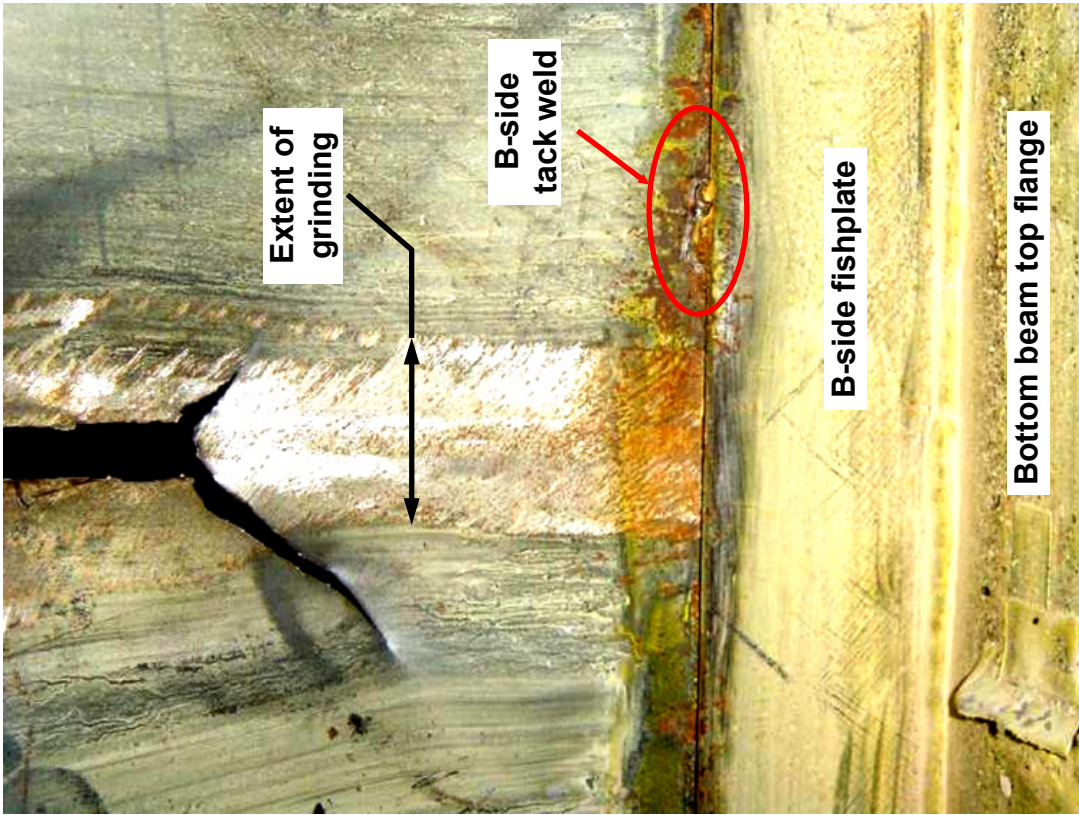
(c) Far seam weld fracture near bottom beam

Labels in image (c): B-side tack weld, B-side fishplate, Bottom beam top flange

(b) Wall seam weld fracture near bottom beam

Labels in image (b): Extent of grinding, B-side tack weld, B-side fishplate, Bottom beam top flange

FIGURE 5-9 (cont'd) Panel fractures adjacent to seam welds (S1: Cycle 24, $\gamma = 3.0\% \approx 10\delta_y$) $\approx 10\delta_y$)

5.3.2 Specimen P

Testing of perforated panel specimen P began with 3 cycles each at interstory drift amplitudes of 0.1% and 0.2% (corresponding to estimated values of 1/3 δ_y and 2/3 δ_y). Elastic buckling of the panel and linear force-displacement behavior was observed. The observed elastic stiffness was approximately 115kN/mm. Panel buckling for this specimen was markedly quieter than during the previous testing of solid panel specimen S1. Yielding was first observed after cycle drift amplitudes were increased to 0.3% ($\approx 1\delta_y$), as base shear reached 850kN. Flaking of whitewash was noted between holes at two locations on the panel. The panel remained slightly buckled when the specimen was returned to zero displacement. By the end of the three cycles at 0.3%, the extent of visible yielding had increased, with additional panel yielding near the far panel weld. This corroborated that the experimentally obtained yield displacement matched relatively well the yield drift estimated per the procedure described in section 5.2.2.

Cycling at 0.6% drift amplitude ($\approx 2\delta_y$) imparted a maximum base shear on the specimen of approximately 1200kN. This produced yielding at the top and bottom panel corners and on the web of the bottom beam/wall-side RBS connection, as shown in figures 5-10 and 5-11, respectively. Yielding spread from locations described previously.

Drift amplitudes of 0.9% ($\approx 3\delta_y$) resulted in a specimen base shear of approximately 1450kN. Yield lines in the whitewash were noted at additional locations on the web and flanges of both bottom beam RBS connections (figure 5-12), and the top of the far and wall columns nearest the panel on the A side and B side (figure 5-13). Extent of panel yielding also increased at the previously noted locations.

Two cycles were then performed at 1.2% drift amplitude ($\approx 4\delta_y$), resisted by a peak base shear of approximately 1600kN. RBS yielding started in the top beam connections and more occurred in the bottom beam connections as shown in figures 5-14 and 5-15. Figure 5-16 displays the yielding observed in the far column web and top flange continuity plate of the bottom beam.

114
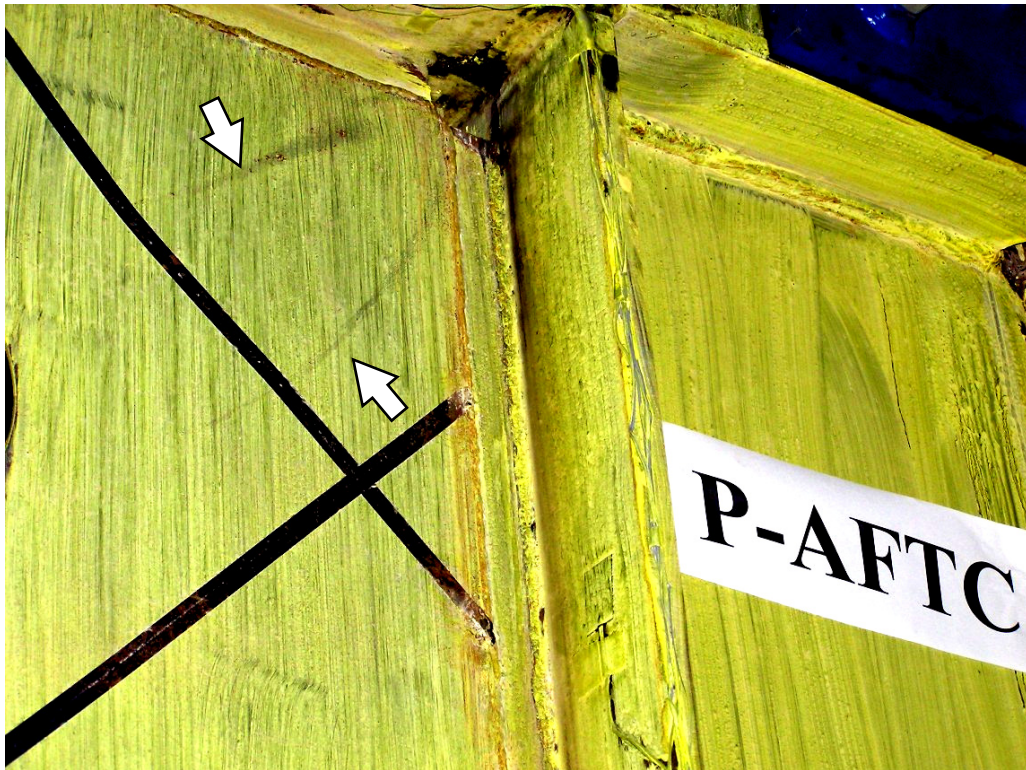
(a) Top Corner of Panel
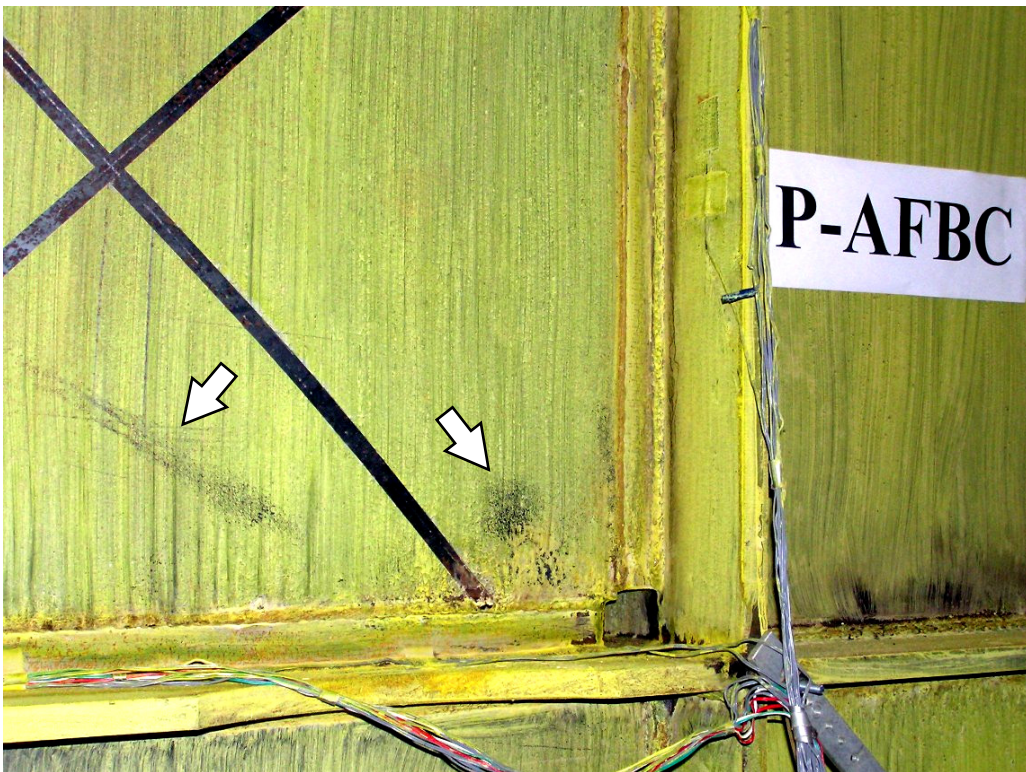
(b) Bottom Corner of Panel

FIGURE 5-10 Panel Yielding (Specimen P: Cycle 12, $\gamma = 0.6\%$, $\approx 2.0\delta_y$)

FIGURE 5-11 Wall side bottom beam RBS web yielding
(P: Cycle 12, $\gamma = 0.6\% \approx 2\delta_y$)

FIGURE 5-12 Wall side bottom beam RBS web yielding (P: Cycle 13, $\gamma = 0.9\% \approx 3\delta_y$)
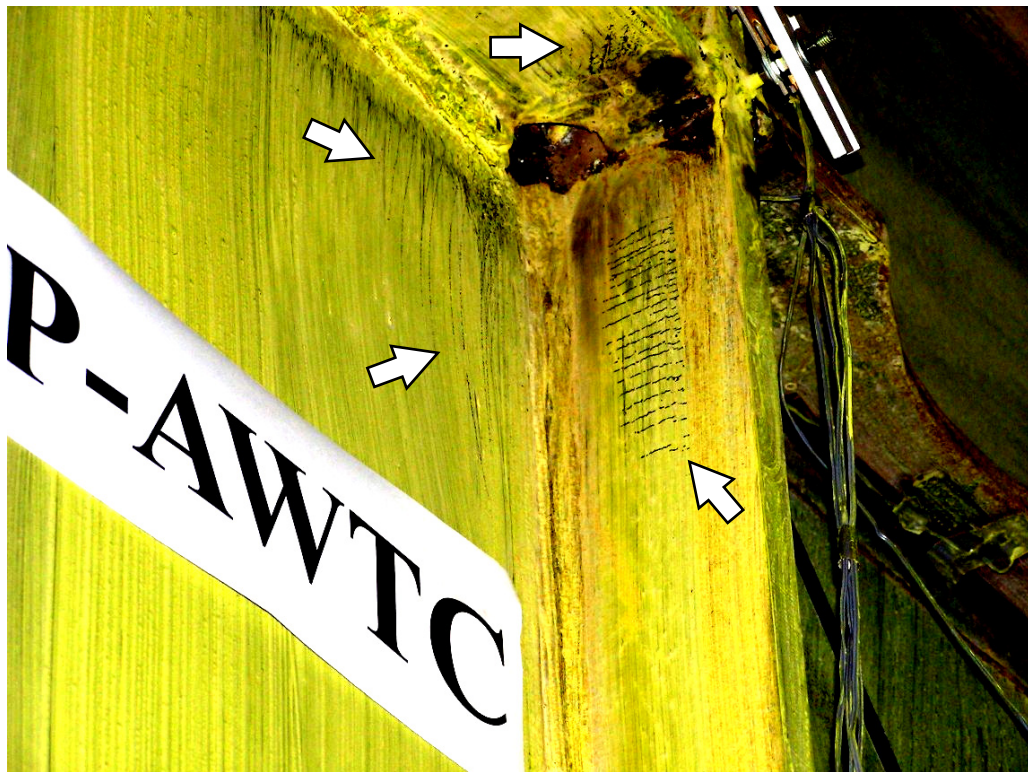
FIGURE 5-13 Wall column at bottom continuity plate of top beam
(P: Cycle 13, $\gamma = 0.9\% \approx 3\delta_y$)
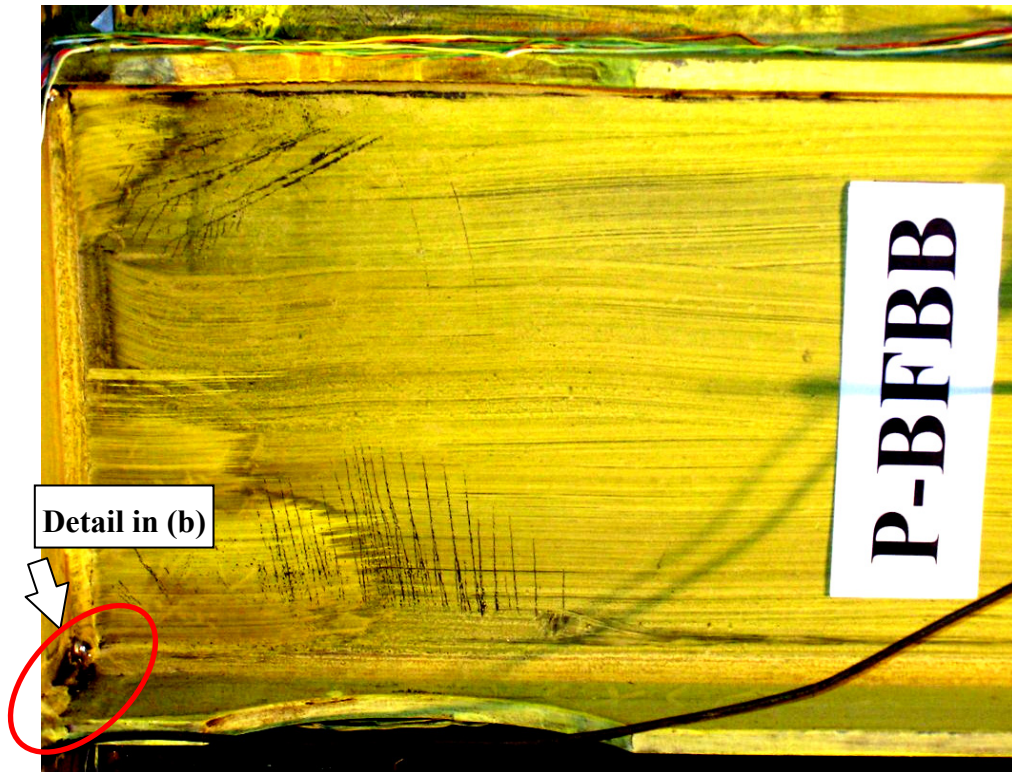
(a) Web Yielding

(b) Bottom flange weld to wall flange of far column

FIGURE 5-14 Far bottom beam RBS connections (P: Cycle 16, $\gamma= 1.2\% \approx 4\delta_y$)
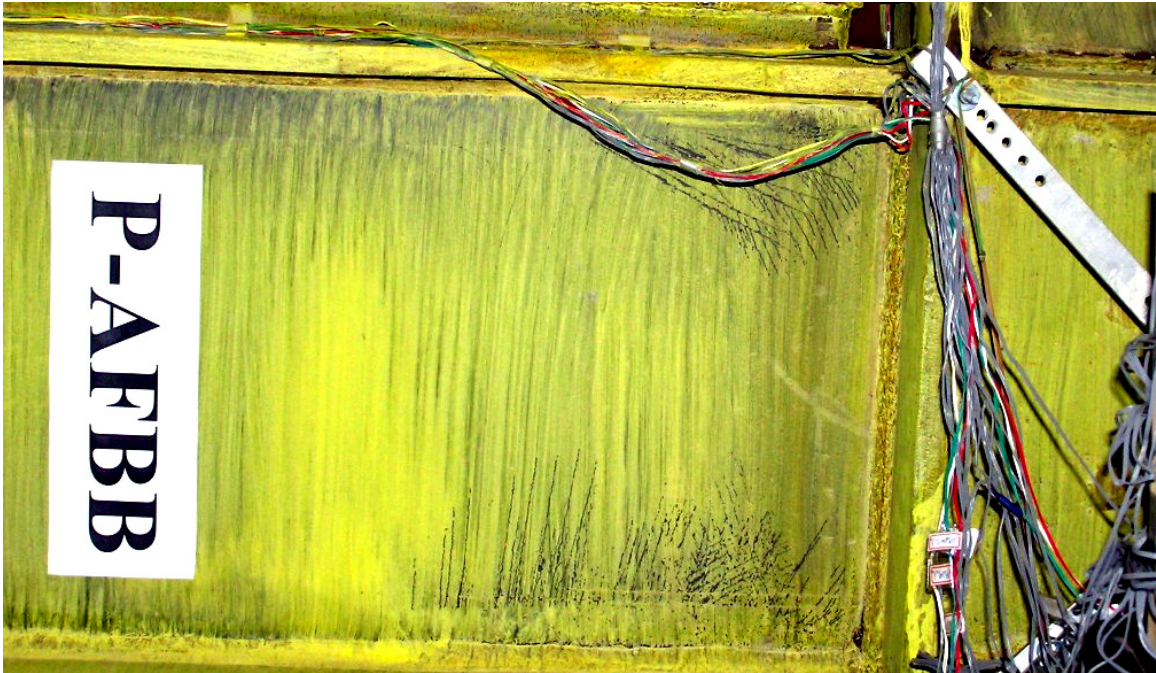
FIGURE 5-15 Far bottom beam RBS connection web yielding (P: Cycle 17, $\gamma = 1.2\% \approx 4\delta_y$)

FIGURE 5-16 Yielding in far column web and bottom beam, top flange continuity plate
(P: Cycle 16, $\gamma = 1.2\% \approx 4\delta_y$)

The first excursion to 1.5% drift ($\approx 5\delta_y$) reached a peak base shear of approximately 1625kN. Yielding in locations mentioned above appeared to spread at the same rate as previously observed. However, as the actuators approached the drift amplitude for the first positive excursion (actuators are pushing the specimen), the "H" loading assembly rotated within its plane approximately 4°, as shown in figure 5-17, twisting the top beam at the midspan point of attachment. The first cycle at 1.5% drift was completed, and the specimen was unloaded; an approximate residual displacement of approximately 11mm (0.55% drift) was recorded at this point of zero force. Visual inspection of the top beam and the rest of the specimen revealed no visible residual effect due to the H rotation. Following the visual inspection, cables with turnbuckles were added and tightened to support the actuators from the strongwall as shown in figure 5-18, in an attempt to prevent further twisting of the H loading assembly.
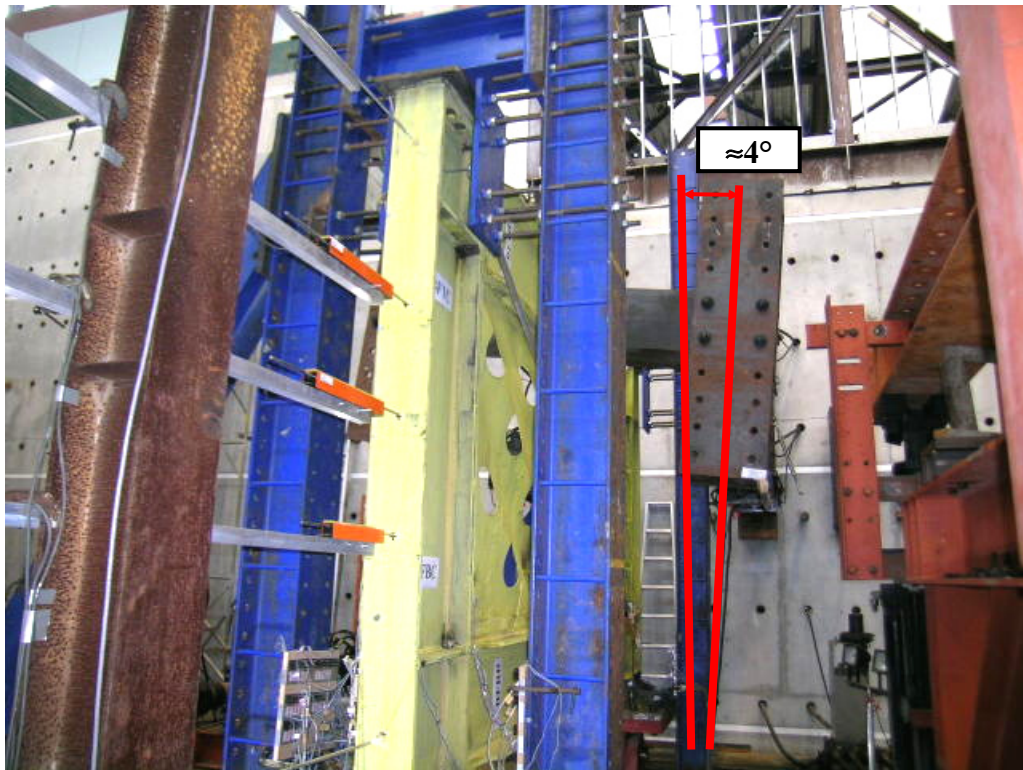
FIGURE 5-17 Rotation of H-shaped loading detail
(P: Cycle 18, $\gamma = +1.5\% \approx 5\delta_y$)

FIGURE 5-18 Added cables supporting actuators

The specimen was pushed to a second cycle at 1.5% drift amplitude after the cables were installed. Unfortunately, the cables did not prevent rotation of the H loading beam as intended. However, this additional cycle allowed observation of further yielding in the panel adjacent to the far column fishplate, and continuous in the RBS connections as shown in figures 5-19 and 5-20, respectively. No change was observed in the column yield lines. Panel "folds" between holes were observed, as shown in figure 5-21.

Testing continued with the two cycles at 2.0% drift amplitude ($\approx 6.667\delta_y$), reaching a peak base shear of approximately 1770kN. During the positive excursions of the cycles, when the actuators were pushing, on the specimen, the H beam continued to rotate as observed earlier. Yielding was observed in the panel zones throughout the specimen, as shown in figure 5-22. Yielding also progressed at the same locations observed previously, with the top beam RBS connections shown in figure 5-23.

FIGURE 5-19 Panel yielding adjacent to far column fish plate (P: Cycle 19, $\gamma = 1.5\% \approx 5\delta_y$)
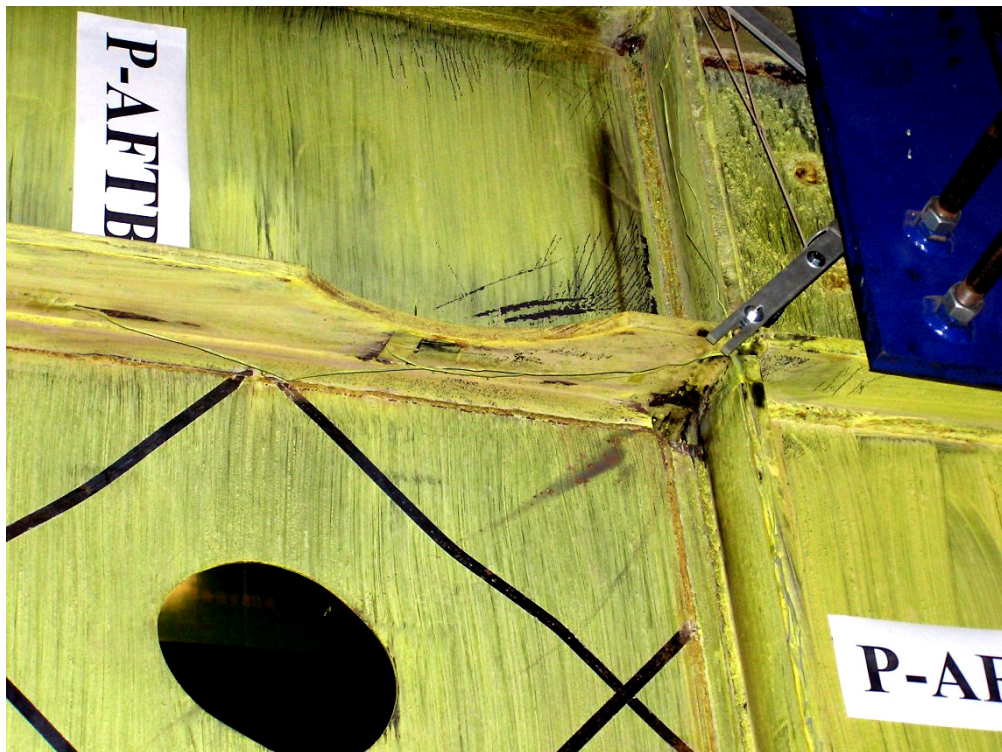
FIGURE 5-20 Yielding in top beam far side RBS connection (P: Cycle 19, $\gamma = 1.5\% \approx 5\delta_y$)
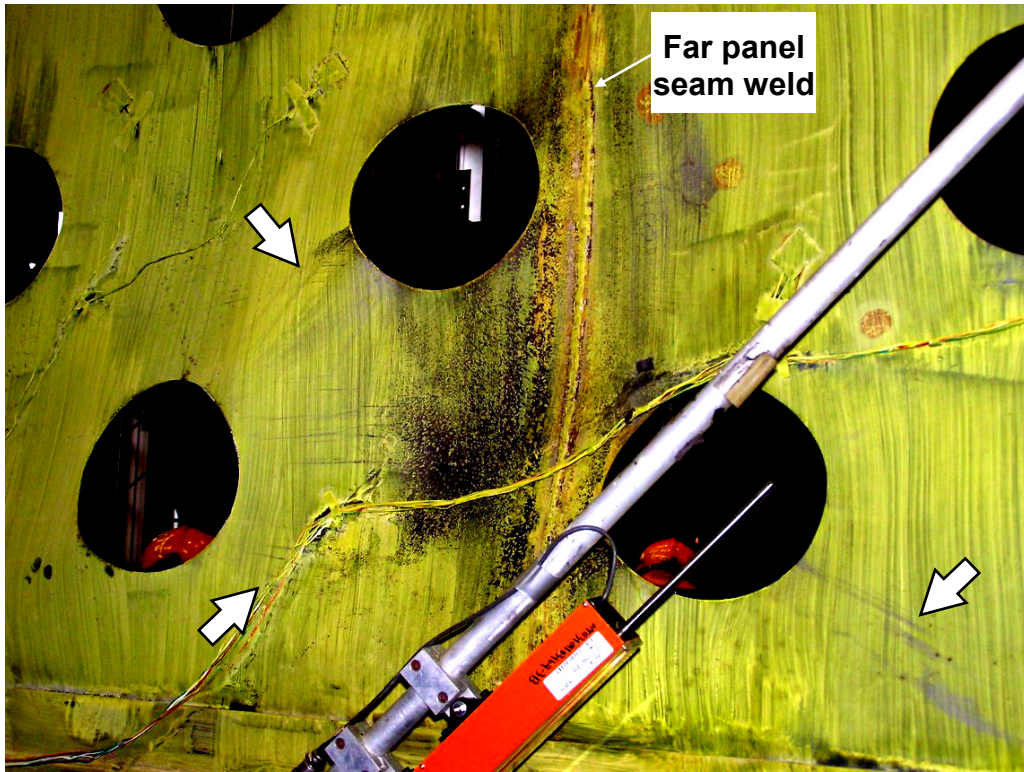
FIGURE 5-21 Yielding and folds between panel perforations (P: Cycle 19, $\gamma = 1.5\% \approx 5\delta_y$)
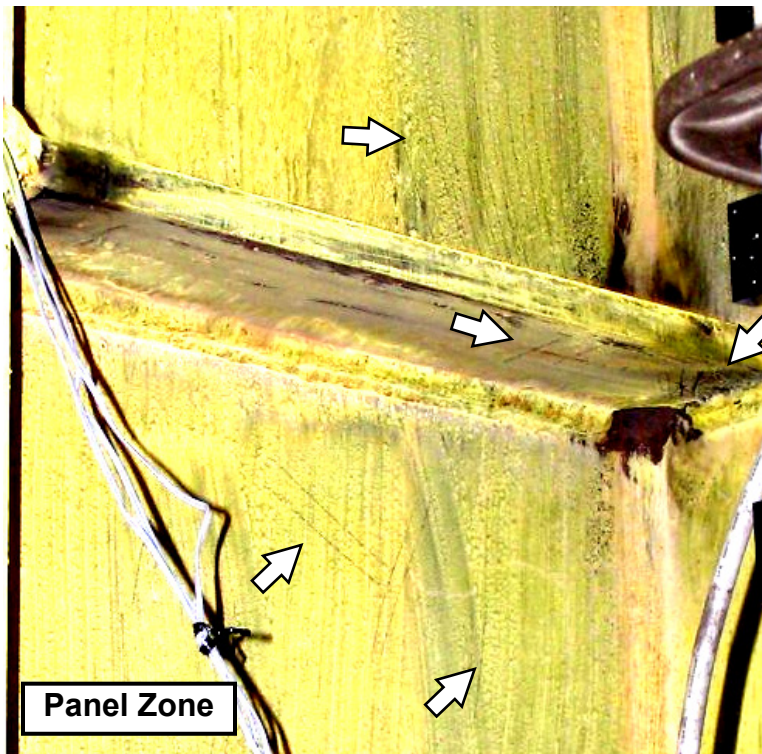
**FIGURE 5-22 Far bottom panel zone and top flange continuity plate yielding
(P: Cycle 20, $\gamma = 2.0\% \approx 6.667\delta_y$)**
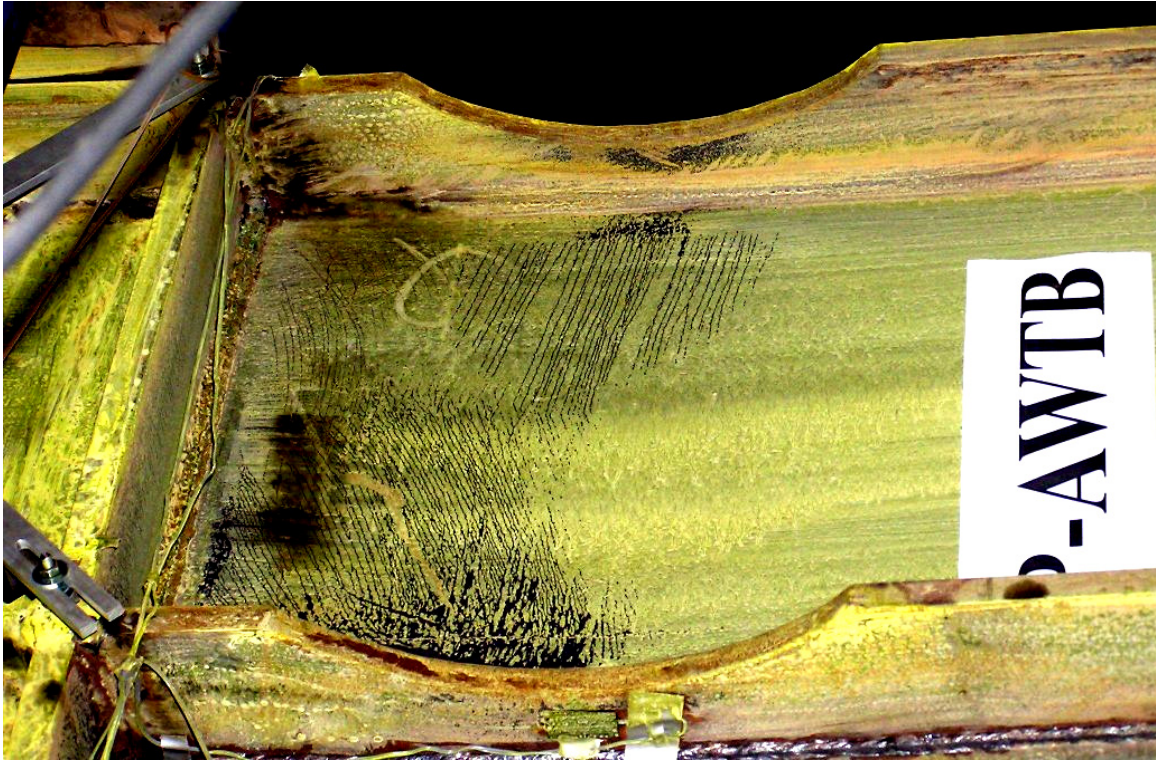
(a) Wall side RBS connection
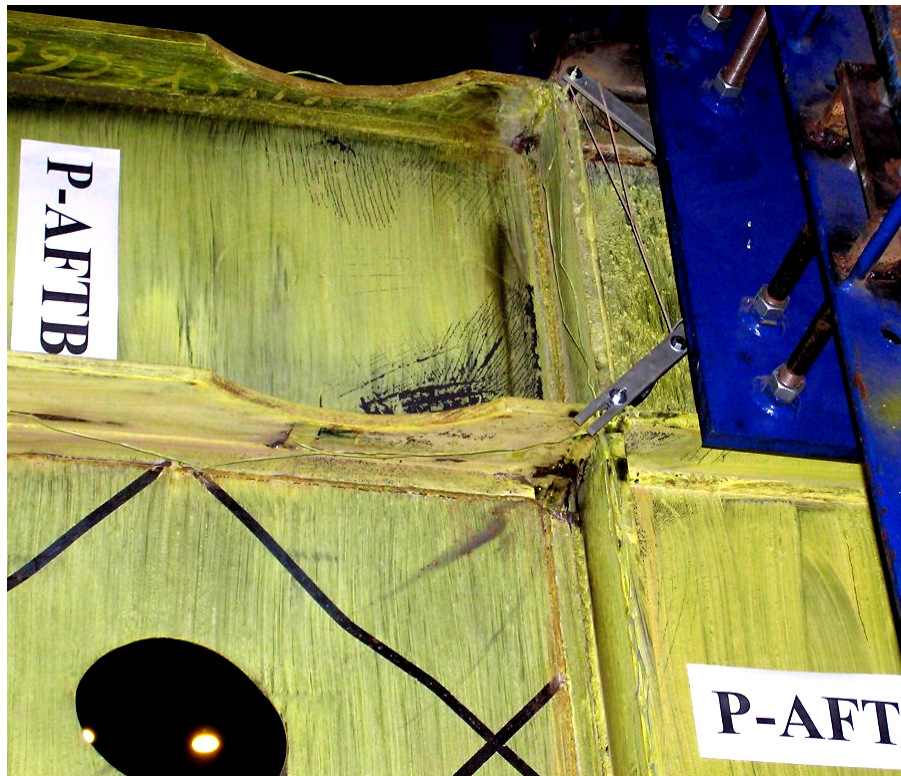
(b) Far side RBS connection

FIGURE 5-23 Yielding in top beam RBS connections (P: Cycle 20, $\gamma= 2.0\% \approx 6.667\delta_y$)

Cycling at 2.5% drift amplitude ($\approx 8.333\delta_y$) resulted in a slight decrease in base shear, to approximately 1750kN. Twisting of the loading beam increased once again, up to approximately 3°, as shown in figure 5-24. As a result, the top of the wall column was observed to have twisted counter-clockwise (looking up), causing damage to the long bolts supporting the column lateral support at that location, as shown in figures 5-25 and 5-26, respectively. Rotation also occurred in the far column, as evidenced by the slip of the lateral support plate located on top of the columns as shown in figure 5-27. Yielding and buckling of the fish plate in the region of the RBS connections was observed and shown in figure 5-28. Web local buckling was observed in the wall side bottom beam RBS connection, as shown in figure 5-29.
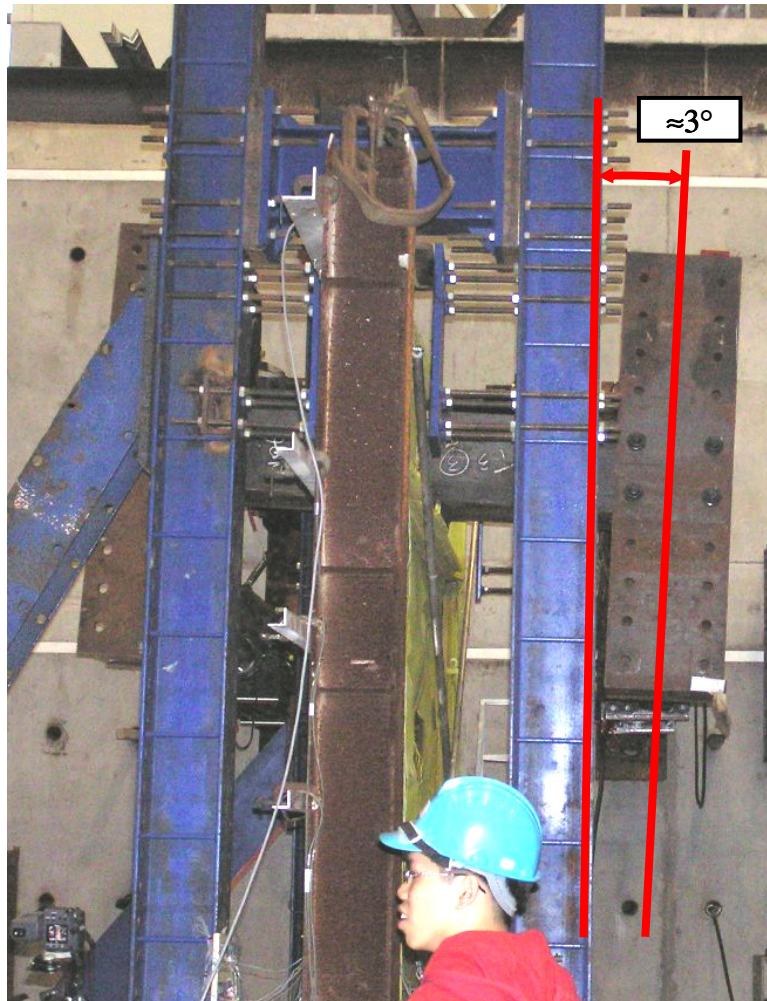
FIGURE 5-24 Rotation of H-shaped loading detail
(P: Cycle 22, γ= +2.5% $\approx 8.333\delta_y$)

FIGURE 5-25 Wall column rotation and damage to bolts supporting column lateral restraint (P: Cycle 22, $\gamma = 2.5\% \approx 8.333\delta_y$)

(a)

(b)

FIGURE 5-26 Damage to wall column lateral support (P: Cycle 22, $\gamma = 2.5\% \approx 8.333\delta_y$)
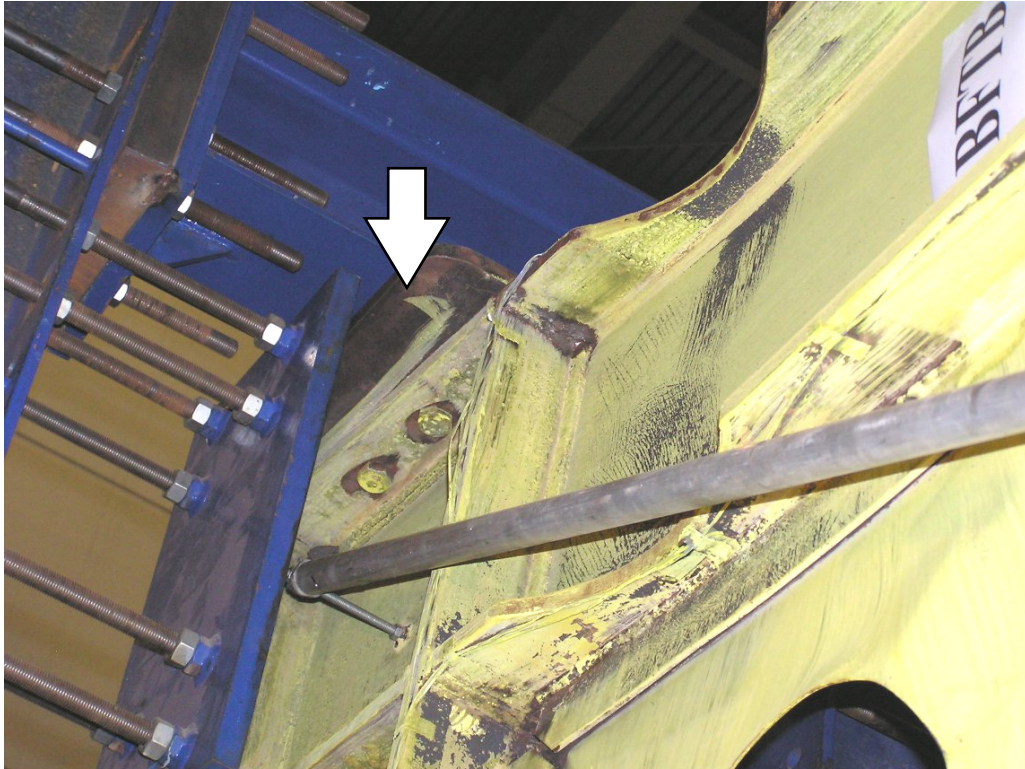
FIGURE 5-27 Far column rotation (P: Cycle 22, γ= 2.5% ≈8.333δ_y)
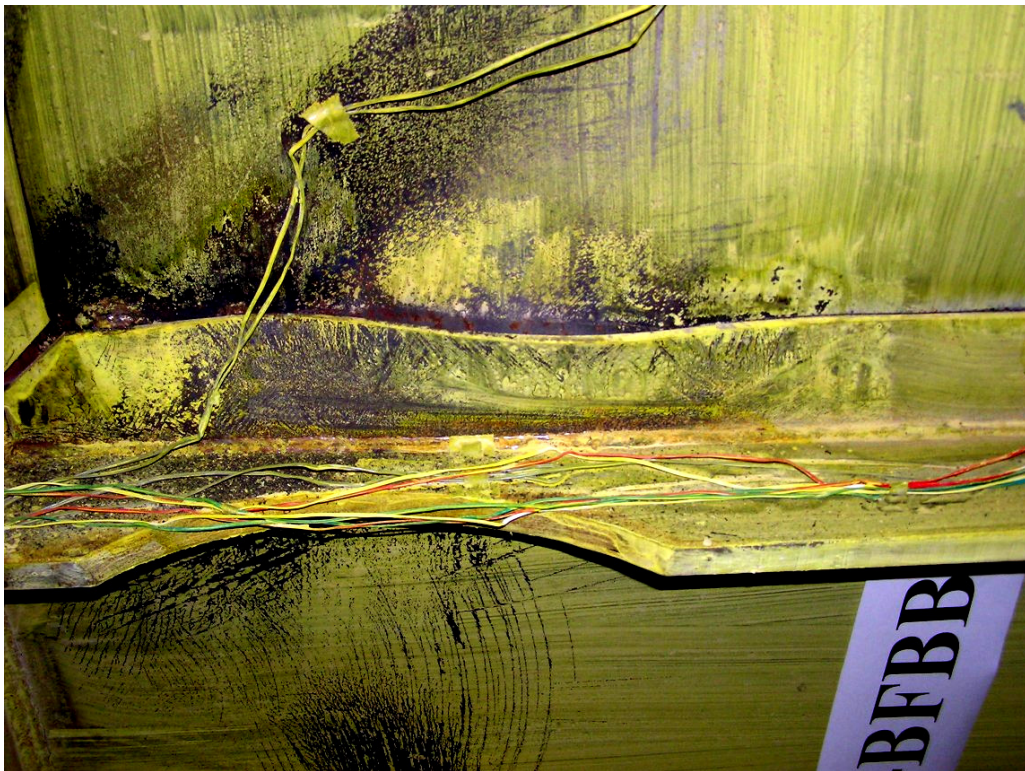
**FIGURE 5-28 Far bottom beam fish plate yielding and buckling
(P: Cycle 22, γ= 2.5% ≈8.333δ_y)**

(a) From A-side

(b) From B-side

FIGURE 5-29 Web local buckling of bottom beam wall RBS connection
(P: Cycle 22, γ= 2.5% ≈8.333δ_y)

Before continuing the test program, restraints were added to reduce loading beam rotation. The restraints consisted of two steel beams, each placed on the horizontal loading beam supported by steel roller bearings allowing movement in a direction parallel to the wall, as shown in figure 5-30. These beams were then tied down into the strong floor using post-tensioning bars.
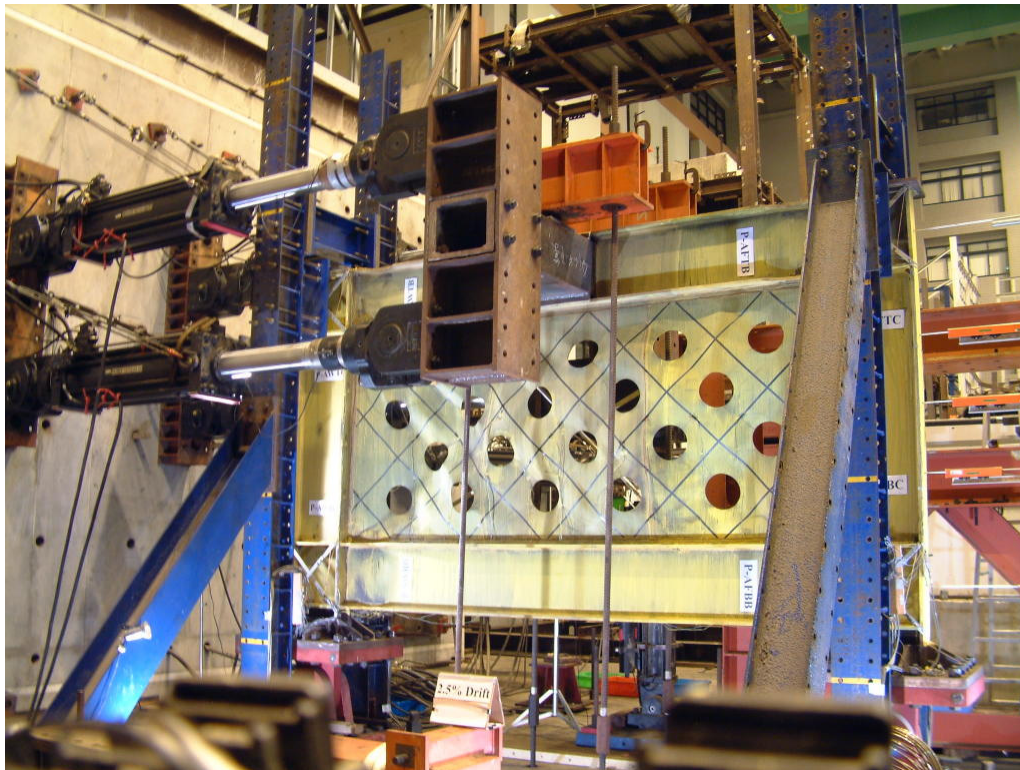
FIGURE 5-30 Added loading beam restraints (P: Prior to cycle 23, $\gamma = 2.5\% \approx 8.333\delta_y$)

A second cycle was carried out at 2.5% drift following the addition of the tie-down beams. Previously damaged areas worsened and while rotation of the H-beam was prevented, the columns still twisted.

Testing continued with cycles at 3.0% drift amplitude ($\approx 10\delta_y$). The peak base shear continued to decrease, with values of 1715kN and 1650kN at the positive and negative peaks of the first cycle, respectively (the small partial unloading/reloading event shown on the positive excursion occurred due to a need to modify a setting in the actuator control software).

Testing concluded after a loud bang was heard and a drop occurred in the strength of the specimen during the second positive displacement excursion. Subsequent inspection revealed a continuity plate fracture on the A-side of the far column at the wall flange, as shown in

figure 5-31. Flange local buckling was observed in the bottom flange of the far bottom beam RBS connection, as shown in figure 5-32. Figure 5-33 shows the severity of the damage to the top beam and lateral supports following the test. An overall view of specimen damage and panel damage is shown in figure 5-34, with details of tears found at infill panel corners shown in figure 5-35. Although the steel plate wall had not yet fractured (beyond the continuity plate problem indicated above), damage and distortions of the specimen made it impractical to continue testing.
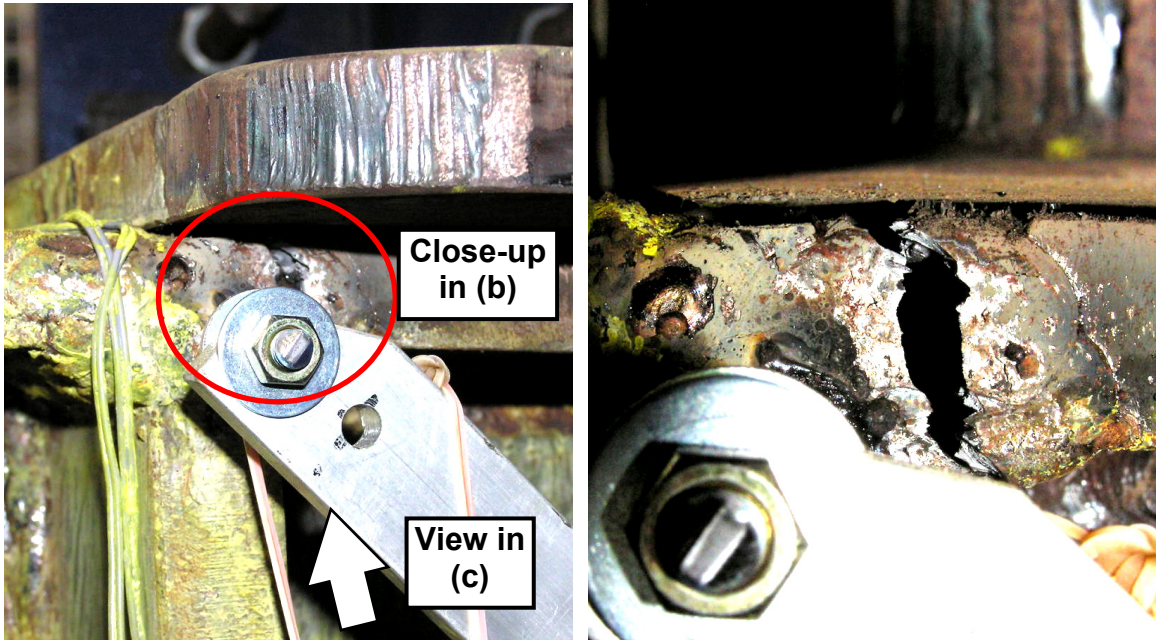
(a) View from side

(b) Zoom view from side
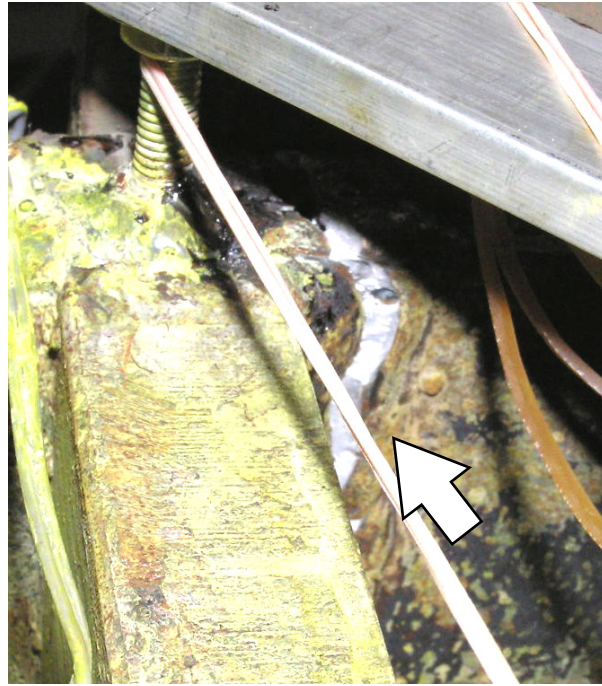
(c) View from bottom

FIGURE 5-31 Fracture of top beam top flange continuity plate at A-side far column
(P: End-of-test, Cycle 24, γ= 3.0% ≈10δ_y)
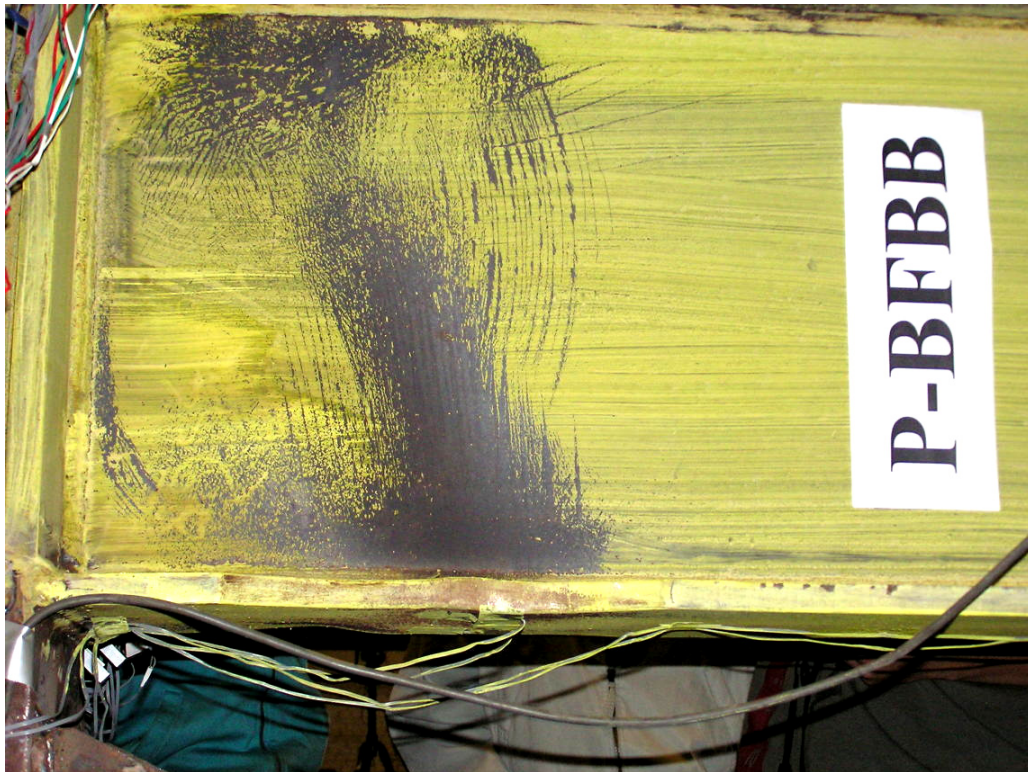
(a) Beam web and bottom flange

(b) Flange local buckling detail

FIGURE 5-32 Yielding and flange local buckling-far bottom beam RBS
(P: End-of-test, Cycle 24, γ= 3.0% ≈10δ_y)

(a) End view of top beam

P-AFTB

(b) A-side far lateral support

FIGURE 5-33 Damage to top beam and lateral supports
(P: End-of-test, Cycle 24, γ = 3.0% ≈10δ_y)

(c) Wall lateral support after testing

FIGURE 5-33 (cont'd) Damage to top beam and lateral supports
(P: End-of-test, Cycle 24, γ= 3.0% ≈10δ_y)
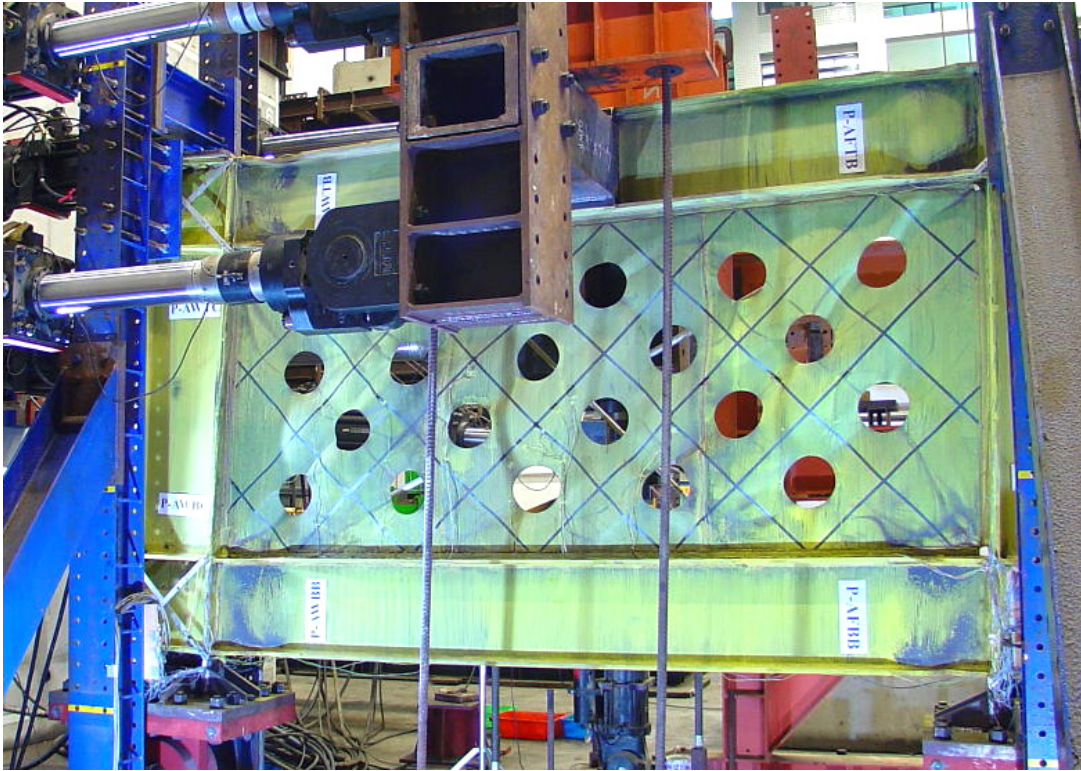
(a) Specimen from A-side

(b) Panel buckling

FIGURE 5-34 Damage to panel and boundary frame
(P: End-of-test, Cycle 24, $\gamma = 3.0\% \approx 10\delta_y$)
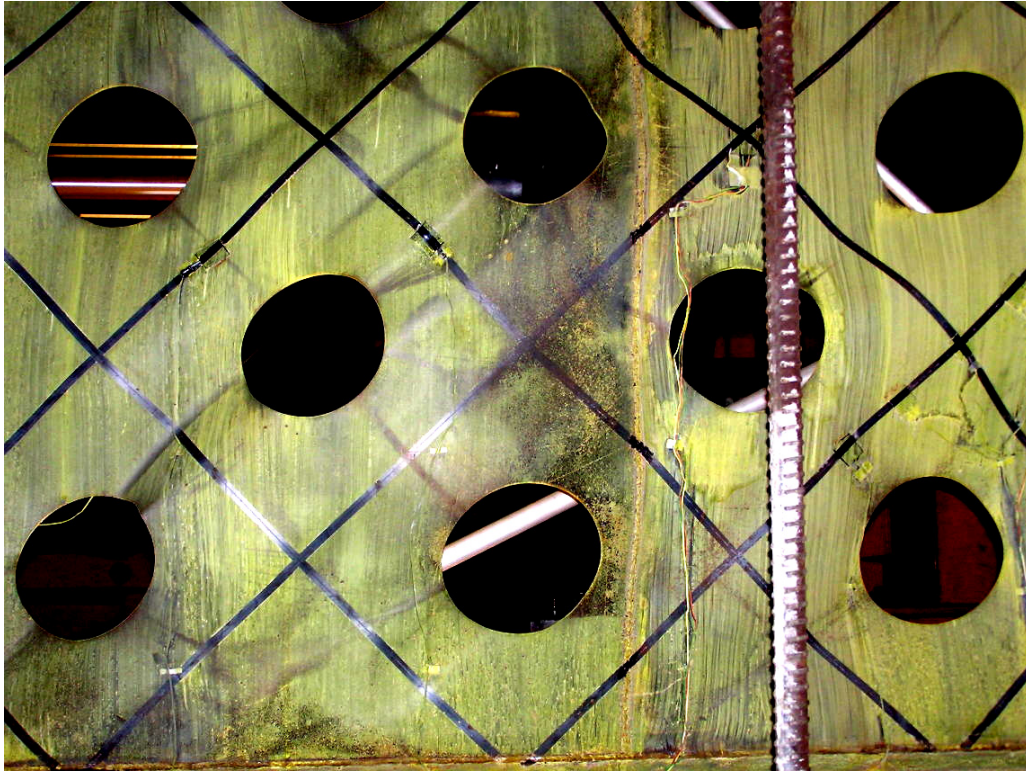
(c) Wall side of panel
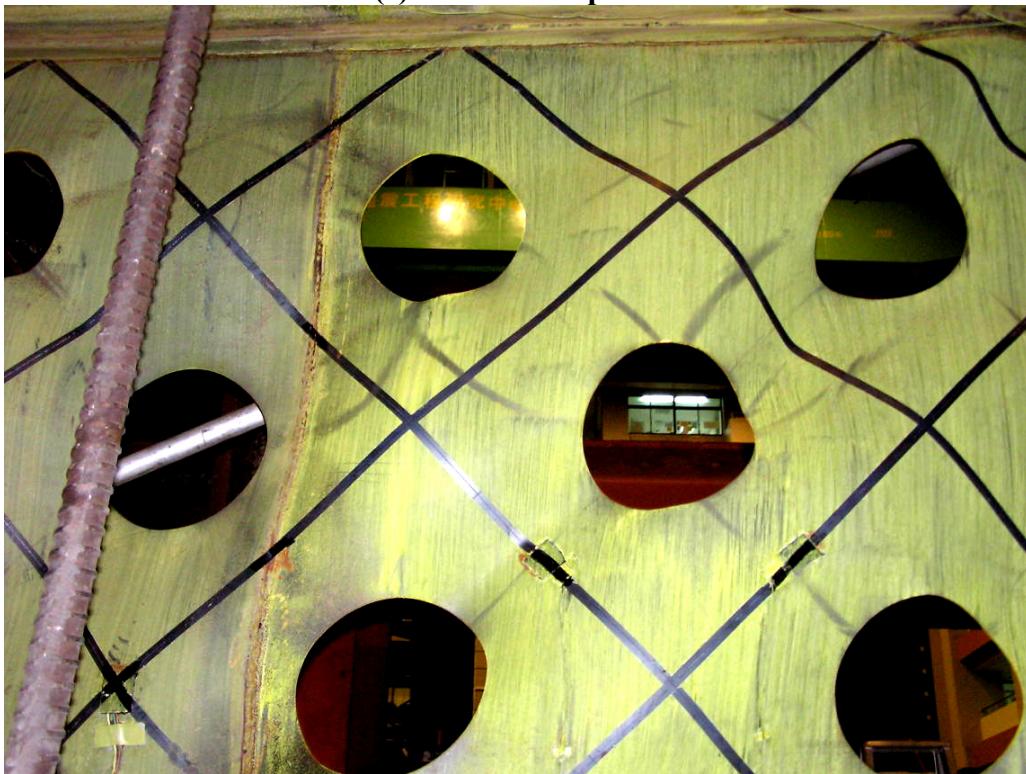
(d) Far side of panel

FIGURE 5-34 (cont'd) Damage to panel and boundary frame
(P: End-of-test, Cycle 24, γ = 3.0% $\approx 10\delta_y$)
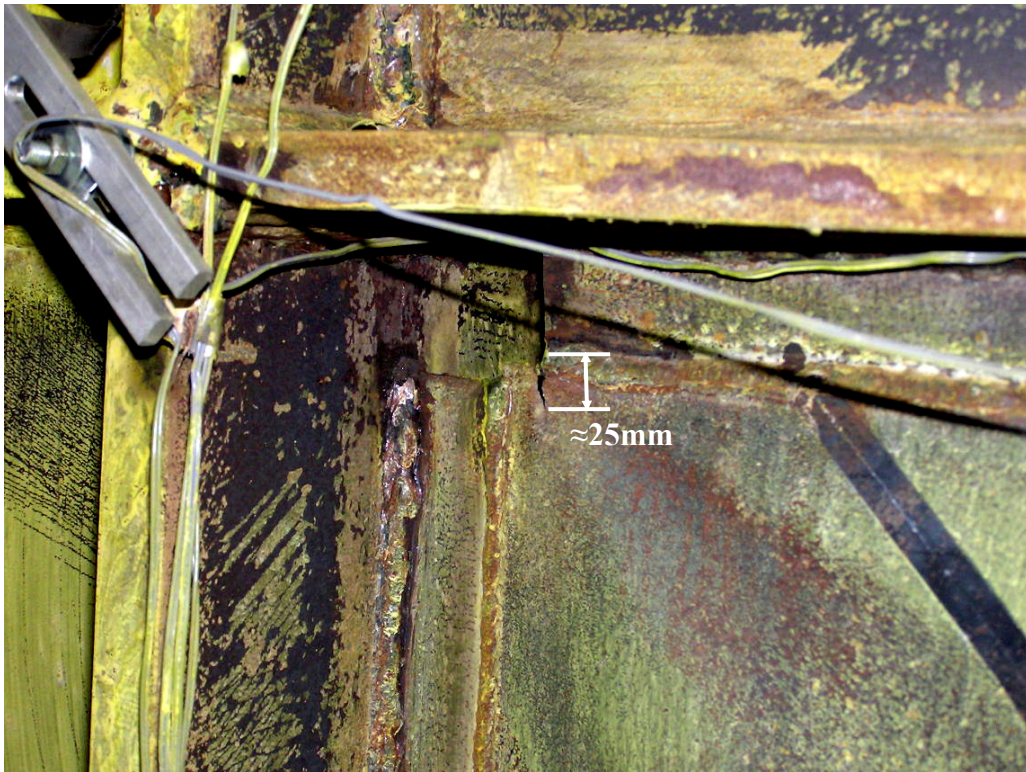
(a) Top A-side corner of infill at wall column

(b) Bottom A-side corner of infill at far column

FIGURE 5-35 Infill panel fractures (P: End-of-test, Cycle 24, $\gamma = 3.0\% \approx 10\delta_y$)

(c) Top A-side corner of infill at far column fishplate

FIGURE 5-35 (cont'd) Infill panel fractures (P: End-of-test, Cycle 24, γ= 3.0% ≈10δ_y)

5.3.3 Specimen CR

Prior to the testing of specimen CR, a number of important issues needed to be addressed. Since all four specimens were fabricated, and the time window for testing was limited, the problems were addressed as thoroughly as possible within the existing constraints. First, the lateral support system provided at the top of each column was modified. The lateral support used in the testing of specimens S1 and P consisted of a steel plate, parallel to the floor, bolted to the top of each column and supported on each side by plate surfaces that are greased to reduce friction. As evidenced during the test of specimen P, this system could not restrain column twist, especially during plastic hinging in the RBS connection; it was believed that this yielding decreased the effective torsional rigidity at the top of the column. The replacement lateral support developed is shown in figures 5-36 and 5-37, and consisted of a stiffened beam, 600mm in length, bolted to the column flanges in the panel zone area, and supported on the exposed flange by two roller bars, greased to reduce friction. The second modification to the testing protocol prior to testing of specimen CR was a change to the load control scheme. The secondary actuator control

scheme, as described in section 5.2.3, was used to impose the displacement loading history at the start of testing, with the intention of reducing the possibility of out-of-plane beam movement observed in the testing of specimen P. The rotation of the loading assembly was monitored during testing by means of tilt-meters, shown in figure 5-38, which were added to the instrumentation scheme.

Sometime during the test preparation and installation of the modifications discussed above, a fabrication error for the specimen was observed. As shown in figure 5-39, the top beam top flange longitudinal axis and plane of the column web were not parallel as specified in the shop drawings. Nevertheless, the specimen preparations and testing continued.

Testing began with three cycles each at 0.1% and 0.2% drift amplitudes, producing peak base shears of approximately 550kN and 900kN, respectively. Elastic buckling was observed in the specimen during the 0.1% drift cycles, with no visible signs of yield. Following the first cycle at 0.2% drift amplitude, a slight flaking of the whitewash was observed in the web of the far column, near the bottom beam. After the remaining two cycles at this amplitude, very slight whitewash flaking was visible near the top flange of both bottom beam RBS connections.

Cycle drift amplitude was then increased to 0.3%, the estimated yield drift in the pre-test analyses ($\approx 1.0\delta_y$). The specimen resisted this displacement with a base shear of approximately 1125kN. The observed elastic stiffness was approximately 140kN/mm. Upon completion of the first cycle at 0.3% drift, the seventh cycle in the loading history, the infill panel remained buckled when the actuator was paused at zero displacement. Yield lines appeared in a number of locations near the far column and top beams on the panel A-side as shown in figure 5-40. Small yield lines appeared on the web of the far side top beam RBS connection.

The tenth cycle in the loading history increased the drift amplitude to 0.6% ($\approx 2.0\delta_y$). Specimen base shear resistance increased to approximately 1470kN. Far column web yield lines adjacent to the bottom beam are shown in figure 5-41. Yielding increased on the far side of the panel, as shown in figures 5-42 and 5-43. RBS connection yielding increased, as shown in figure 5-44.

Three cycles were next performed at 0.9% drift amplitude ($\approx 3.0\delta_y$), resulting in a base shear of approximately 1700kN. Figure 5-45 shows the observed yielding in the far bottom panel zone

140

and adjacent column web. RBS web and flange yielding continued to spread, including, on the flanges, outside the radius cut of the RBS, as shown in figure 5-46. Yielding increased at locations described previously.

(a) With actuators and wall column support frame

(b) Zoom of (a)

FIGURE 5-36 New wall column lateral support (Specimen CR: Pre-test)

FIGURE 5-37 New far column lateral support (CR: Pre-test)
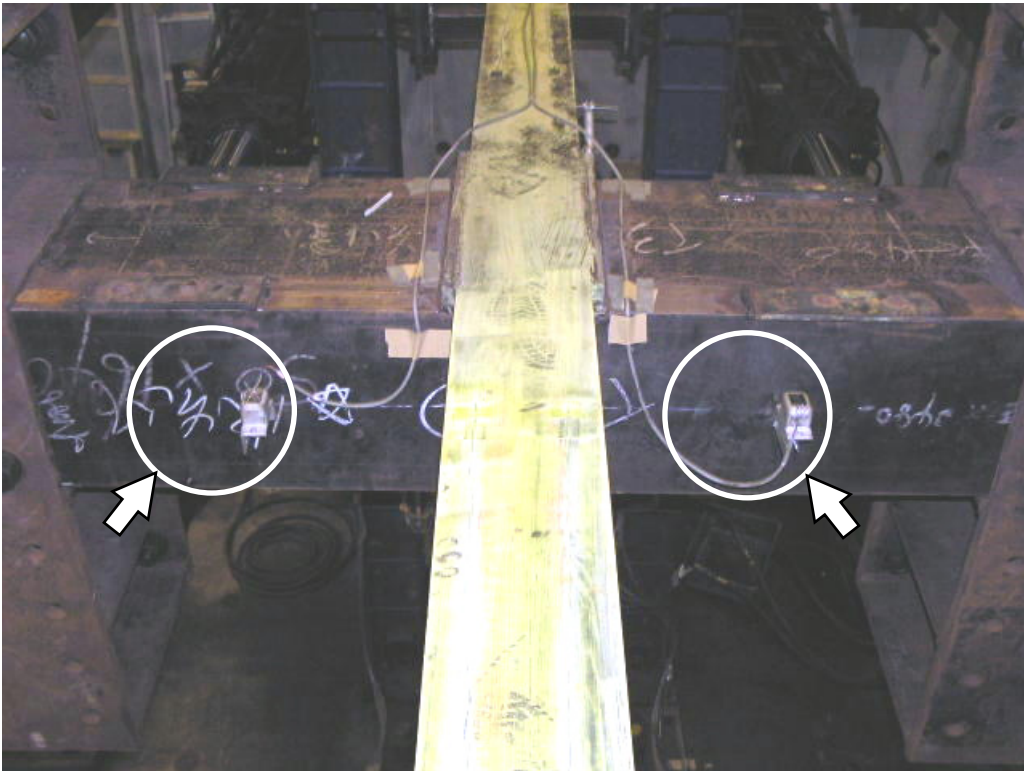
FIGURE 5-38 Tiltmeters (CR: Pre-Test)

142
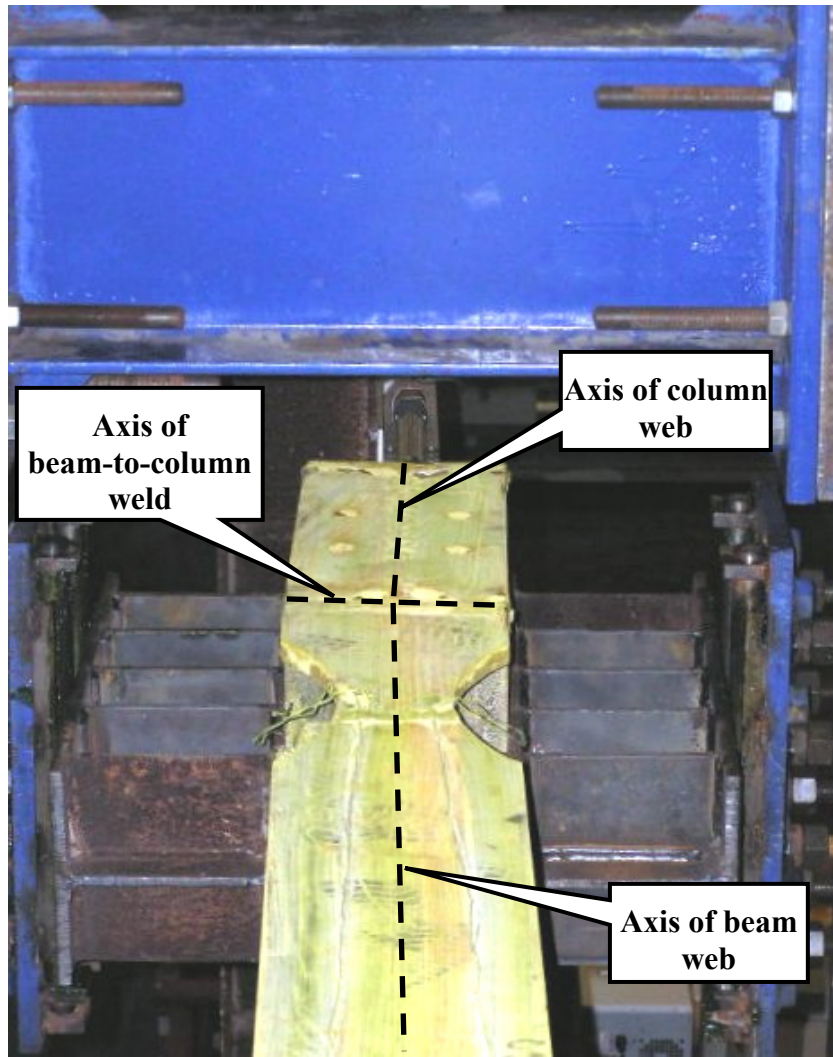
FIGURE 5-39 Initial far column twist at top beam connection (CR: Pre-Test)
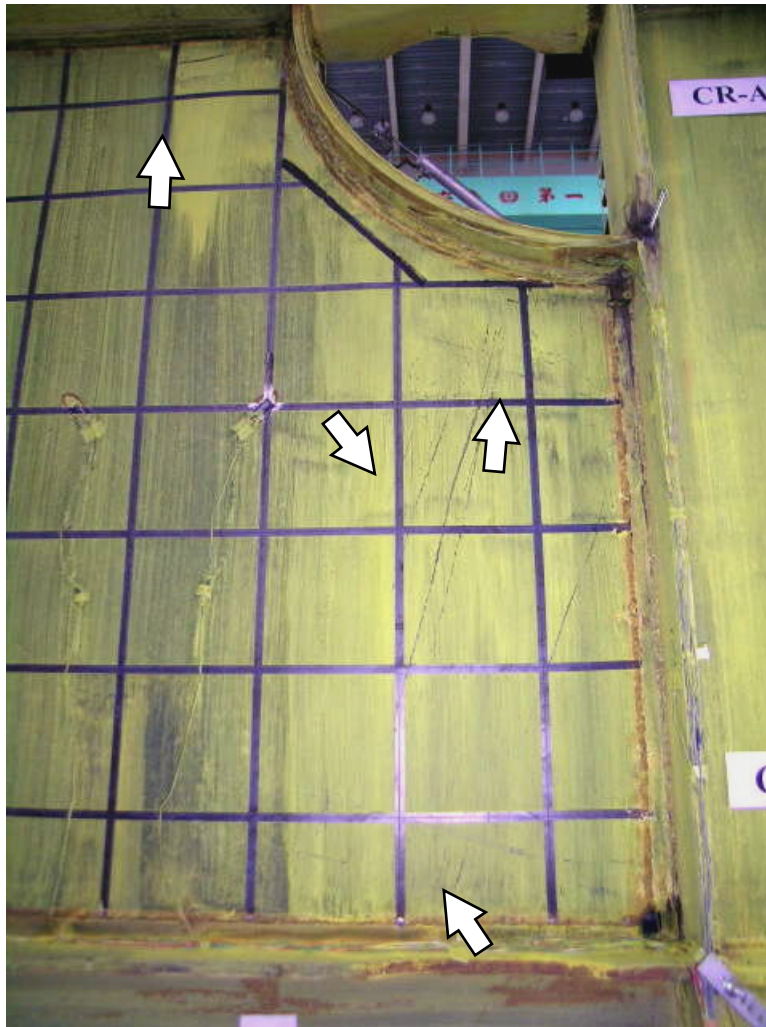
FIGURE 5-40 Panel yielding (CR: Cycle 9, $\gamma= 0.3\% \approx 1\delta_y$)

FIGURE 5-41 Far column web yielding at bottom beam (CR: Cycle 10, $\gamma = 0.6\% \approx 2\delta_y$)

FIGURE 5-42 panel yielding at far column (CR: Cycle 12, $\gamma = 0.6\% \approx 2\delta_y$)

(a) Face view

(b) Skewed view

FIGURE 5-43 Panel yielding at top beam and far arch (CR: Cycle 12, $\gamma = 0.6\% \approx 2\delta_y$)

FIGURE 5-44 Bottom beam wall RBS web yielding (CR: Cycle 12, $\gamma = 0.6\% \approx 2\delta_y$)

FIGURE 5-45 Web and panel zone yielding – bottom of far column
(CR: Cycle 15, $\gamma = 0.9\% \approx 3\delta_y$)

(a) Web yielding
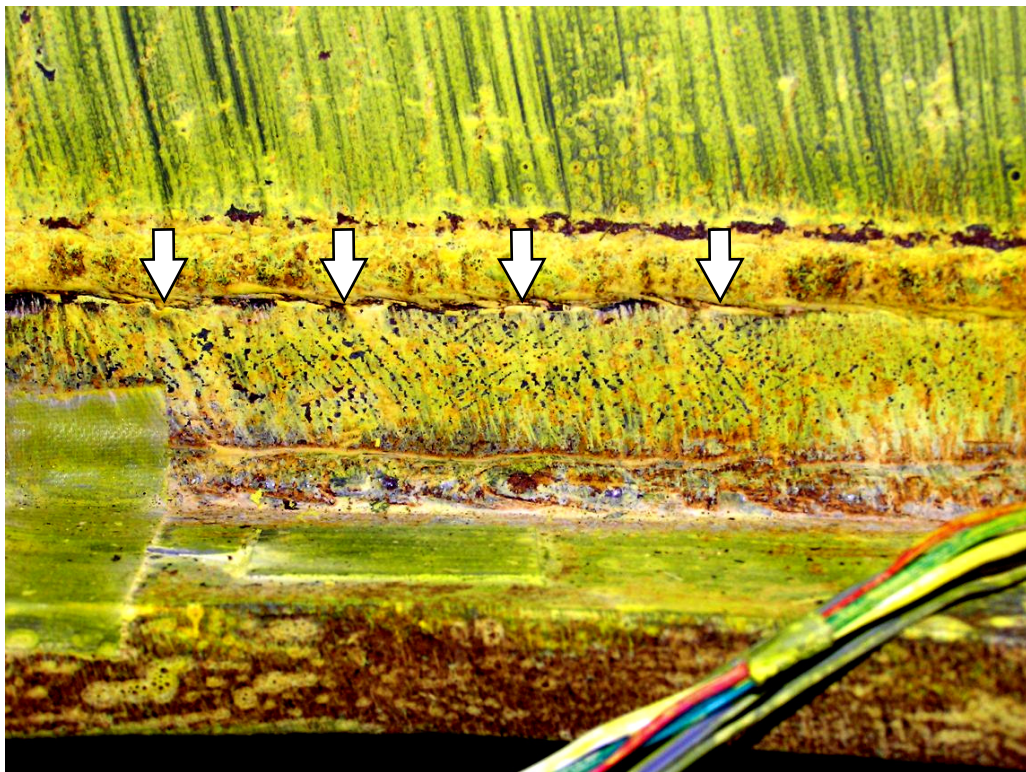
(b) Fishplate yielding

FIGURE 5-46 Bottom beam wall RBS yielding (CR: Cycle 15, γ= 0.9% ≈3δ_y)

(c) Top flange yielding

(d) Bottom flange yielding

FIGURE 5-46 (cont'd) Bottom beam wall RBS yielding (CR: Cycle 15, $\gamma = 0.9\% \approx 3\delta_y$)

Testing continued with two cycles per drift amplitude, starting with 1.2% ($\approx 4.0\delta_y$). The specimen resisted the displacement with a base shear of approximately 1850kN. In addition to the locations noted previously, yielding was more prominently visible in RBS locations of the top beam as shown in figure 5-47 and 5-48.

Cycling the specimen at 1.5% drift amplitude ($\approx 5.0\delta_y$) produced a specimen base shear of 1935kN and more yielding in the above locations. Buckling of the bottom beam fishplate was observed in the region of the far RBS connection, as shown in figure 5-49. The first signs of web local buckling were observed in the bottom beam RBS connections as shown in figures 5-50 and 5-51, for the far and wall connections, respectively. Yielding of the bottom flange adjacent to the RBS region was observed in the bottom beam wall connection, as shown in figure 5-52.

During the first cycle at 2.0% drift amplitude ($\approx 6.667\delta_y$), a loud "bang" was heard just before the peak of the first excursion, at approximately 1.75%, and a reduction in base shear of nearly 20kN occurred. However, the specimen continued to resist more load, reaching approximately 2025kN at the cycle maximum displacement. The excursion was completed, pausing at approximately zero force to visually inspect the specimen. The cycles at 2.0% continued, after inspection revealed no severe damage other than the continued spreading of yielding in the areas previously described. The yielding and web local buckling observed in the bottom beam RBS connections continued to increase in severity, as shown in figure 5-53.

Column web and bottom panel zone yielding spread from the locations described previously, while additional areas of yielding were observed. Figure 5-54 shows yield lines at the top of the far column, in the web and wall flange, and the adjoining top beam bottom flange continuity plate. Yield lines were also observed on column flanges adjacent to the top beam and the arches, as shown in figures 5-55 and 5-56. The initiation of small cracks in the infill panel was observed at the connection of each arch to the respective column, as shown in figure 5-57.

Two cycles at 2.5% drift amplitude ($\approx 8.333\delta_y$) were imposed on the specimen, resulting in a maximum strength of approximately 2060kN. Significant column twisting was observed, as shown in figure 5-58. Yielding in previously described areas continued to spread, and the initiation of panel tear resulting from fatigue at a buckle location, as shown in figure 5-59, was observed near the bottom of the wall column.

FIGURE 5-47 Infill panel and RBS yielding (CR: Cycle 16-17, $\gamma = 1.2\% \approx 4\delta_y$)
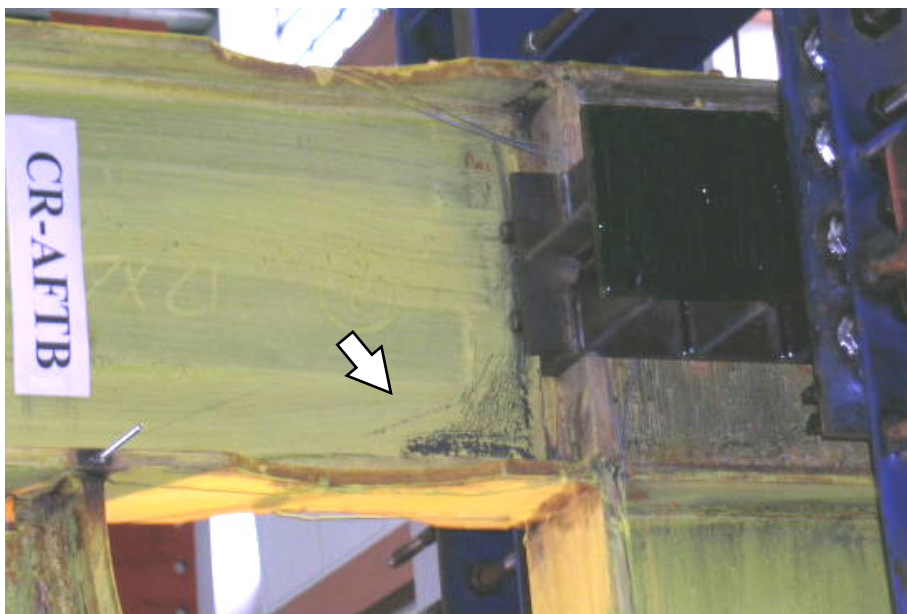
FIGURE 5-48 Top beam far RBS web yielding (CR: Cycle 16-17, $\gamma = 1.2\% \approx 4\delta_y$)
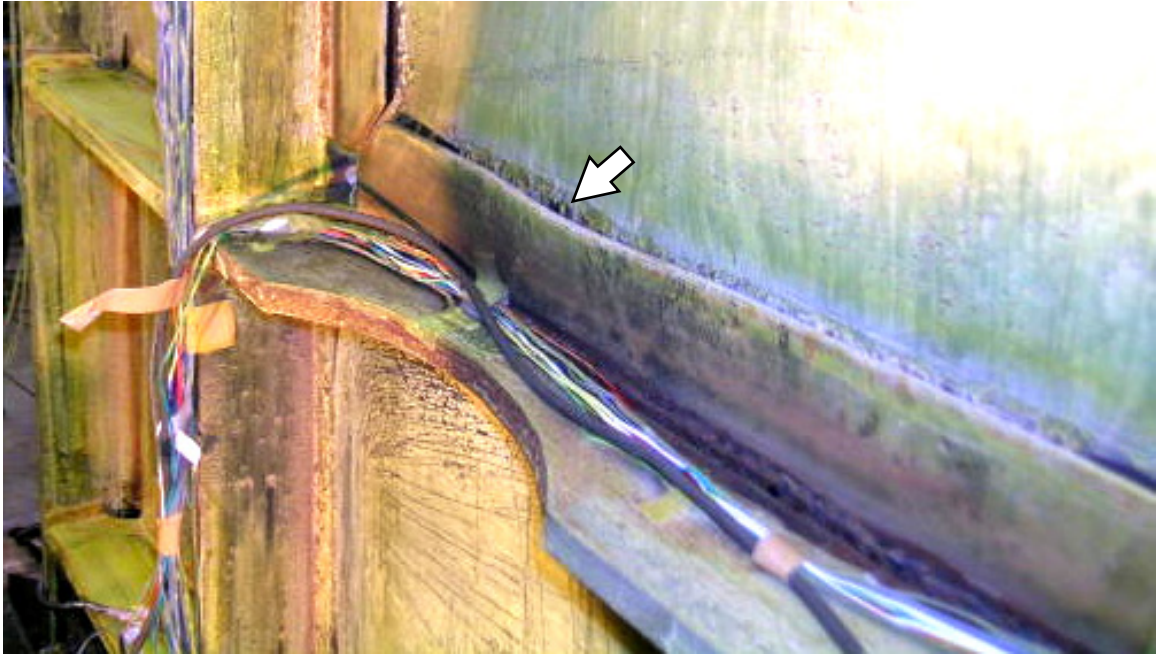
**FIGURE 5-49 Fishplate yielding and buckling at far bottom beam RBS
(CR: Cycle 18-19, $\gamma = 1.5\% \approx 5\delta_y$)**

FIGURE 5-50 Bottom beam far RBS web local buckling (CR: Cycle 18-19, $\gamma = 1.5\% \approx 5\delta_y$)

(a) From A-side

(b) From B-side

FIGURE 5-51 Initiation of bottom beam wall RBS web local buckling
(CR: Cycle 18-19, $\gamma = 1.5\% \approx 5\delta_y$)

154
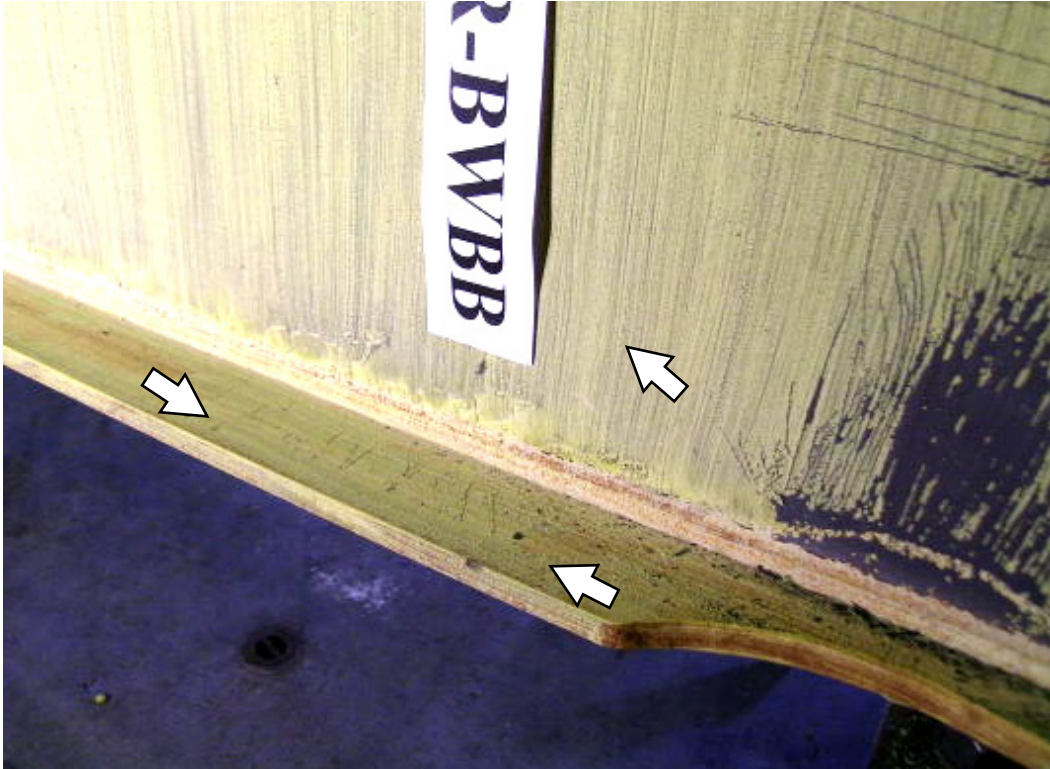
(a) Bottom flange yielding near bottom beam wall RBS
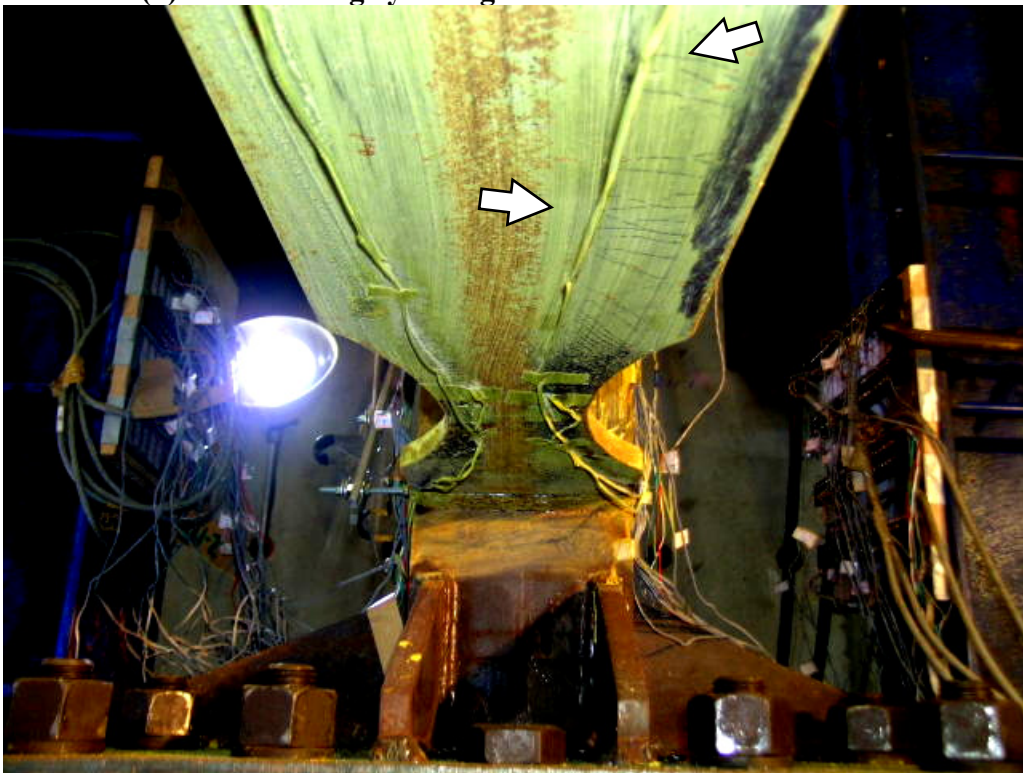
(b) Looking at wall column from underneath bottom beam

FIGURE 5-52 Bottom beam bottom flange yielding (CR: Cycle 18-19, $\gamma = 1.5\% \approx 5\delta_y$)
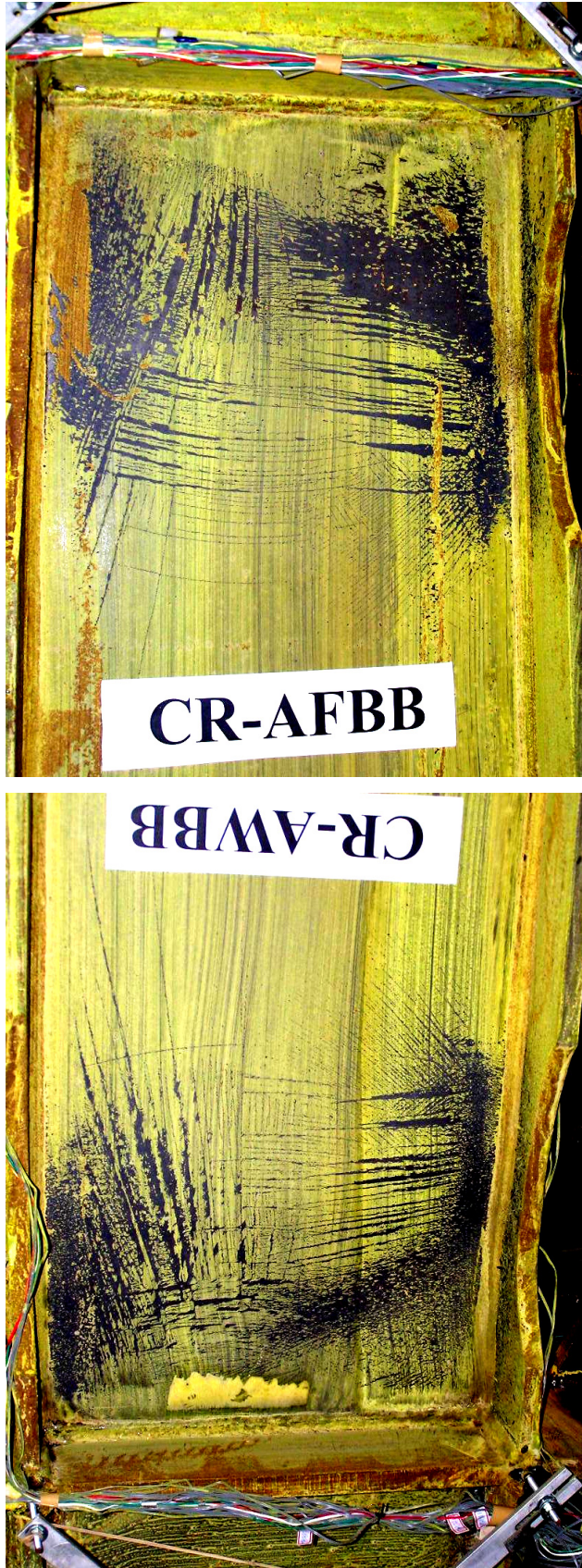
(a) Wall RBS connection

(b) Far RBS connection

FIGURE 5-53 Bottom beam RBS web yielding and local buckling (CR: Cycle 21, $\gamma = 2.0\% \approx 6.667\delta_y$)

FIGURE 5-54 Far column web and flange & top beam continuity plate yielding
(CR: Cycle 21, $\gamma= 2.0\% \approx 6.667\delta_y$)

FIGURE 5-55 Far column wall flange yielding at bottom of far arch
(CR: Cycle 21, $\gamma= 2.0\% \approx 6.667\delta_y$)

(a) Wall arch/column

CR-AFTB

CR-AWTB
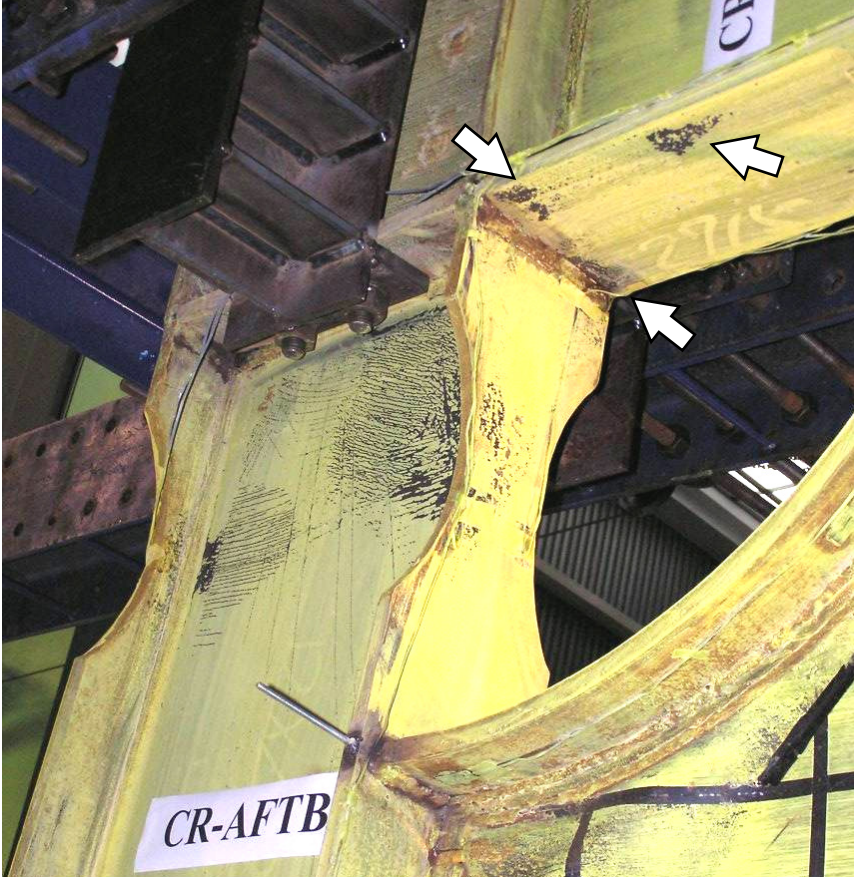
(b) Far arch/column

FIGURE 5-56 Column flange yielding (CR: Cycle 21, $\gamma = 2.0\% \approx 6.667\delta_y$)

(a) Infill panel crack at wall column/wall arch
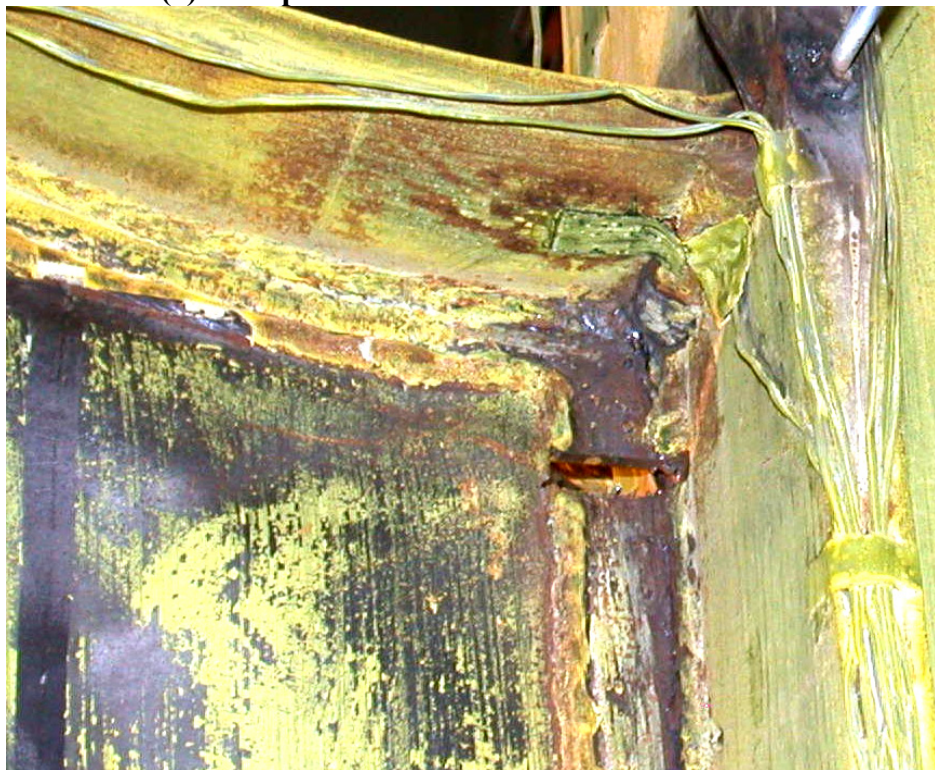
(b) Infill panel crack at far column/far arch

FIGURE 5-57 Fracture of infill panel at arch-to-column connections
(CR: Cycle 21, $\gamma = 2.0\% \approx 6.667\delta_y$)
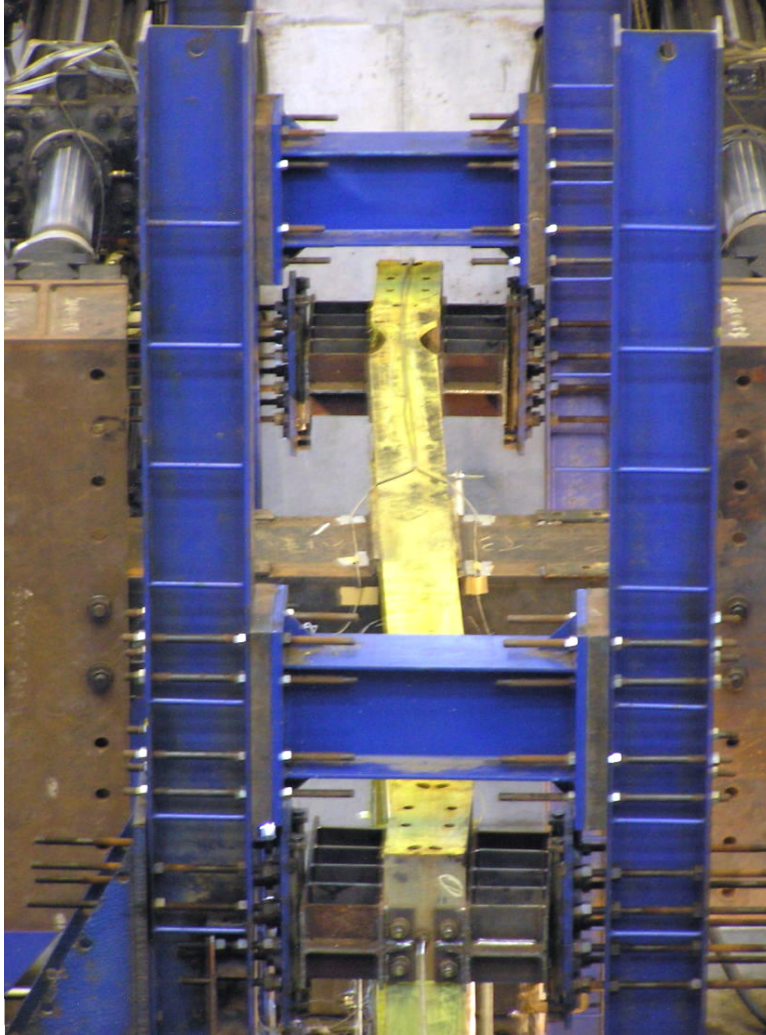
FIGURE 5-58 Column and top beam twisting (CR: Cycle 23, γ= 2.5% ≈8.333δ_y)

FIGURE 5-59 Panel fatiguing near bottom of wall column
(CR: Cycle 23, $\gamma = 2.5\% \approx 8.333\delta_y$)

A sharp reduction in specimen strength was observed at approximately 2.0% drift while approaching the peak of the second positive excursion, as shown in figure 5-5. Actuator pairs, as defined in the control scheme, developed a large difference in force, such that during the positive excursions, the A-bottom/B-top pair was pushing on the specimen, while the top A-top/B-bottom was pulling-therefore working *against* the progress of the loading history. This difference in actuator forces continued to increase, eventually resulting in an actuator reaching its force limit of 1000kN, causing the observed drop in total applied load.

Rather than increase the cycle amplitude to 3% drift as originally specified in the loading history, a third cycle was performed at 2.5% drift amplitude ($\approx 8.333\delta_y$) after adjusting the tolerance on the force errors triggering actuator shutdown, to avoid the drop in force observed previously. Approaching the peak of this cycle's positive excursion, the drop in total force occurred once again. The test was paused following the third negative excursion to 2.5% drift with approximately zero total force on the specimen. The actuator control scheme was then changed before proceeding further with the loading history, by reverting to the primary control scheme, as described in section 5.2.3. A fourth cycle was performed at 2.5% following this change,

161

reaching a peak positive excursion force of approximately 1980kN, without any force drop of the type observed in the two previous positive excursions at this drift amplitude.

Cracks were noted in a number of locations in the specimen following the four cycles at 2.5% drift. Some panel buckles previously observed progressed to fracture as shown in figure 5-60. Fractures were also observed at varying degrees of severity in the bottom beam bottom flange of the RBS connection regions as shown in figures 5-61 to 5-64.

FIGURE 5-60 Panel fracture near bottom of wall column
(CR: Cycle 25, γ= 2.5% ≈8.333δ_y)

(a) Overall view

(b) Flange fracture detail

FIGURE 5-61 Bottom beam B-side far RBS connection (CR: Cycle 25, γ= 2.5% ≈8.333δ_y)

(a) Overall view

(b) Detail of flange cracking

FIGURE 5-62 Bottom beam B-side wall RBS connection (CR: Cycle 25, γ= 2.5% ≈8.333δ_y)

(a) Overall View

(b) Detail of flange local buckling and cracking

FIGURE 5-63 Bottom beam A-side wall RBS connection (CR: Cycle 25, $\gamma = 2.5\% \approx 8.333\delta_y$)
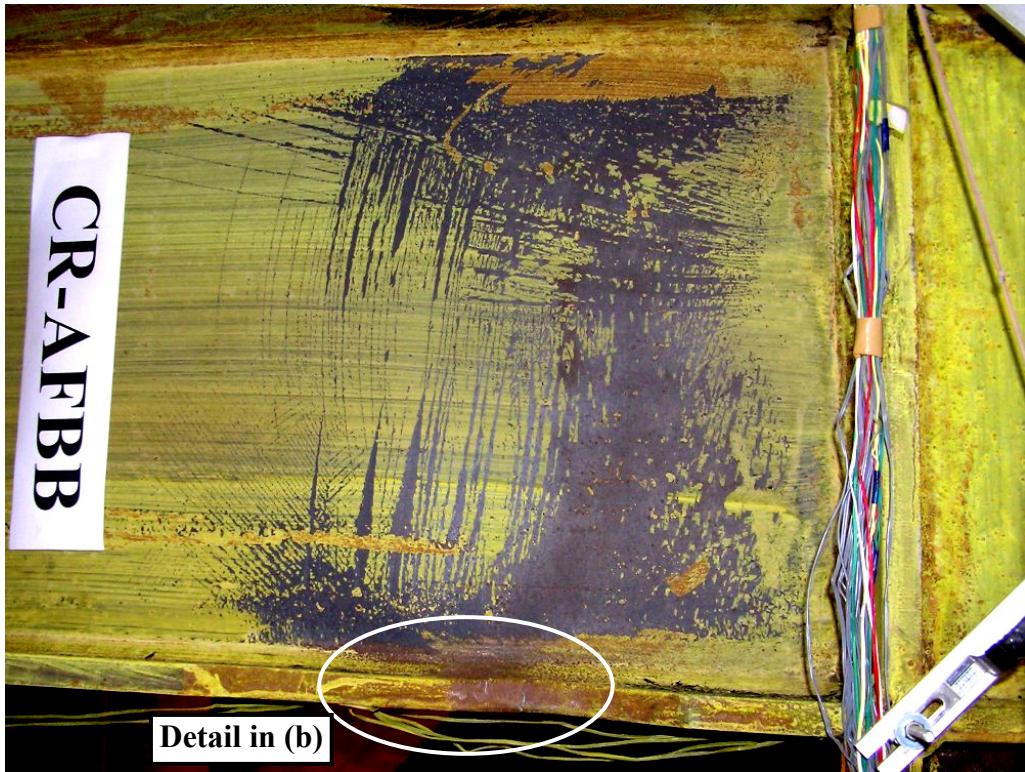
(a) Overall view
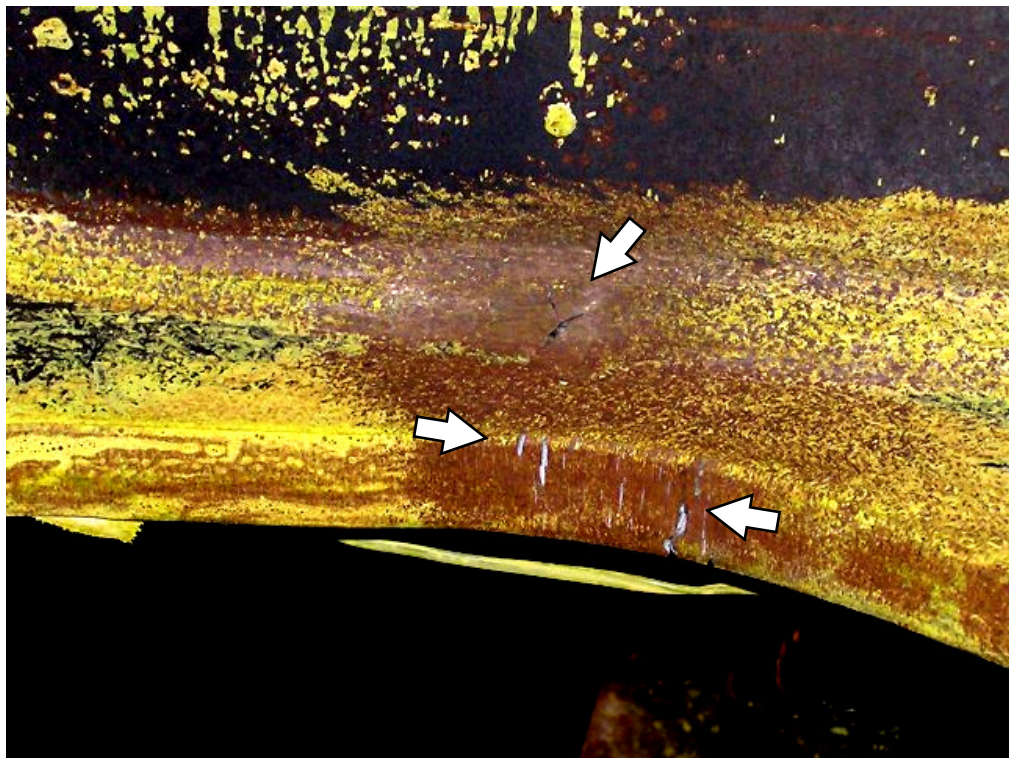
(b) Detail of flange local buckling and cracking

FIGURE 5-64 Bottom beam A-side far RBS connection (CR: Cycle 25, γ = 2.5% ≈8.333δ_y)

The beams and tension bars utilized as restraints against rotation of the loading assembly in the specimen P testing and described in the previous section were added to specimen CR prior to continuing the test program. The drift amplitude was then increased to 3.0% ($\approx 10.0\delta_y$). As shown in figure 5-65, the bottom flange of the bottom beam wall side RBS fractured during the first positive excursion at this amplitude, resulting in a drop in specimen strength, to approximately 1800kN at the positive peak, and 1840kN at the negative peak. During the second cycle at 3.0% drift, the far side bottom beam RBS bottom flange fractured at two points, further reducing the specimen strength to 1700kN and 1500kN at the positive and negative peaks, respectively. Figure 5-66 shows the bottom flange of the far RBS connection before and after complete fracture during, and at the conclusion of the cycle.
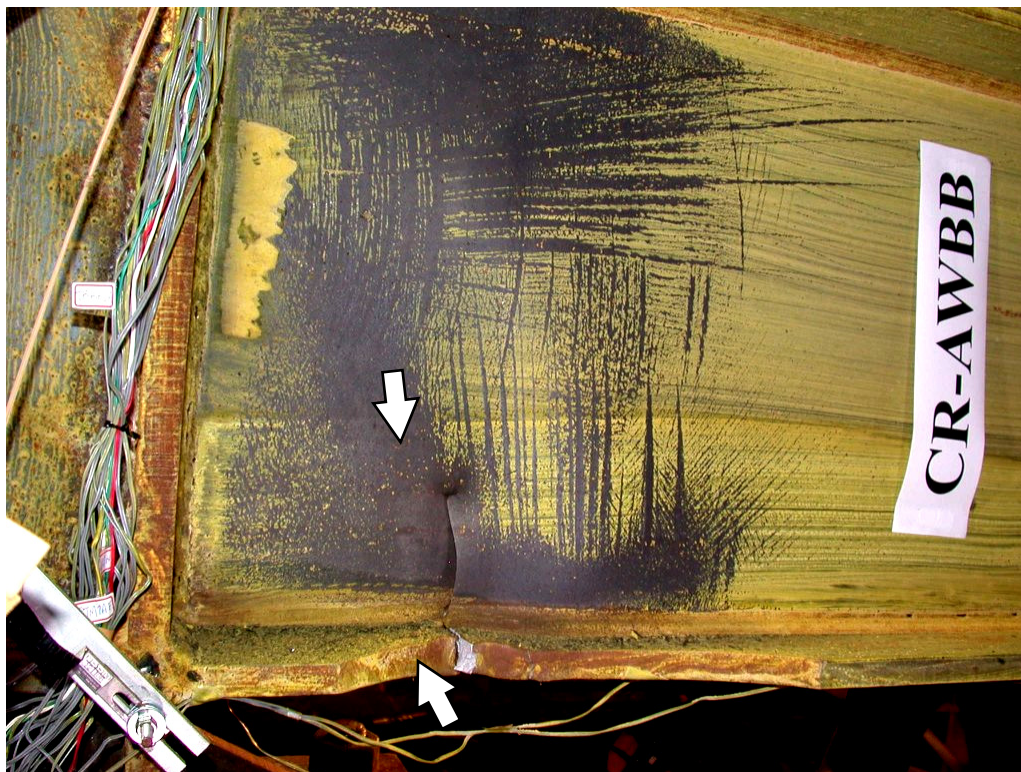
(a) A-side view

(b) B-side view

FIGURE 5-65 Bottom beam wall RBS bottom flange and web fracture
(CR: Cycle 26, $\gamma = 3.0\% \approx 10\delta_y$)

(c) Bottom view

FIGURE 5-65 (cont'd) Bottom beam wall RBS bottom flange and web fracture
(CR: Cycle 26, $\gamma = 3.0\% \approx 10\delta_y$)
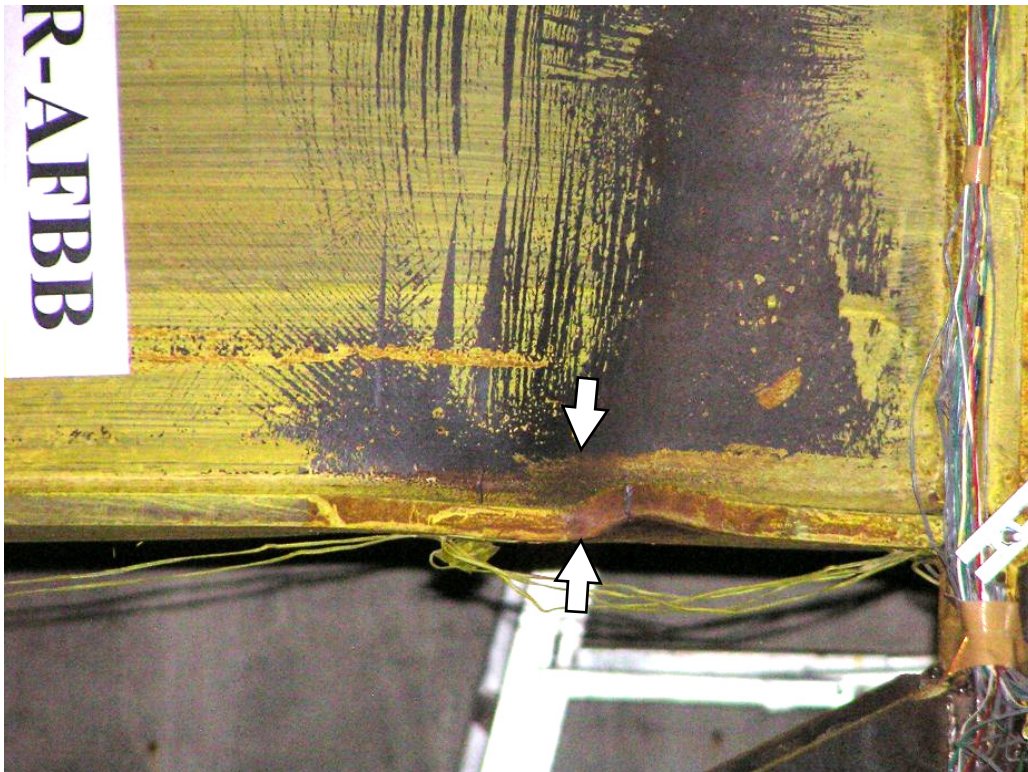
(a) Initial fracture and local buckling during loading
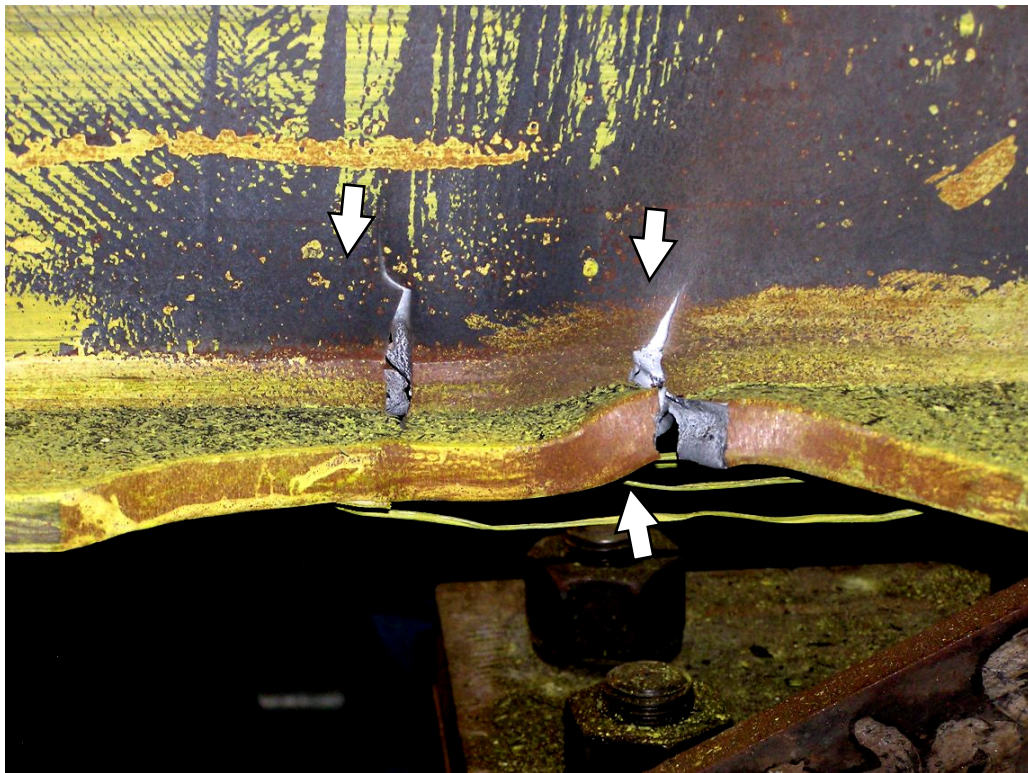
(b) Full fracture during loading

FIGURE 5-66 Bottom beam far RBS bottom flange and web fractures
(CR: Cycle 27, γ = 3.0% ≈10δ_y)

(c) From B-side after cycle completion
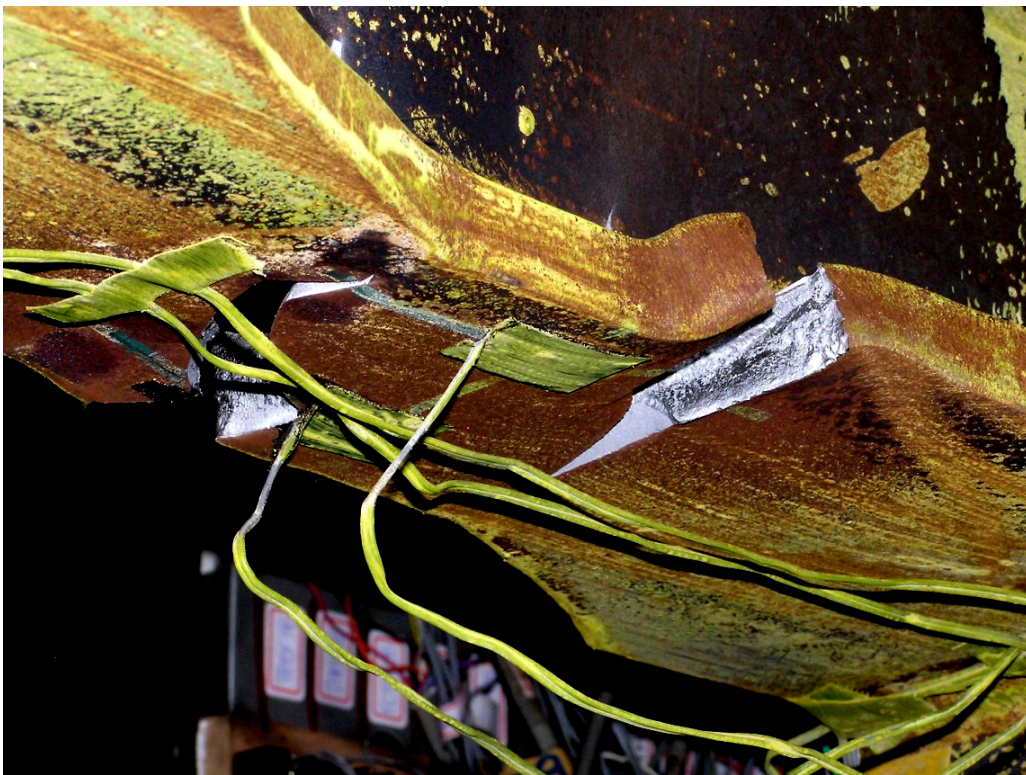
(d) From bottom after cycle completion

FIGURE 5-66 (cont'd) Bottom beam far RBS bottom flange and web fracture
(CR: Cycle 27, γ= 3.0% ≈10δ_y)

Loading displacement increased to 4.0% drift amplitude ($\approx 13.333\delta_y$), which produced specimen strengths of approximately 1750kN and 1560kN, during the positive and negative excursions of the first cycle, respectively. Loud bangs were heard during the cycles at this amplitude and during the second cycle, specimen strengths during the positive and negative excursions reduced to approximately 1560kN and 1340kN, respectively. These strength values correspond to drops of 24% and 35% from the positive and negative strength peaks for the duration of the test, respectively.

The overall behavior of the specimen suggested that it could continue to resist loading to larger displacements. However, testing was concluded to prevent lateral support damage and ensure the safety of those observing the test. In addition, at that point, the load path in the specimen had changed significantly from the intended design, with the bottom beam providing significantly less resistance to anchor the tension field forces from the infill panel because of fractures of the RBS, and the fractures in the continuity plates at the top of the wall column. This behavior will be discussed further in the next chapter.

Local buckling of the fishplate was observed at the arch to frame connections, as shown in figure 5-67. Post-test inspection of the specimen revealed fracture of the welds of both top beam top flange continuity plates in the wall column, as well as in the column web at that location, as shown in figure 5-68. At the far column, fracture also occurred in the top beam top flange B-side continuity plate, shown in figure 5-69. Top of column and top beam twisting had also increased severely, as shown in figure 5-70. Panel damage following the test is shown in (a) and (b) of figure 5-71. The extent of tears at panel corners increased, and the panel was found to be tearing away from the weld to the arch as shown in (c) through (f) of figures 5-71. Tears in the panel interior worsened as well, as shown in (g) through (i) of figure 5-71.

Column yielding was observed in a number of locations. Yielding of the continuity plate at the bottom beam top flange and the adjacent far column web had increased as the test progressed, from the state shown previously in figure 5-41, to that as shown in figure 5-72. The upper portion of the far column exhibited yielding of the wall flange (adjacent to the corner cutout-reinforced arch), as well as the web from the top beam bottom flange continuity plate to the

region near the lower end of the arch, as shown in figure 5-73. Similar yielding patterns were observed in the wall column.

(a) Arch to column flange connection

(b) Arch to beam flange connection

FIGURE 5-67 Wall arch fishplate local buckling (CR: Cycle 29, $\gamma = 4.0\% \approx 13.333\delta_y$)

(a) Top View
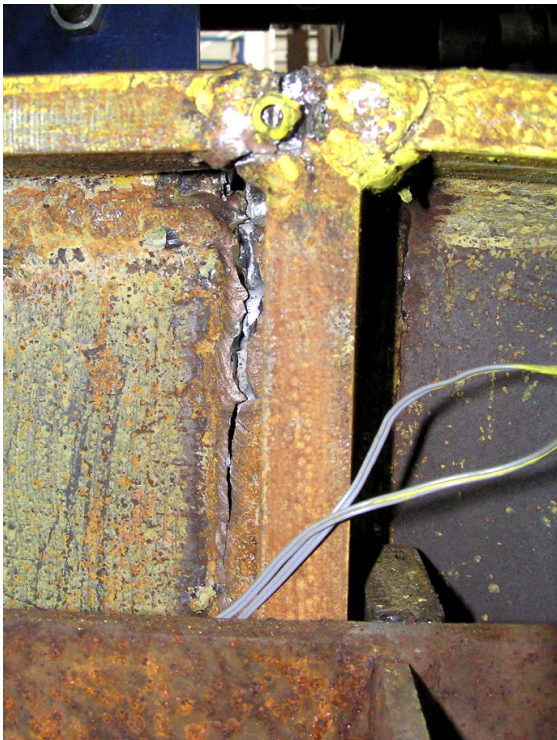
(b) View from A-Side of specimen

(c) View from B-Side of specimen

FIGURE 5-68 Continuity plate and web fractures at top of wall column
(CR: End of Test, γ= 4.0% ≈13.333δ_y)

(a) Top view
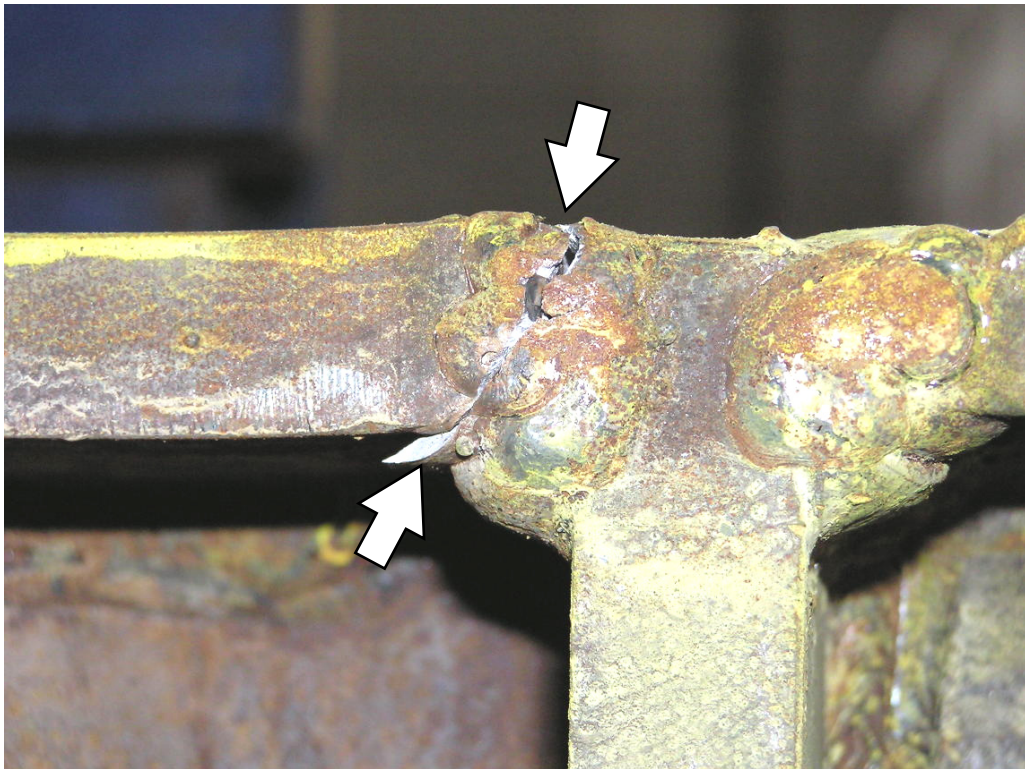
(b) View from B-Side of specimen

FIGURE 5-69 Continuity plate and web fractures at top of far column
(CR: End of Test, $\gamma = 4.0\% \approx 13.333\delta_y$)
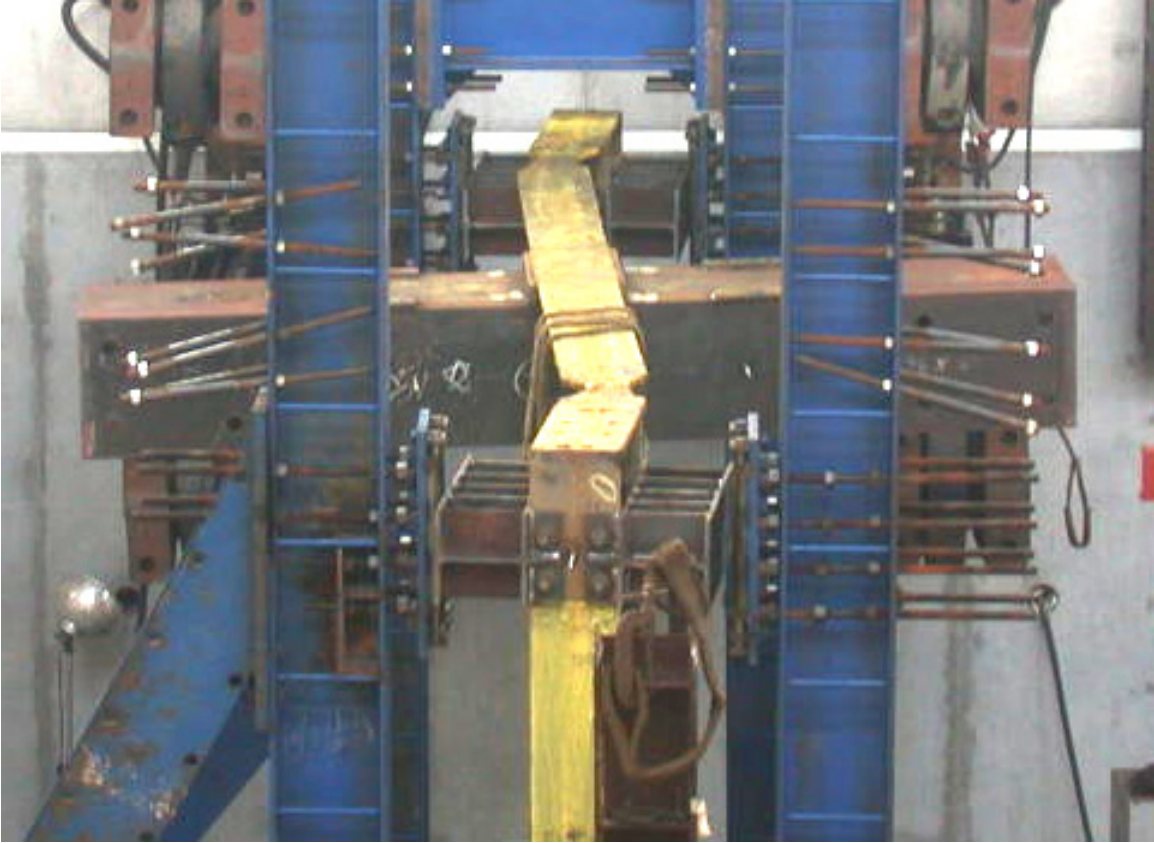
**FIGURE 5-70 Twisting of top beam and top of columns following testing
(CR: $\gamma = 4.0\% \approx 13.333 \delta_y$)**
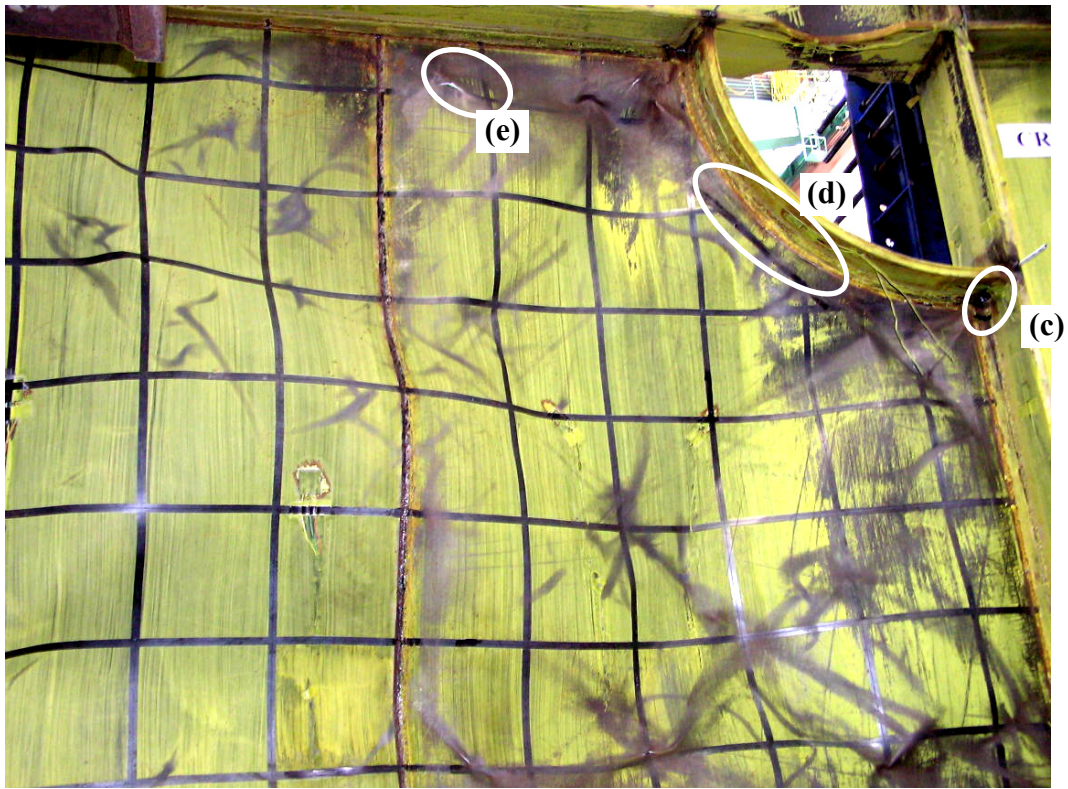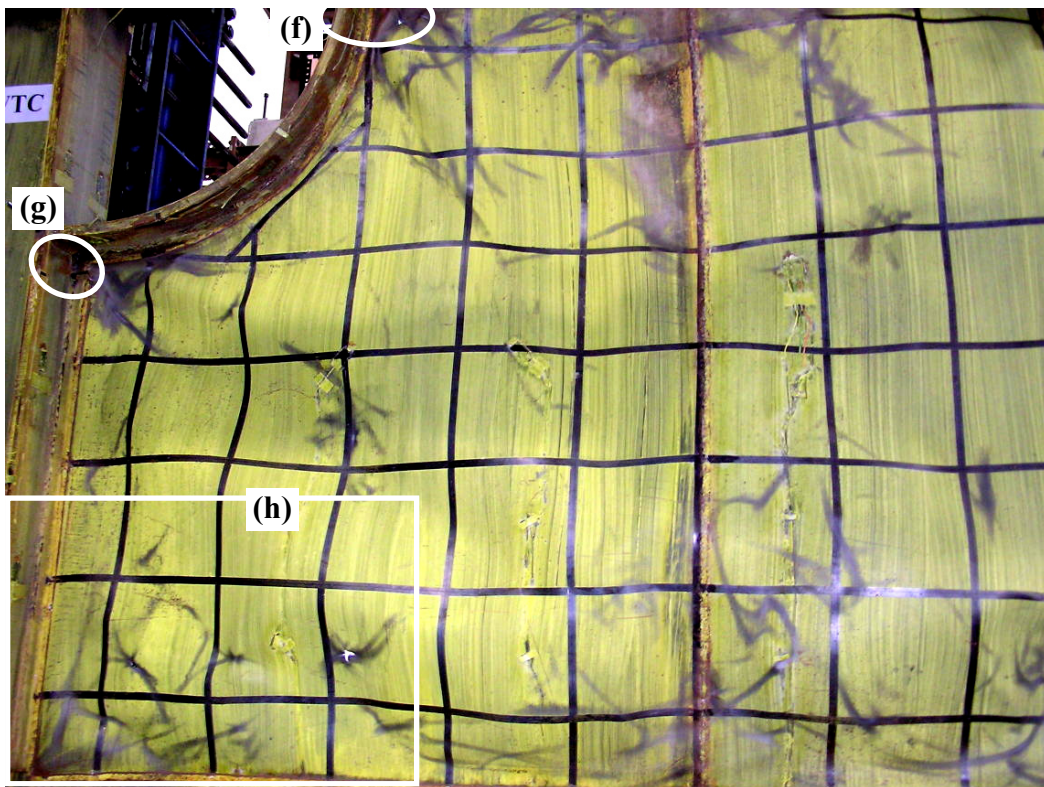
(a) Far side

(b) Wall side

FIGURE 5-71 Panel damage following testing (CR: $\gamma = 4.0\% \approx 13.333\delta_y$)

(c) Panel tear at far arch to column connection

(d) Tearing of panel at far arch weld

FIGURE 5-71 (cont'd) Panel damage following testing (CR: $\gamma = 4.0\% \approx 13.333\delta_y$)

(e) Fatigue tear near top beam, far side

(f) Panel tears at wall arch at top beam connection and panel interior

FIGURE 5-71 (cont'd) Panel damage following testing (CR: $\gamma = 4.0\% \approx 13.333\delta_y$)

(g) Panel tear at wall arch to column connection

(h) Fatigue tears near bottom beam, wall side

FIGURE 5-71 (cont'd) Panel damage following testing (CR: γ= 4.0% ≈13.333δ_y)

(i) Panel fatigue tear detail from (h)

FIGURE 5-71 (cont'd) Panel damage following testing (CR: $\gamma= 4.0\% \approx 13.333\delta_y$)
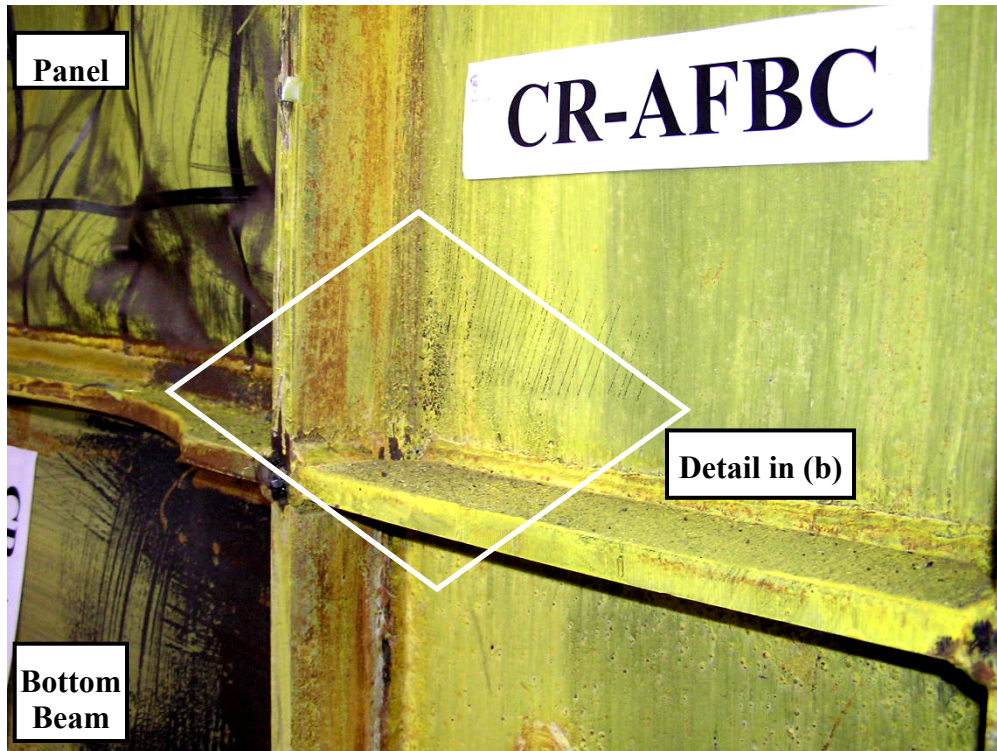
(a) Bottom of far column, A-side

(b) Zoom in of detail from (a)

FIGURE 5-72 Web and continuity plate yielding at bottom of far column (CR: End of Test, $\gamma = 4.0\% \approx 13.333\delta_y$)
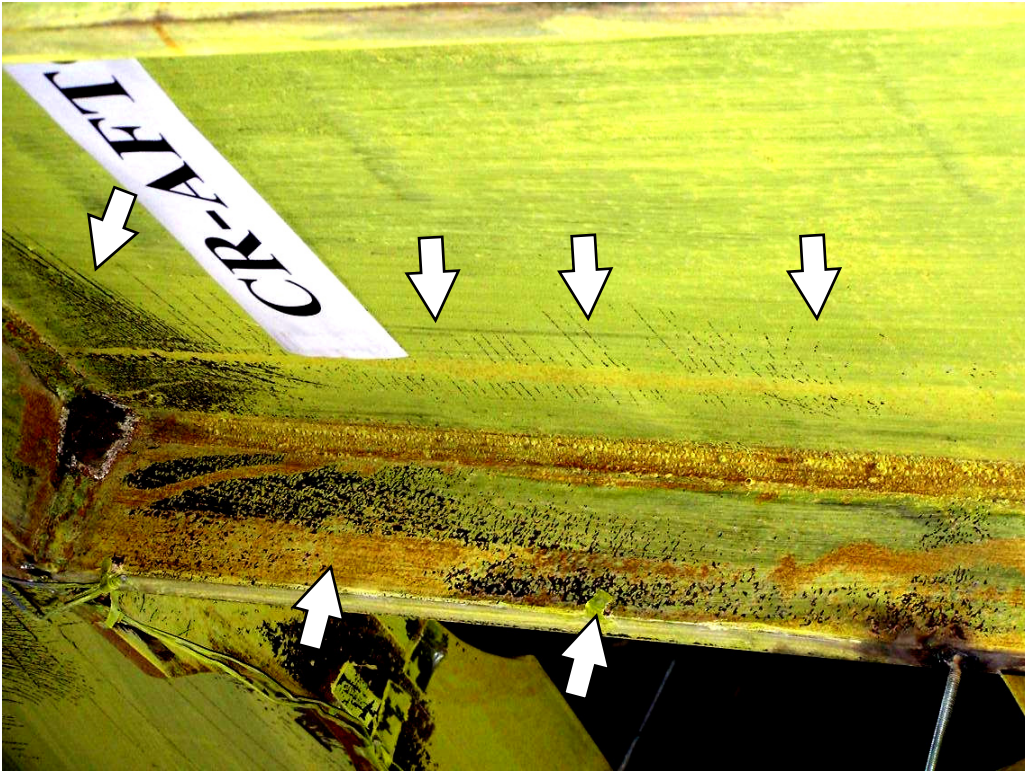
(a) A-side of column

(b) B-side of column

FIGURE 5-73 Web and wall flange yielding at top of far column (CR: End of Test, $\gamma= 4.0\% \approx 13.333\delta_y$)

(c) Detail of web and inside of wall flange yielding from (a)

(d) Wall side of top of far column wall flange

FIGURE 5-73 (cont'd) Web and wall flange yielding at top of far column (CR: End of Test, γ= 4.0% ≈13.333δ_y)

5.3.4 Specimen S2

Testing of the second solid panel specimen, S2, was carried out using the same methodology as implemented for specimen CR. The secondary actuator control scheme, as described in section 5.2.3, was used to apply the specified displacement history to the specimen at the beginning of the test, with an understanding that if the specimen and top beam deformed in such way that one actuator pair pushed as the other pulled on the specimen, control would be switched to the equal-force primary control scheme described in section 5.2.3. Following that, if loading once again became unstable, then the beams and tension bars used as restraints against rotation of the loading assembly in previous tests would be added prior to continuing the test program. For reference, the top beam alignment of the virgin specimen prior to testing is shown in figure 5-74.
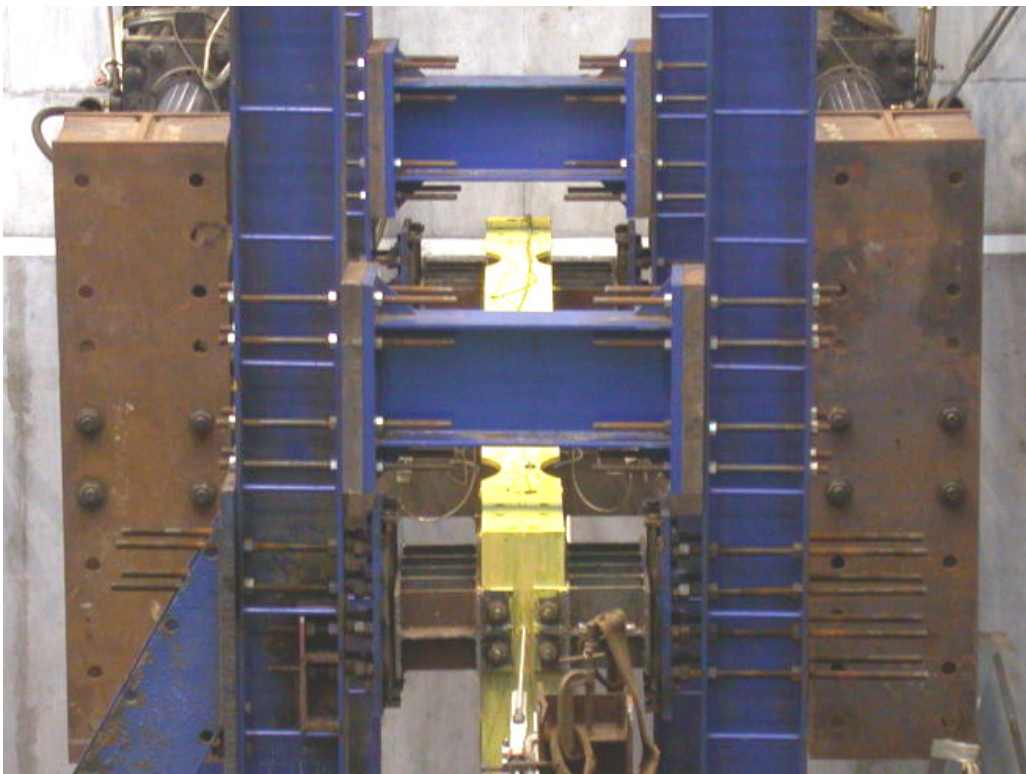
FIGURE 5-74 Initial top beam alignment prior to testing (Specimen S2)

Testing began with three cycles at 0.10% drift amplitude, which resulted in a peak base shear of approximately 500kN. Elastic buckling was observed, with no visible signs of yield. Audible creaking of bolts or the lateral support was noted, but the overall behavior was elastic and stable.

Three cycles at 0.2% drift amplitude were next applied to the specimen. A peak base shear of 900kN was observed, with elastic behavior for the first cycle. Yield lines in the flaked whitewash were noted on the webs at the bottom of the far and wall columns.

Cycle drift amplitude was then increased to 0.3%, the estimated yield drift in the pre-test analyses ($\approx 1.0\delta_y$). The peak base shear was approximately 1150kN. The observed elastic stiffness was approximately 130kN/mm. Additional yielding was observed in the column webs as described previously, and the infill panel was slightly buckled when the actuators returned to zero displacement. Yield lines were noted on the infill panel near one of the seam welds. Slight yielding was also noted in the top beam far RBS connection webs as well as both bottom beam RBS connection webs.

Three cycles were performed at 0.6% drift amplitude ($\approx 2.0\delta_y$), with a peak base shear of approximately 1500kN. More yielding was observed in the bottom beam RBS web and the top beam far connections, as shown in figure 5-75. Web yielding continued at the bottom of column locations, as shown in figure 5-76, while additional web yielding was observed at the top of the far column adjacent to the top beam bottom flange continuity plate. Infill panel buckling was visually observed at approximate orientations of 27 to 35 degrees during the cycles. More yield lines were observed on the B-side of panel, as shown in figure 5-77. Residual panel buckles upon returning the specimen to zero displacement increased in amplitude. Some yield lines were observed in the bottom beam far panel zone.

Drift amplitudes were next increased to 0.9% ($\approx 3.0\delta_y$) for three cycles, resulting in a maximum base shear of approximately 1750kN. Yielding in bottom beam RBS locations spread into flanges. Cycles at the previous drift amplitude produced yielding in top beam bottom flange continuity plates and the adjacent column webs. This observed yielding spread to the inside face of the column flanges, as shown in figure 5-78. Light yielding was observed on the wall column wall flange adjacent the bottom beam bottom flange continuity plate.

(a) Bottom beam wall connection

(b) Top beam far connection

FIGURE 5-75 RBS web yielding (S2: Cycle 12, $\gamma = 0.6\% \approx 2\delta_y$)

(a) Far column

(b) Wall column

FIGURE 5-76 Bottom of column web yielding (S2: Cycle 12, $\gamma = 0.6\% \approx 2\delta_y$)

(a) Cycle 10

(b) Cycle 12

FIGURE 5-77 B-side panel yielding (S2: $\gamma = 0.6\% \approx 2\delta_y$)
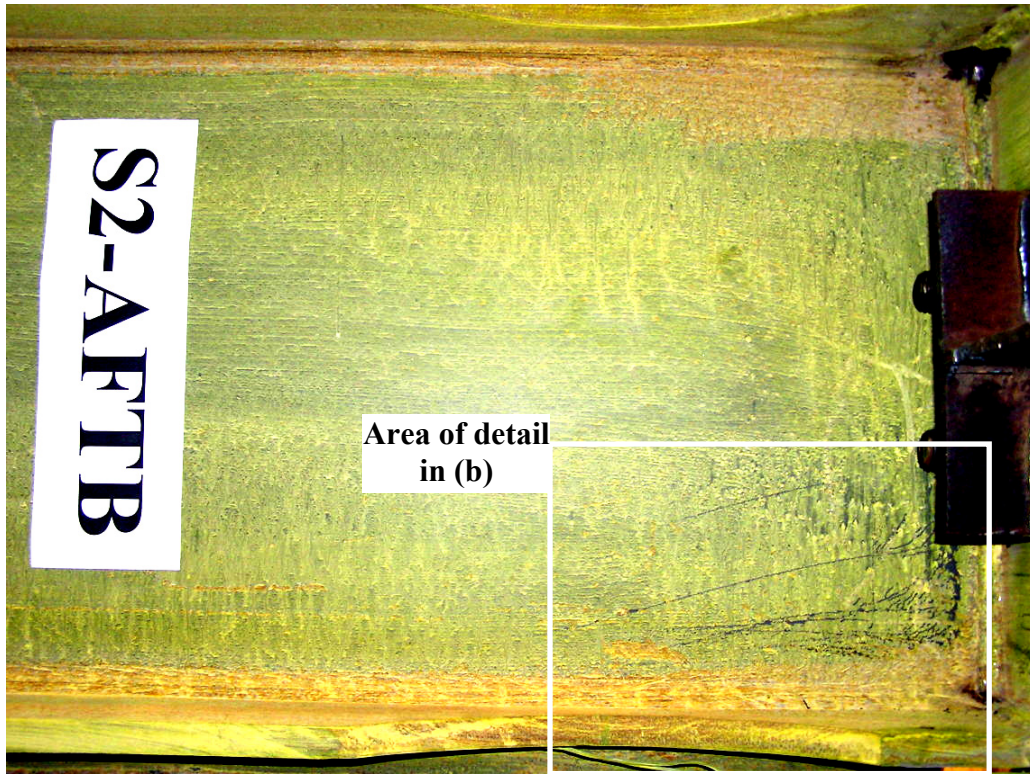
(a) Web yielding

(b) Yielding of adjacent far column wall flange

FIGURE 5-78 Top beam far RBS yielding (S2: Cycle 15, $\gamma = 0.9\% \approx 3\delta_y$)

Two cycles were carried out at 1.2% drift amplitude ($\approx 4.0\delta_y$), with peak base shear of approximately 1900kN. The extent of yielding in the far column web, flange and continuity plates spread from locations observed previously, as shown in figures 5-79 and 5-80. In the wall side bottom beam RBS, yielding was observed in the adjacent fishplate, and web local buckling was observed in the connection region, as shown in figures 5-81 and 5-82, respectively.

FIGURE 5-79 Far column wall flange yielding near top beam
(S2: Cycle 17, $\gamma = 1.2\% \approx 4\delta_y$)

FIGURE 5-80 Web, flange, and continuity yielding at top of far column (S2: Cycle 17, $\gamma = 1.2\% \approx 4\delta_y$)

(a) Web yielding from A-side

FIGURE 5-81 Wall bottom beam RBS yielding (S2: Cycle 17, $\gamma = 1.2\% \approx 4\delta_y$)

(b) Fishplate yielding from B-side

FIGURE 5-81 (cont'd) Wall bottom beam RBS yielding (S2: Cycle 17, $\gamma = 1.2\% \approx 4\delta_y$)

**FIGURE 5-82 Wall bottom beam RBS web local buckling (S2: Cycle 17, $\gamma = 1.2\% \approx 4\delta_y$)**

Drift amplitude was increased to 1.5% ($\approx 5.0\delta_y$) for two cycles, with peak base shear of approximately 2000kN. More yielding was observed at the locations described above. Web local buckling in the bottom beam wall side RBS increased in severity, as shown in figure 5-83. Bottom beam RBS region web yielding is shown in figure 5-84. At the peak of the positive excursions at this drift amplitude, the average force values were approximately 600kN and 200kN in each actuator of the A-bottom/B-top pair and the A-top/B-bottom pair, respectively, indicating some out-of-plane twist in the top beam.

The loading history increased to 2.0% drift amplitude ($\approx 6.667\delta_y$), resulting in a peak base shear of approximately 2050kN. As the specimen approached the peak of the first positive excursion, forces in the A-bottom/B-top and A-top/B-bottom pairs redistributed such that the average in each actuator was approximately 815kN and 125kN, respectively. At the peak of the second positive excursion, these average values further diverted from one another to approximately +1150kN (pushing) and -95kN (pulling), respectively. A loud "bang" was heard as the loading history approached the peak of the second positive excursion. Following the cycles at this drift amplitude, yield lines were noted in the top beam web on the far A-side, near the horizontal beam of the loading detail. A crack was found in continuity plate weld on the bottom beam bottom flange A-side at the far column wall flange, as shown in figure 5-85. Cracks were noted at both panel corners at the wall column, as shown in figure 5-86. Bottom beam wall RBS connection web local buckling worsened and bottom flange local buckling become more evident, as shown in figure 5-87. After yielding at previous drift amplitudes, buckling occurred in the fishplate adjacent to the RBS connections, as shown in figure 5-88. Yielding increased at the top of column webs, in the top beam panel zones, and the adjacent top beam bottom flange continuity plates, as shown in figure 5-89.

(a) View along A-side
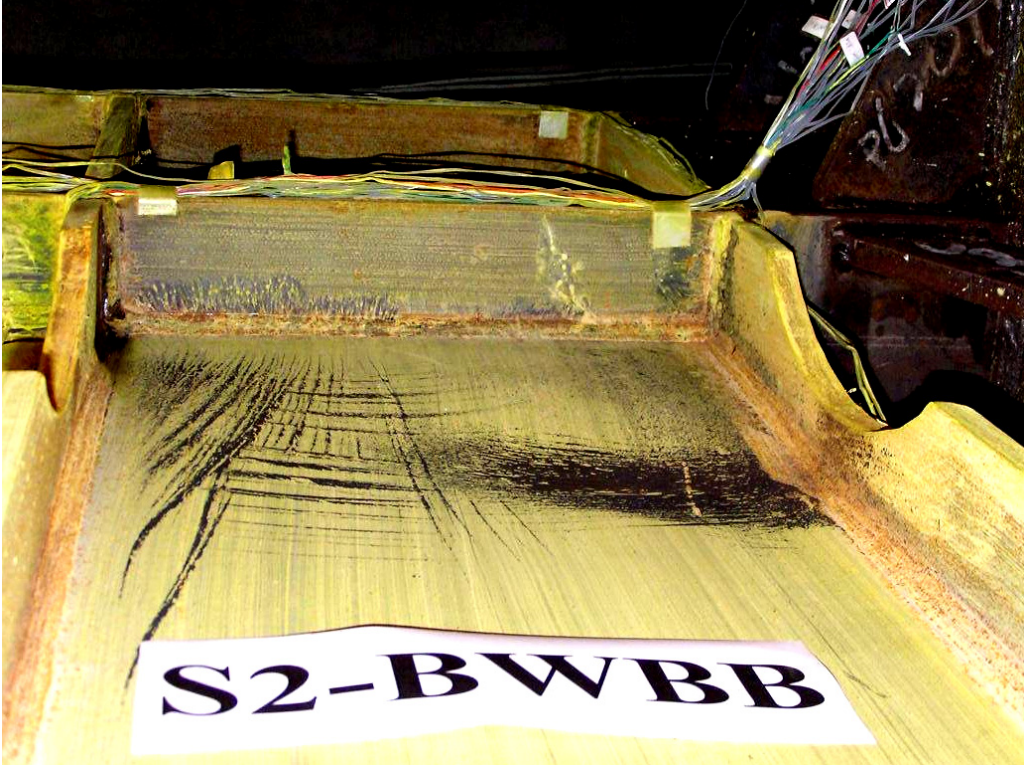
(b) View along B-side

FIGURE 5-83 Bottom beam wall RBS web yielding and local buckling (S2: Cycle 19, $\gamma = 1.5\% \approx 5\delta_y$)

195
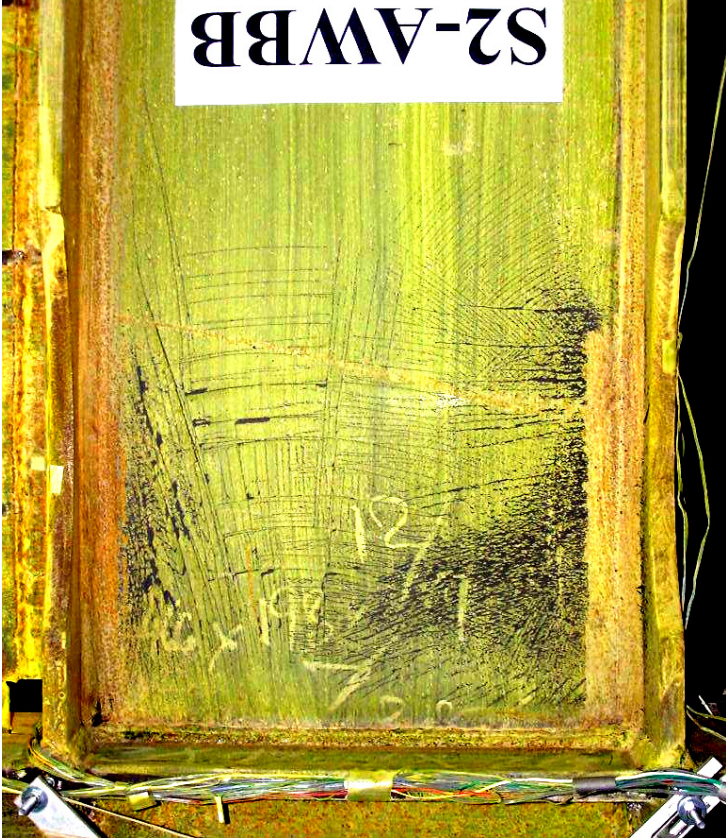
(a) Wall end RBS connection

(b) Far end RBS connection

FIGURE 5-84 Bottom beam RBS web yielding (S2: Cycle 19, $\gamma = 1.5\% \approx 5\delta_y$)
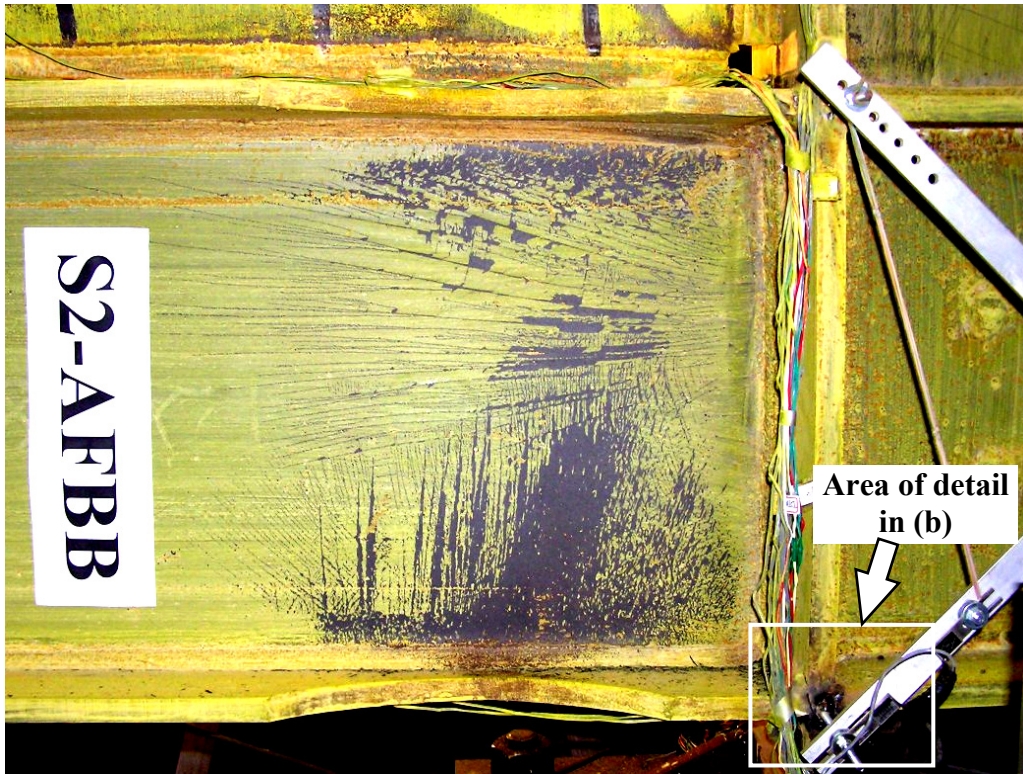
(a) Bottom beam far RBS connection
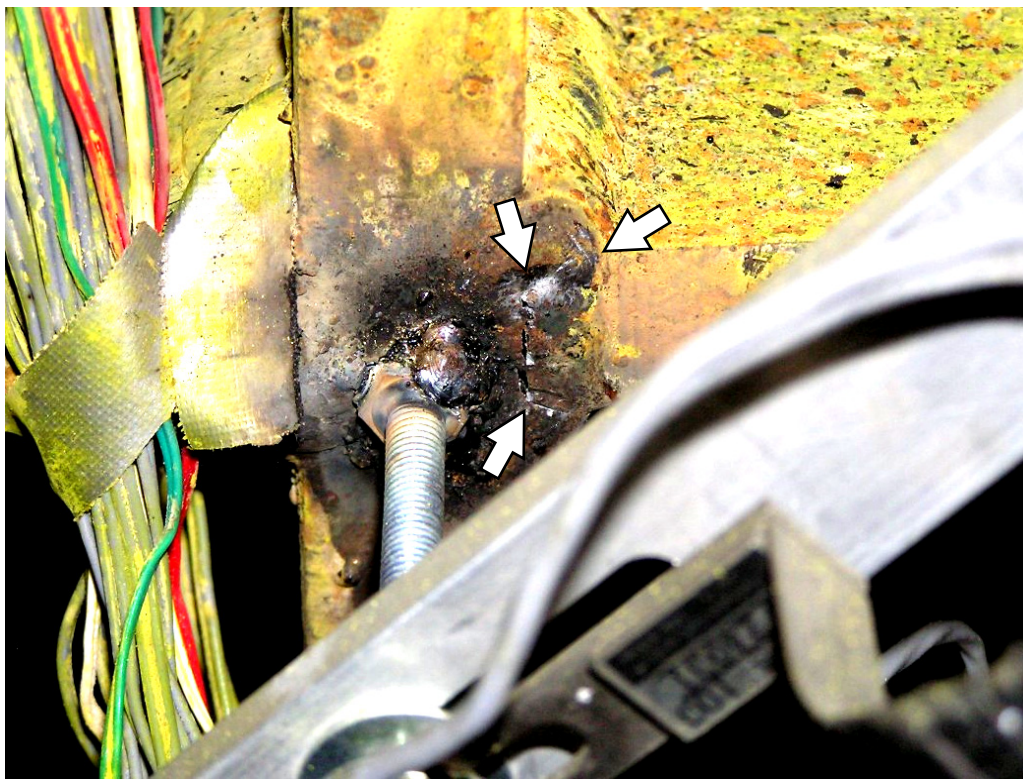
(b) Crack in bottom flange continuity plate weld

FIGURE 5-85 Far bottom beam RBS yielding (S2: Cycle 21, γ= 2.0% ≈6.667δ_y)

(a) Panel corner at wall column and top beam
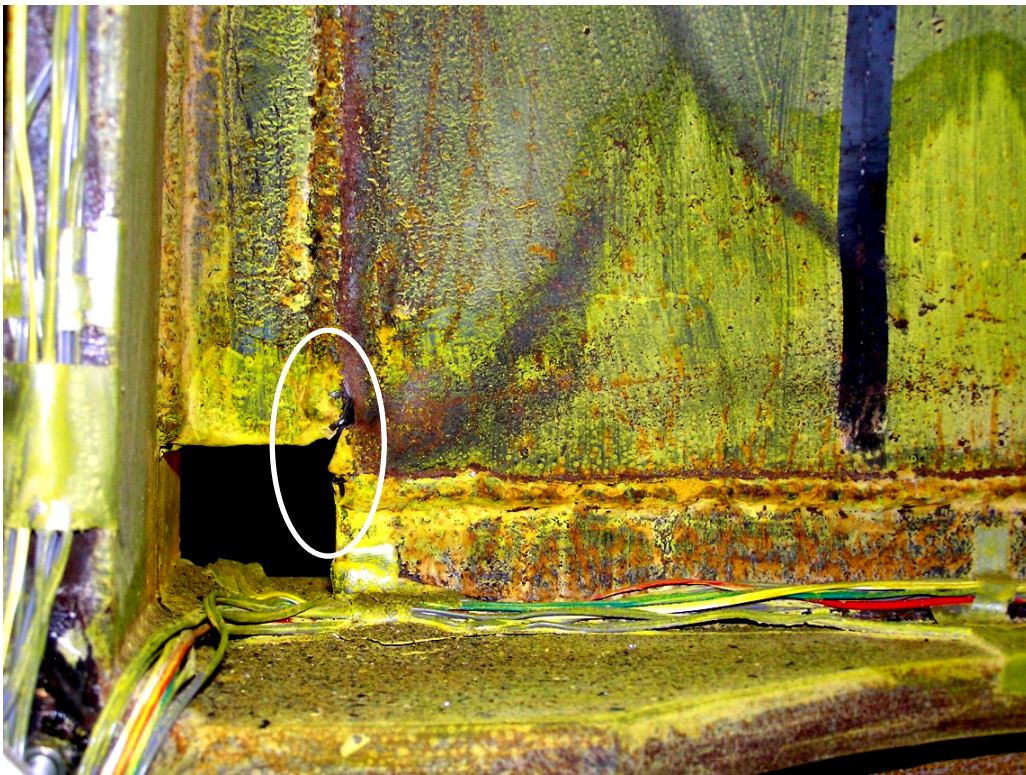
(b) Panel corner at wall column and bottom beam

FIGURE 5-86 Fractures at infill panel corners (S2: Cycle 21, γ = 2.0% ≈6.667δ_y)
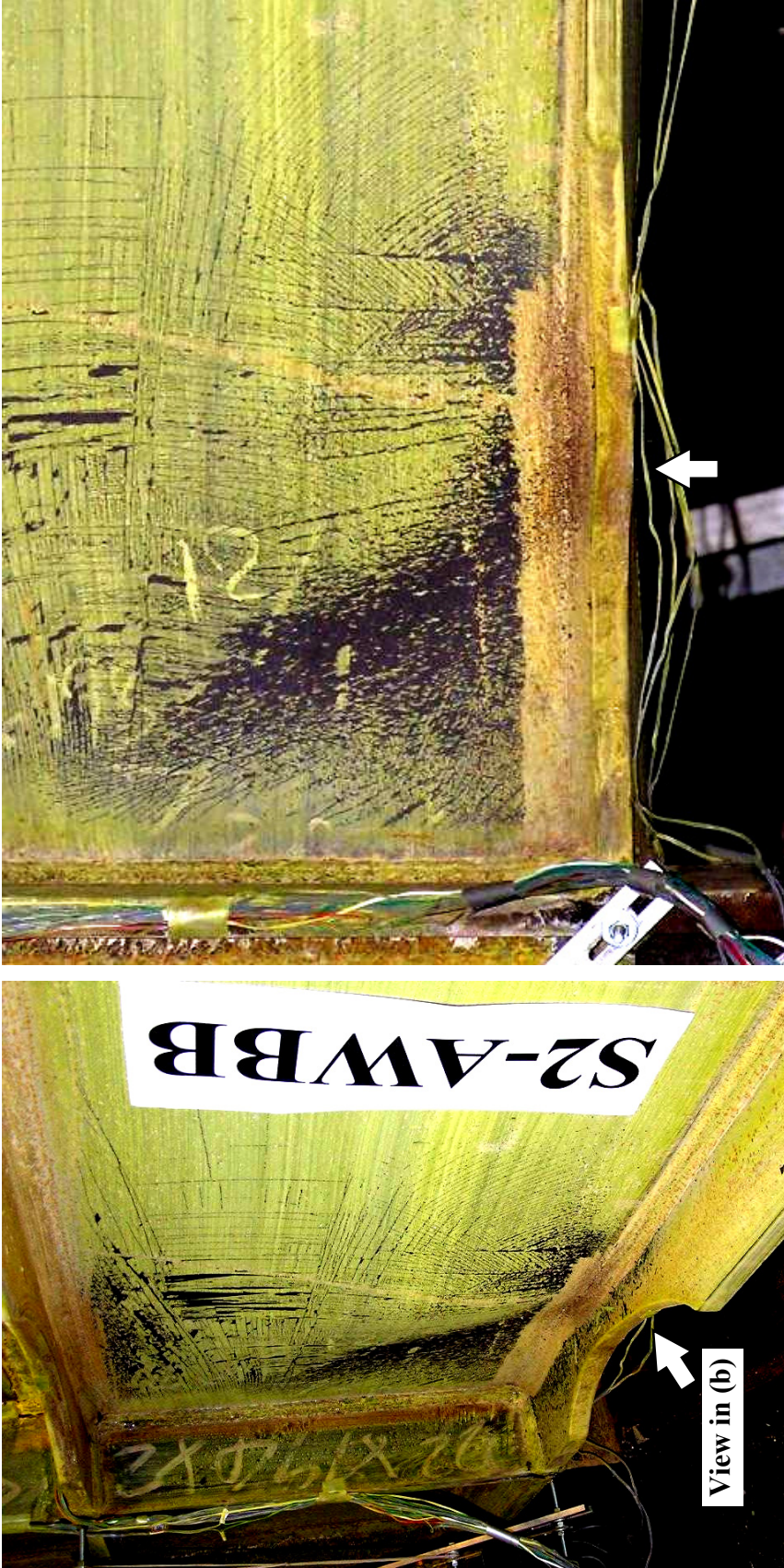
(a) Web local buckling

(b) Flange local buckling

FIGURE 5-87 Bottom beam wall RBS connection (S2: Cycle 21, $\gamma = 2.0\% \approx 6.667\delta_y$)

199

(a) Top beam wall RBS connection
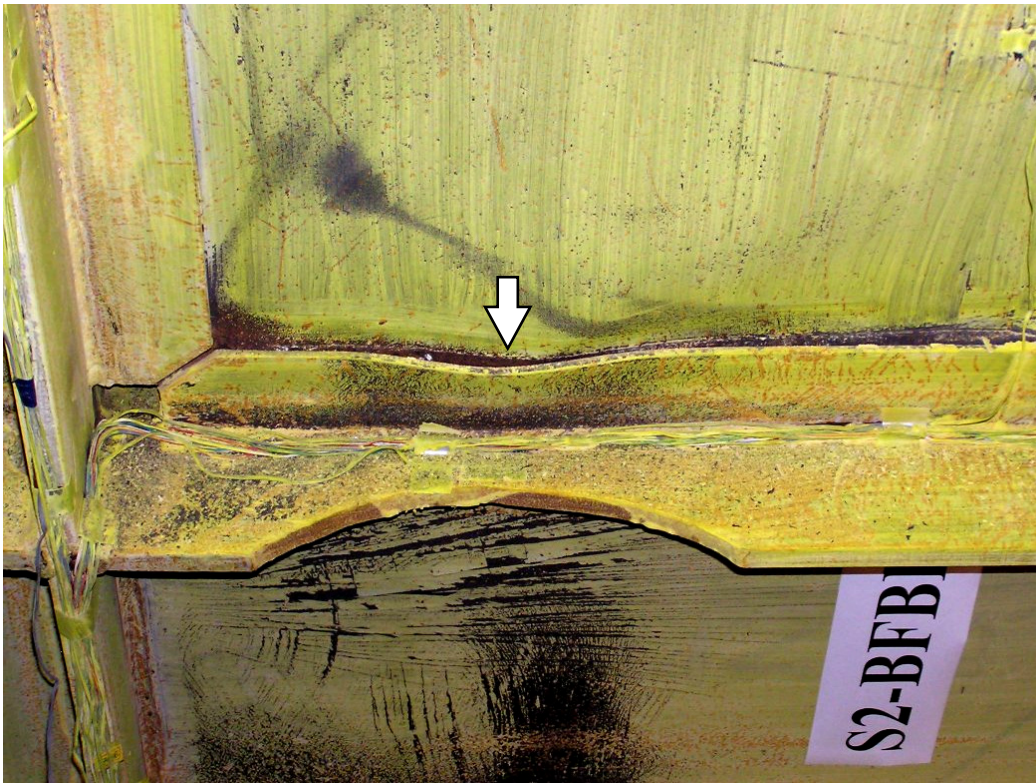
(b) Bottom beam far RBS connection

FIGURE 5-88 Fishplate local buckling (S2: Cycle 21, $\gamma = 2.0\% \approx 6.667\delta_y$)

(a) Above far column lateral support

(b) Under far column lateral support

FIGURE 5-89 Top beam far panel zone (S2: Cycle 21, $\gamma = 2.0\% \approx 6.667\delta_y$)

Prior to further application of the displacement history, the actuator control method was changed to the primary scheme described in section 5.2.3. The loading sequence then continued with two cycles at 2.5% drift amplitude ($\approx 8.333\delta_y$), resulting in peak base shear of approximately 2085kN. A 2° twist in the H-shaped loading detail was observed upon reaching the peak of the first positive excursion. Loading was paused following completion of the negative excursion of the first cycle, at a base shear of approximately zero, to allow installation of the tie-down beams used previously for safe continuation of the test. The addition of these restraints held the loading detail twisting to below 1° during the second cycle. By this point, however, the top beam distorted in its horizontal plane, as occurred in previous specimen tests, and shown in figure 5-90. The bottom beam continuity plate weld crack at the far column grew in size. A small crack was found in the bottom flange of the bottom beam far RBS, as shown in figure 5-91.
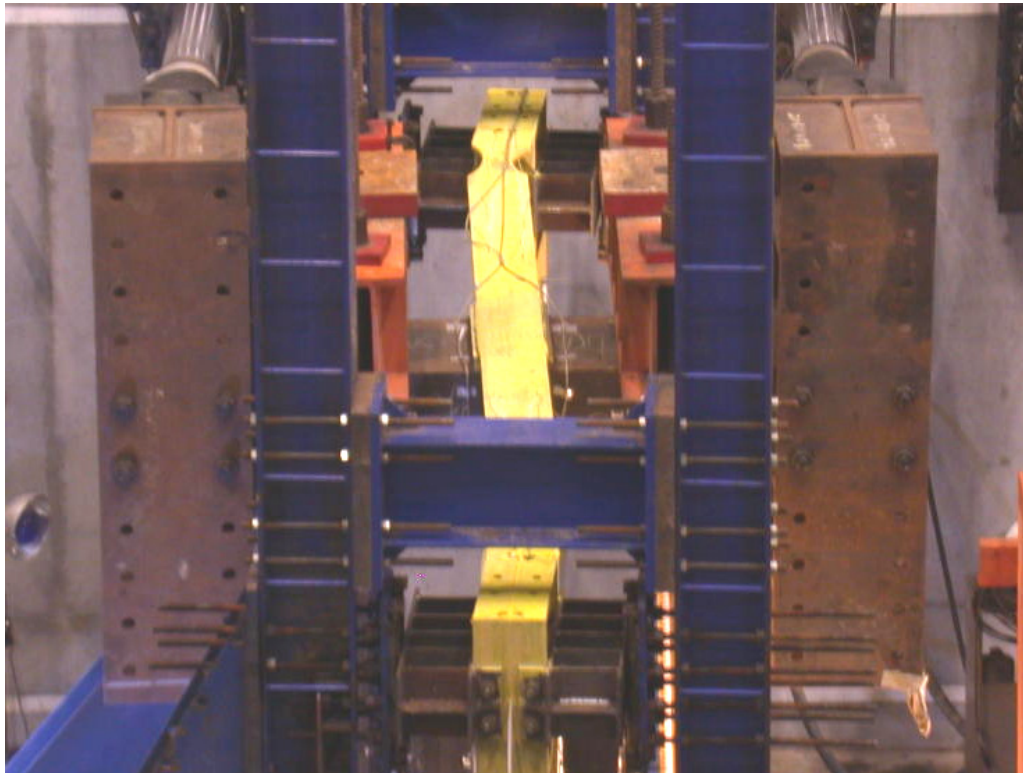
FIGURE 5-90 Top beam twisting (S2: Cycle 23, γ= 2.5% $\approx 8.333\delta_y$)

**FIGURE 5-91 Bottom beam far RBS connection yielding and
bottom flange cracking (S2: Cycle 23, γ= 2.5% $\approx$8.333δ_y)**

Cycle drift amplitude was increased to 3.0% ($\approx 10.0\delta_y$) for two cycles. Yielding increased at the locations described above. A 15% strength reduction occurred during the second positive excursion at this drift amplitude, after a fracture of the bottom beam wall RBS bottom flange, which spread into the web as the specimen approached the peak displacement, as shown in figure 5-92. During the second cycle at 3.0% drift amplitude, a 20% drop in strength at the peak of the negative excursion resulted from the fracture of the bottom beam far RBS bottom flange, as shown in figure 5-93. In addition, the cracked continuity plate weld adjacent to this connection had fully fractured by the end of the second cycle at 3.0% drift amplitude, as shown in (f) of figure 5-93. Testing ceased after completion of the second cycle. The specimen columns had twisted severely about their respective axes, and top beam was bent out-of-plane in an "S" shape, as shown in figure 5-94. Top beam web yielding and fishplate damage are shown in figure 5-95. Yielding was also observed in the top flange near the wall RBS connection, as shown in (c) of figure 5-95. Yield lines were also noted near the horizontal loading beam, as shown in (e) through (g).

(a) Web and bottom flange rupture

(b) Bottom flange rupture from bottom

FIGURE 5-92 Bottom beam wall RBS connection (S2: Cycle 25, $\gamma = 3.0\% \approx 10\delta_y$)
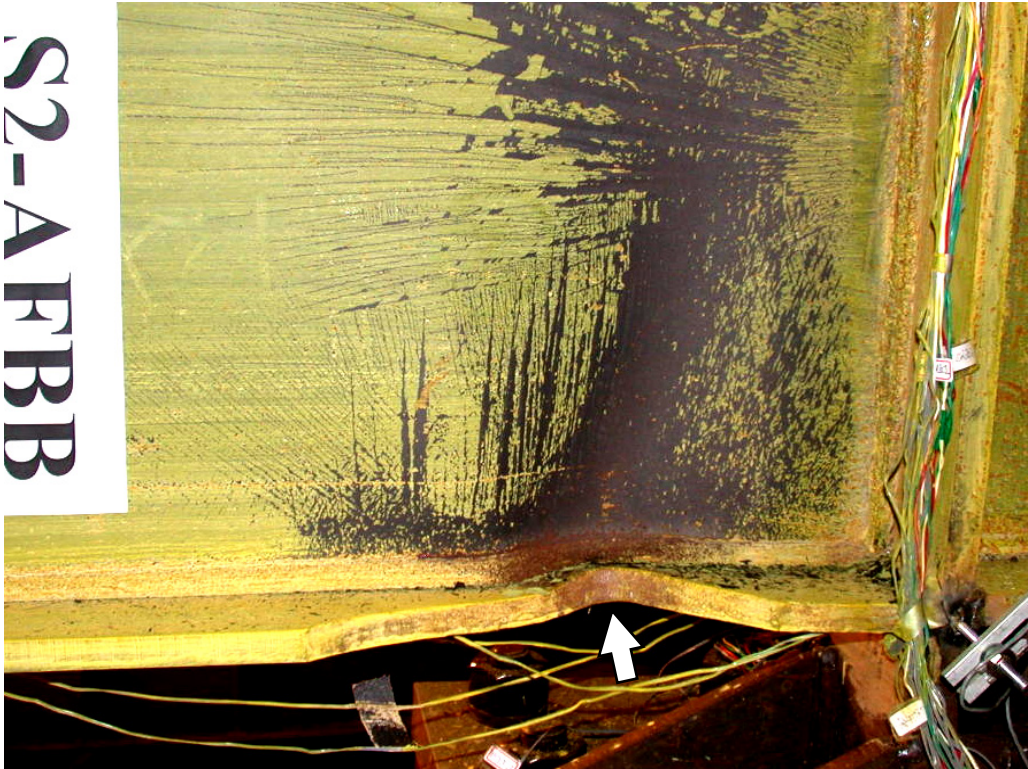
(a) Flange and web local buckling prior to rupture
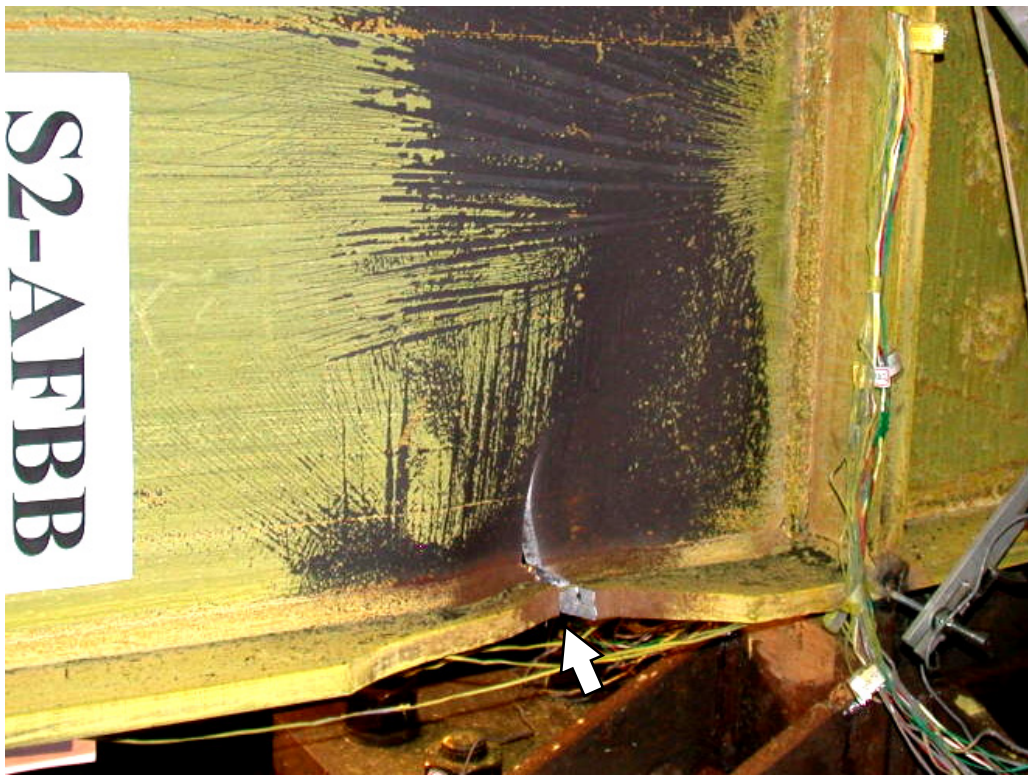
(b) Flange and web rupture

FIGURE 5-93 Bottom beam far RBS connection (S2: Cycle 25, $\gamma= 3.0\% \approx 10\delta_y$)

(c) From B-side of web

(d) Bottom flange rupture from below

FIGURE 5-93 (cont'd) Bottom beam far RBS connection (S2: Cycle 25, $\gamma = 3.0\% \approx 10\delta_y$)

(e) Bottom flange rupture detail
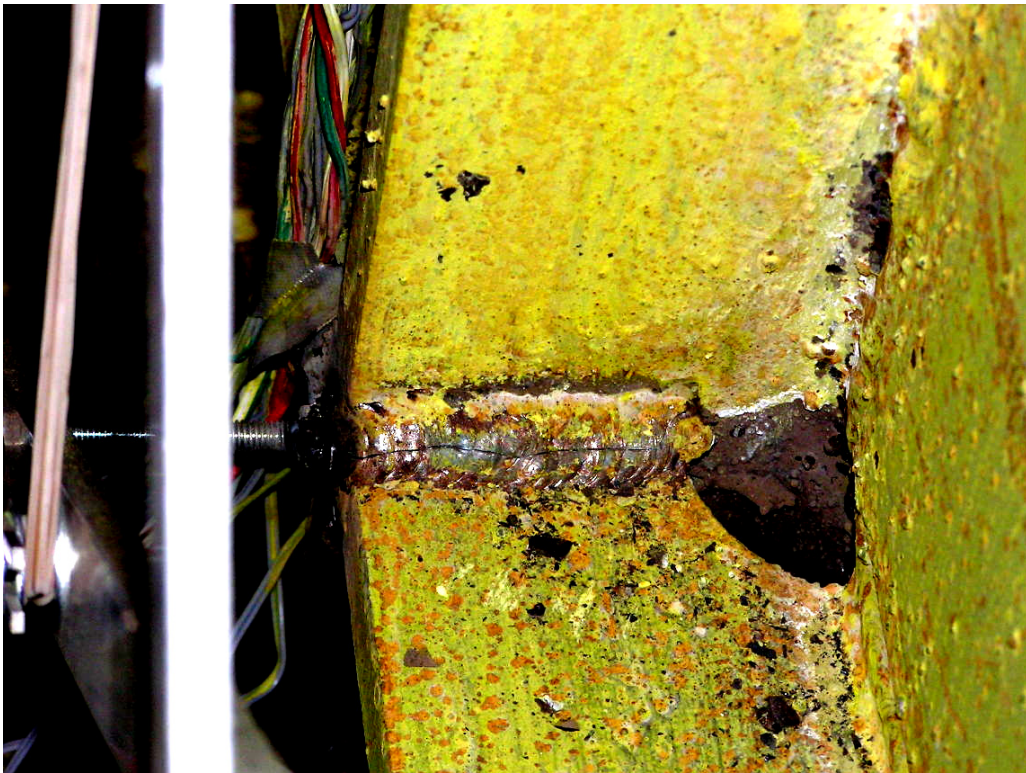
(f) Full fracture of bottom flange continuity plate weld

FIGURE 5-93 (cont'd) Bottom beam far RBS connection (S2: Cycle 25, γ= 3.0% ≈10δ_y)

(a) End view

≈9°
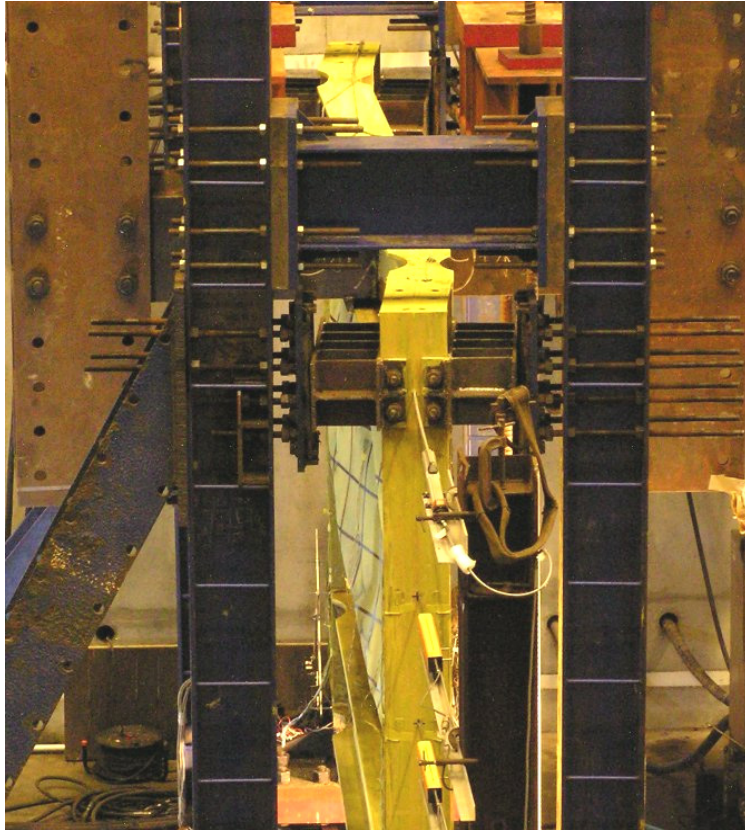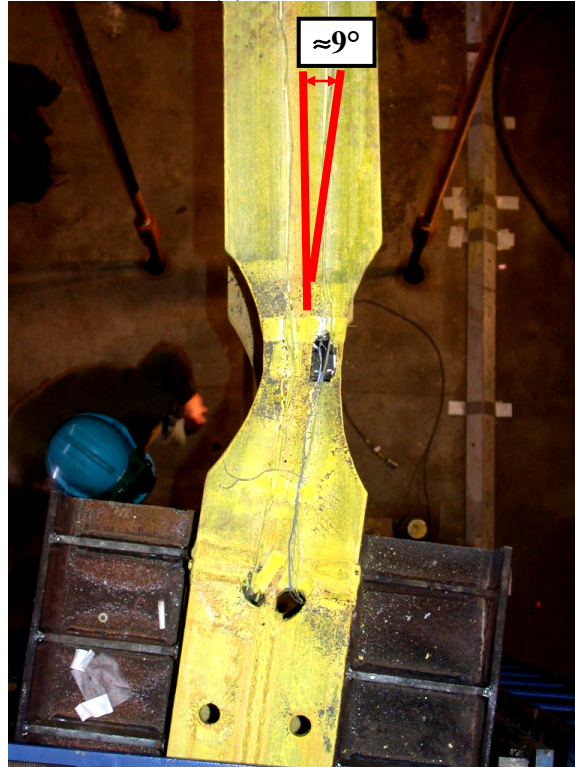
(b) Top beam far RBS rotation

FIGURE 5-94 Top beam and column twisting (S2: End of test, $\gamma = 3.0\% \approx 10\delta_y$)

(a) Top beam wall RBS web yielding on B-side
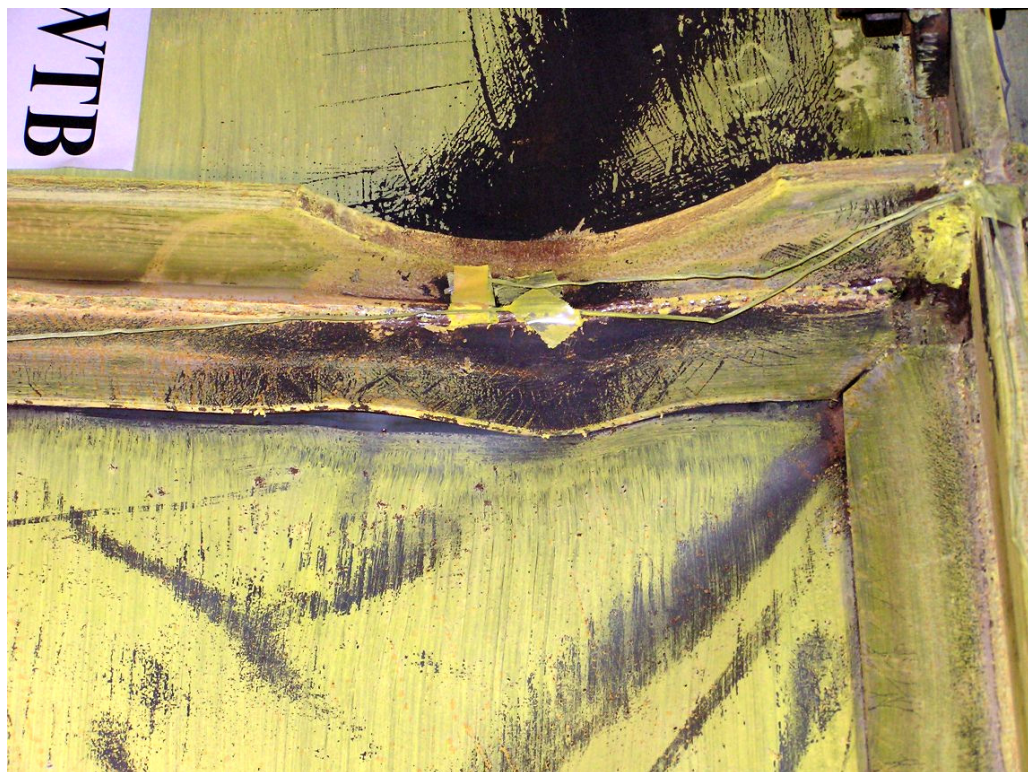
(b) Top beam wall RBS fishplate yielding and buckling on B-side

FIGURE 5-95 Top beam yielding (S2: End of test, $\gamma = 3.0\% \approx 10\delta_y$)
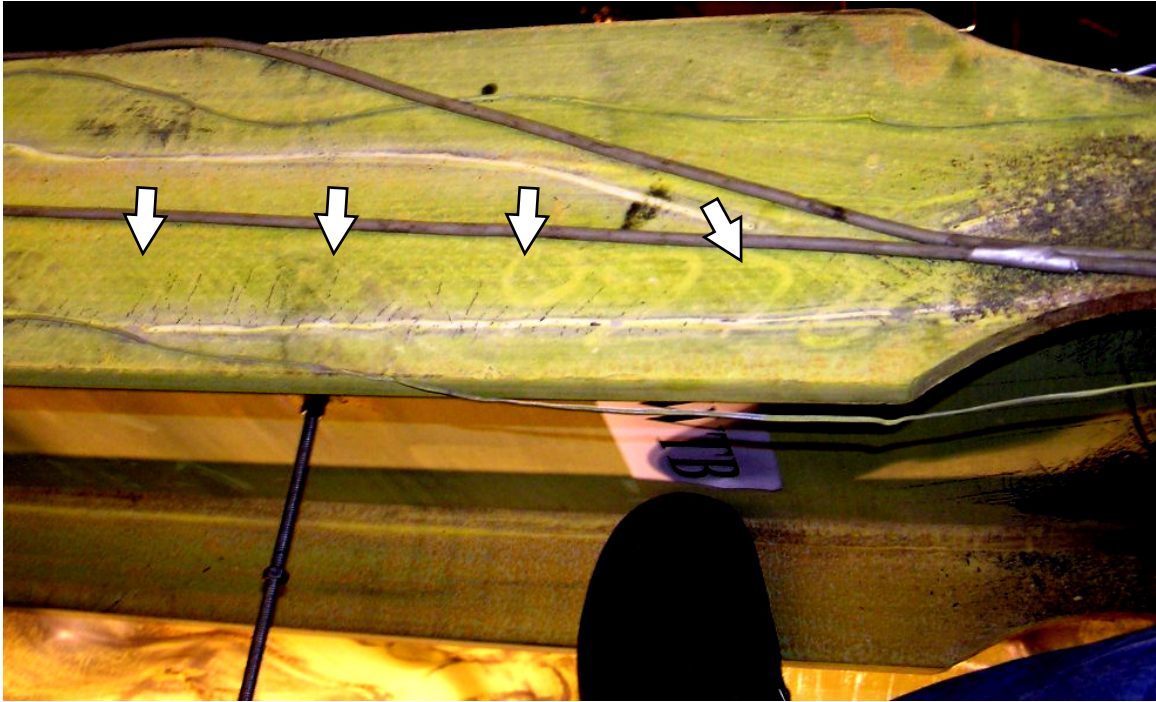
(c) Top beam top flange yielding near wall RBS connection

(d) Top beam far RBS connection

FIGURE 5-95 (cont'd) Top beam yielding (S2: End of test, γ = 3.0% ≈10δ_y)

(e) A-side web and flanges adjacent to wall side of loading detail

FIGURE 5-95 (cont'd) Top beam yielding (S2: End of test, γ = 3.0% ≈ 10δ_y)
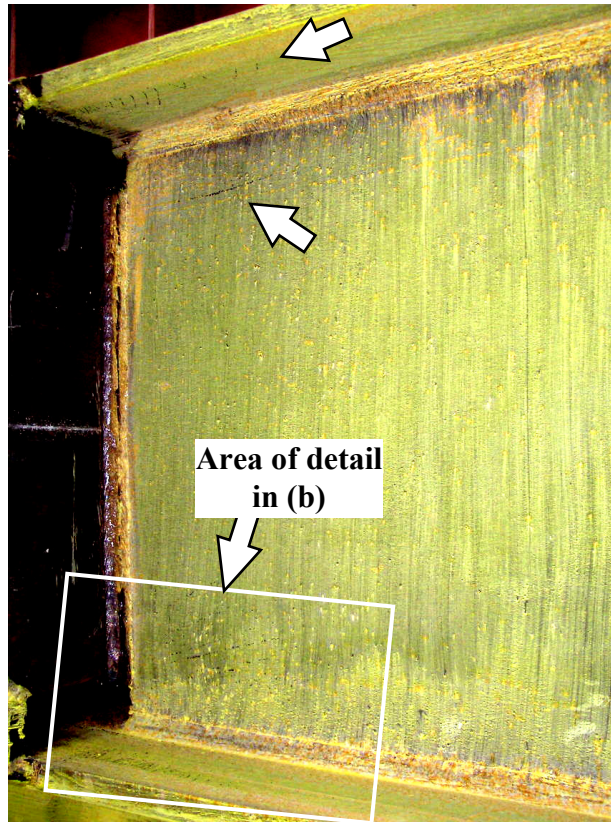
(f) B-side web and flanges adjacent to wall side of loading detail

(g) B-side web and bottom flange adjacent

FIGURE 5-95 (cont'd) Top beam yielding (S2: End of test, $\gamma = 3.0\% \approx 10\delta_y$)

Column yielding had increased substantially by the conclusion of testing. Yielding in the far column web, wall flange, and adjacent bottom beam top flange continuity plate is shown in figure 5-96. Top of column yielding in the web, the flange adjacent to the infill panel, and top beam panel zone, is shown in figure 5-97. Infill panel damage across the entire panel consisted of tension yielding and folds from buckling, as well as cracks at the corners, as shown in figure 5-98.

(a) A-side web and bottom beam top flange continuity plate

(b) B-side web and wall flange

FIGURE 5-96 Bottom of far column yielding (S2: End of test, $\gamma = 3.0\% \approx 10\delta_y$)

(a) Far column on A-side

**FIGURE 5-97 Top of column web, panel zone, and continuity plate yielding
(S2: End-of-test, $\gamma = 3.0\% \approx 10\delta_y$)**

(b) Top of far column

(c) Top of wall column

FIGURE 5-97 (cont'd) Top of column web, panel zone, and continuity plate yielding (S2: End-of-test, $\gamma = 3.0\% \approx 10\delta_y$)

216
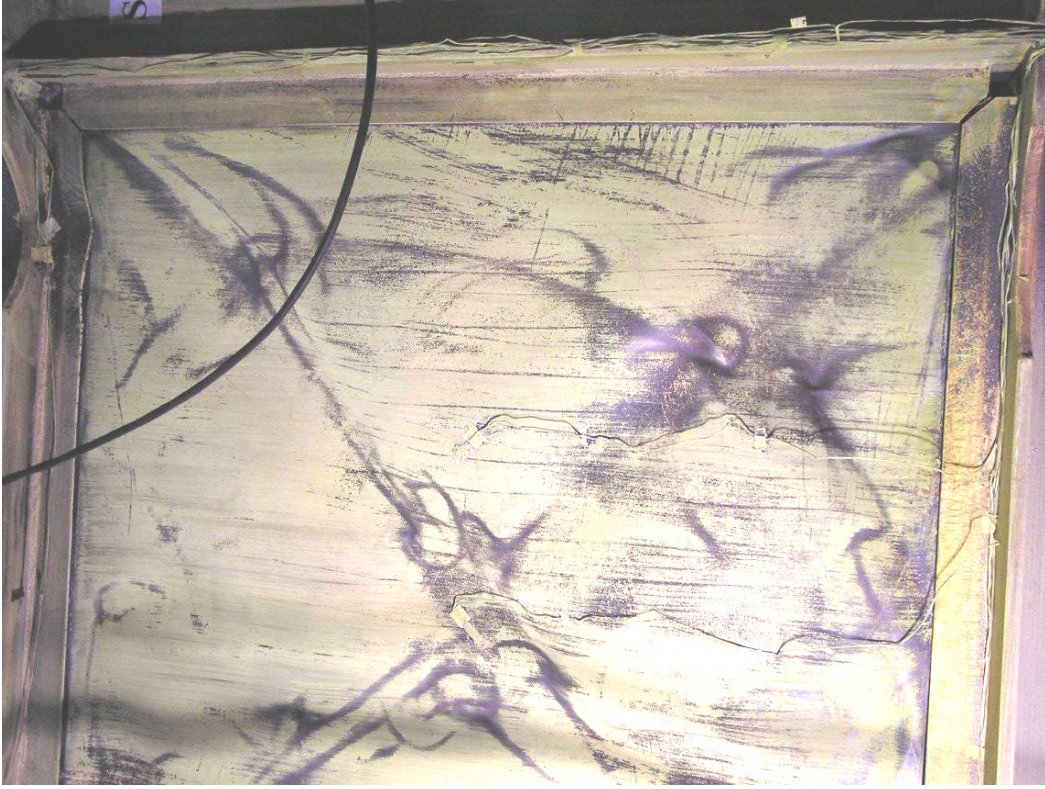
(b) Wall section of panel

(a) Far section of panel

FIGURE 5-98 Panel damage following testing (S2: $\gamma = 3.0\% \approx 10\delta_y$)
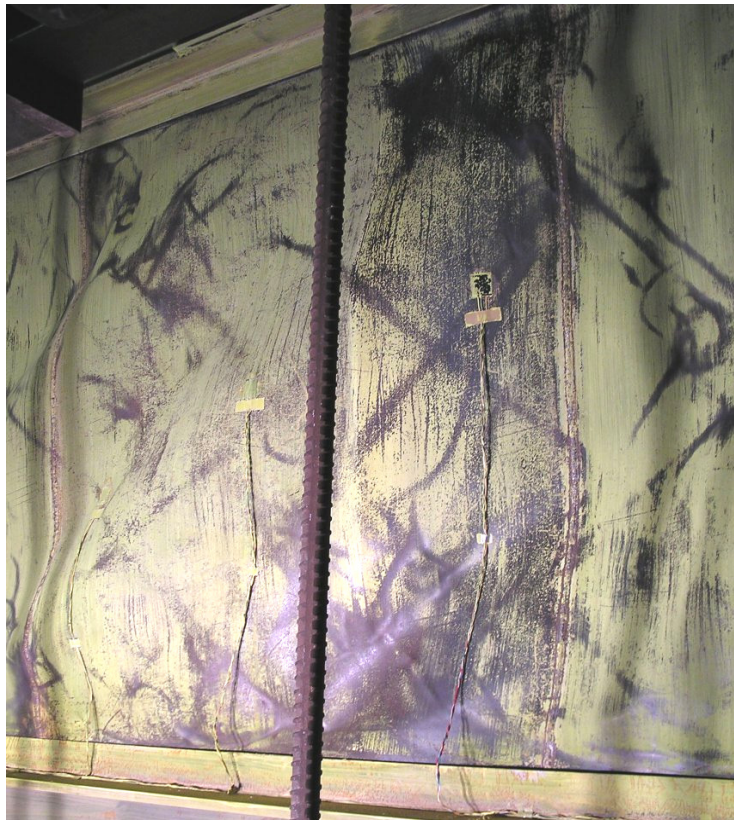
(c) Center section of panel

(d) Buckling and yielding from A-side

FIGURE 5-98 (cont'd) Panel damage following testing (S2: $\gamma = 3.0\% \approx 10\delta_y$)
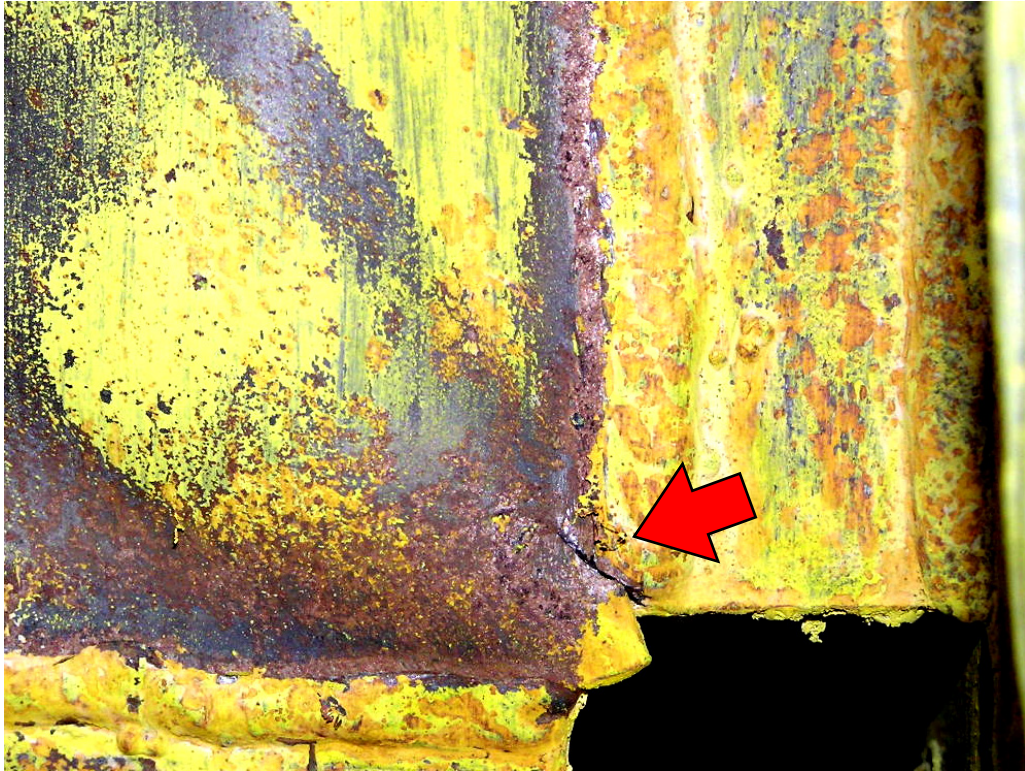
(e) Infill panel crack at far bottom corner

(f) Infill panel crack at wall bottom corner

FIGURE 5-98 (cont'd) Panel damage following testing (S2: γ= 3.0% ≈10δ_y)

5.4 Summary

Four low yield strength steel plate shear wall specimens were tested using displacement controlled quasi-static loading. Specimen S1, a "trial" specimen utilizing a solid panel, performed well until a poor weld at a beam to column connection fully fractured as the tests cycled at 3% drift amplitude. The partial penetration weld with backing fillet weld of the beam flange to the column flange was intended by the fabricator to perform as a full penetration weld. This detail was changed to a full penetration weld for the remaining three specimens. Fractures also appeared in the infill panel, adjacent to the seam welds, where the fabricator had ground the weld down. This step in the fabrication was also eliminated from subsequent specimens.

The values of peak base shear strength, ductility, drift, and elastic stiffness are summarized for each specimen in table 5-2. Specimen P, containing twenty circular perforations in the infill panel, was successfully tested to a maximum interstory displacement of 60mm (3%, $10\delta_y$) and maximum base shear of 1790kN at 2% drift. Although not their main intended purposes, the perforations quieted the sound of the panel buckling. The specimen strength and elastic stiffness were approximately 85.5% and 81.5% lower, respectively, than the values obtained for a similar solid panel specimen at comparable drift levels. Although the specimen could have carried additional loading, testing stopped because significant fractures had occurred in the bottom beam RBS and the top beam and top of the columns had twisted severely, damaging the lateral supports at those locations.

Specimen CR, utilizing reinforced quarter-circle cutouts in the panel corners, was successfully tested to a maximum interstory displacement of 80mm (4%, $13.333\delta_y$) and maximum base shear of 2050kN at 2.5% drift. At the peak displacement, the overall specimen strength had dropped by an average of 30% from the peak value, following fracture of the bottom flange in both bottom beam RBS connections. Again, the specimen could likely have resisted significant loads up to larger displacements, after a redistribution of the load path from that of the virgin specimen, but, top beam horizontal distortions and top of column twisting made restraint of the specimen too difficult to continue the testing up to larger drifts.

Specimen S2, a solid infill panel specimen, was successfully tested to a maximum interstory displacement of 60mm (3%, $10\delta_y$) and maximum base shear of 2115kN at -3% drift. Specimen

strength had reduced by an average of 18% at the conclusion of testing, due to fracture of the bottom flange of each bottom beam RBS connection. Again, top beam and top of column twisting made restraint of the specimen difficult at larger drifts, necessitating the conclusion of testing.

TABLE 5-2 Summary of Peak Results

Specimen	Elastic Stiffness	Maximum Base Shear Strength	Approximate Maximum Displacement Ductility	Maximum Interstory Drift	Strength Reduction at Max. Drift
	(kN/mm)	(kN)	$(\mu = \Delta/\Delta_y)$	(%)	(%)
P	115	1790	10	3	14.5
CR	140	2050	13.33	4	30
S2	135.5	2115	10	3	18

SECTION 6

FINITE ELEMENT MODELING OF TESTED SPECIMENS

6.1   General

This chapter describes the modeling and analysis of the experimental specimens using the commercially available finite element software package ABAQUS/Standard (HKS 2002b). The selection of element types, boundary conditions, material properties, and loading input are each described in the sections below. Results are presented for the analysis of each specimen and the effectiveness of the models is discussed.

6.2   Description of the Finite Element Model

6.2.1   General

In order to investigate the behavior of the tested specimens, finite element models were developed, to better capture the interaction between frame members and the infill panel. Local buckling and plastic hinging observed in the boundary frame during testing could be best investigated by explicitly modeling each frame member as built-up sections of plate elements. Therefore, rather than utilize "beam" or "frame" elements, i.e. one-dimensional idealizations of a structural member, whose range of behavior may be limited by underlying assumptions, generalized shell elements were used to model the flanges and webs and panel zones of the boundary frame, as well as the SPSW infill panel, as described below.

6.2.2   Geometry Definition and Mesh Generation

The graphical interface program ABAQUS/CAE, was used to define the geometry of the FEM models (HKS 2002a). In this package, the user defines "parts" to be analyzed, as net geometry only, specifying whether the final model will consist of line (1-D), shell (2-D), and/or solid (3-D) elements. A model may consist of different "parts", with the interaction between those parts defined through connector elements, which impose compatibility constraints. However, for the models described here, the approach was to create the model as a single part, so that the meshes at the interface of different model sections, say, the infill panel and the boundary frame, would

have nodes in common. This ensures compatibility of deformations between pieces, eliminating the need for connector elements or other additionally computationally expensive means to impose these constraints.

The connection tab, or "fish plate", used in the experiments to connect the infill panel with the surrounding frame, was neglected in the finite element modeling. Instead, a direct connection was assumed to take place between the two structural elements, an approximation whose effects on analysis results were found to be very small (Driver *et al*. 1997).

The specimen models were meshed with quadrilateral elements, properties of which are described in the next section. All elements were located at the mid-thickness of the physical element they represent. Following the manual layout of basic geometry, the mesh was generated by a module within ABAQUS/CAE. This establishment of basic geometry simplified steps of mesh refinement to verify the reliability of results.

Different segments of each model were meshed using varying methods. Webs and flanges of frame members for all specimen models were meshed using the "structured meshing technique", which is most appropriate for regular geometric shapes. The curved geometry of the corner cutout arch reinforcement of specimen CR was meshed using the "swept meshing technique".

The infill panels of each specimen model were meshed using the "free meshing technique", and specifically, the "Medial axis control algorithm". This algorithm initially subdivides the region to be meshed into a group of simpler regions. Following that process, structured meshing techniques are used to fill each simple region with elements (HKS 2002a).

6.2.3 Element Selection (S4R Shells)

The infill panel and boundary frame members were modeled using the four-noded S4R element, a general purpose, doubly-curved shell, with reduced integration (HKS 2002b). Each node has six degrees of freedom: three translational (u_x, u_y, u_z) and three rotational (θ_x, θ_y, θ_z). Transverse shear deformation is allowed for by the use of thick shell theory as the thickness increases, or become discrete Kirchhoff thin shell elements, with transverse shear deformation becoming very small, as the thickness decreases.

The S4R element accounts for finite member strains and large rotations, and allows for change in thickness. It is therefore suitable for large-strain analysis involving materials with a nonzero effective Poisson's ratio, as well as applications in which geometric and material nonlinearities are anticipated, as cross-sectional properties are calculated by numerical integration through the shell thickness.

The S4R element utilizes a reduced integration scheme, with just a single integration point at the center of the shell. This scheme can provide more accurate results and significantly reduce run time compared with fully integrated elements, especially in three-dimensional problems, if the elements are not distorted. However, under certain loading conditions, a phenomenon in which singular spurious energy modes are present, known as "hourglassing", may occur. Mesh size refinement and distributing concentrated loads in the model over multiple nodes are ways of reducing the possibility of this effect. Moreover, an artificial stiffness is added by ABAQUS to both the membrane and bending terms of the shell stiffness formulation to counteract this phenomenon. While the user may explicitly define the values of these terms, the default values are typically sufficient to control "hourglassing". The accumulation of strain energy dissipated by hourglass control over the history of each analysis was negligible, as shown in the results discussed below.

6.2.4 Boundary Conditions

The hinge at the base of each specimen column was not modeled explicitly in the ABAQUS model. Instead, "CONN3D2" connector elements were used to connect a reference node at the location of the hinge center with nodes at the tip of each flange and the intersection of the flanges and web. This connector element allows all six DOFs (three translation and three rotation) to be constrained as dictated by the problem requirements. The BEAM connector property definition, a pre-defined assembly of basic connection components constraining translation (LINK and SLOT) as well as rotation (ALIGN), and thereby providing a rigid beam connection between the two nodes involved, was assigned to these elements. Fixed boundary conditions were applied to all DOFs except rotation about the out-of-plane axis at the reference nodes, to replicate the hinge rotation permitted during testing.

The out-of-plane resistance provided by the lateral supports at the top of columns during the experiments was modeled by fixing displacements in that direction. The exterior nodes of the flange elements around the perimeter of the panel zones were restrained against movement in the z-direction (out-of-plane). Note that these locations aren't identical to those constrained in the experiment (as shown in figures 4-20, 5-36, and 5-37), and as noted in the previous chapter the lateral supports and towers did not provide full restraint against column rotation at those locations. However, the selected DOF constraints provide the support as intended for the experiments and full modeling of the support towers was deemed beyond the scope of the project and not expected to provide addition useful information with regards to observed overall specimen behavior.

6.2.5 Initial Conditions

The initial shape of each specimen infill panel was not recorded, although some very slight deviation from perfect flatness was visually observed prior to testing. These imperfections help precipitate the global panel buckling during even the first small amplitude cycles of testing.

An eigen value buckling analysis was performed to determine the first ten infill panel buckling modes prior to cyclic analysis of each specimen model, as described below. An amplitude of 1mm was multiplied by the first mode nodal displacements, and applied as the initial condition of the specimen panels using the imperfection command within ABAQUS/Standard. When analyses were conducted without using this procedure, the panel would remain flat, carrying the increasing load via panel shear until either shear yielding occurred, or bifurcation shear buckling occurred, then transmitting the load via tension field action. This did not agree with experimental observations, where, due to panel imperfections, shear buckling occurred almost immediately under very low lateral loads, and was both audible and visible. Therefore, the introduction of the initial imperfection into the analytical model was deemed appropriate and necessary to capture the observed experimental behavior.

6.2.6 Material Properties

A constitutive relationship for use in the analyses was selected to fully represent the cyclic behavior of both materials in the specimens. Since only standard monotonic tension tests (not cyclic) were performed on specimen material coupons, as described in chapter 4, the

specification of inelastic material properties for the analytical model required some assumptions. Using properties of steel documented in the literature, an appropriate cyclic hardening rule could be selected, as described below.

A two-surface, "combined" hardening model was used to represent the stress-strain behavior of both the infill panel material and the frame member material. This pressure and rate independent material model implements the concepts of both isotropic hardening (i.e. an expansion of the yield surface while undergoing plastic strains) and kinematic hardening (i.e. a shifting of the yield surface without expansion during plastic straining), overcoming inadequacies exhibited by using either of these hardening rules alone in modeling cyclic problems. While a number of nested surface models appear in the literature (Hodge 1957; Dafalias and Popov 1975; Krieg 1975), the model provided within ABAQUS/Standard, based on the work of Lemaitre and Chaboche (1990), was utilized for the analyses.

ABAQUS/Standard performs calculations for element behavior based on "true" stress (Cauchy stress) and logarithmic strain, σ_{true} and ε_{ln}, respectively. Therefore, test data based on nominal values (i.e. those based on the original geometry of the coupon) for isotropic material, was converted to those measures for input by the following simple relations (HKS 2002b):

$$\sigma_{true} = \sigma_{nom} \cdot \left(1 + \varepsilon_{nom}\right) \tag{6-1}$$

$$\varepsilon_{ln}^{pl} = \ln\left(1 + \varepsilon_{nom}\right) - \frac{\sigma_{true}}{E} \tag{6-2}$$

The kinematic hardening component of the material model could be defined in multiple ways, depending on the type of test data available, using pairs of (ε_{ln}, σ_{true}) data points. For the infill panel material, the available half-cycle test data was used to generate input for ABAQUS to define kinematic hardening.

The boundary frame members were built up sections, fabricated from plate material specified as ASTM A572 Gr. 50 ($F_y = 345$MPa). As with the infill panel material, only monotonic uniaxial tension tests were performed on material coupons. During the coupon tension tests, which were primarily used to confirm the material yield and ultimate strengths, the relative displacement between testing machine grips was measured, while strain was not. However, since the material was specified to conform with ASTM A572 and exhibited a nearly identical yield plateau stress,

227

the cyclic behavior – for the purposes of the analysis – was assumed equivalent to that of "Steel A" documented in an ATLSS study of cyclic inelastic strain behavior on properties of A572 Gr. 50 steel (Kaufmann *et al*. 2001). That study investigated the cyclic inelastic strain behavior of the materials under tension-compression loading using the ASTM E606 standard strain controlled fatigue test methodology in which a cylindrical coupon of 0.375in (9.5mm) diameter was subjected to 10 tension-compression cycles at a single strain range, loaded at a constant displacement rate of 0.005in/min. Figure 6-1 shows a plot of cyclic test results for "Steel A", for stabilized cycles at 2%, 4%, 6%, and 8% strain ranges. From this figure, (ε_{ln}, σ_{true}) data points following the backbone curve of a stabilized cycle at 6% strain range were used as input to calibrate the parameters of the kinematic hardening component.
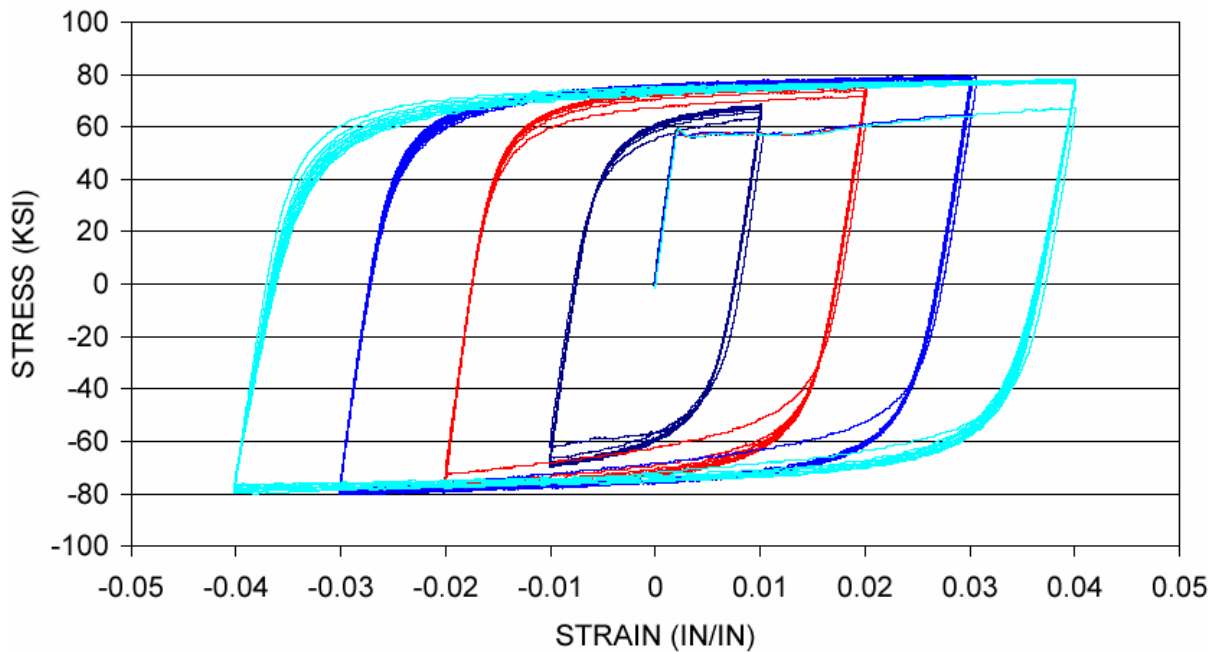
**FIGURE 6-1 Composite Plot of Cyclic Axial Strain Behavior of "Steel A"
(4 different specimens, respectively subjected to 10 cycles at 2%, 4%,
6%, and 8% Strain Range). (from Kaufmann *et al*. 2001)**

6.2.7 Loading of the ABAQUS model

An *interstory* displacement history was used to apply load to the top beam of each specimen as described in section 5.2.2 of the previous chapter. For finite element analysis however, a *top beam* displacement history was used to apply loading to the models. Therefore, the test data was used to determine the average top beam displacement amplitude for each series. Table 6-1 lists,

228

for specimens P, CR, and S2, the average top displacement amplitude during the testing, and the analysis duration for each series step. A general displacement amplitude curve was defined in ABAQUS for a series of cycles at unit amplitude, as shown in figure 6-2. During the analysis, this curve was scaled to the required displacement amplitudes listed in Table 6-1. The program uses a step "time" to increment the solution, which is discussed further in the next section.
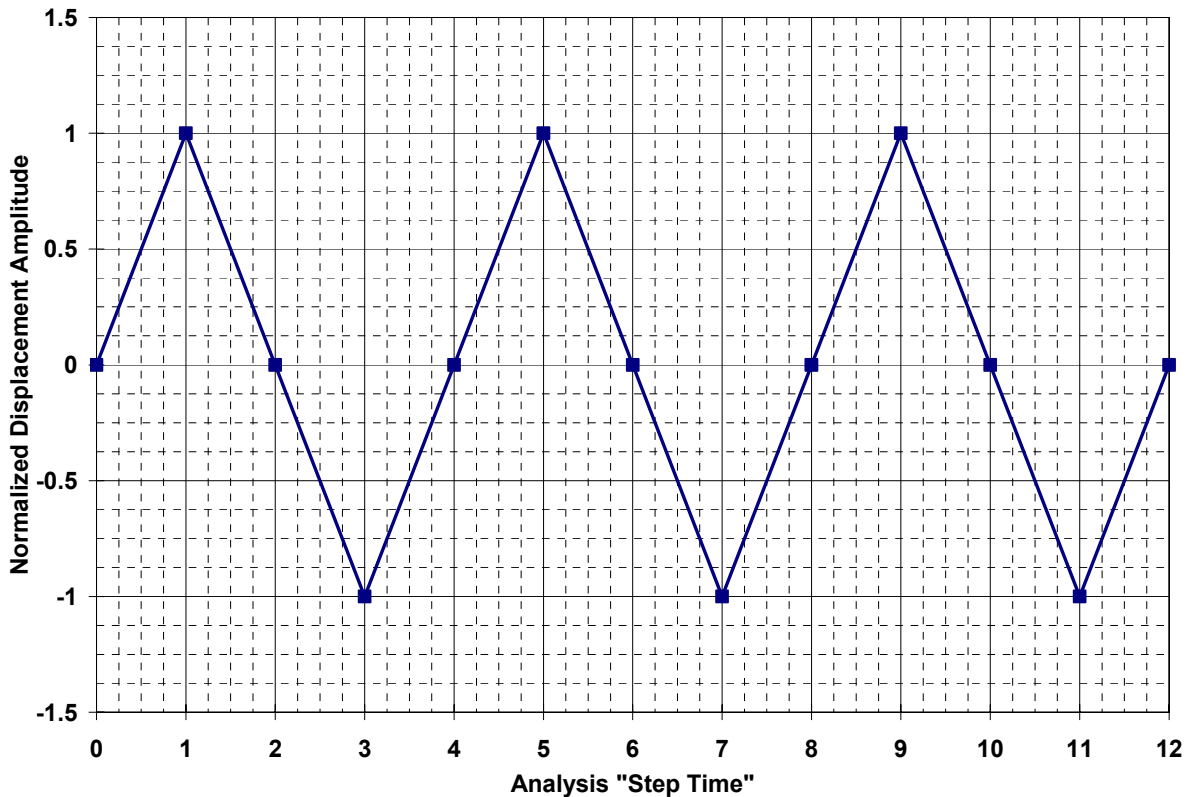
FIGURE 6-2 Normalized Displacement Amplitude History

During testing, the displacement loading history was applied to the specimen using four actuators and an H-shaped loading detail, at the center of the top beam as described in chapters 4 and 5. This loading scheme was idealized for the finite element analysis, by means of a control node, defined at the middle of the top beam, which was used for the application of the displacement loading history. A distributing coupling constraint was used to distribute the total load from this control node, to a nodal surface, defined as two planes, 300mm apart, centered on the top beam. Reactions and displacements at these nodes were recorded throughout the analysis to calculate the total force on the model and the total top beam displacement, for comparison with the experimental results.

TABLE 6-1 Top Displacement Summary for Analysis Amplitude

Analysis Step	Number of Cycles	Step "Time"	Cumulative "Time"	Average Tested Top Displacement (mm)
Specimen P				
1	3	12	12	3.52
2	3	12	24	6.82
3	3	12	36	9.97
4	3	12	48	19.01
5	3	12	60	28.03
6	2	8	68	37.05
7	2	8	76	45.92
8	2	8	84	60.72
9	2	8	92	75.48
10	1	4	96	89.73
Specimen CR				
1	3	12	12	3.90
2	3	12	24	7.31
3	3	12	36	10.43
4	3	12	48	19.46
5	3	12	60	28.54
6	2	8	68	37.64
7	2	8	76	46.71
8	2	8	84	61.62
9	2	8	92	75.86
10	2	8	100	75.47
11	2	8	108	91.72
12	2	8	116	121.57
Specimen S2				
1	3	12	12	3.78
2	3	12	24	7.32
3	3	12	36	10.64
4	3	12	48	19.85
5	3	12	60	29.02
6	2	8	68	38.20
7	2	8	76	47.24
8	2	8	84	62.26
9	2	8	92	76.77
10	2	8	100	92.35

6.2.8 Non-Linear Problem Solution

The displacement loading history was applied to the model as a static load, since the testing was carried out in a slow, quasi-static manner. Therefore, dynamic effects were not considered in the models. However, the inherent instability of panel shear buckling, and in this case, cyclic buckling, creates some challenges to overcome during the problem solution. The S4R shell elements described above allowed for the use of large deformation (geometric nonlinear) analysis, with element formulations updated as the model deforms, to the current deformed configuration, for use in the subsequent increment. The nonlinear material properties discussed above provide additional complexity to the solution. ABAQUS contains time incrementation and solution stabilization techniques, briefly summarized below, to overcome these challenges and perform a robust analysis.

ABAQUS/Standard solves nonlinear problems using the Newton method. The nonlinear solution response curve is calculated by specifying the loading as a function of "time" (artificial in the case here, as it is a slow, quasi-static loading) and incrementing the time to obtain nonlinear response (HKS 2002b). The approximate equilibrium configuration is calculated at the end of each time increment, a task that may take several iterations to determine an acceptable solution. ABAQUS uses an automatic incrementation control scheme for efficient calculation of a solution after the program is supplied with an initial time increment.

During testing, as a specimen was cycled from one extreme displacement (i.e. positive amplitude) to another (i.e. negative amplitude), the tension field action shear buckles developed in the infill panel would, at a limiting value, "snap-through" to the opposite configuration once the load-displacement curve passed through the point of zero load. As observed in the tests, this generally happened quickly during the early cycles, with a pop and then small oscillations in the panel in the new configuration. However, in later cycles, after accumulation of significant plastic strains and severe permanent deformation from the original plane of the wall, the reorientation of the infill panel tension field would progress in a slower manner, with localized portions of the wall gradually conforming to the new tension field. This cyclic reorientation of the tension field presented a significant challenge to the solution calculation during finite element analysis of the specimen models.

Solution difficulties presented by the localized instability discussed above were minimized by using the "STABILIZE" option within ABAQUS/Standard, which provides an automatic addition of volume-proportional damping to the model during a nonlinear static analysis. Since this option is used for a static and not dynamic analysis, an artificial mass matrix is introduced into the model and an additional damping force term is added to the model's global equilibrium equations (HKS 2002b). This option was specified for each step of the analyses discussed below. The default for this option calculates a new damping factor internally after the first increment of each step. After the completion of the analysis of a particular specimen, the energy dissipated by the stabilization option was qualitatively evaluated from the energy history throughout the analysis. When a marked increase in stabilization-dissipated energy was observed for a particular analysis step, the internally calculated damping factor (which is reported in an output file) from the previous step was manually added to the model input file for a subsequent analysis. Evaluating the energy history of this subsequent analysis was the means of verifying that the effect of static stabilization on the analysis results had been reduced to an acceptable fraction of total energy dissipated by the specimen, while providing enough damping to allow the analysis to progress forward with fewer numbers of iterations.

6.3   Specimen P

Figure 6-3 shows the FEM model mesh and the first eigen-buckling mode for specimen P. An amplitude of 1mm was assigned to the infill panel nodal displacements for this mode and used as the initial deformed shape of the model prior to analysis. This amplitude was large enough to precipitate panel shear buckling and diagonal tension field formation as observed experimentally.

The total force versus top beam displacement hysteresis is shown in figure 6-4 for the experiment, as well as monotonic pushover and cyclic ABAQUS analyses. Note that the backbone of the cyclic analysis follows the monotonic analysis curves. Though the analytical model slightly underestimates the experimental strength, very good agreement between the experimental and cyclic analytical results is observed in this figure for cycles up through an approximate top displacement amplitude of 37mm, analysis step 6 listed in Table 6-1. However, control of the experiment was hampered after this point, due to the loading assembly rotation, subsequent column twisting, and distortion of the top beam and lateral support frames, as

232

described in section 5.3.2. The lateral support frames were not modeled explicitly in ABAQUS, but were idealized as rigid out-of-plane roller supports, as described above. These modeling assumptions do not allow to analytical replication of the succession of distortions observed in the experiments. However, the overall specimen behavior is well represented, as shown in figure 6-5. Part (a) of this figure shows the specimen during testing at 3% drift, while (b) displays the deformed shape of the FEM model at the same displacement. The FEM results also show contours representing the magnitude of the von Mises yield surface (in 10^{-3}MPa), which particularly highlight the yielding and strain hardening at the RBS locations.
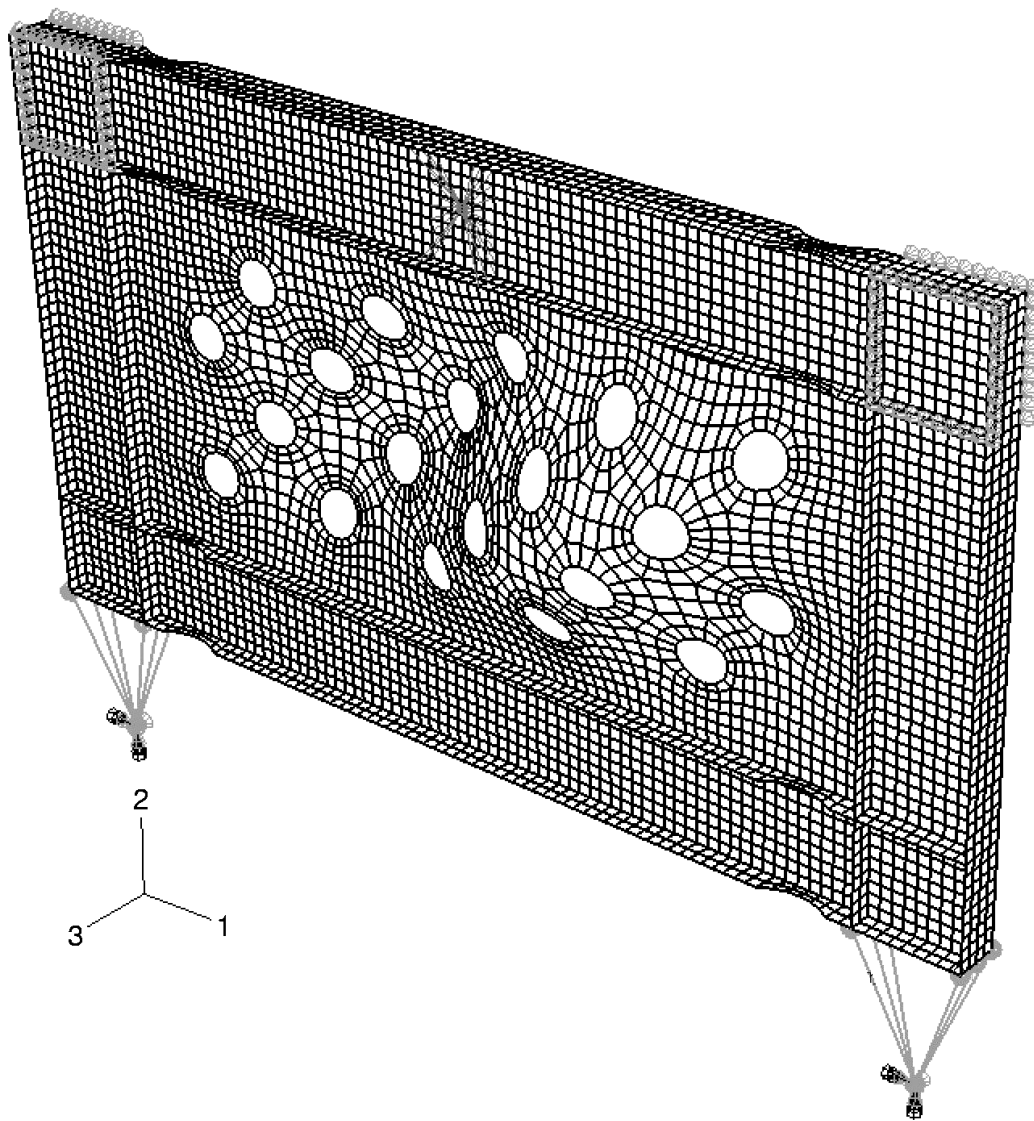
FIGURE 6-3 Specimen P Finite Element Model Mesh with 1ˢᵗ Panel Buckling Mode
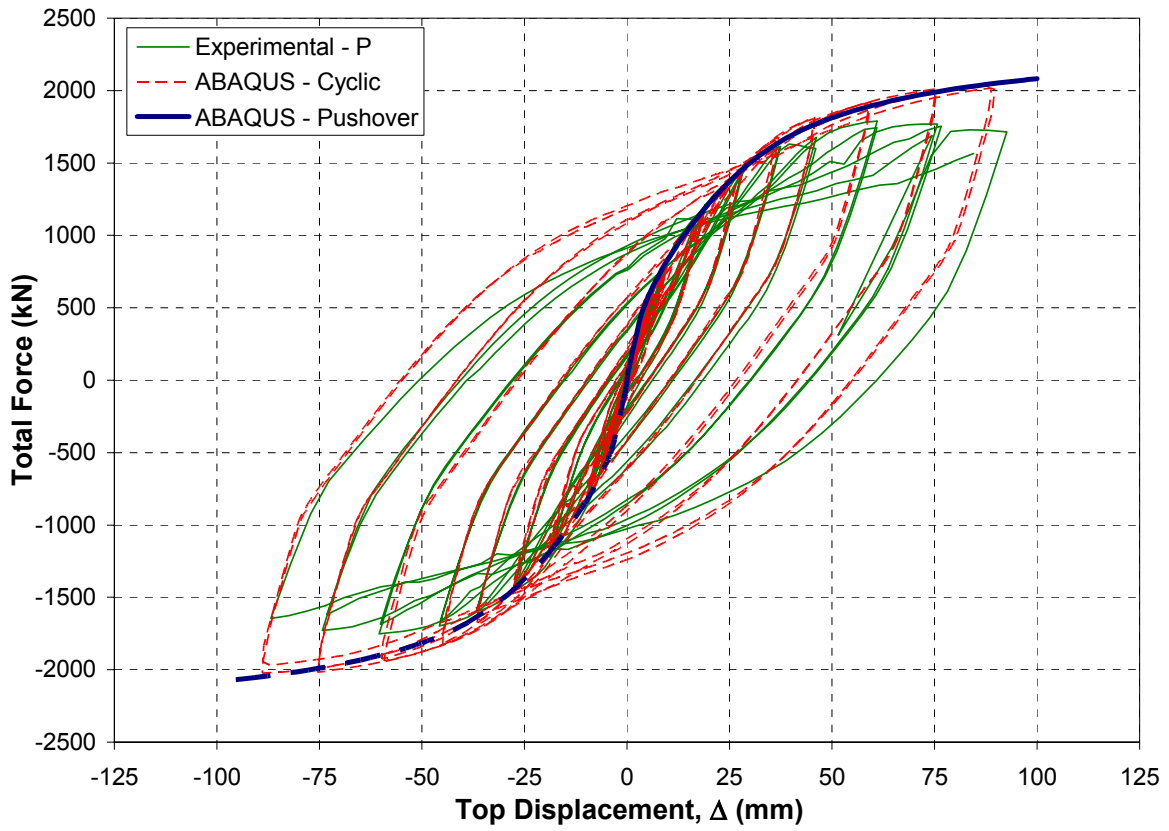
FIGURE 6-4 Specimen P Hysteresis with Experimental Results
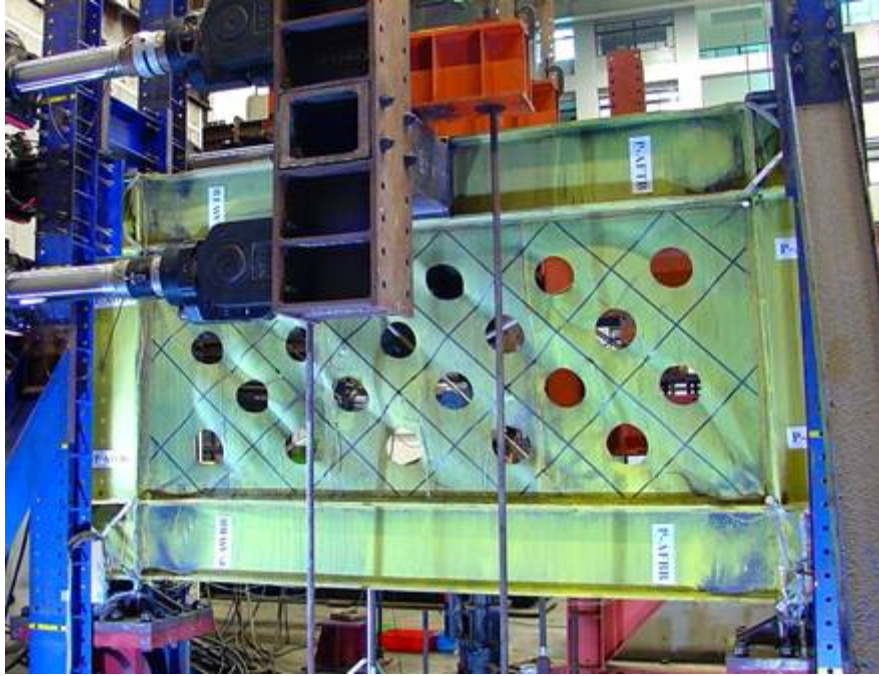
(a) Experimental

S, Mises
SNEG, (fraction = -1.0)
(Ave. Crit.: 75%)
+5.337e-01
+4.897e-01
+4.456e-01
+4.015e-01
+3.574e-01
+3.134e-01
+2.693e-01
+2.252e-01
+1.812e-01
+1.371e-01
+9.302e-02
+4.894e-02
+4.870e-03
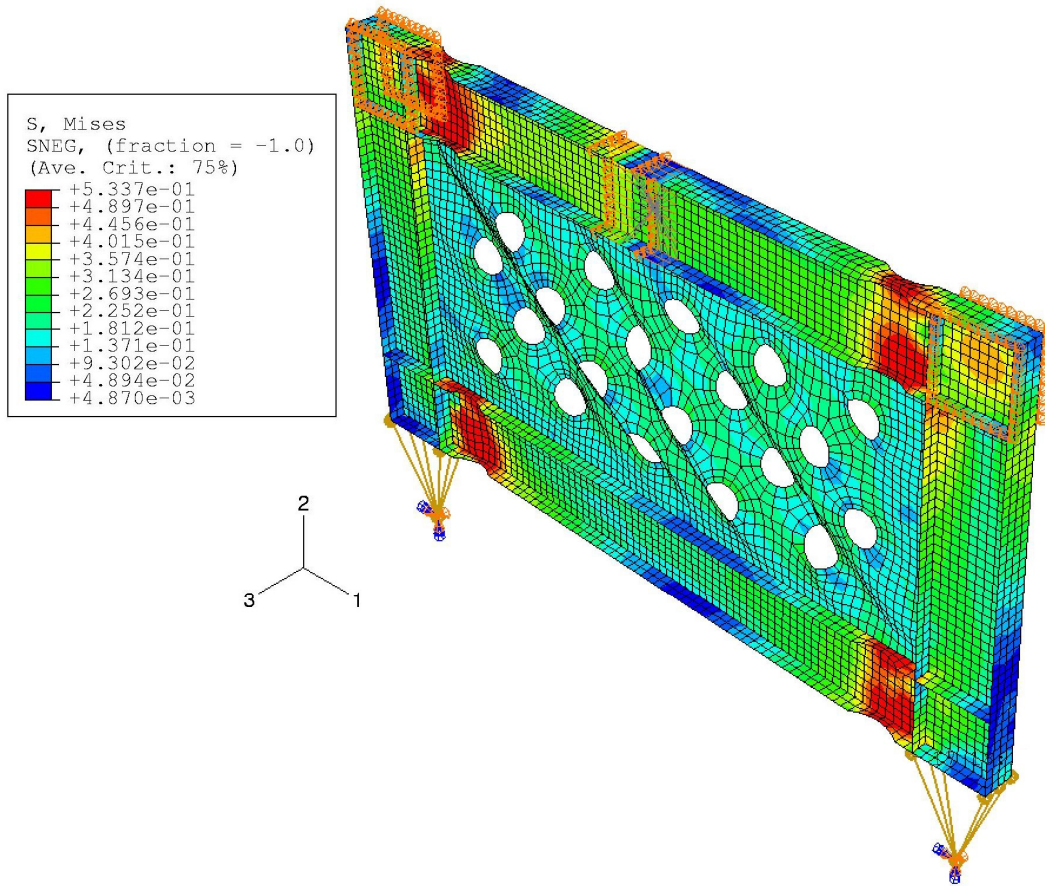
(b) Analytical: Deformed shape with von Mises yield surface contours (in 10^{-3}MPa)

FIGURE 6-5 Specimen P at 3% Drift

It is useful to investigate the accumulation of dissipated energy during the history of the analysis to aid in validating the analytical results. Figure 6-6 shows a plot of energy dissipated by various components in an analytical model of specimen P. These are defined as follows:

- ALLAE: "Artificial" strain energy associated with constraints used to remove singular modes, such as hourglass control discussed in section 6.2.3 above
- ALLPD: Energy dissipated by plastic deformation
- ALLSD: Energy dissipated by static stabilization discussed in section 6.2.8 above
- ALLSE: Recoverable strain energy
- ALLWK: External work
- ETOTAL: Total energy balance (=ALLAE + ALLPD + ALLSD + ALLSE − ALLWK)
- $\Sigma \delta W_{ext}$: External work done by the actuators during the experiment, calculated as a cumulative sum of the following:

$$\delta W_{ext.i} = \frac{\delta_i - \delta_{i-1}}{2} \cdot \left(F_{i-1} + F_i \right) \qquad (6\text{-}3)$$

where δ_i and F_i and δ_{i-1} and F_{i-1} are, for the step "i" and step "i-1", the top beam displacement, δ, and total actuator force, F, respectively.

These energy histories are plotted versus "Step Time" the artificial time defined for the analysis of this static problem. As noted above, the default values for control of hourglass modes in the S4R reduced-integration shell element were used; an appropriate selection verified by the minimal amount of energy, "ALLAE", dissipated by those constraints. The static stabilization energy, "ALLSD", increases gradually throughout the history of the analysis, but remains at a relatively small fraction of the plastic dissipation and external work. The recoverable strain energy oscillates between nearly zero and a peak value, which gradually increases in magnitude with increasing drift amplitudes. The energy dissipated by plastic deformations increases steadily throughout the history, as expected.

Ideally, the total energy balance, "ETOTAL", should equal zero. However, for nonlinear problems, the tolerance on the equilibrium equations that allows the analysis to continue will accumulate error over the course of the analysis, leading to a deviation from zero, as observed in

figure 6-6. This deficit is very small in comparison with the total work done by the system, and as such, is deemed acceptable.
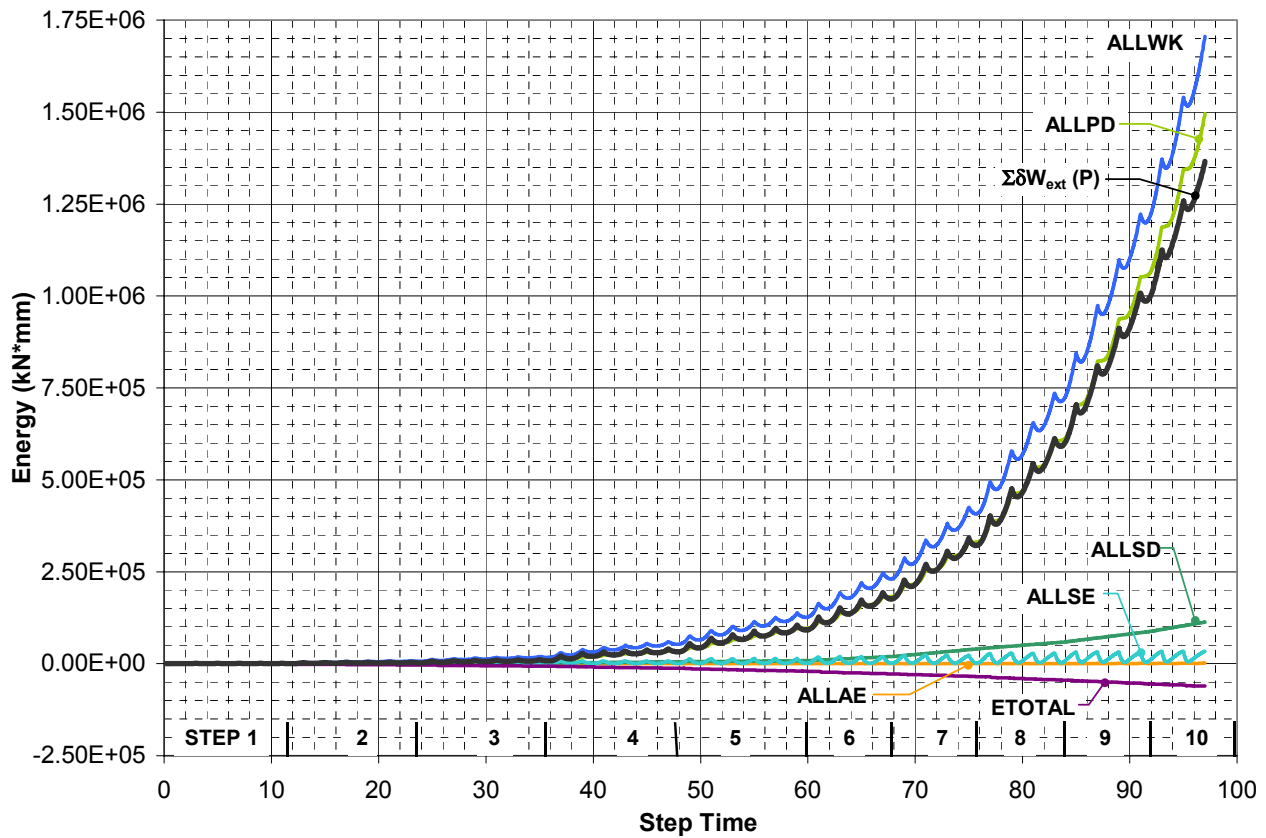
FIGURE 6-6 Specimen P Energy History with Experimental Results

6.4   Specimen CR

The FEM model mesh and the first three eigen-buckling modes for specimen CR are shown in figure 6-7. An amplitude of 2mm was assigned to the infill panel nodal displacements for each of these modes, which were superimposed as the initial deformed shape of the model prior to analysis. Although this was a larger initial imperfection as compared with specimen P, complete formation of the diagonal tension field did not occur until after the first cycle of the analysis. While the stiffness of the analytical model is larger than the test during this first cycle, after tension field formation, the system stiffness reduced, and the overall force versus top beam displacement hysteresis compared well with the experimental results, as shown in figure 6-8. The results of monotonic ABAQUS analyses, which follow the "backbone" of the cyclic analysis, are also shown in this figure.

237
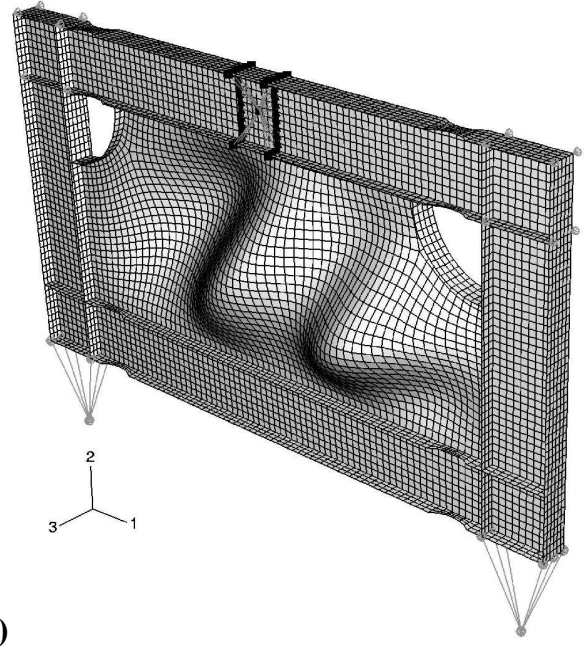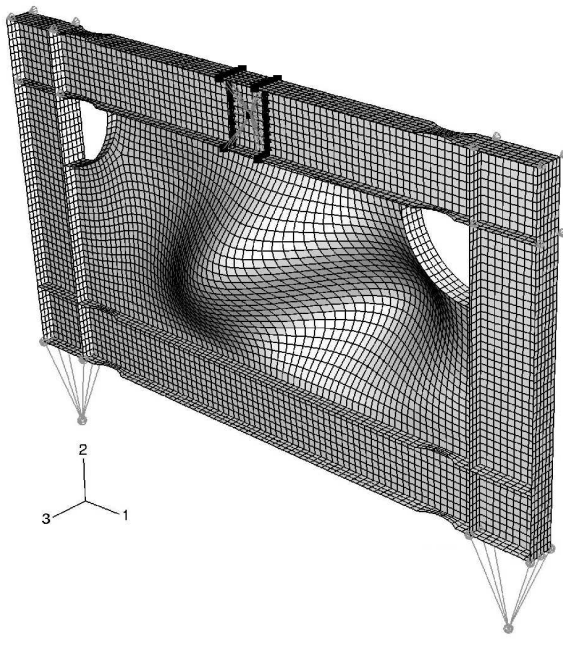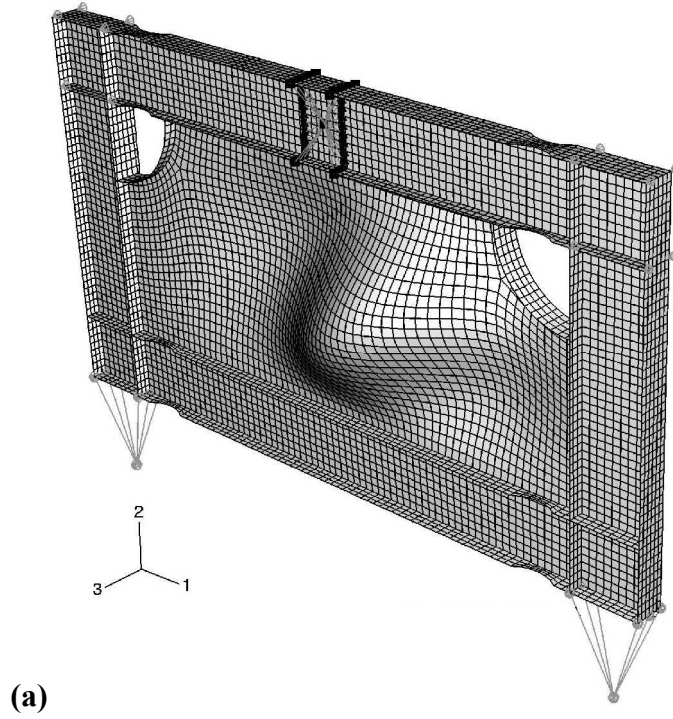
FIGURE 6-7 Specimen CR Finite Element Model Mesh with Panel Buckling Modes
(a) 1st Mode; (b) 2nd Mode; (c) 3rd Mode

238
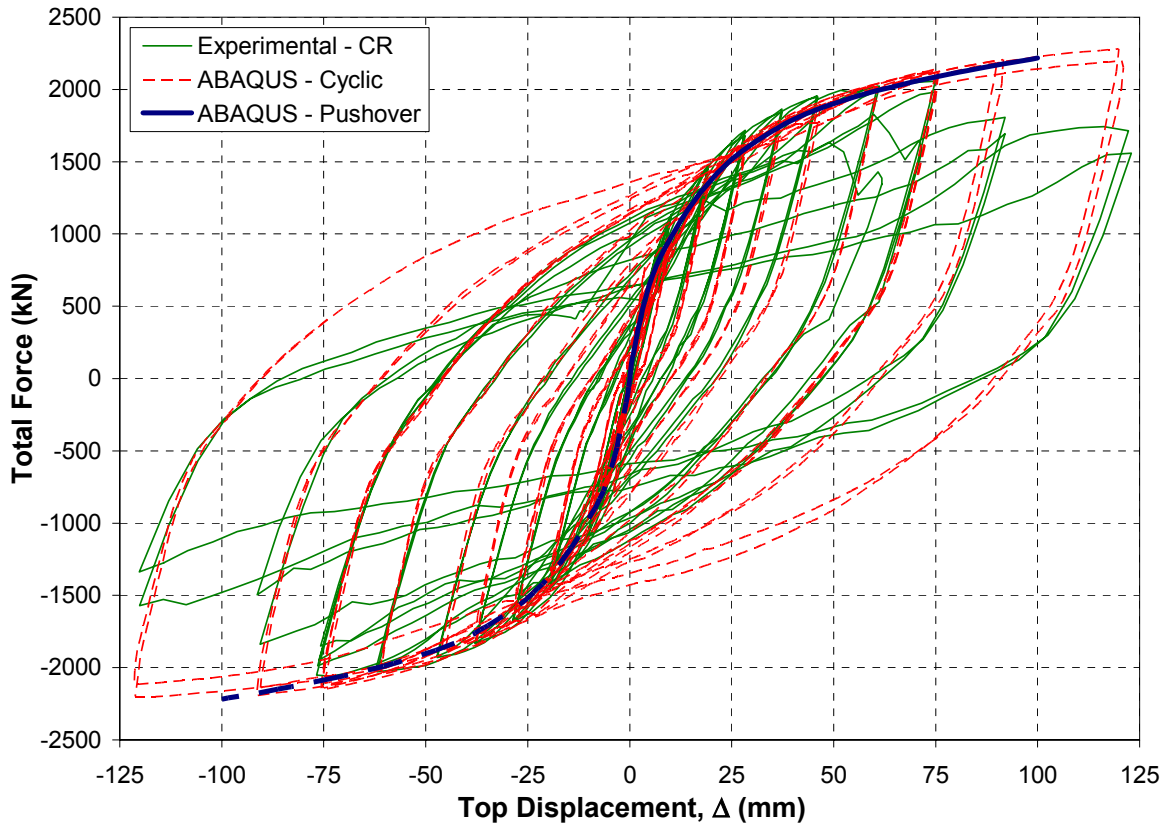
FIGURE 6-8 Specimen CR Hysteresis with Experimental Results

Although the strength is at times slightly underestimated by the analysis, good agreement between the experimental and cyclic analytical results is observed in figure 6-8, for cycles up through top displacements of amplitude of 76mm, analysis step 9 listed in Table 6-1. However, during the experiment and the second positive excursion at this displacement amplitude, a drop in the applied load occurred due to complications in the actuator control scheme, as described in section 5.3.3. During this cycle during testing, the flanges in the bottom beam RBS connections ruptured, further decreasing the load that could be resisted by the specimen. The FEM model was not developed to consider material fatigue life, however, and so this behavior is not captured in the analysis; instead a continued gradual strengthening of the system along the overall trend of the monotonic pushover analysis was observed. The magnitude of the von Mises yield surface contours, as shown in figure 6-9 (b) display the amount of yielding and strain hardening observed in the RBS locations. This figure is compared with figure 6-9 (a), which shows the specimen during testing at 3% drift.

239

(a) Experimental
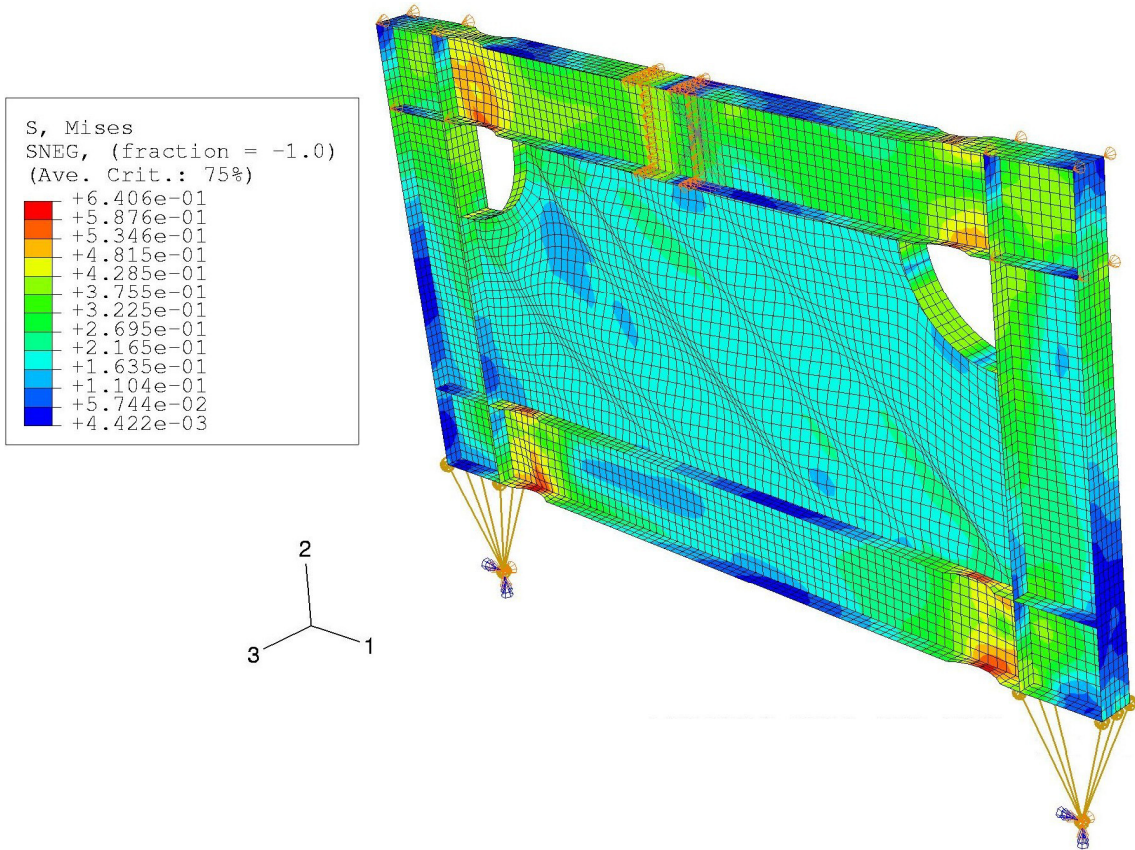
(b) Analytical: Deformed shape with von Mises yield surface stress contours (in 10^{-3}MPa)

FIGURE 6-9 Specimen CR at 3% Drift

Figure 6-10 shows the "step time" history of energy dissipated by various components in the analytical model of specimen CR, along with the external work done by the tested specimen. The decrease in specimen strength observed during testing as described above, at which the experimental and analytical hysteresis plots begin their largest deviation from one another, occurred at an approximate analytical "step time" of 88.5. Note that after this point on the energy history the calculated external work (experimental results) deviates from the previous trend of progressively increasing in value along with the analytical external work, and follows a path of increasing value that appears nearly linear, since the overall strength of the system is no longer increasing (in fact, it was decreasing).
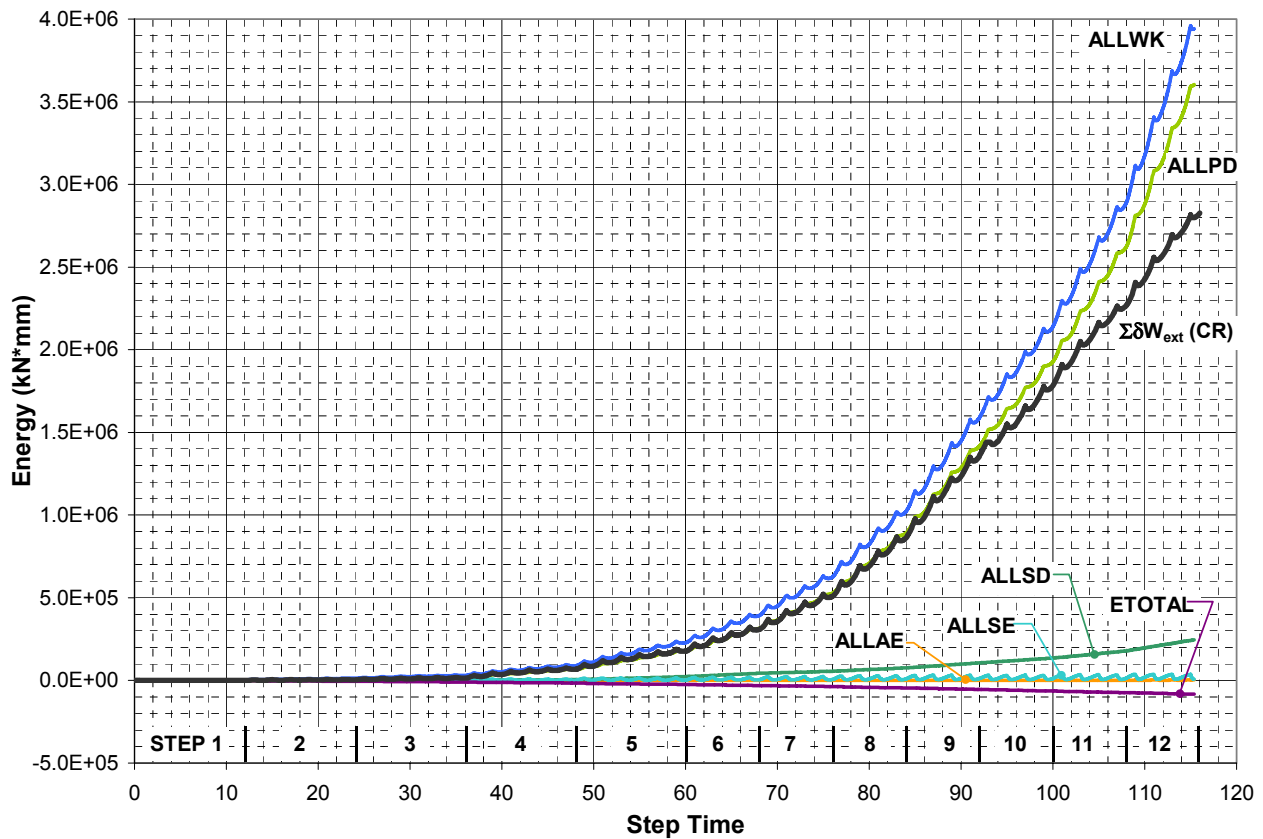
FIGURE 6-10 Specimen CR Energy History with Experimental Results

The artificial energy dissipated by hourglass control constraints is essentially zero, as in the model of specimen P discussed above, verifying that the shell behavior is not extremely modified by the control scheme. In addition, total energy balance and static stabilization energy, though increasing gradually throughout the history of the analysis, both remain at a very small fraction

of the plastic energy dissipation and external work done, and therefore confirm the acceptability
of this model to represent the behavior of the tested specimen.

6.5   Specimen S2

Figure 6-11 shows the FEM model mesh and the first eigen-buckling mode for specimen S2. An
amplitude of 1mm was assigned to the infill panel nodal displacements for this mode, and this
was superimposed as the initial deformed shape of the model prior to analysis. This amplitude
was large enough to initiate shear buckling and diagonal tension field formation in the infill
panel almost immediately after starting the analysis, as observed experimentally.
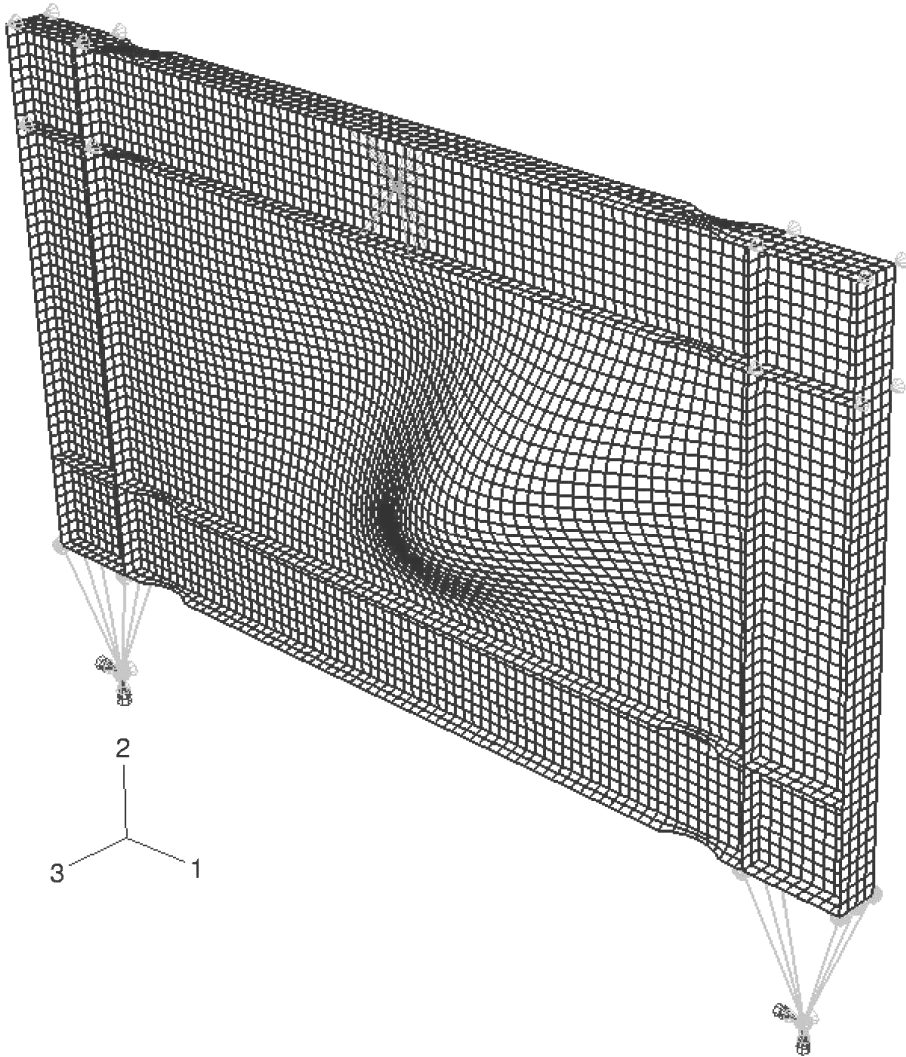
FIGURE 6-11 Specimen S2 Finite Element Model Mesh with 1st Panel Buckling Mode

The total force versus top beam displacement hysteresis compared very well with the experimental results, as shown in figure 6-12. The results of monotonic ABAQUS analyses, which follow the "backbone" of the cyclic analysis, are also shown in this figure. Excellent agreement in hysteretic behavior is observed until the final cycle, during which fracture occurred in the bottom flange of each bottom beam RBS connection and the strength of the specimen dropped by approximately 20% as described in section 5.3.4. Further comparison between experimental and analytical is shown in figure 6-13, which shows the specimen at 3% drift, and the FEM model displaced to the same drift, with von Mises yield surface contours.
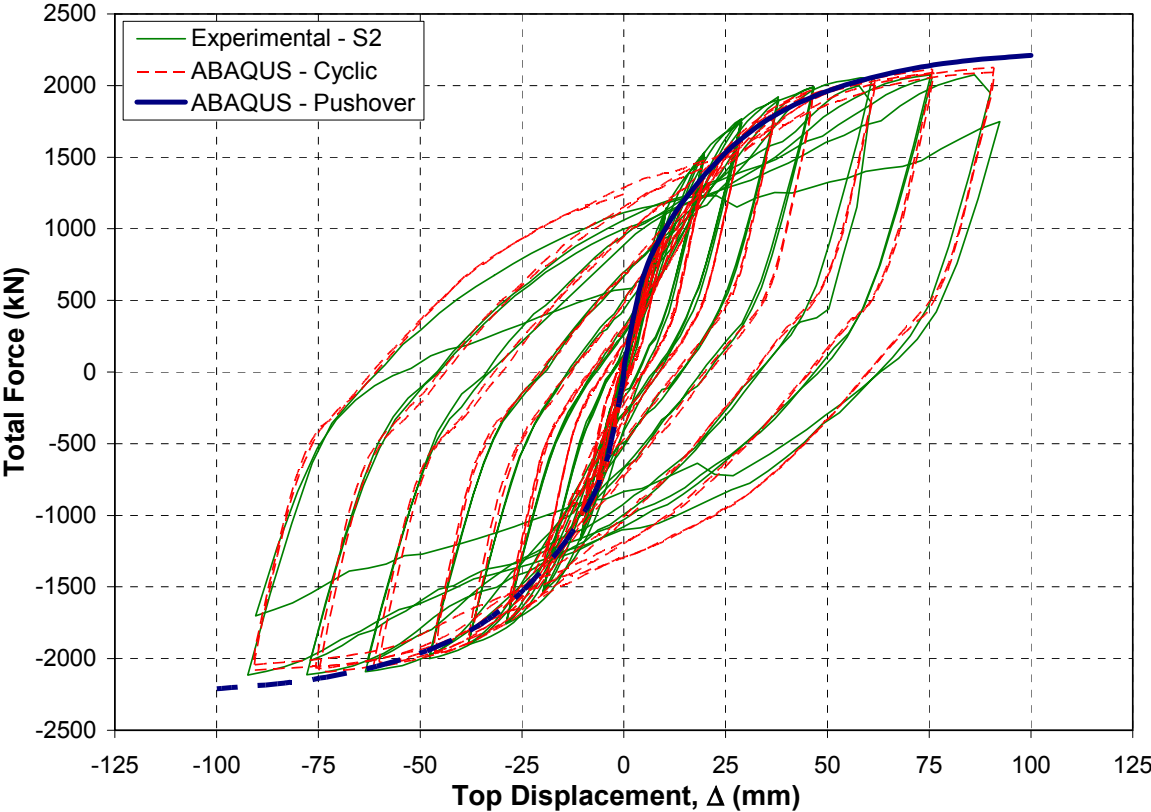
FIGURE 6-12 Specimen S2 Hysteresis with Experimental Results
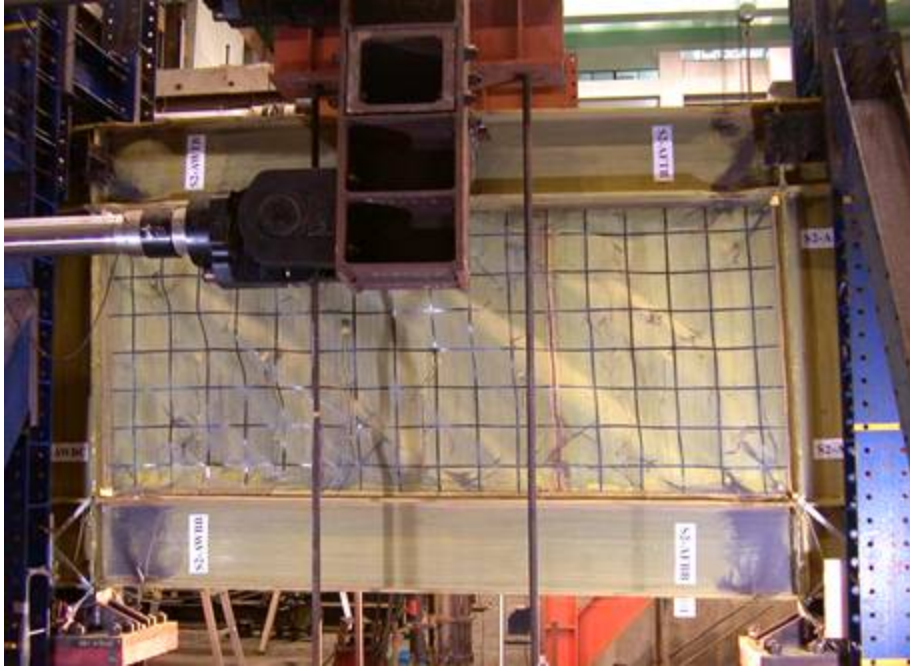
(a) Experimental


```
S, Mises
SNEG, (fraction = -1.0)
(Ave. Crit.: 75%)
    +5.317e-01
    +4.876e-01
    +4.435e-01
    +3.994e-01
    +3.554e-01
    +3.113e-01
    +2.672e-01
    +2.231e-01
    +1.790e-01
    +1.350e-01
    +9.087e-02
    +4.679e-02
    +2.710e-03
```
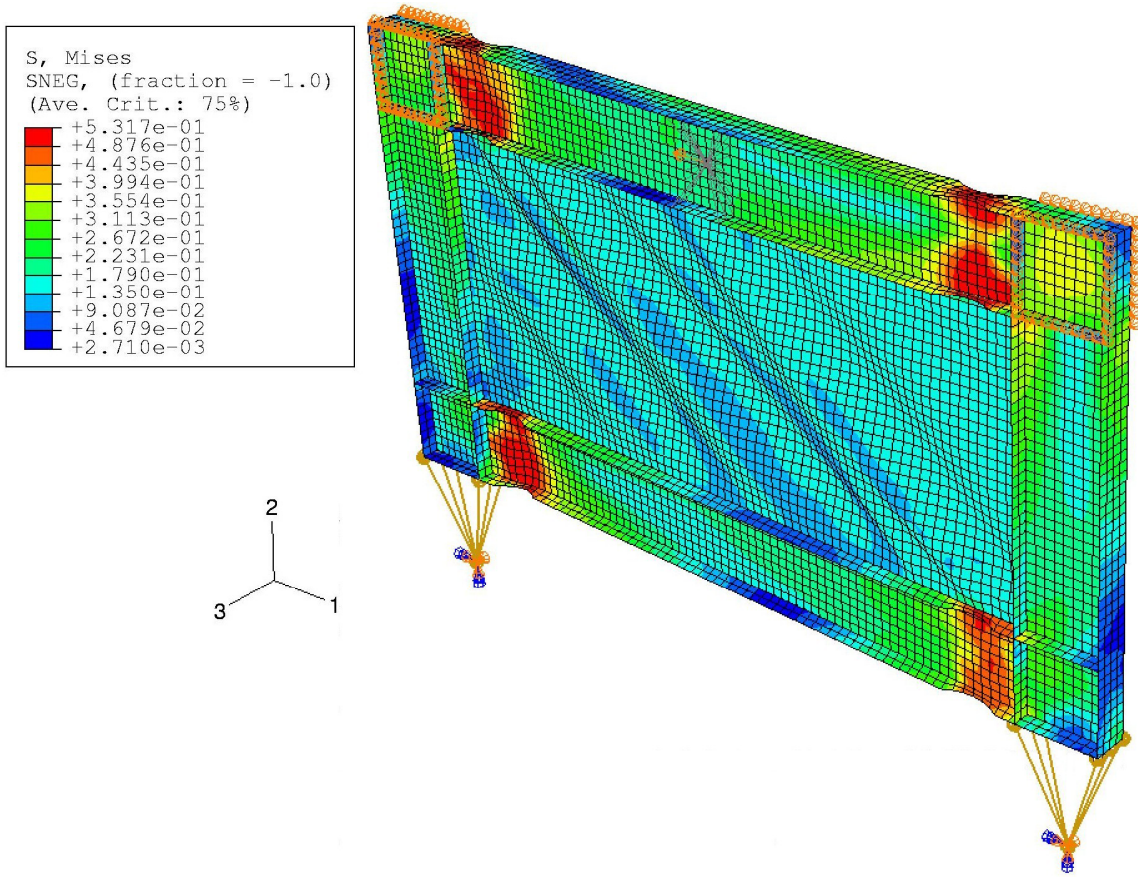
(b) Analytical: Deformed shape with von Mises yield surface contours (in 10^{-3}MPa)

FIGURE 6-13 Specimen S2 at 3% Drift

Figure 6-14 shows the "step time" history of energy dissipated by various components in the analytical model of specimen S2, along with the external work done by the tested specimen. The artificial energy dissipated by hourglass control constraints is effectively zero, as in the previously discussed models of specimens, verifying that the shell behavior is not adversely affected by this control scheme. In addition, total energy balance and static stabilization energy, though increasing gradually throughout the history of the analysis, confirm the acceptability of this model to represent the tested specimen, by both remaining at a very small fraction of the plastic energy dissipation and external work done.
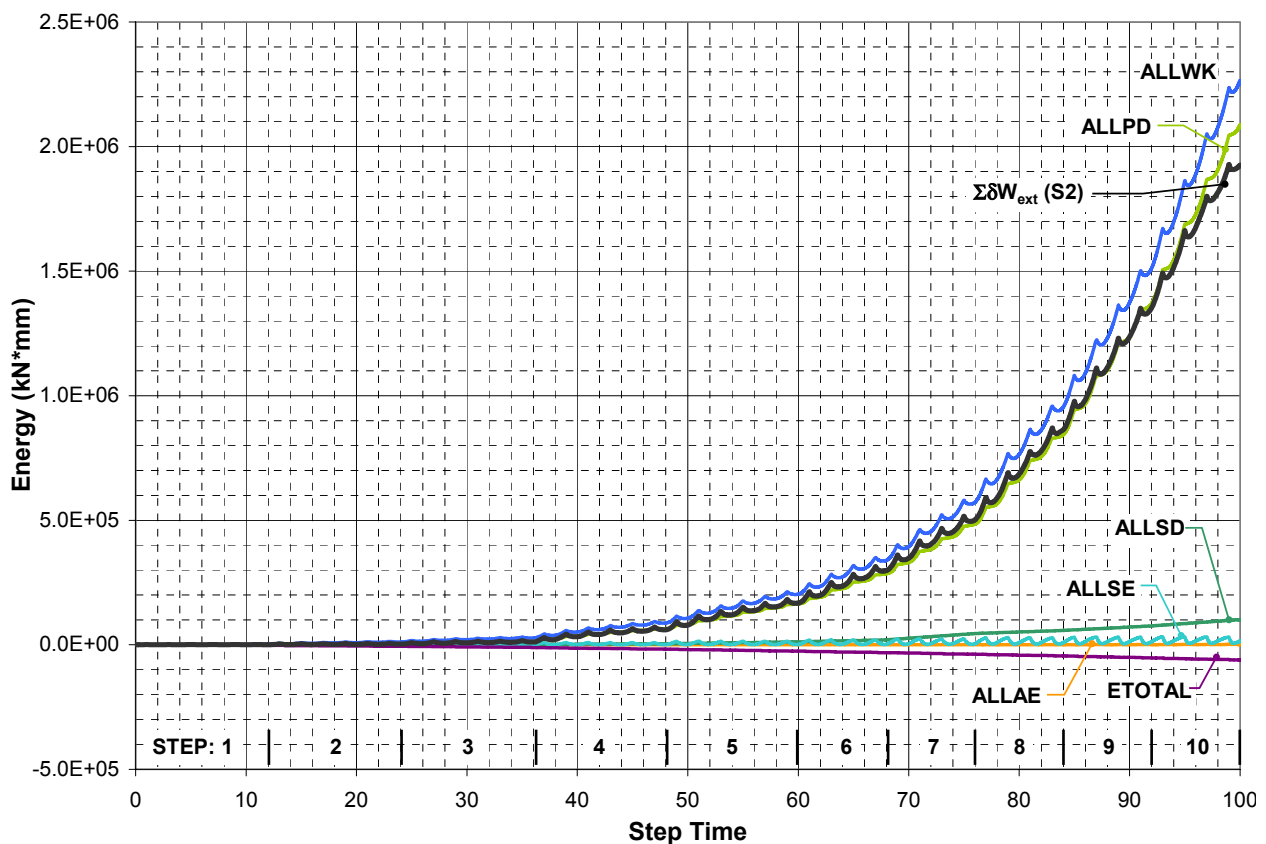
FIGURE 6-14 Specimen S2 Energy History with Experimental Results

6.6 Discussion of Results

Recall that in chapter 4, a pushover analysis in SAP2000 was used to estimate the stiffness and yield drift of the solid panel specimen to establish the displacement loading history. In addition, strength results of that analysis were verified against the combination of component strengths for both the boundary frame and the infill panel. Figure 6-15 shows the specimen S2 "backbone

curve" (the peaks of each cycle) of the experimental results as well as results from the SAP2000 analysis and from the strength equations presented in chapter 4 (previously shown in figure 4-6).
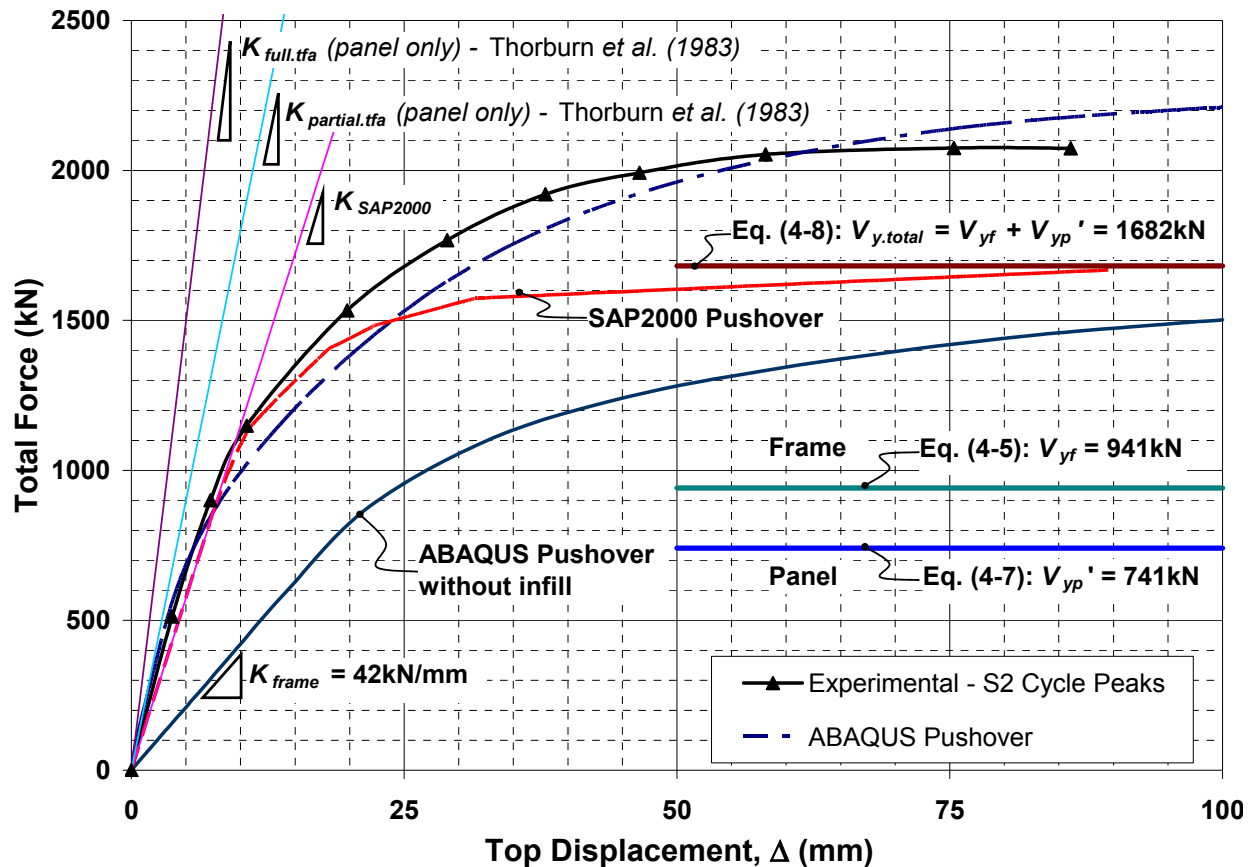
FIGURE 6-15 Specimen S2 backbone force versus top displacement compared with various analytical methods

Both the SAP strip model and the ABAQUS shell element model captured the elastic stiffness of the specimen well. The experimental stiffness was calculated as 135.5kN/mm while the SAP and ABAQUS models had elastic stiffnesses of 114.8 and 149.3kN/mm, respectively. These analytical values underestimated, in the case of SAP2000, and overestimated, in the case of ABAQUS, the experimental stiffness by -15.2% and +10.2%, respectively. The values for panel stiffness given by expressions provided by Thorburn *et al.* (1983) for full tension field action, $K_{full.tfa}$, and partial tension field action, $K_{partial.tfa}$, are plotted on figure 6-15 for comparison. These models assume boundary frame members that are rigid against bending, and therefore significantly overestimate the panel stiffness as compared with the case considered here.

The SAP and ABAQUS models both estimated the yield strength of the system fairly well, as shown in figure 6-15. However, as anticipated in the initial SAP analysis, the ultimate strength was underestimated by the SAP model, since that model did not account for cyclic strain hardening of the boundary frame elements contrary to the ABAQUS model. Figure 6-15 also shows ABAQUS pushover analysis results for an analysis performed on a model without the infill panel, to investigate the frame's contribution to total system strength. After a top displacement of about 50mm, the ABAQUS pushover curves are essentially parallel to one another, with the difference between the two providing an estimate of the panel strength, equal to 714kN at a top displacement of 76mm, or about 96% of the estimate provided by (4-7) that is shown in figure 6-15.

Table 6-2 lists the relative stiffness and strength of each specimen, K_{total} and $V_{y.total}$, respectively, in comparison to the values of solid panel specimen S2, $K_{total.S2}$ and $V_{y.total.S2}$. The contributions of the infill panel to stiffness (i.e. K_{panel}) and strength (i.e. V_{yp}) are determined by first calculating the bare frame stiffness, K_{frame} (=42kN/mm), and strength, V_{yf} (=1350kN at Δ_{top}=60mm, where the backbone curve of the experimental results meets the curve for the ABAQUS pushover analysis), from the ABAQUS bare frame analysis results shown in figure 6-15, and then subtracting those values from the observed values for each specimen. By this calculation, the perforated panel in Specimen P had a stiffness of 78.1% that of the solid panel. This agreed well with the values predicted by (3-36) and (3-46) of 86.3% and 82.2% respectively, which slightly underestimated the reduction in panel stiffness. Figure 6-16 shows a design curve similar to figure 3-18, but re-derived for the 1.6D edge distance of the as-built specimen P panel. The perforation ratio for the specimen was D/S_{diag} = 0.4714, which is noted and plotted with a bold line on the figure. The intersection of this line with the line for perforation rows N_r = 4 represents the estimated stiffness reduction (82.2%), as discussed above. Also plotted is the observed panel stiffness reduction 78.1%, which is in close agreement with the predicted value (note that the vertical axis in figure 6-16 is truncated, which makes the difference seem more significant visually).

The perforated panel strength was approximately 440kN, after the specimen P strength was adjusted for the frame contribution, exhibiting a 57.5% reduction in strength as compared with

that of the solid panel (765kN). The strength reduction was 52.9% for the perforated panel as predicted by (3-33), with "S_{diag}" substituted for "d" of that expression.

TABLE 6-2 Comparison of Peak Results with Simplified Perforated Panel Models

Spec	$K_{total}/K_{total.S2}$	$V_{y.total}/V_{y.total.S2}$	Observed K_{panel} [1]		Predicted K_{perf}/K_{panel}		$V_{yp.perf}/V_{yp}$ [2]	
	(%)	(%)	(kN/mm)	(%$K_{panel.S2}$)	(3-36) (%)	(3-46) (%)	Observed (%$V_{yp.S2}$)	Predicted (3-33)
P	88.5	84.6	73.0	78.1	86.3	82.2	57.5	52.9
CR	103.3	96.9	98.0	104.8	-	-	-	-
S2	-	-	93.5	-	-	-	-	-

1: Assumes $K_{frame} \approx 42$kN/mm as calculated from ABAQUS bare frame analysis shown on figure 6-15

2: Assumes $V_{yf} \approx 1350$kN as calculated from ABAQUS bare frame analysis at $\Delta_{top} \approx 60$mm
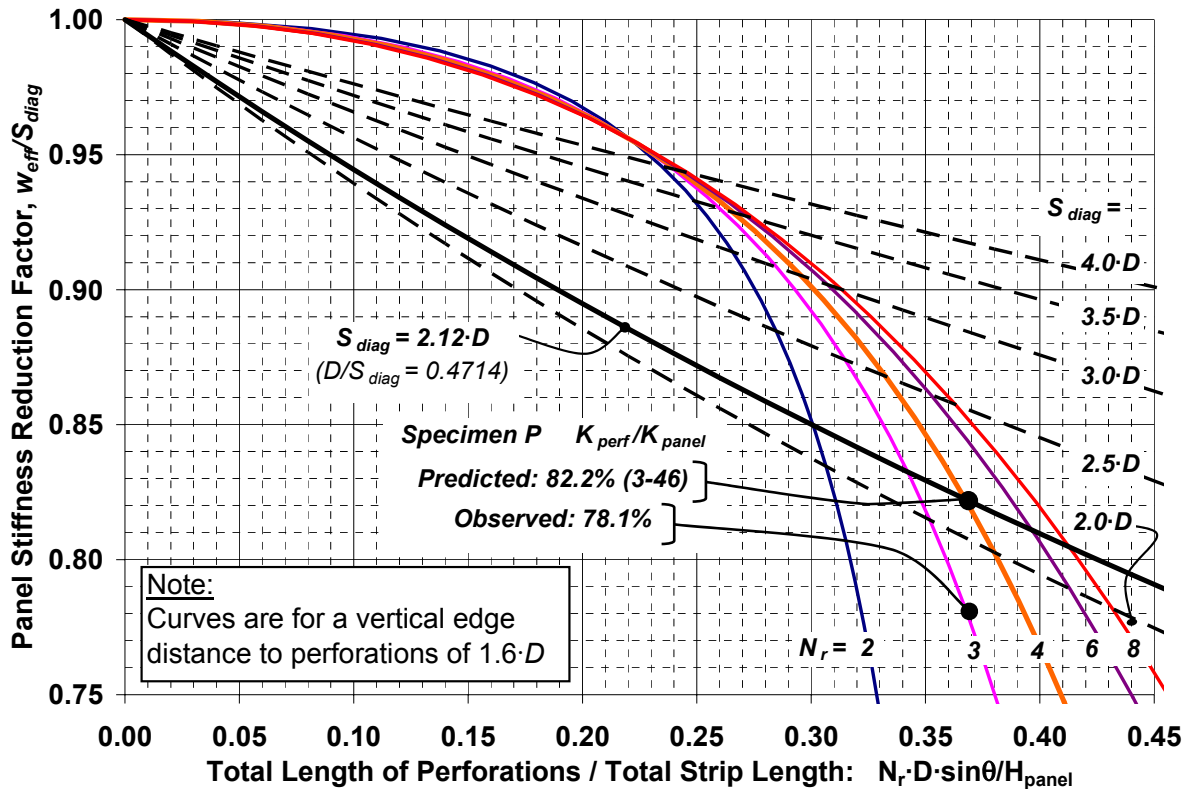
FIGURE 6-16 Predicted vs. Observed Perforated Panel Stiffness Reductions

Note that the stiffness (both total and panel-only) and total strength of specimen CR displayed less than 5% difference from the values for specimen S2. This is satisfactory given that the design intent was that the strength and stiffness of a specimen with corner cut-outs designed as considered here would be effectively identical to those of the corresponding solid panel.

248

6.7 Summary

The finite element analysis software package ABAQUS/Standard was used to perform non-linear quasi-static cyclic analysis of models representing the tested specimens described in the previous two chapters. Good agreement in overall behavior between the test results and the analyses was observed, suggesting that the modeling assumptions utilized in this case are appropriate for modeling other SPSW problems. Results and assumptions used in model development were verified by observation of the history of various sources of energy dissipation.

Finally, the results were compared with the simpler strip models and manual calculations presented in chapter 4, which were used in the design of the specimens and development of the experimental displacement loading history. It is observed that simpler strip models also provide a reasonable estimate of displacement and strength at initial yield. Very good agreement with observed experimental results was given by the expressions estimating the relative strength and stiffness reduction for perforated panels as compared to a solid panel.

SECTION 7

ADDITIONAL OBSERVATIONS AND DESIGN CONSIDERATIONS FOR ENSURING DUCTILE BEHAVIOR OF STEEL PLATE SHEAR WALL SYSTEMS

7.1 General

The preceding chapters presented design concepts and an experimental study for SPSWs, including perforated SPSWs as well as the use of RBS connections in the anchor beams of SPSWs. This chapter presents additional considerations for the design of such systems to ensure reliable ductile behavior.

7.2 Behavior of Thin Perforated Plates Subjected to Shear Loading

7.2.1 General

Chapter 3 introduced a method for selecting a perforation layout for perforated SPSW panels based on the elastic stiffness reduction of a solid infill panel. The system strength reduction, as compared with a solid panel, was determined from a simple equation presented by others (Roberts and Sabouri-Ghomi 1992). Although this equation was developed for a single hole in a panel, Brady and Drucker (1955) conducted analytical and experimental work to determine the ultimate strength of a tension member with various configurations of multiple holes and obtained identical results (i.e. based on comparing the net to gross widths).

While the above work suggests that calculation of perforated panel strength (or strength reduction from the solid panel) can be consistent with accepted limit analysis of tension members, additional design constraints should be considered to ensure ductile behavior of perforated panels, based on the ultimate strength of the infill panel material (in relation to the yield strength), the elongation capacity of the material, and the local effects of perforation layout on the stress and strain concentrations. The following sections discuss some of these factors and utilize results from research on the strength of tension members with holes, supplemented by a finite element analysis study, to suggest methods for ductile design of perforated SPSWs.

251

7.2.2 Specimen P Models

7.2.2.1 LYS165 Infill

Specimen P was fabricated using an infill panel with uniaxial stress versus strain behavior as shown in figure 4-8. As tested, this material had an elongation capacity of approximately 45%, greater than twice the minimum elongation required by the A36 and A572 material specifications. Strain gages were not placed close to perforation edges at locations of highest strains on this panel. However, the uniaxial gages between holes, PU1 to PU4 (as well as PU5 to PU8 covering the width of a typical strip in between perforations), and the three strain rosettes PTM2 to PTM4, recorded specimen infill panel strains that correlated well with those of the ABAQUS model at their corresponding locations, which are shown schematically in figure 4-24.

The ABAQUS model developed in the previous chapter was verified versus global behavior of the specimen and internal energy calculations. Nonetheless, an additional model with finer mesh, shown in figure 7-1, was used to investigate the localized distribution of panel stress and strain between perforations. This refined model was subjected to a monotonic pushover loading, producing maximum computed infill strains of 13% (approximately one third of the maximum elongation of the tension tests) at locations adjacent to perforations when the drift reached the maximum value measured during testing.
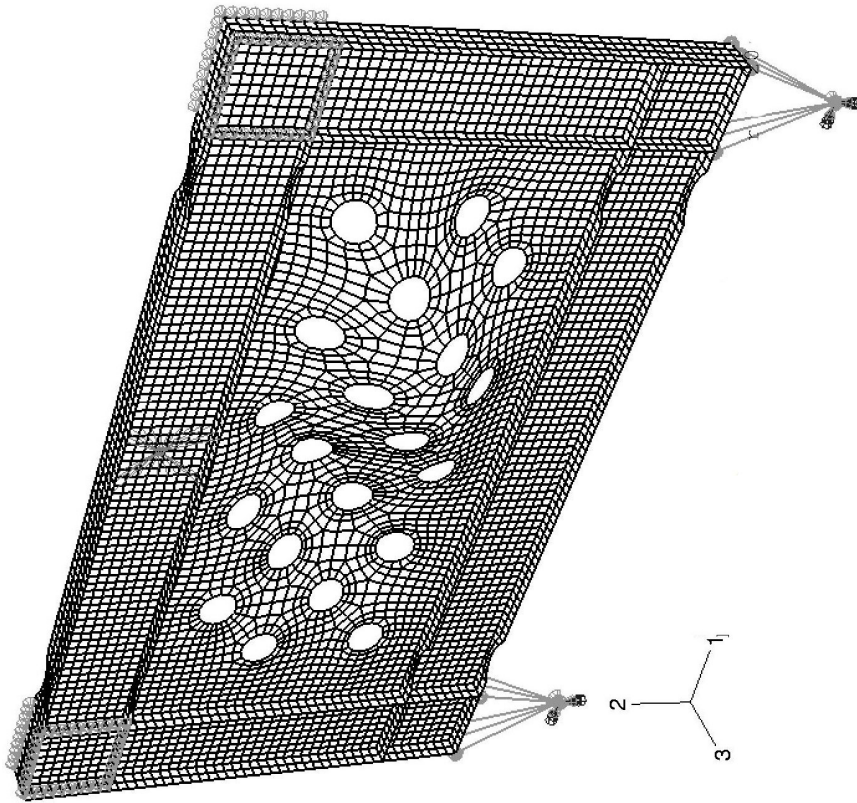
(a)
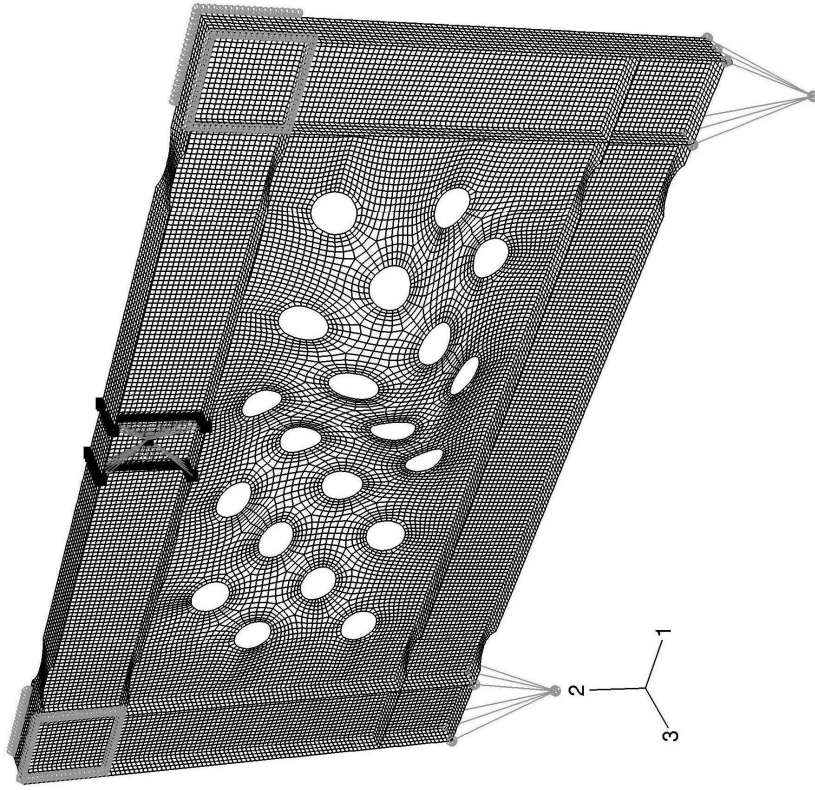
(b)

FIGURE 7-1 Specimen P Finite Element Model Mesh with 1st Panel Buckling Mode
(a) Original Mesh for Chapter 6 System Behavior Investigation; (b) Refined Mesh for Local Panel Behavior Investigation

7.2.2.2 A572 Infill Panel

The refined model of Specimen P was re-analyzed using a different infill panel material to examine the effect of material properties on maximum strains adjacent to perforations. Infill panel properties were assigned, as in section 6.2.6, using a cyclic stabilized backbone curve for A572 Grade 50 steel ("Steel A" from Kaufmann *et al*. 2001). The panel thickness was modified from the 2.6mm tested, to 1.5mm, such that the ultimate strength per unit panel width, $F_u \cdot t$, was approximately equal to the tested LYS165 panel. This thickness is 58% of the tested LYS165 panel, and 30% of the typical minimum available thickness for A572 plate: 5mm (0.1875in).

A monotonic pushover displacement loading was applied to the revised model, as was done for the models presented in the previous chapter, to investigate the strain concentrations around panel perforations. Figure 7-2 shows the force versus displacement relationship obtained from this analysis, compared with the specimen P experimental hysteresis and analysis results discussed in section 6.3. Maximum principal in-plane strains adjacent to the perforations reached 10% at a frame drift of 1.23%, equivalent to 49% of the drift reached by the LYS infill panel specimen when its maximum strain reached the same value of 10%. Pushed further, the higher strength infill panel reached a local maximum strain of 20%, at 1.78% drift, or 39% of the drift in the LYS panel reached at a similar strain of 20%. Note that 20% is roughly equal to the minimum elongation required by the ASTM A572 specification.

The tested perforated infill panel specimen exhibited very ductile behavior but part of that good behavior is arguably attributable to the panel low yield strength steel, LYS165. This material exhibits an elongation at failure in tension coupons equal to twice the specified minimum elongation for A36, A572, and A992 steels (the material grades commonly specified in North American construction projects). Guidelines to ensure adequate ductility of perforated infill panels using A36 ($F_y = 36$ksi (248MPa)) and A572 ($F_y = 50$ksi (345MPa)) steel grades are needed for engineers to consider this perforated panel structural system in North American applications.

Design limits for SPSWs with perforated plates based on minimum specified tensile properties (i.e. per the relevant ASTM material specification) for yield and ultimate strength, as well as minimum elongation, would be practical for this purpose. The sections below successively

254

discuss some relevant research towards this goal, use finite element models of typical perforated strips (i.e. figure 3-16) to investigate panel strain behavior for a range of hole-geometries, and finally, make some recommendations for limiting perforation sizes to facilitate ductile response.
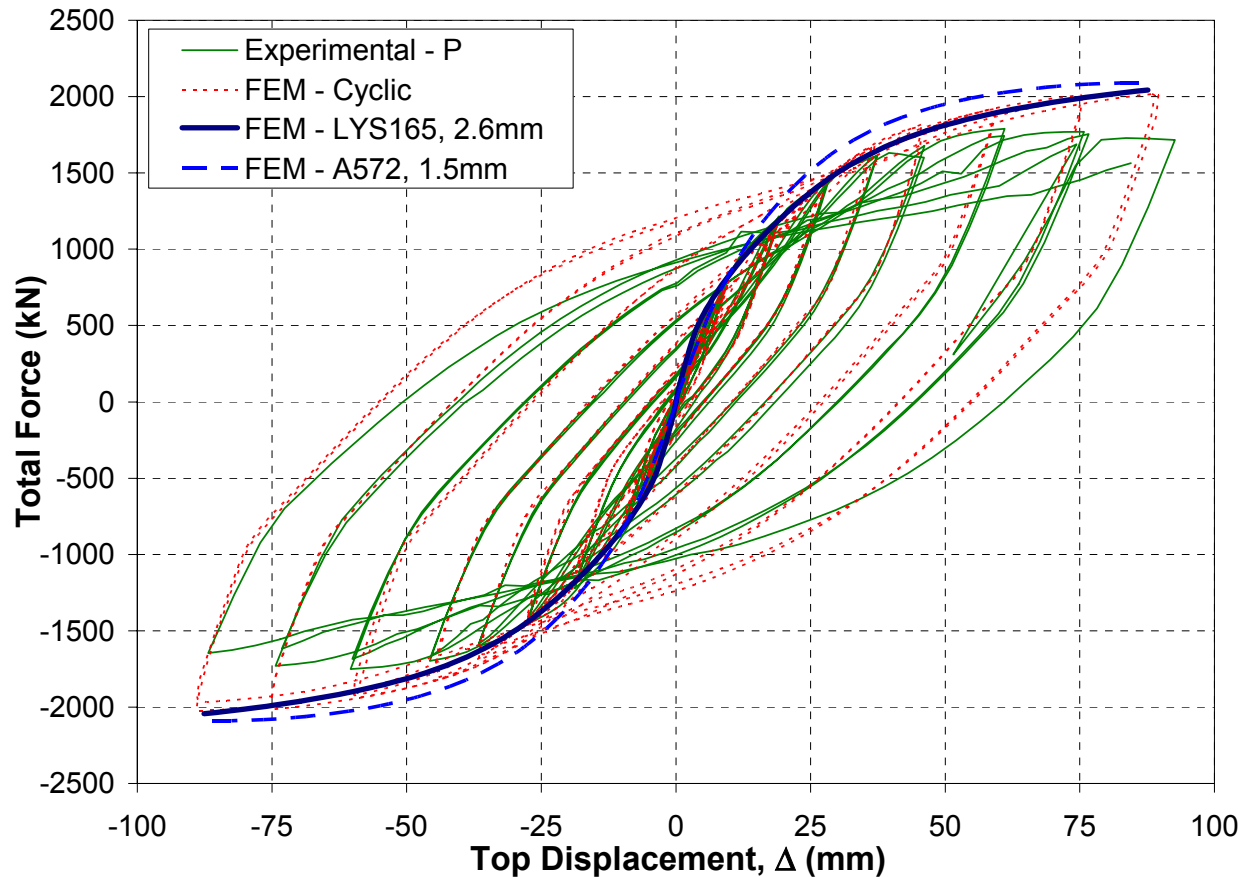
FIGURE 7-2 Specimen P Experimental Results with ABAQUS (FEM) Results for: Cyclic Analysis of Specimen P model (LYS165 Infill); and Pushover Analysis of LYS165 and A572 Grade 50 Infill Models

7.2.3 Selected Relevant Research on Strength of Perforated Steel

Codified equations have long existed for the strength of bolted plates in tension and similar concepts could be used for the design of perforated plates, providing an element of familiarity for structural engineers. In addition, one recent study on groups of holes is helpful in the current context and is reviewed here.

Dexter *et al.* (2002) studied the strength and ductility performance of tension members and girder tension flanges having holes and fabricated from high performance steel such as HPS70W. The study was conducted to determine the appropriateness of the AASHTO specifications for the use of that material in bolted bridge girder flanges.

Dexter *et al.* experimentally and analytically investigated tension strength of coupons with holes of various diameters spanning a range of net-to-gross area ratios. In addition, the study included other material strengths, such as HPS100W (F_y = 690MPa) and A709 Grade 50 (F_y = 416MPa), to provide a range of initial yield strengths and yield to tensile strength ratio (F_y/F_u).

Typical yielding patterns observed are shown in figures 7-3 (a) and 7-3 (b), for HPS70W specimens having a single hole and 12-holes and having A_n/A_g values of 0.806 and 0.735, and net to gross area strength ratios, A_nF_u/A_gF_y, of 0.90 and 0.82, respectively. In addition, figure 7-3 (c) shows a single hole specimen with area and strength ratios of 0.964 and 1.10, respectively. In all three specimens, the yielding region initiated adjacent to the hole, and then expanded within radial lines at approximate 45°. In the third specimen, with strength ratio greater than unity, the strain hardening within this yielding wedge allowed the gross section to yield as well, gradually along the entire gauge length of the specimen.

On the basis of their research results, Dexter *et al.* recommended that the full plastic moment capacity of a section may be considered provided the following condition is met:

$$F_u \cdot A_{fn} \ge Y_t \cdot F_y \cdot A_{fg}$$
(7-1)

where A_{fg} is the gross flange area; A_{fn} is the net flange area; F_u is the specified minimum tensile strength; F_y is the specified minimum yield strength; and Y_t is equal to 1.0 for $F_y/F_u \le 0.8$, or 1.1 otherwise.

If this equation is satisfied, under increasing tensile force, after yielding in the net section, subsequent strain hardening will allow yielding to occur in the gross section, distributing inelastic action throughout the member to provide ductile behavior. Alternatively, if (7-1) is not satisfied, then the gross section may remain elastic under increasing load, and inelastic action would be localized to the region adjacent to the perforation, and failure would occur before the development of adequate total member elongation.

256

(c) HPS70W-1.1-H Specimen
($A_nF_u/A_gF_y = 1.10$)

b) HPS70W-12h Specimen
($A_nF_u/A_gF_y = 0.82$)

(a) HPS70W-0.9-L Specimen
($A_nF_u/A_gF_y = 0.90$)

FIGURE 7-3 Final State of Various Tensile Specimens Tested by Dexter *et al.* (2002)

257

The thin SPSW perforated panels studied in this report exhibit behavior analogous to the tension strips with holes investigated by Dexter *et al*., particularly if one focuses on behavior of an individual strip of a SPSW shown in figure 3-16 and observed to develop yielding during testing as shown in chapter 5. For simplicity, as the infill panel buckles one may consider the plate to be a series of strips oriented along a diagonal tension field flowing between the panel perforations. Based on this observation a finite element study was performed using models of perforated strips under tension, which were also compared with results of specimen P analyses, and parametric variations based on Specimen P, as described in the next section. This does not perfectly replicate the infill plate continuity, but allows one to rapidly obtain some additional perspective on behavior next to the perforations using refined meshes and focusing on local behavior.

7.2.4 Finite Element Study

7.2.4.1 Typical Perforated Strips

Finite element analyses were performed to examine the elongation behavior of typical perforated diagonal strips and the spread of yielding throughout the gross and net sections. Standard strip dimensions of L equal to 2000mm, S_{diag} equal to 400mm, N_r equal to 4, and t equal to 5mm were selected for this purpose/exercise. The length and diagonal spacing were selected to be similar to that of the tested specimen discussed in previous chapters; whereas the strip thickness of 5mm (approx. 0.1875in.) was set equal to the typical minimum available thickness for the A36 and A572 materials. The perforation diameter, D, varied from 0mm (no hole) to 200mm, for a range of perforation ratios, D/S_{diag}, from 0 to 0.5. Idealized tri-linear stress-strain models were used to represent the behavior of A36 and A572 Gr. 50 steel, as shown in figure 7-4.

The typical strip was analyzed in ABAQUS/Standard, in the configuration of a "quadrant model" to represent the typical strip (and to reduce computational time from a full-strip model), as shown schematically in figure 7-5. The model was discretized into S4 general purpose shell elements. The DOF perpendicular to transverse and longitudinal centerlines was constrained against movement along those lines.
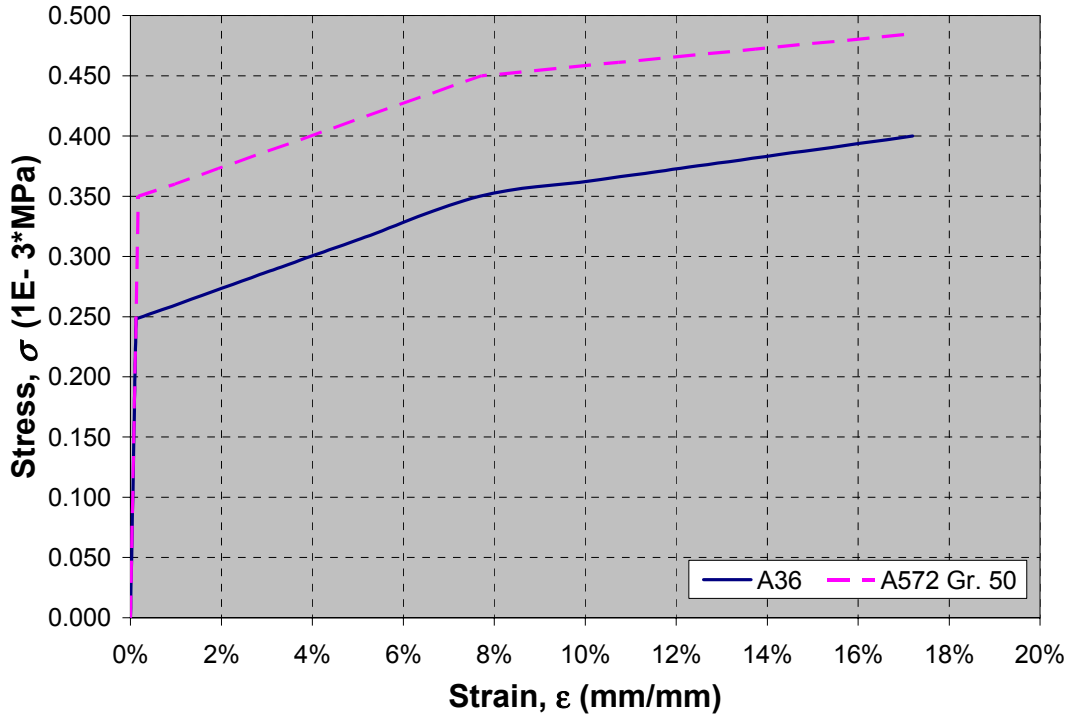
FIGURE 7-4 Idealized Stress-Strain Models for A36 and A572 Steels

(a)

Geometry of Perforated Strip
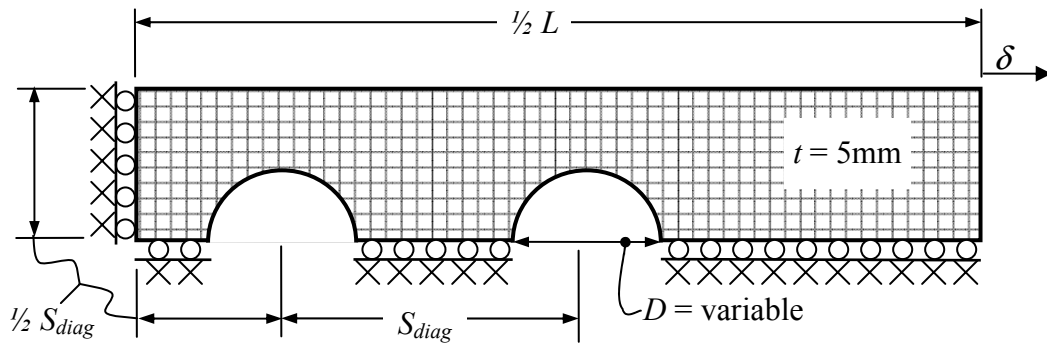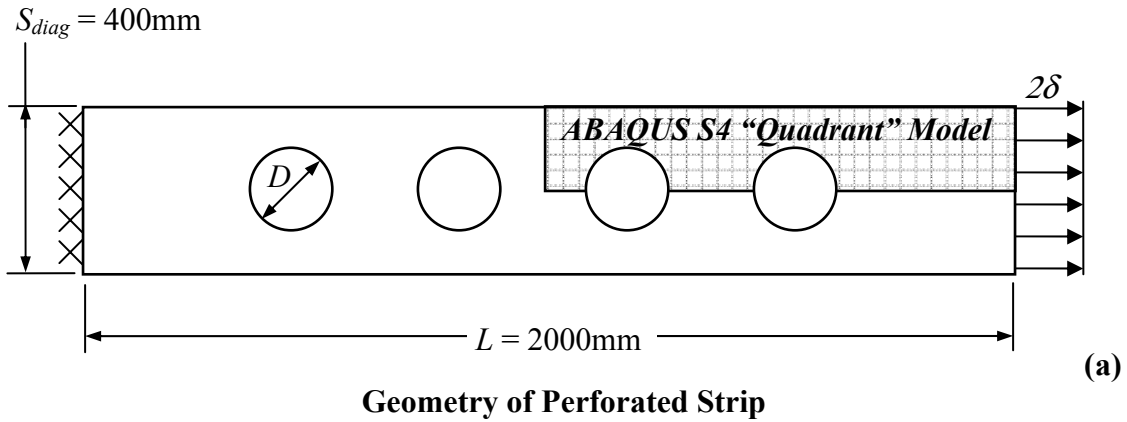
(b) Schematic Representation of "Quadrant" Model (*not actual mesh*)

FIGURE 7-5 Analyzed Typical Strip Model Properties

259

Loading was applied to strip models by imposing an increasing displacement, δ, on the entire width of the free edge to produce tension in the strip, until reaching a total uniform strip elongation, ε_{un}, of five percent. The maximum local strain adjacent to the perforation was monitored during the analysis. Total strip elongation was noted when the local maximum principal strain reached values of 1, 10, 15, and 20%, and plotted versus the perforation ratio, D/S_{diag}, and section net fracture-to-gross yield, $A_n \cdot F_u / A_g \cdot F_y$, as shown by the solid lines in figures 7-6 and 7-7 for the idealized A36 and A572 materials, respectively. Typical plate deformations, stress contours, and strain contours are shown in figures 7-8 and 7-9 for ABAQUS quadrant models with 75mm and 150mm perforation diameters, respectively, at 20% strain. The distribution of in-plane principal stress and strain contours shown in these figures compares with the yielding observed by Dexter *et al.* in the test results shown in figure 7-3, initiating at the perforation edge and radiating at an approximate 45° angles with respect to the tensile force. Results from the series of strip analyses are discussed in section 7.2.4.3.
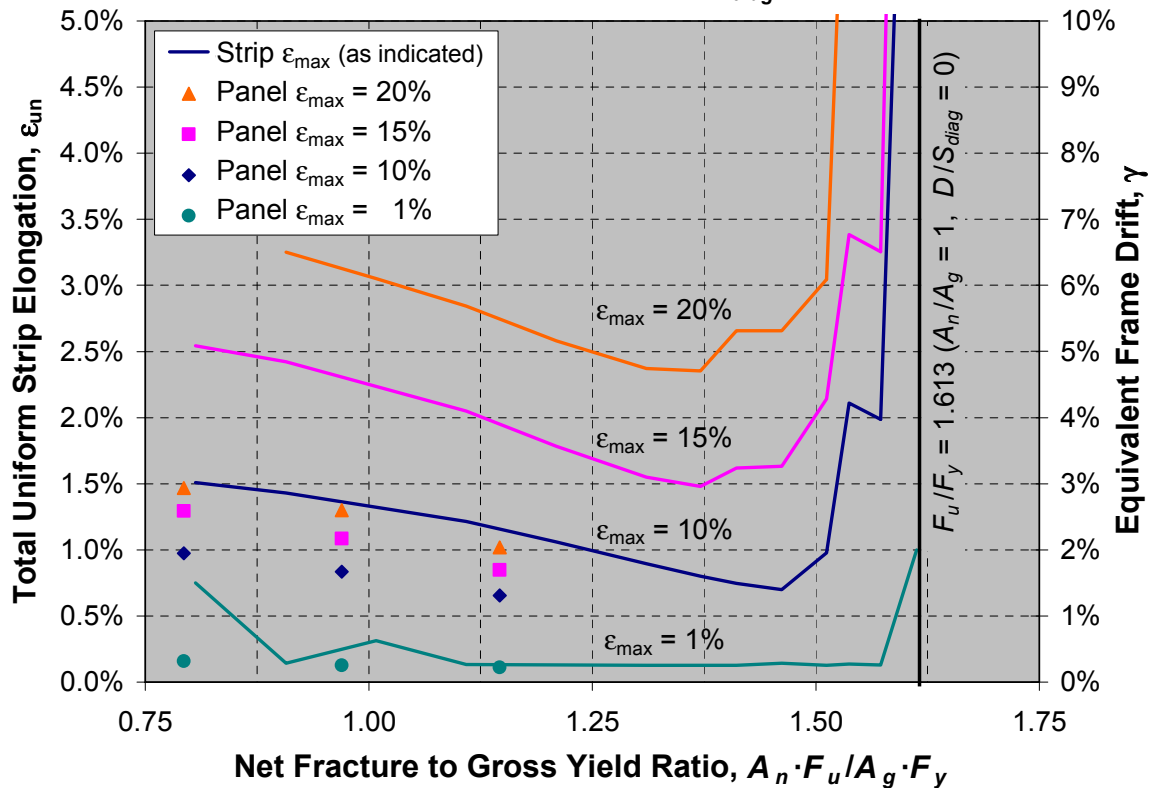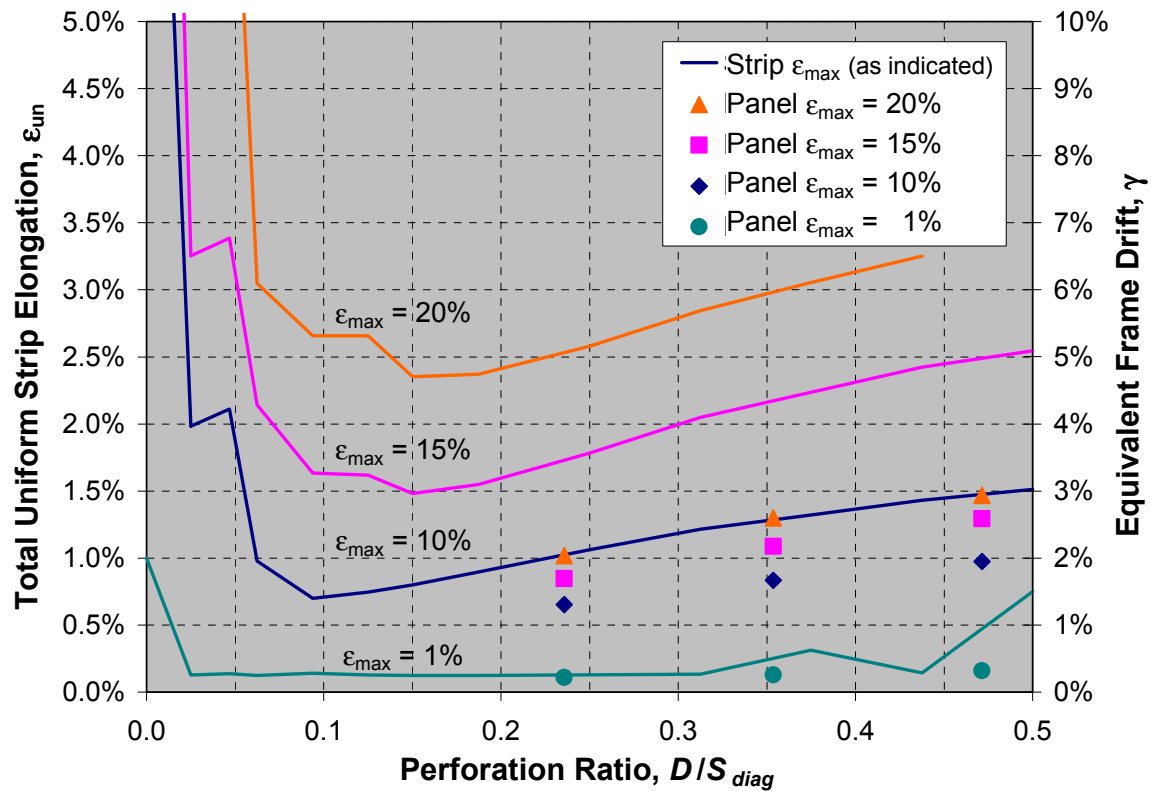
**FIGURE 7-6 Uniform Distributed Strip Axial Strain, ε_{un} versus
(a) Perforation Spacing Ratio, D/S_{diag}; (b) Net Fracture to Gross Yield, $A_n F_u/A_g F_y$
Idealized A36 Steel**

261
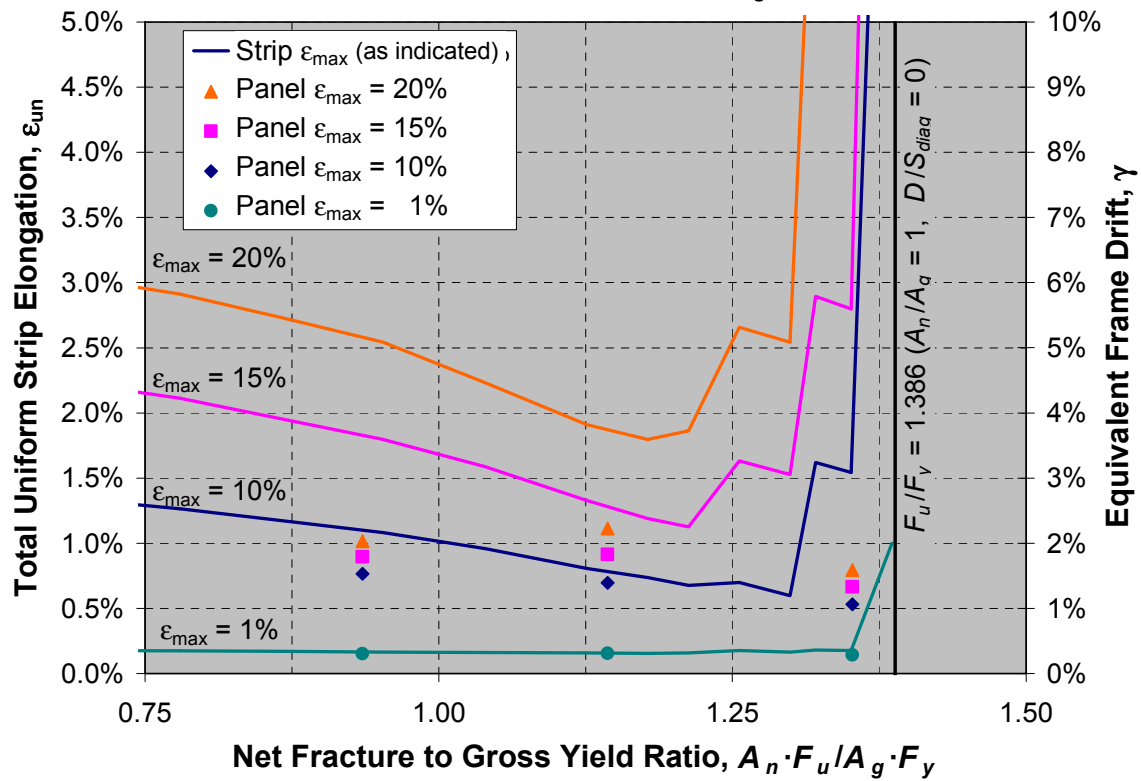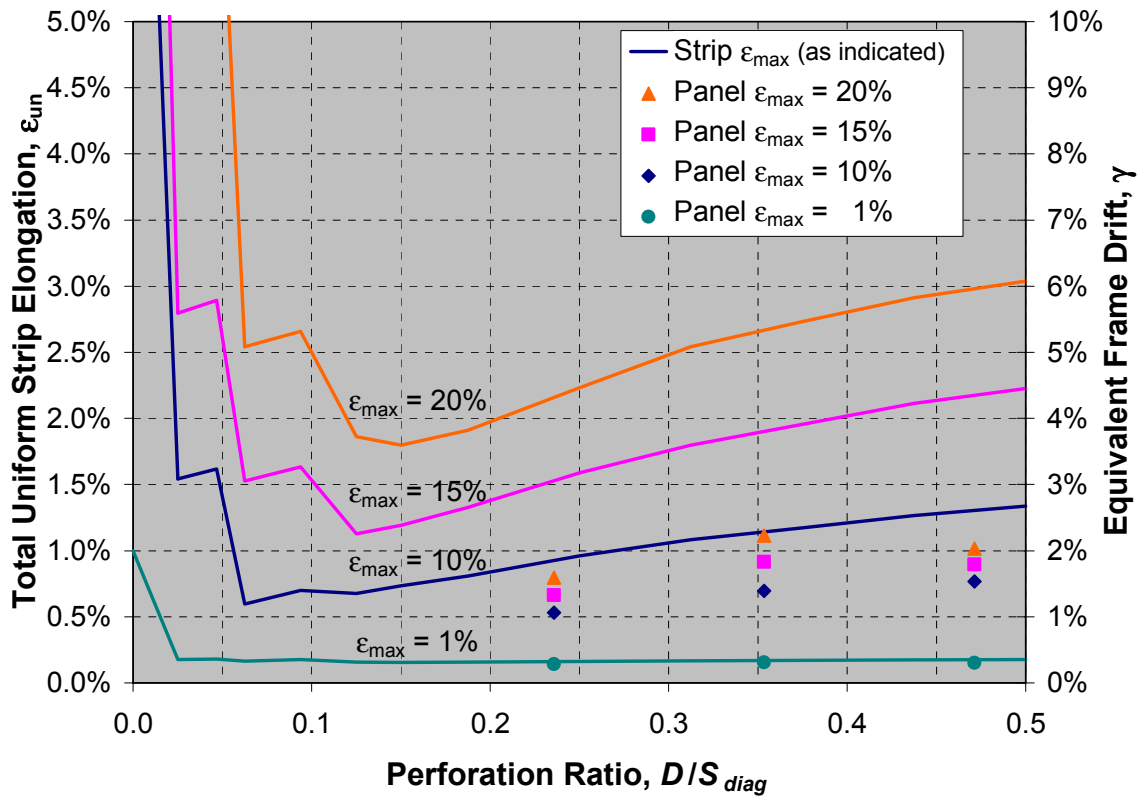
**FIGURE 7-7 Uniform Distributed Strip Axial Strain, ε_{un} versus
(a) Perforation Spacing Ratio, D/S_{diag}; (b) Net Fracture to Gross Yield, A_nF_u/A_gF_y
Idealized A572 Steel**

(a) Strip Mesh and Deformed Shape

(b) Maximum In-Plane Principal Stress Contours

(c) Maximum In-Plane Principal Strain Contours
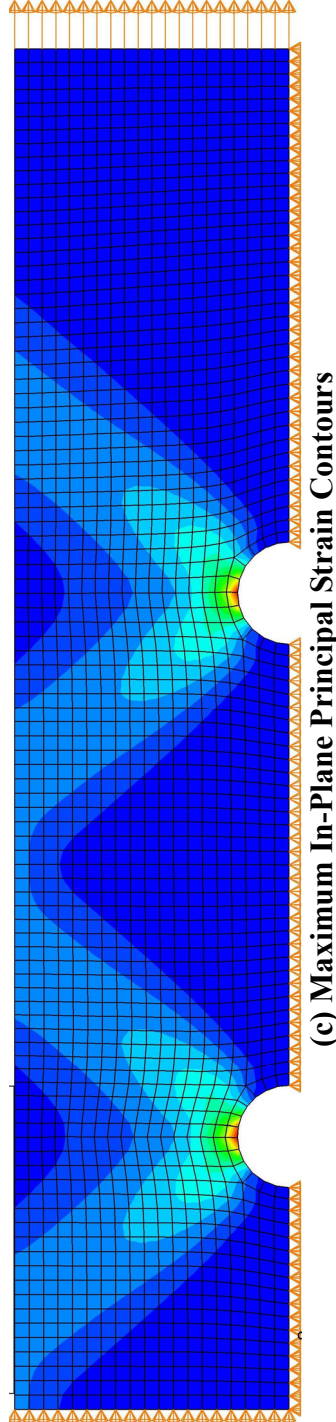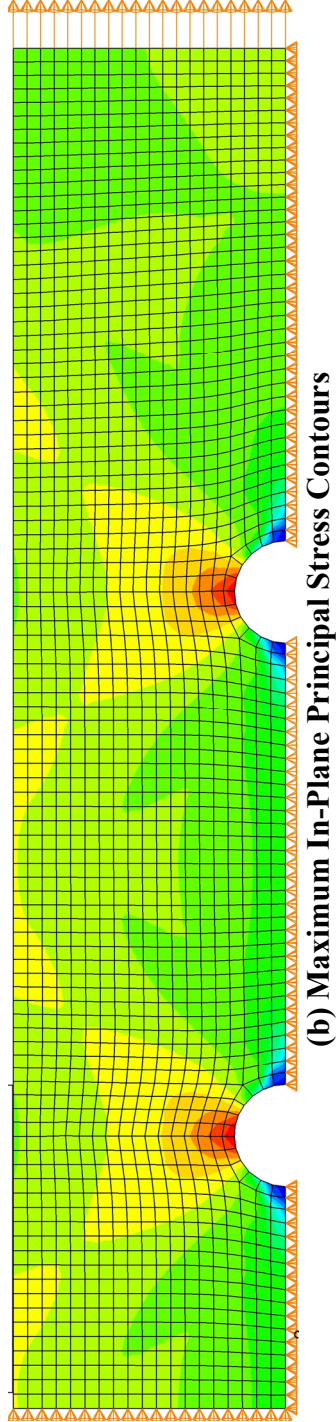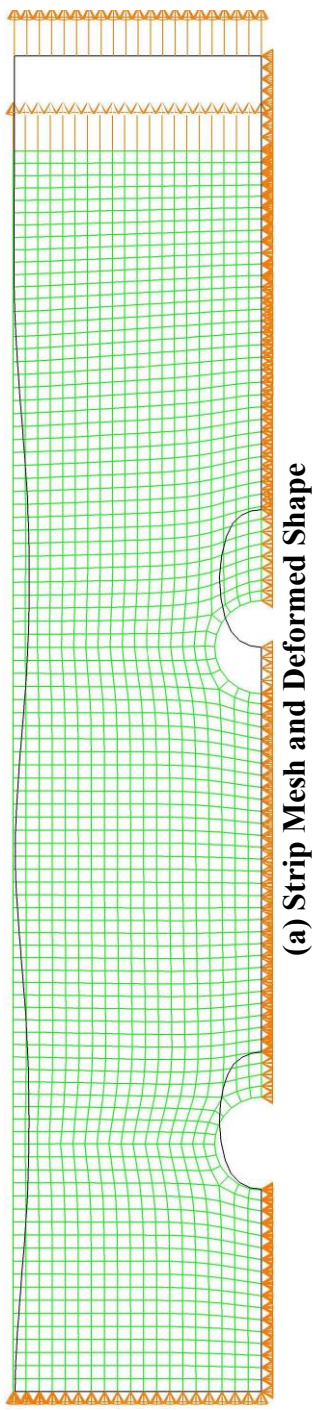
FIGURE 7-8 Typical Strip Analysis Results at 20% Maximum Local Strain
A572 Gr. 50 Steel, D = 75mm (D/S_{diag} = 0.1875, A_nF_u/A_gF_y = 1.126)

263

(a) Strip Mesh and Deformed Shape

(b) Maximum In-Plane Principal Stress Contours

(c) Maximum In-Plane Principal Strain Contours
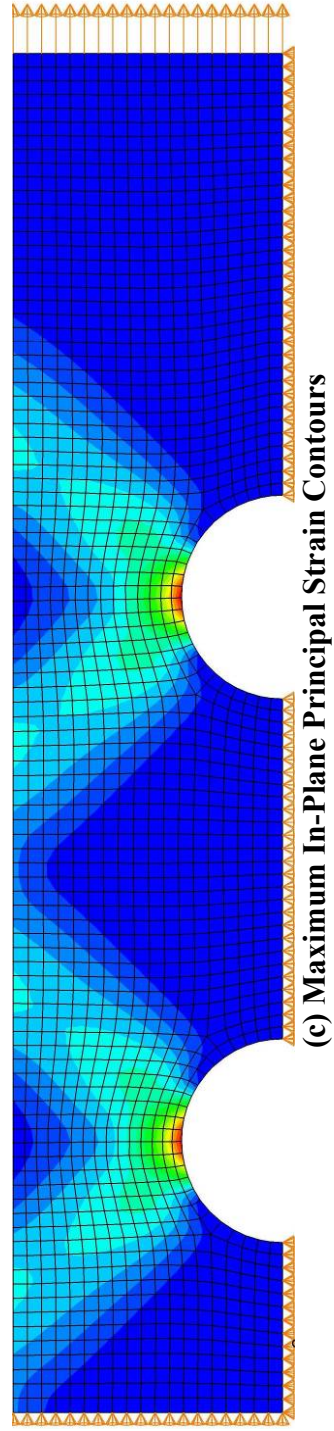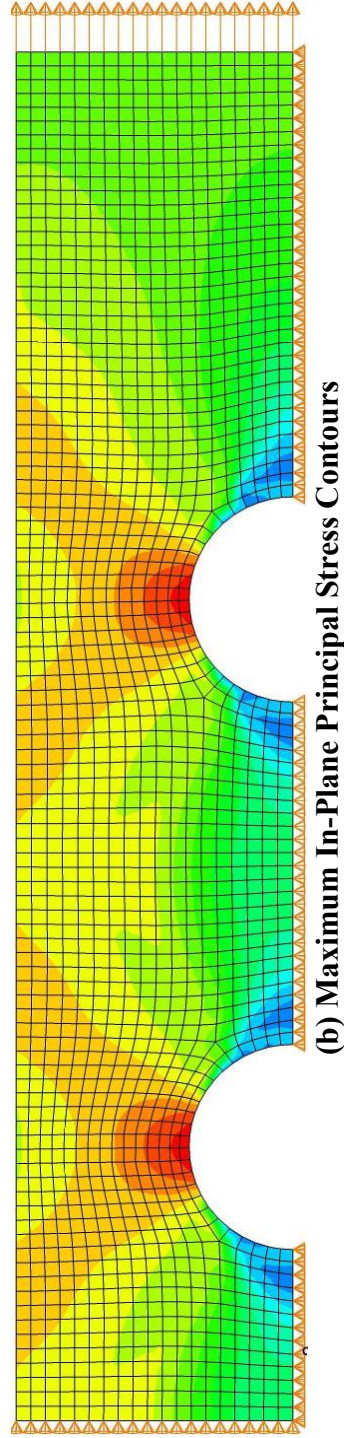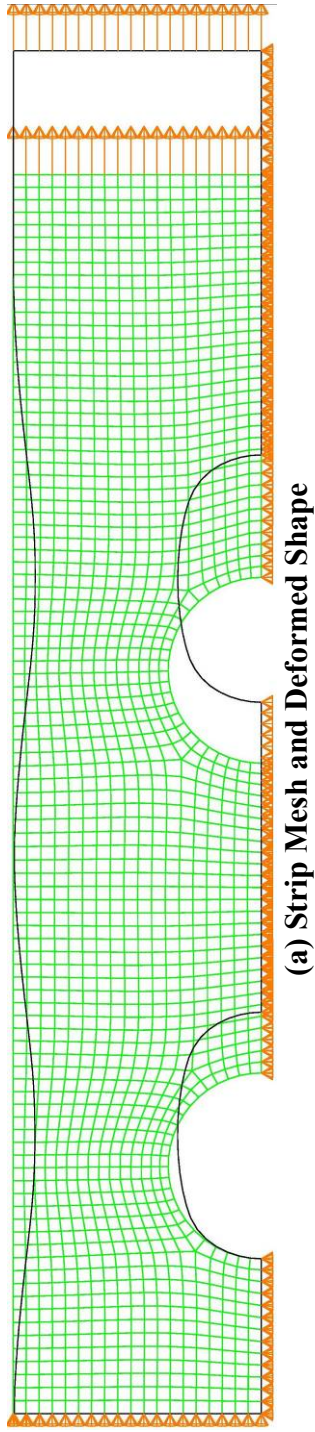
FIGURE 7-9 Typical Strip Analysis Results at 20% Maximum Local Strain
A572 Gr. 50 Steel, D = 150mm (D/S_{diag} = 0.375, A_nF_u/A_gF_y = 0.866)

7.2.4.2 Models based on Specimen P SPSW

The ABAQUS model of Specimen P was modified to perform a related investigation on the panel local maximum principal strains. Eight models were developed (in addition to the original model of the experimental specimen, and the model discussed in section 7.2.2.2 above) with perforation diameters of 100, 150, and 200mm, and panel materials of LYS165, A36, and A572 Gr.50. Panel thicknesses were 1.5, 2.0, or 2.6mm, based on approximately equivalent ultimate strength per unit panel width for A572, A36, and LYS165, respectively. Material properties for A36 and A572 were based on cyclic stabilized stress-strain curves for Steel "D" and "A", respectively, in the ATLSS study (Kaufmann *et al.* 2001) discussed in section 6.2.6 (the cyclic stress strain curve for Steel "D" is shown in figure 7-10). Model properties, including those described in section 7.2.2 above, are summarized in table 7-1.

A monotonic pushover displacement loading was applied to each model as was done in the previous frame analyses. Panel principal strains were monitored during each analysis and frame drifts were noted when local maximum panel strains adjacent to perforations reached values of 1, 10, 15, and 20%. These values are reported in table 7-1.

The frame drift results can be compared with the axial displacements of the typical strips analyzed in section 7.2.4.1 by multiplying the drift values in table 7-1 by $\frac{1}{2} \cdot \sin 2\theta$ (equal to 0.5 for $\theta = 45°$), to obtain the equivalent strip elongations, ε_{un}. These values, for each monitored local maximum strain, ε_{max}, are plotted on figures 7-6 and 7-7 for A36 and A572 infill panels, respectively, for comparison with the results obtained for the individual strips analyzed in section 7.2.4.1. The uniform strip elongation and equivalent frame drift for these data points are given on these figures on the left and right vertical axes, respectively. Typical in-plane principal stress and strain contours are shown in figure 7-11, for the 150mm perforation diameter model with A36 infill panel at 20% local maximum principal strain. These figures display a similar distribution of tension field action around the perforations to that observed in the results of the Dexter *et al.* study and "typical strip" analyses discussed above, with stress and strain concentrations initiating at the perforation edges, radiating out from this location at approximately 45° with respect to the diagonal tension field orientation, and then joining with similar effects in the adjacent perforation regions.
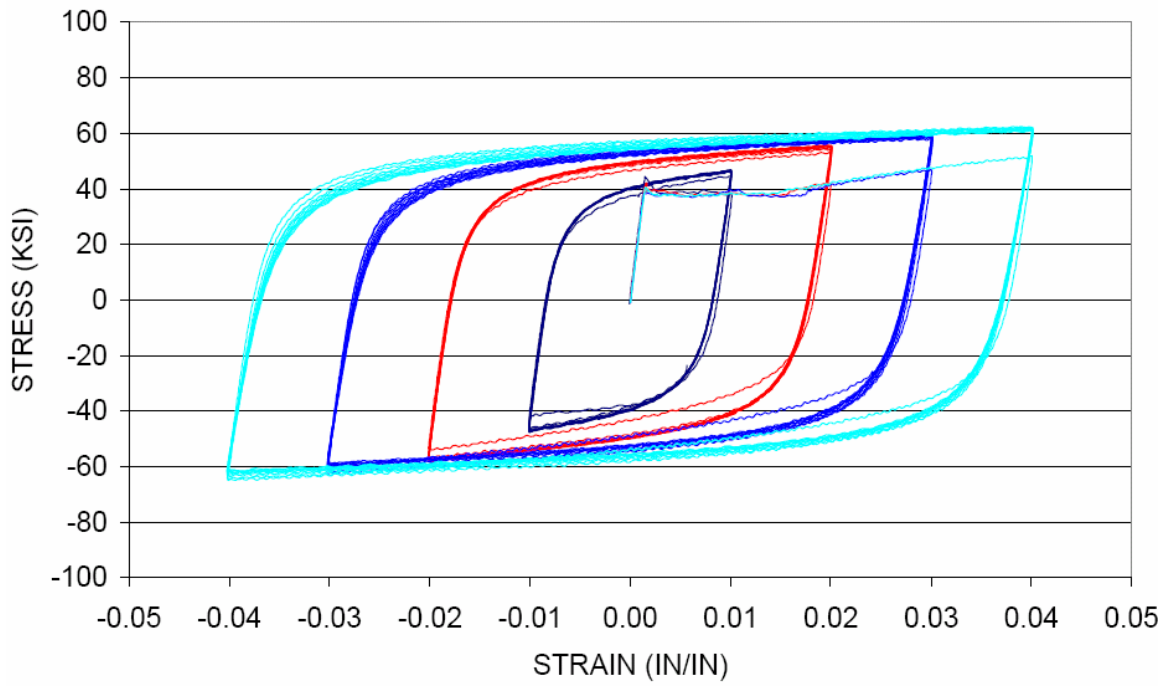
FIGURE 7-10 Composite Plot of Cyclic Axial Strain Behavior of Steel D (A36) (4 different specimens, respectively subjected to 10 cycles at 2%, 4%, 6%, and 8% Strain Range). (from Kaufmann *et al*. 2001)

TABLE 7-1 Summary of Perforated Infill Panel Properties and Frame Drifts at local principal strains of 1, 10, 15, and 20%

Material	t_p (mm)	D (mm)	D/S_{diag}	F_y (MPa)	F_u (MPa)	A_nF_u/A_gF_y	γ at $\varepsilon = 1\%$	γ at $\varepsilon = 10\%$	γ at $\varepsilon = 15\%$	γ at $\varepsilon = 20\%$
LYS165	1.5	100	0.2357	165	306	1.416	0.15%	1.62%	2.43%	3.25%
A36	1.5	100	0.2357	276	414	1.146	0.22%	1.31%	1.69%	2.04%
A572	1.5	100	0.2357	299	529	1.352	0.28%	1.06%	1.33%	1.59%
LYS165	2	150	0.3536	165	306	1.197	0.18%	2.03%	3.11%	4.18%
A36	2	150	0.3536	276	414	0.970	0.25%	1.67%	2.17%	2.60%
A572	2	150	0.3536	299	529	1.144	0.31%	1.39%	1.83%	2.23%
LYS165	2.6	200	0.4714	165	306	0.979	0.19%	2.49%	3.55%	4.59%
A36	2.6	200	0.4714	276	414	0.793	0.32%	1.95%	2.58%	2.94%
A572	2.6	200	0.4714	299	529	0.935	0.30%	1.53%	1.79%	2.03%
A572	1.5	200	0.4714	299	529	0.935	0.33%	1.23%	1.52%	1.78%
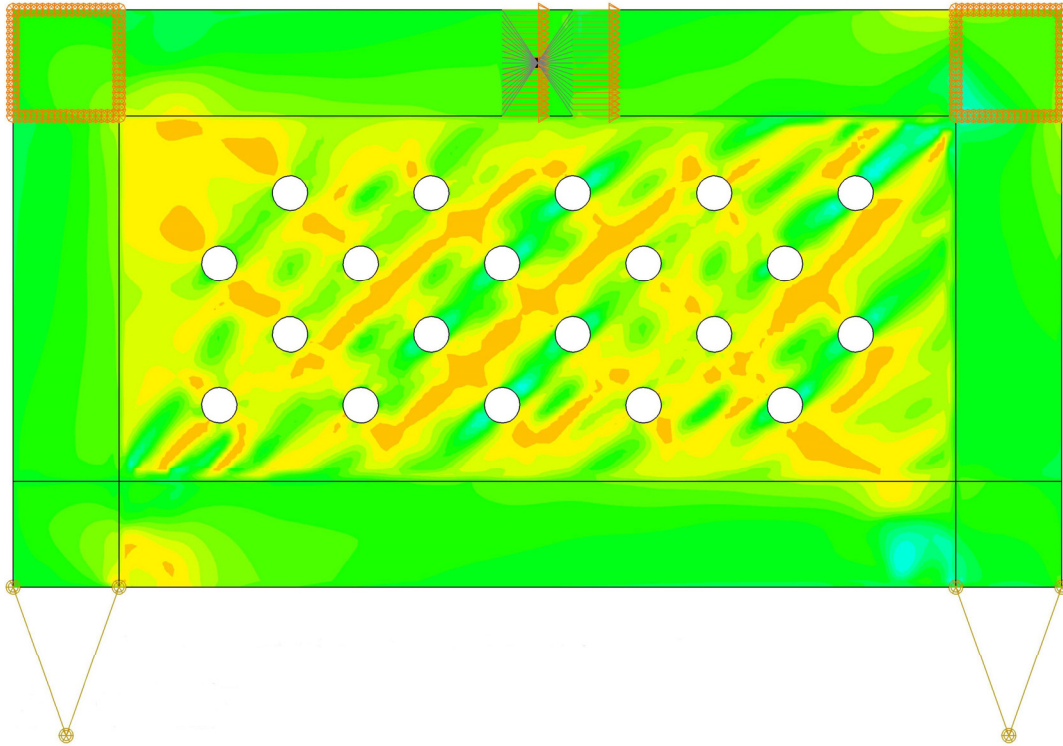
(a) Maximum In-Plane Principal Stress Contours
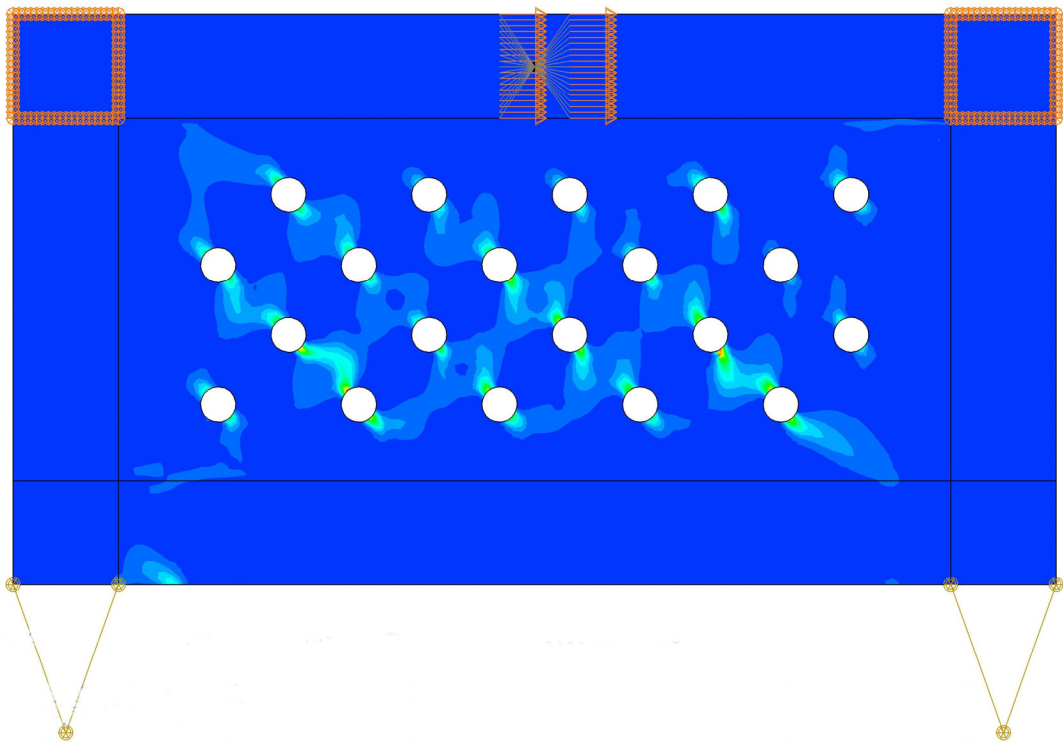
(b) Maximum In-Plane Principal Strain Contours

FIGURE 7-11 Typical Frame-Panel Analysis at 20% Maximum Local Strain
A36 Panel, D = 150mm (D/S_{diag} = 0.3536, A_nF_u/A_gF_y = 0.970)

268

7.2.4.3 Observations

A number of observations are possible from figures 7-6 and 7-7. When the perforation ratio is zero in (a), the total uniform strip elongation is equal to the maximum strain being monitored (i.e. 1, 10, 15, or 20%). For these monitored maximum strains, the total strip elongation decreases significantly, and then gradually increases, as the perforation ratio increases between 0.1 and 0.5. Similarly, when the net-to-gross strength ratio, $A_n{\cdot}F_u/A_g{\cdot}F_y$, is equal to the ultimate-to-tensile ratio, F_u/F_y (i.e. $A_n/A_g = 1$, $D = 0$), the total uniform elongation is equal to the strain being monitored. The total elongation, ε_{un}, decreases sharply as this ratio decreases, but then gradually increases as observed in (a) comparing elongation to the perforation ratio.

Considering that the significant inelastic action in the strips occurs over the total length of the perforations, the slight increase in strip elongation with increasing perforation ratio (or decreasing net fracture to gross yield ratio) is not as counterintuitive as may initially appear. This can be shown by normalizing the total uniform elongation, ε_{un}, in figures 7-6 and 7-7 by the ratio $N_r{\cdot}D/L$ (the ratio of "perforated length" to overall length in a strip, also used in chapter 3). This has been done in figures 7-12 and 7-13. In this case, ε_{un} is equal to $2{\cdot}\delta/L$, and therefore the resulting ratio $\varepsilon_{un}/[N_r{\cdot}D/L]$ is also equal to $2{\cdot}\delta/N_r{\cdot}D$ (where $2{\cdot}\delta$ is the total strip end displacement as shown in figure 7-5 (a)), which is effectively the total strip elongation divided by the cumulative length of perforations over the entire strip.

Note that some of the trends observed above, and some of the "jaggedness" of the curves in figures 7-6 and 7-7, may be an artifact of the finite element modeling, such as the coarseness of the mesh (chosen for expediency) and other factors. For example, for different mesh geometries, the location of the interpolation points may not be identical, which affects the maximum strain calculation. In addition, the selected material model will influence the spread of inelastic action in the strip. The sensitivity of the effect of various material models (the post-elastic stiffness, for example) on the strip elongation at limit state should be investigated.

Although only a few data points are available in figures 7-6 and 7-7 for the analyses of the entire wall, some of the same trends observed above can be seen for the range of specimen P models analyzed in the previous section. However, the maximum local strains are reached at significantly lower values of total elongation for the full wall compared to the strips analyses.

This is significant and cannot be explained at this time. Full wall models present additional complexities, such as the out-of-plane panel buckling during tension field formation, which are not accounted for in the typical strip models. It would be interesting to investigate the role that these additional boundary conditions play in the behavior of perforated strips in tension. In neglecting these conditions, however, the strip models provide an upper bound limit to the axial behavior of the tension field acting between perforations, which is supported by the plots of figures 7-6 and 7-7.

In the typical strip analyses, for 5mm material thickness, the minimum total elongation reached when the maximum strain reached 15% was approximately 1.5% and 1.125% (corresponding to frame drifts of 3% and 2.25%, by dividing these elongations by the $\frac{1}{2} \cdot \sin 2\theta$ conversion factor discussed in section 7.2.4.2) for A36 and A572, respectively. For maximum strain of 20%, the minimum total elongation achieved was approximately 2.35% and 1.8% (frame drifts of 4.7% and 3.6%) for A36 and A572, respectively.

In the analyses modeled after specimen P, the minimum frame drifts reached at local maximum strains of 15% were 2.43%, 1.69%, and 1.33%, for LYS165, A36, A572, respectively. For maximum panel strain of 20%, the frame drifts reached were 3.25%, 2.04%, and 1.59%, for infill panels of the same respective grades. Note that the maximum local strain values were arbitrarily chosen for the purpose of comparing the performance of the considered systems and that the value of 20% is significant as it correspond to the minimum specified elongation at failure for the materials. Lower limit values may be appropriate for design purposes. Tests reported in the previous chapters showed that 13% strain could be reached without any plate fracture observed next to the perforation using low yield steel. Also note that while each model was subjected to single-direction, monotonic loading, accumulated plastic strains during cyclic loading may contribute additional detrimental effects on the perforated panel system that have not yet been observed.
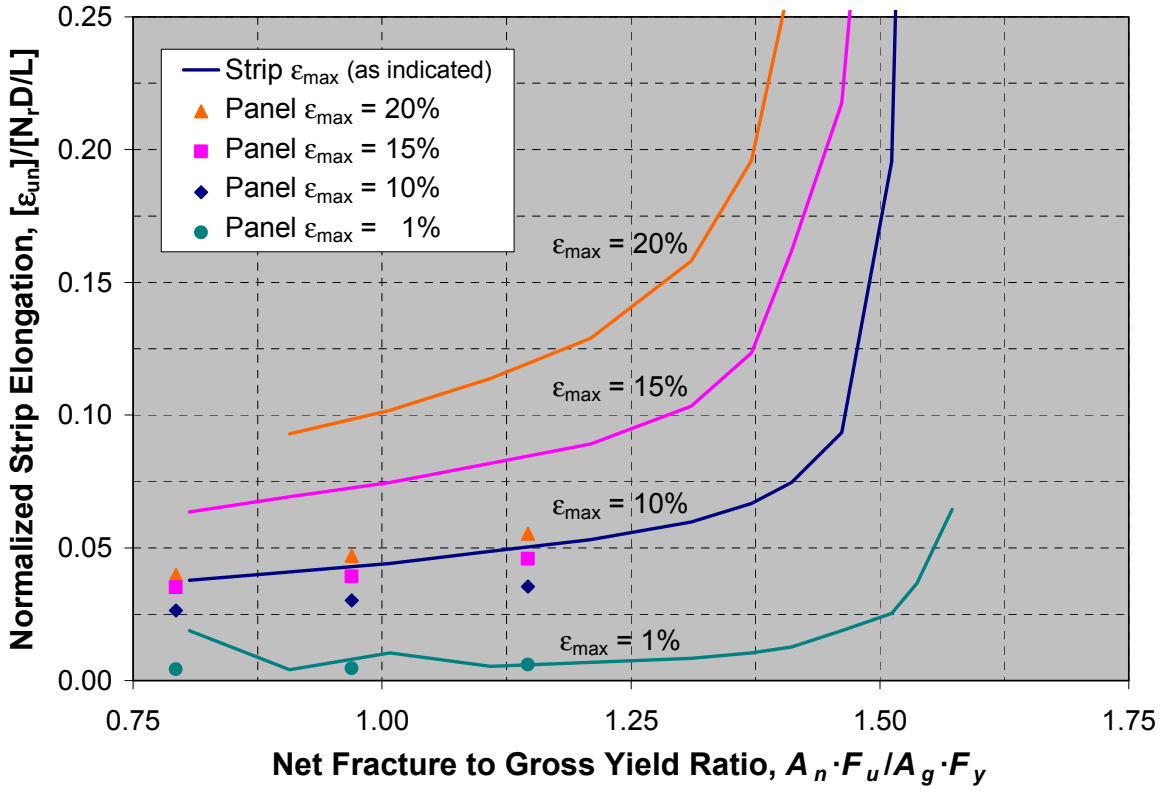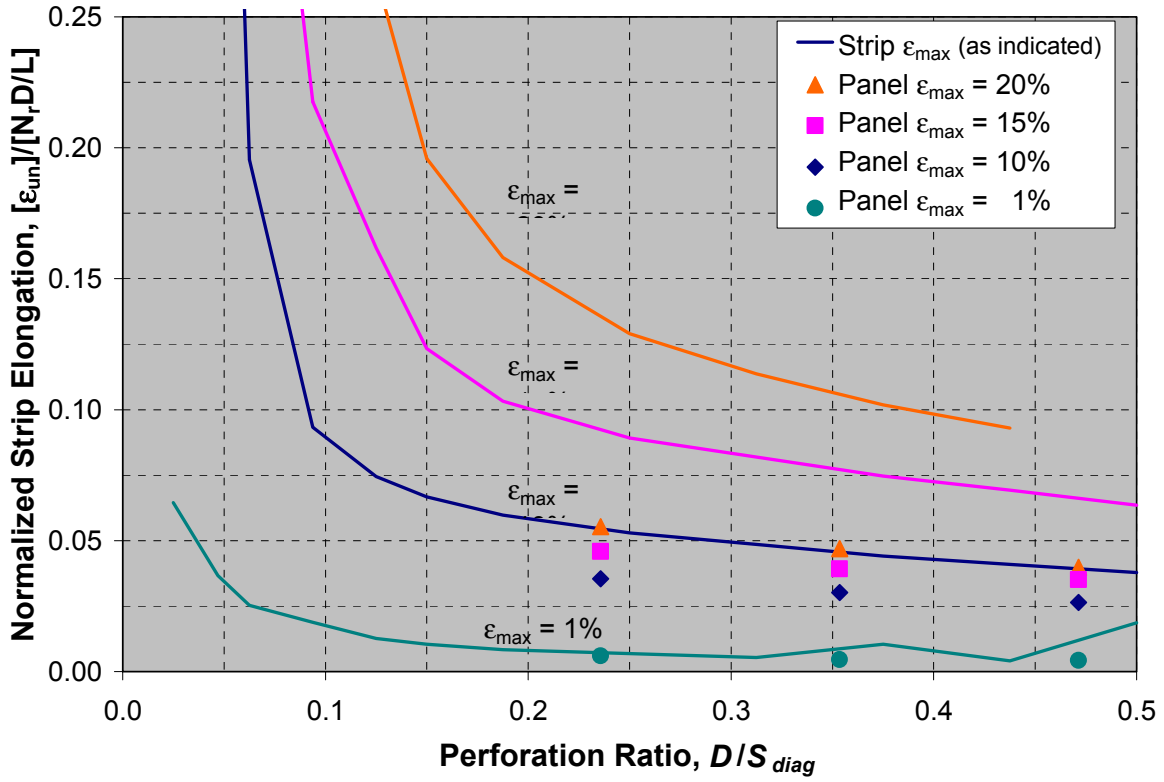
**FIGURE 7-12 Normalized Strip Elongation, $\varepsilon_{un}/(N_r D/L)$ versus
(a) Perforation Spacing Ratio, D/S_{diag}; (b) Net Fracture to Gross Yield, $A_n F_u/A_g F_y$
Idealized A36 Steel**

271
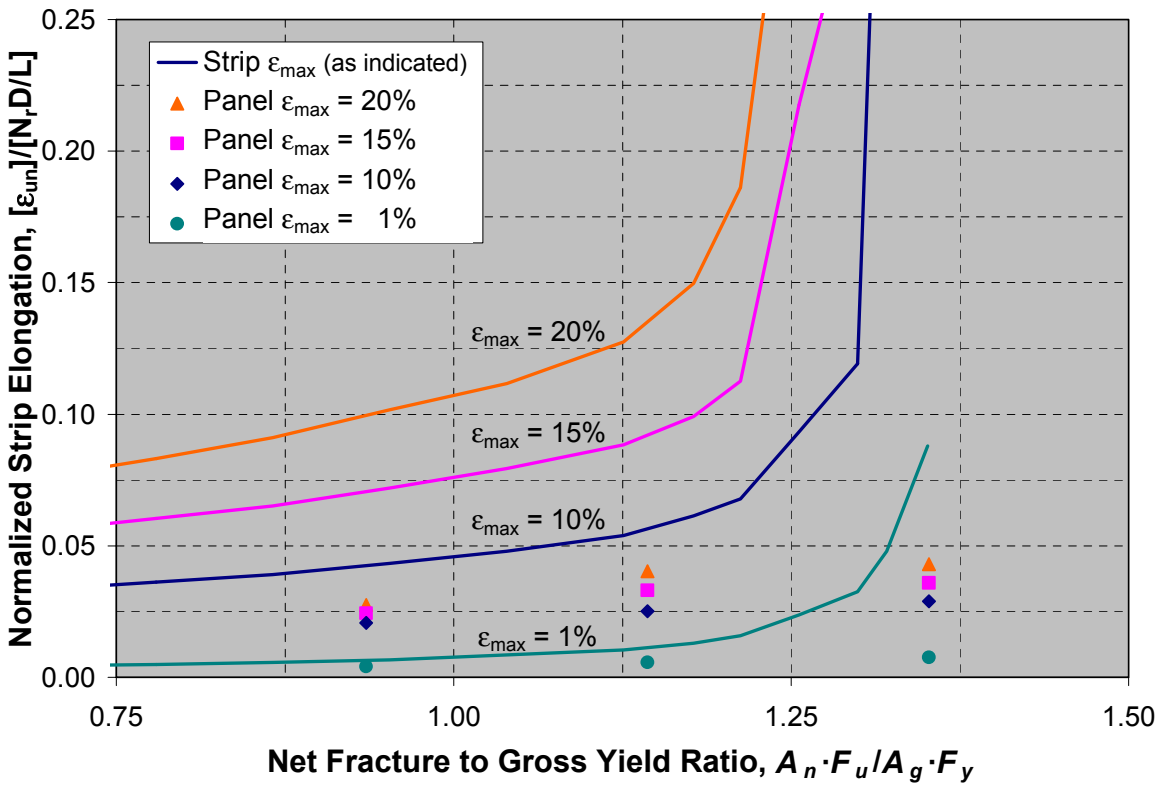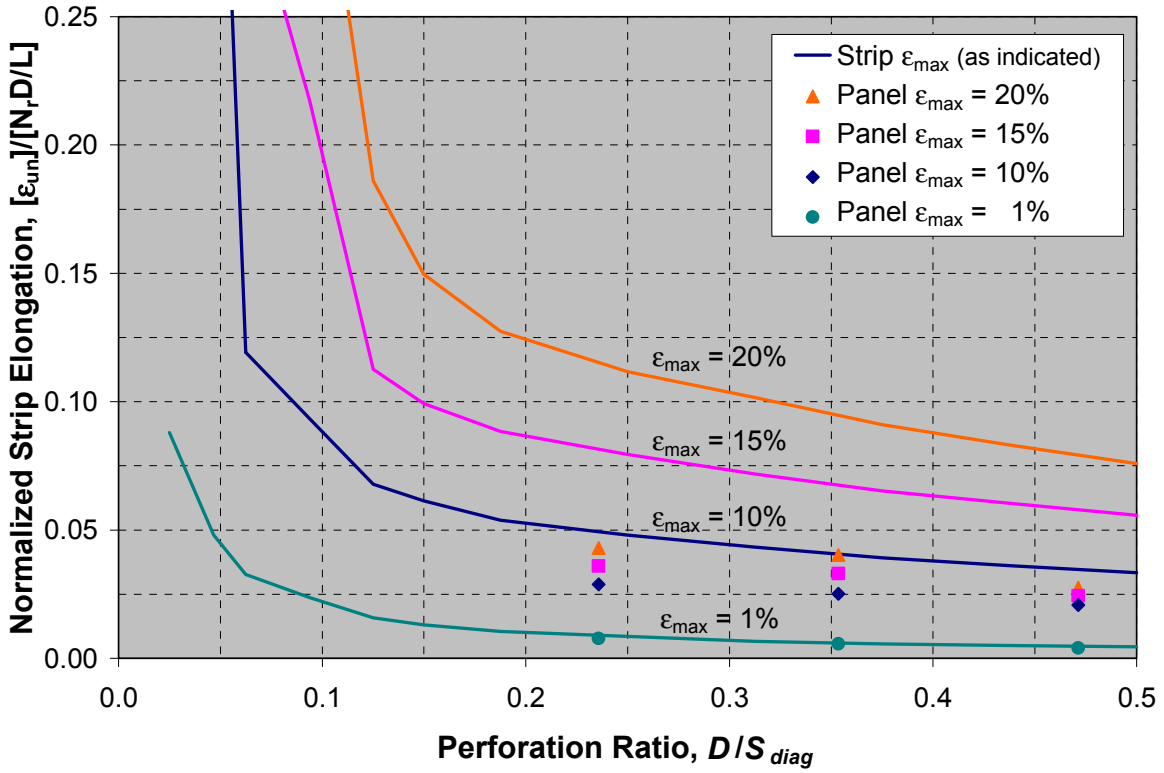
**FIGURE 7-13 Normalized Strip Elongation, $\varepsilon_{un}/(N_rD/L)$ versus
(a) Perforation Spacing Ratio, D/S_{diag}; (b) Net Fracture to Gross Yield, A_nF_u/A_gF_y
Idealized A572 Steel**

272

7.2.5 Design Recommendations and Considerations

Design recommendations are suggested below for the perforation sizes and layout necessary to ensure the ductile behavior of perforated panel SPSWs.

7.2.5.1 Panel Overstrength and Frame Design

As discussed in Chapter 3 (section 3.4.1.1), the perforated panel strength yield strength, $V_{yp.perf}$, can be calculated by reducing the strength of a solid panel yield force, V_{yp}, with same overall dimensions by use of the factor, $1 - D/S_{diag}$, i.e.:

$$V_{yp.perf} = \left(1 - \frac{D}{S_{diag}}\right) \cdot V_{yp} \tag{7-2}$$

where an expression for V_{yp} was given in (4-6). For capacity design of the frame members to ensure elastic behavior and/or satisfy the fuse concept, the distributed panel forces acting on the boundary frame (such as those presented for the anchor beam in equation (4-2)) can be reduced by this factor to account for the presence of the perforations. However, these distributed panel forces should also be amplified to account for strain hardening induced overstrength by substituting F_{up}, the ultimate panel material strength, in place of the panel yield strength, F_{yp}, in the appropriate expressions, such as (4-2), which represents the components for distributed loads from the panel for anchor beams, using figure 4-4 (where σ is used for the panel stress at a given loading). Similar relations can be easily derived for loads on the columns.

7.2.5.2 Ratio of Diameter to Spacing of Perforations

Rewriting (7-1) with perforated SPSW panel typical strip properties substituted in place of those for the tension flange (for which the study was originally developed):

$$F_u \cdot \left(S_{diag} - D\right) \cdot t \geq Y_t \cdot F_y \cdot S_{diag} \cdot t \tag{7-3}$$

where all variables have been previously defined. This expression can be reorganized as follows:

$$\frac{D}{S_{diag}} \leq \left(1 - Y_t \cdot \frac{F_y}{F_u}\right) \tag{7-4}$$

where it is recommended to use values of Y_t equal to 1.0 for $F_y/F_u \le 0.8$, or 1.1 otherwise, as suggested by Dexter *et al*. (2002) and specified for design of tension flanges with holes by AISC (2005b). Based on the finite element analyses and the review of research discussed above, this relation provides a reasonable conservative limit for selecting a perforated panel geometry for the design of perforated SPSWs such that ductile behavior can be achieved.

7.2.5.3   Perforation Layout

The panel perforation layout should be selected such that the orientation angle, θ, as shown schematically in figure 3-15, is equal to or near the solid panel SPSW tension field inclination angle, α, given by equation (2-2). This angle is typically near 45° with respect to surrounding frame members (Driver *et al*. 1997). This angle is indirectly limited to range between approximately 35° and 55° in the forthcoming version of the AISC seismic provisions (AISC 2005a) by limiting the ratio of panel length to height, L/h, to: $0.8 \ge L/h > 2.5$. Hence, the practical range of a values is fairly limited, and it is recommended (for simplicity) to adopt a constant 45° angle. The resulting distortion in the diagonal tension stress field is presumably minimized, but this phenomenon still remains to be quantitatively defined by future research.

7.2.5.4   System Drift and Material Elongation

Steel moment frames with perforated SPSWs should be designed for maximum interstory drifts of 1.5%. Based on the analyses discussed above, for panels with very thin plates and perforated strips of 5mm thickness, this drift should limit the maximum strains adjacent to perforations to less than the material specifications' minimum elongation requirements.

Steel used in perforated SPSWs should have enough ductility to provide an approximate minimum elongation of 20% at ultimate tensile strength. The most commonly used steels for building construction in the North American market, such as A36 and A572, specify this minimum elongation (i.e. ASTM A572 requires a minimum of 18% and 21% elongation in 200mm (8in) and 50mm (2in) gauge lengths, respectively). Since the minimum elongation requirement of the ASTM standards does not coincide with the strain at maximum applied force in a tensile test coupon (i.e. the measured engineering stress drops prior to reaching the elongation at failure), one could argue that 20% strain is too liberal a limit. However, in this case, there is a pronounced strain gradient, in which a local loss of strength over a small region

274

could be redistributed to the rest of the cross section. In addition, strip analysis suggests that limits may be less conservatively set than what is presented here. At this time, 20% is kept as a limit state, to be re-assessed in future studies.

Note that, although usage of the A992 specification for structural steel has increased, it is only available for structural shapes (i.e. wide flange columns, angles, etc.) (Zoruba and Grubb 2003), and not yet available for wide thin plates of the type that would be used for a SPSW infill panel (as of this writing). This may change as steel mills continue to produce more products meeting this specification.

7.3   Use of RBS connections in SPSW Anchor Beams

Chapter 3 developed concepts for SPSW anchor beam design that rely on reducing the beam end moment strength. This is intended to control anchor beam yielding by ensuring plastic hinges form at beam ends, to provide efficient resistance of SPSW panel forces at the top and bottom of a multistory frame. The experiments discussed in chapters 4, 5, and 6 utilized RBS beam-to-column connections to provide the required moment strength reduction, and implemented these connections in a tested SPSW system for the first time.

The experimental results detailed in chapter 5 demonstrated that plastic hinging was essentially limited to the RBS locations as intended in the developed design concepts. However, it was also observed that at increasing drift levels, the cyclic plastic hinging resulted in local instabilities of the RBS regions, precipitating frame instabilities in the form of beam lateral-torsional buckling (LTB) and column twisting. This was partly attributable to problems with the test setup as described earlier. Future tests of multistory SPSWs with composite floors will help determine the extent of required bracing of RBS. In the interim, a brief review of recent research on RBS connections is presented below, along with suggested guidelines for their design against LTB and column twisting in conjunction with SPSW systems.

7.3.1   Research on Stability of RBS Connections

In a series of studies at the University of California, San Diego (Uang and Fan 1999; Gilton *et al*. 2000; Yu *et al*. 2000), various factors influencing the design of RBS beam-to-column connections were studied. Uang and Fan (1999, 2001) compiled a database of experimental

results and performed a statistical study on the cyclic instability of RBS connections based on the influence of dimensional limits for flange local buckling (FLB), web local buckling (WLB), and LTB. Linear and nonlinear regression analyses showed that response quantities (such as plastic rotation capacity and rate of strength degradation) were highly dependent on the WLB slenderness ratio but not on LTB. They made recommendations on web and flange slenderness limits for a target plastic rotation, for member sizes similar to those in the tested database, urging caution in the extrapolation of results to other cases, such as when columns deeper than those in the database were used.

The response of RBS connections in conjunction with deep columns was investigated (Gilton *et al*. 2000; Chi and Uang 2002). The UCSD researchers found that deep column RBS connections were prone to twisting caused by the eccentric beam flange force due to beam LTB. Column warping torsion stress was found, through a comparison of test results and an analytical study, to be highly dependent on the section depth, h, and flange thickness, t_f, specifically the h/t_f^3 ratio.

The beam sections from the experimental portion of the study satisfied compactness requirements for FLB, WLB, and LTB. However, the interaction of these limit states, as observed and documented by previous studies (Uang and Fan 1999, 2001), occurred, and then precipitated the column twisting that was unreported in previous tests with shallow columns (i.e. W14 sections). From this study, a procedure was proposed to determine if column twisting is a concern during design, and additional bracing near the RBS region was recommended if high stresses were expected (as defined subsequently below).

Lateral torsional buckling was observed in the beam sections of the specimens tested by Chi and Uang (2002). The LTB produces an eccentricity, e_x, in the beam section at the RBS location, which causes the beam flange force to impart torsion and biaxial bending on the column, as shown in figure 7-14. The design procedure proposed by Chi and Uang assumes an eccentricity of $e_x = 0.2b_f$ at 4% story drift. Then, the inclined angle of the beam flange force, θ, is calculated based on the beam geometry shown in figure 7-15. The flange force at yield is estimated, and then by resolving it into biaxial forces and a torsion on the column, the combined stresses from bi-axial bending and warping torsion can be calculated. If the combined stresses exceed a limit

276

specified in section 7.3.2.1, the designer may change the column size to improve torsional properties, or brace the beam near the RBS region to minimize the LTB amplitude (e_x).

$$T=F\,(e_x\cos\theta + e_y\sin\theta)$$

(b)

(a)
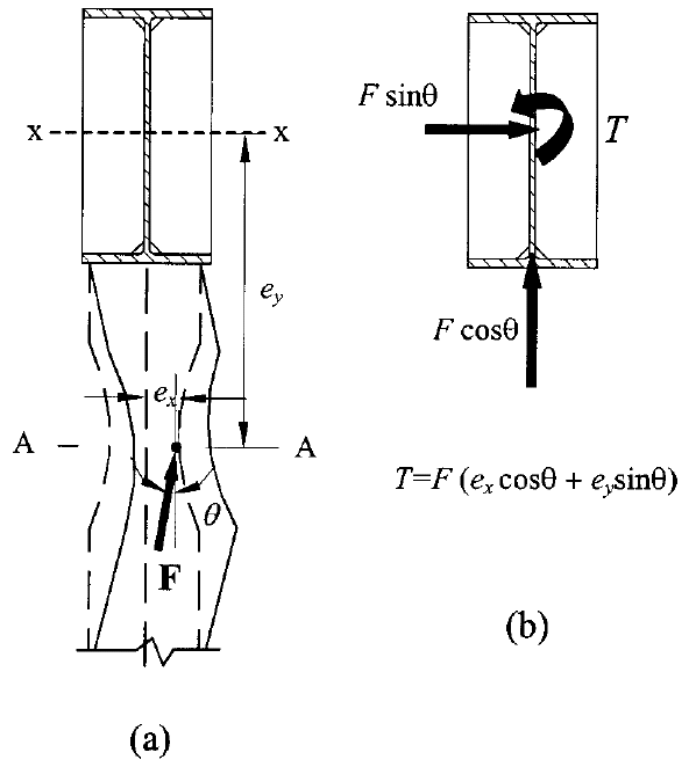
FIGURE 7-14 Column Torsion and Weak-Axis Bending Produced by Lateral Torsional Buckling of Beam: (a) Inclined Beam Flange Force Due To LTB; (b) Out-Of-Plane Forces Acting on Column. (From Chi and Uang 2002)
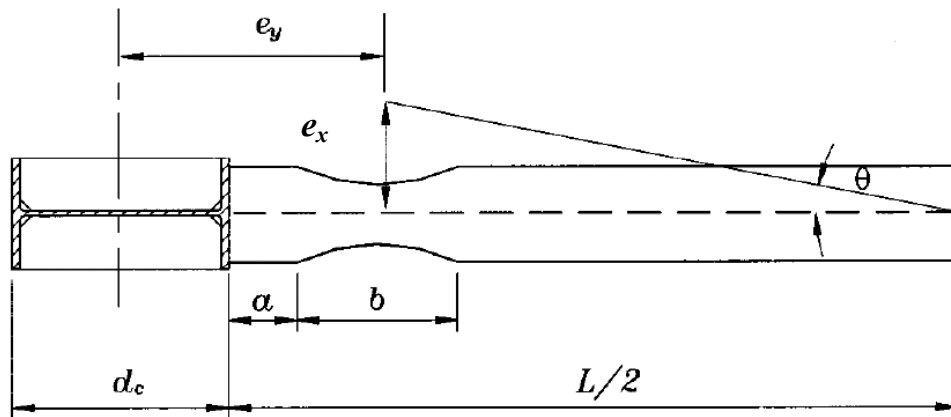
FIGURE 7-15 Inclined Angle of Beam Flange Force (From Chi and Uang 2002)

7.3.2 RBS Stability in SPSW Applications

7.3.2.1 Stability of Tested Specimens

As described in chapter 5, for the testing conducted as part of the current study in each specimen, local section instabilities began with WLB, followed by FLB and LTB, then combining to initiate twisting in the frame columns. Assuming that this behavior would occur irrespective of the test setup problems encountered, it would be desirable to follow the recommendations from the Chi and Uang study.

The following investigates how Chi and Uang's approach would relate to the performance of the specimens tested here. The experimental setup used by Chi and Uang to investigate RBS behavior with deep columns tested an edge column between assumed mid-story inflection points and a beam stub cycled at the assumed mid-span inflection point, as shown in figure 7-16. The column was considered to have torsionally-simple end supports during analysis of torsional stresses. That is, column rotation and the second derivative of rotation, φ, and φ'', respectively, are equal to zero. Therefore, the section is restrained against rotation at the ends, but free to warp (i.e. stresses due to pure torsion and warping torsion do not develop at the ends).
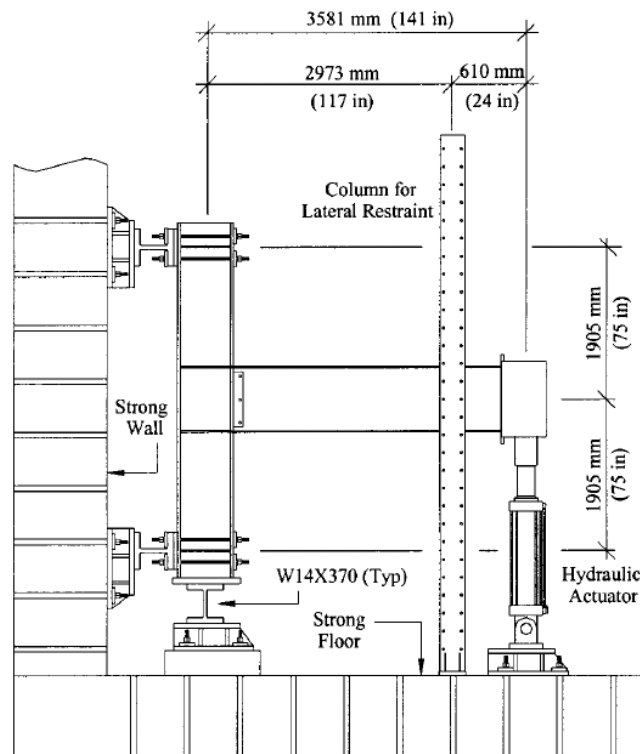
FIGURE 7-16 Test Setup and Overall Dimensions – Chi and Uang (2002)

278

The specimens tested in the current study had different boundary conditions, in that the beams were connected to the tops of the columns. Also, the column bases, although hinged in the plane of the wall, were torsionally restrained against both rotation and warping. Therefore, analysis of these specimens for torsional stresses requires the solution of the governing differential equation using the proper boundary conditions, namely, φ, and φ' equal to zero at the column base, and φ'' equal to zero at the top of the column.

For $0 \leq y \leq \alpha H$:

$$\varphi(y) = \frac{T \cdot a_c}{G \cdot J} \left[\begin{array}{l} \left(\sinh \dfrac{\alpha \cdot H}{a_c} - \tanh \dfrac{H}{a_c} \cdot \cosh \dfrac{\alpha \cdot H}{a_c} + \tanh \dfrac{H}{a_c} \right) \times \cdots \\[2mm] \left(\cosh \dfrac{y}{a_c} - 1.0 \right) - \sinh \dfrac{y}{a_c} + \dfrac{y}{a_c} \end{array} \right] \qquad (7\text{-}5)$$

$$\Gamma = \frac{\varphi''(y) \cdot G \cdot J \cdot a_c}{T} = \left(\begin{array}{l} \left(\sinh \dfrac{\alpha \cdot H}{a_c} - \tanh \dfrac{H}{a_c} \cdot \cosh \dfrac{\alpha \cdot H}{a_c} + \tanh \dfrac{H}{a_c} \right) \times \cdots \\[2mm] \left(\cosh \dfrac{y}{a_c} \right) - \sinh \dfrac{y}{a_c} \end{array} \right) \qquad (7\text{-}6)$$

For $\alpha H \leq y \leq H$:

$$\varphi(y) = \frac{T \cdot a_c}{G \cdot J} \left[\begin{array}{l} \left(\tanh \dfrac{H}{a_c} \cdot \cosh \dfrac{\alpha \cdot H}{a_c} - \tanh \dfrac{H}{a_c} - \sinh \dfrac{\alpha \cdot H}{a_c} \right) - \cdots \\[2mm] \left(\cosh \dfrac{\alpha \cdot H}{a_c} - 1.0 \right) \cdot \left(\tanh \dfrac{H}{a_c} \cdot \cosh \dfrac{y}{a_c} \right) + \cdots \\[2mm] \left(\cosh \dfrac{\alpha \cdot H}{a_c} - 1.0 \right) \cdot \sinh \dfrac{y}{a_c} + \dfrac{\alpha \cdot H}{a_c} \end{array} \right] \qquad (7\text{-}7)$$

$$\Gamma = \frac{\varphi''(y) \cdot G \cdot J \cdot a_c}{T} = \left[\begin{array}{l} \left(1.0 - \cosh \dfrac{\alpha \cdot H}{a_c} \right) \cdot \tanh \dfrac{H}{a_c} \cdot \cosh \dfrac{y}{a_c} + \cdots \\[2mm] \left(\cosh \dfrac{\alpha \cdot H}{a_c} - 1.0 \right) \cdot \sinh \dfrac{y}{a_c} \end{array} \right] \qquad (7\text{-}8)$$

where: Γ is a parameter that contains the second derivative of φ, and is used later; T is the concentrated torque acting on the column; H is the column height; α is the fraction of the column height at which T acts; J is the torsional constant for the column section; and $a_c = \sqrt{E \cdot C_w / G \cdot J}$, where C_w is the section warping constant; and G is the shear modulus of steel.

Using the procedure described by Chi and Uang, the specimen column combined stresses considering the appropriate support conditions are obtained as follows. As recommended by Chi and Uang, the flange yield force was calculated and assumed to act at an eccentricity, e_x, of $0.2b_f$ to account for LTB at higher specimen drifts, producing the torque to be applied to the column. The torque, T, was assumed to act at the bottom flange of the top beam, or approximately $\alpha = 0.9$ along the column height. Warping stresses in the column flange due to this torsion, f_{ws}, were calculated at this location using the torsional function, Γ, given by (7-7), using a relation presented by Seaburg and Carter (1997):

$$ f_{ws} = \frac{E \cdot W_{no} \cdot \Gamma}{G \cdot J \cdot a_c} \cdot T \qquad (7-9) $$

where W_{no} ($= h \cdot b_f / 4$) is the normalized warping function at a point on the column flange edge, and $h = d - t_f$.

Analysis of the tested specimen frame for combined stresses (using as-built member material initial yield strengths) due to in-plane beam bending moment, and torsion caused by LTB of the RBS connection at the suggested eccentricity of $0.2b_f$, as recommended by Chi and Uang, gave a value of $f_{ws} = 74$MPa, which when combined with the bending stress from the beam on the column face due to the plastic moment and shear at the RBS location, 340MPa, is greater than the yield strength of the column using as-built material properties ($F_{yc} = 365$MPa for the flanges). Furthermore, the combined stress is equal to the as-built column flange yield stress when a smaller eccentricity of just $0.066 \cdot b_f$ ($= 12.7$mm (0.5in)) is assumed.

The design verification procedure proposed by Chi and Uang (2002) nonetheless provides a means to assess whether utilizing an RBS connection in an SPSW anchor beam could be susceptible to stability issues. Although more investigation is necessary to fully define this behavior, it appears that this is generally of most concern in a top story anchor beam (especially at an exterior column), where the top of the column presumably has less restraint against torsion compared with a bottom story anchor beam adjacent to column baseplate foundation connections.

7.3.2.2 Lin and Tsai (2004) Tests

Lin and Tsai (2004) conducted quasi-static cyclic tests on SPSWs almost identical to the solid panel specimen described in chapters 4, 5, and 6 and using almost the same test setup. In order to reduce the effects of LTB contributing to column twist in the system, benefiting from the knowledge generated from the testing of specimens S1, S2, P and CR, beam bracing was added to the test setup, as shown in figures 2-13 and 2-14. The choice of location of the bracing was constrained by the presence of the strong floor anchorage points, and as such, the bracing was not immediately adjacent to the RBS regions, but approximately 1/3 of the beam length from the connections, as shown in these figures. The loading beam was also relocated on these specimens, from the mid-span of the top beam as tested in the specimens of chapter 5, to approximately 1/3 of the beam span, providing some measure of bracing to the nearer RBS connections, while allowing the support tower at the other third point to laterally brace both the top and bottom beams.

This approach was moderately successful in reducing the RBS stability issues discussed by Chi and Uang and observed in the tests of chapter 5. While the magnitude of the column twisting was reduced, the phenomenon was still present in these tests. This can be partly explained because in that case too, equation (7-10) would still give f_{ws} = 26MPa, which when added with the column bending stress from RBS yielding and initial panel yielding is equal to the column flange yield stress for an assumed eccentricity of $0.026 \cdot b_f$ (=5mm (0.197in)). In addition, the beam lateral restraint assumed in the calculation pictured in figure 7-15 at the right end in the figure was taken at a distance of $L/3$ from the column instead of $L/2$. The challenge lies in being able to calculate the impact of e_x for various lateral bracing conditions, and how this theory can be implemented in SPSWs where sizeable column strength is required due to capacity design.

Ricles *et al*. (2004) studied the effect of RBS connection stability with deep columns considering the presence of a floor slab. Based on analytical parametric studies, and a six-specimen experimental program, they modified the Chi and Uang procedure and proposed various compression flange stress distributions (and resultant force eccentricity, e_x) for RBS connections with and without supplemental bracing.

Ricles *et al.* found that the design procedure recommended by Chi and Uang overestimates the column flange stress in most cases. Ricles *et al.* concluded that out-of-plane movement of the RBS bottom flange and column twist are not sensitive to the beam section size and beam web slenderness when a floor slab is present. They also observed that the lateral movement of the beam bottom flange in the presence of a floor slab is less than the value of 20% of the beam flange width proposed by the Chi and Uang design procedure.

The tests described in this report, as well as the subsequent tests by Lin and Tsai (2004) did not utilize a floor slab in the specimen, and exhibited the column twisting described above in both cases. Beyond utilizing the RBS research cited above, proper design of bracing for RBS connections used in SPSW anchor beam applications requires further study to ensure desired behavior.

7.4   Future Research Needs

7.4.1   Perforated panel walls

A number of items should be investigated further to better define the behavior of perforated SPSWs. These include, but are not limited to investigating:

1. The factors that can explain why the drift predicted by the strip model for an assumed local strain adjacent to a perforation differs so greatly from that predicted by the wall panel model.
2. The effect of panel buckling on the assumed boundary conditions of the typical strip analyses and how changes in panel thickness contribute to this effect.
3. The statistical variation in F_y/F_u for various steel grades and plate thicknesses anticipated for use in SPSW systems. Studies of the performance of tension flanges with holes (Dexter *et al.* 2002) cited above considered material thicknesses greater than 12.7mm (0.5in). Adopting recommendations from that study is tantamount to assuming that the thin plates used for SPSWs would inherently have equal or smaller variation in the specified yield and ultimate strengths. This assumption should be verified.
4. Conditions that may exist (if any) leading to panel fracture during testing, possibly due to low cycle fatigue as a result of buckling and yielding deformations that occurred between

perforations. Testing of panels with various perforation sizes and spacing would be required for this purpose.

5. The effect of the inelastic material model (i.e. post elastic stiffness and hardening rule) on the panel drift (or strip elongation) when local strain limit states are reached.

7.4.2 RBS connections in SPSW anchor beams

The tests presented in this report are the first SPSW specimens utilizing RBS beam-to-column connections. Twisting observed in the columns was of significance and attributed partly due to poor performance of the test setup, but this should be the subject of further study. The work of Chi and Uang (2002) and Ricles *et al*. (2004) could be further developed in the context of the proposed SPSW implementation to properly design columns and surrounding framing to prevent such twisting of columns. Future tests of multistory SPSWs may use composite floors to observe if these can provide positive bracing effect against column twisting.

7.4.3 SPSWs with Cutout Corners

Although not further analyzed in this chapter, the cutout reinforced corner (CR) specimen concept tested in the preceding chapters also deserves further investigation. Chapter 3 presented a preliminary design procedure, but utilized some conservative assumptions with respect to frame deformations imparting forces on the corner reinforcing arch. Refinement of this procedure and defining of acceptable mechanisms for the ultimate behavior of the arch component could ensure the robust performance of the entire system for various geometries and frame properties.

SECTION 8

SUMMARY, CONCLUSIONS, and RECOMMENDATIONS

8.1   Summary

In this report, new design concepts were proposed and developed for frames using Steel Plate Shear Walls (SPSW) as a lateral force resisting system. After a review of previous research, a method for efficient design of the anchor beams located at the top and bottom levels of a multistory SPSW-infilled frame was formulated. This method suggested that the use of Reduced Beam Section (RBS) end detailing can be effective to prevent plastic hinging within the beam span, while simultaneously resulting in a lighter anchor beam design.

Some approximate drift limits to avoid yielding in intermediate beams and SPSW-adjacent columns were developed. These expressions could serve as aids for design, particularly as initial indicators of the appropriateness of a selected SPSW system to be implemented within the structural "fuse" concept, by which the infill panels and the aforementioned anchor beams serve as sacrificial elements in a seismic event, dissipating the input energy while the remainder of the frame is intended to behave elastically. This approach would allow for minimal disruption to building operations after a damaging earthquake, by only requiring replacement of the infill panels and possibly the upper and lower anchor beams.

Two methods were proposed to accommodate utility pass-through in SPSWs. One method slightly alters a solid panel by introducing a reinforced, quarter-circle cutout into each upper corner of the infill panel. This system is intended to transfer the full panel diagonal tension field forces to the boundary frame, and therefore provide the same overall strength as a solid panel, and simultaneously provide a means for utilities to penetrate the infill, as required in a retrofit or new design situations. A simple method was presented for the preliminary design of these reinforcement members.

Another proposed system introduces multiple circular perforations, arranged in regularly-spaced diagonal strips within the perimeter of the infill panel. This system would allow utility pass-through, while also serving as a means of reducing the strength and stiffness of a solid panel

285

uniformly throughout the panel by distributing the effects of perforations throughout the panel tension stress field. A stiffness reduction factor was derived for the proposed perforation layout, and a design method for selecting a perforation size and spacing based on a desired stiffness reduction was proposed. This option may be beneficial to designers who feel an SPSW system is suited to a particular structure, but the required solid infill thickness is unreasonably small. A method of estimating strength reduction due to the presence of a single perforation within a panel, as presented in past research, was discussed as suitable for this system.

An experimental program was designed to investigate some of the above concepts. Quasi-static, cyclic testing was carried out on four single-story, single-bay specimens, of approximately half scale in size. These experiments implemented low yield strength (LYS) steel into an SPSW for the first time, in addition to investigating the anchor beam design and utility-accommodating concepts discussed above. Each system behaved in a robust, ductile manner, resisting imposed displacement loading to a drift of 3% or greater. Detailed finite element models were developed for each specimen and showed good correlation with the experimental results.

A "trial" specimen, utilizing a solid panel, performed well until a weld with an incomplete penetration (faulty workmanship) at a beam to column connection fully fractured during cyclic testing. The weld detail was changed and prevented the occurrence of this behavior in the subsequently tested three specimens. Fractures also appeared in the infill panel of the trial specimen, adjacent to where the seam welds had been ground down, a fabrication step that was also eliminated from subsequent specimens.

Specimen P contained twenty circular perforations in the infill panel and was tested to a maximum interstory drift of 3% ($10\delta_y$) and base shear of 1790kN. Specimen strength and elastic stiffness were approximately 85.5% and 81.5% lower, respectively, than the values obtained for a similar solid panel specimen at comparable drift levels. Testing was stopped after significant fractures had occurred in the bottom beam RBS and severe twisting had occurred in the top beam and top of the columns, damaging the lateral supports at those locations.

Specimen CR utilized reinforced quarter-circle cutouts in the panel corners and was tested to a maximum interstory drift of 4% ($13.3\delta_y$) and maximum base shear of 2050kN. Following fracture of the bottom flange in both bottom beam RBS connections at the peak displacement,

the overall specimen strength had dropped by an average of 30% from the peak value. Top beam horizontal distortions and top of column twisting made restraint of the specimen too difficult to continue the testing up to larger drifts.

Specimen S2, a solid infill panel specimen, was successfully tested to a maximum interstory drift of 3% ($10\delta_y$) and maximum base shear of 2115kN. Fracture of the bottom flange of each bottom beam RBS connection resulted in a specimen strength reduction of approximately 18% at the conclusion of testing. The top beam distortions and top of column twisting observed previously were also observed here, requiring the conclusion of testing.

Finite element models of the tested specimens were developed and analyzed using non-linear quasi-static cyclic analysis to investigate their behavior. Shell elements were chosen to explicitly model parts of the tested specimen, including the panels, and boundary frame member webs and flanges. Good agreement in overall behavior between the test results and the analyses was observed. Analysis results were compared with the simpler strip models and manual calculations used in the specimen design and development of the experimental displacement loading history. The simpler strip models provided a reasonable estimate of displacement and strength at initial yield.

A finite element study of the behavior of perforated plates in tension was conducted using the model of the perforated panel specimen, and idealized "typical perforated strips" for a range of geometries. Results of this study, along with those of a study on the strength of tension flanges with holes, were used to formulate recommend design guidelines for perforated SPSWs.

A review of literature examining the stability of RBS connections was conducted and used to investigate the stability of the beams in the tested specimens. Recommendations were made for the design of SPSWs with RBS connections in the anchor beams.

8.2   Conclusions and Recommendations

During cyclic testing, each specimen exhibited behavior in which beam plastic hinging was located at the connection locations. This was desired as it ensured that the beam could continue to "anchor" the infill panel tension field forces without developing a collapse mechanism, with

mid-span plastic hinging that could compromise the overall system strength. This, together with the design concepts developed in chapter 3, showed the effectiveness of RBS connections in SPSW anchor beams and is recommended to control boundary frame yielding during a significant earthquake. In this application, measures must be taken to prevent column twisting, as described in chapter 7.

A specially detailed perforated panel SPSW specimen exhibited ductile behavior during testing. This result, combined with that of an FEM analytical study, demonstrated that this system is a viable alternative to a solid panel SPSW, without the need for stiffeners around the perforations as required by current seismic design specifications (AISC 2005). This system could allow utility access through the panel. This system is also recommended for use in SPSW applications for which, if the minimum available plate thickness is too large, the effective strength of the solid panel must be reduced to minimize the force demand (from capacity design) on the surrounding frame.

It is recommended that future seismic design specifications follow the proposed guidelines suggested for perforation layout in relation to material yield and ultimate strengths, to ensure ductile performance of this system during a seismic event. It is estimated that SPSW system drifts during the design earthquake should be typically less than 1.5% and all systems tested as part of this project performed satisfactorily at the drift.

The cutout reinforced corner system also performed well during testing and appears to be an effective solution for SPSW implementation and allows for the passage of utilities at panel corners near to the columns. The suggested design steps for this system presented in chapters 3 and 4 are recommended at this time.

8.3   Recommendations for Future Research

8.3.1 Multistory Frame Design with SPSWs

1. The yield drift limits for frame and panel behavior for use in the structural "fuse" concept for SPSWs should be studied further. The work presented here suggested limits derived based on a number of assumptions. A parametric study should investigate the appropriateness of these assumptions, how various member sizes and frame aspect ratio affects these limits, and

the effectiveness of these limits to prevent the formation of plastic hinges in columns during actual earthquake excitation.

2. The effect on the seismic performance of secondary building systems, due to the addition of SPSWs in a building, should be investigated. A parametric study, subjecting a SPSW building to a suite of ground motions with various characteristics, is desirable to study the effect of variation in panel thickness and panel strength on floor displacement and acceleration response spectra.

3. Low yield steel is advantageous for use in SPSWs. However, until the use of LYS is more prevalent in construction, the more commonly specified steel grades should be considered during research, to ensure the acceptability of research findings in promoting the potential benefits of the SPSW system.

8.3.2 Perforated Panel Walls

1. The drift predicted by finite element analysis of an individual perforated strip for an assumed local strain adjacent to a perforation differs from that predicted for a finite element analysis of an entire SPSW wall panel. This difference should be studied further to determine the factors influencing this behavior and aid in improving the recommended design procedure for these systems.

2. Detailed finite element mesh refinement studies on a series of perforated strips and on various SPSW panels should be conducted to determine the influence of mesh size on stress/strain concentration adjacent to perforations, and the corresponding effect on the assumed limit states. These additional studies should also be used to generate continuous curves of maximum frame drift versus maximum panel strain to aid in selecting a design with a desired performance limit.

3. The effect of panel buckling on the assumed boundary conditions of the finite element analysis of individual strips should be studied, and how variations in panel thickness contribute to this effect.

4. The effect of statistical variation in F_y/F_u for various steel grades and plate thicknesses anticipated for use in SPSW systems should be studied. The assumption that the specified yield and ultimate strengths in thin plates used for SPSWs would have equal or smaller variation than those considered in the tension flange study (Dexter *et al*. 2002) upon which some of the design recommendations are based should be verified.

5. A parametric study should be conducted to determine the effect of the choice of inelastic material model (i.e. post elastic stiffness and hardening rule) on the panel drift (or strip elongation) when local strain limit states are reached.

6. Conditions that may exist (if any) leading to panel fracture during testing, possibly due to low cycle fatigue as a result of buckling and yielding deformations that occurred between perforations, should be studied. Testing of panels with various perforation sizes and spacing would be required for this purpose. This could provide additional limit states to define the expected behavior during a seismic event.

7. The effect of perforated layout on the panel performance should be studied. Whereas the tested specimen placed strips at a layout angle of $\theta = 45°$ (near the typical angle of tension field formation), the placement of strips at other angles should be studied.

8.3.3 RBS Connections in SPSW Anchor Beams

1. The twisting observed in the columns of tested specimens at drift in excess of 3% was of significance and attributed partly due to poor performance of the test setup, but this should be the subject of further study. The work of Chi and Uang (2002) and Ricles *et al*. (2004) could be further developed in the context of the proposed SPSW implementation to design columns and surrounding framing to prevent undesirable twisting of columns. Future tests of multistory SPSWs may use composite floors to observe if these can provide positive bracing effect against column twisting.

2. The low cycle fatigue strength of RBS connections should be investigated in the context of SPSW anchor beams. The additional strains imposed on the connection (as compared with bare frame non-SPSW applications) due to infill panel forces should be considered.

8.3.4 SPSWs with Cutout Corners

1. The effect of frame deformations imparting forces on the corner reinforcing arch should be studied further. While the deformed shape used in developing the preliminary design steps presented in chapters 3 and 4 was appropriate for the tested specimen, which used RBS beam-to-column connections, intermediate floors in a multistory building would presumably undergo less deformation, making the proposed design procedure conservative for the design of the corner arches.

2. The presented design procedure assumed a flat plate arch in calculations. A fish plate was added to facilitate attachment of the infill panel to the arch. The potential effect of this plate in providing stiffer and stronger arch behavior should be investigated.

SECTION 9

REFERENCES

AISC. (2002). "Seismic Provisions for Structural Steel Buildings." *ANSI/AISC 341-02*, American Institute of Steel Construction, Inc., Chicago, Ill, May 21, 2002.

AISC. (2005a). "Seismic Provisions for Structural Steel Buildings – Draft dated 3/9/05." *ANSI/AISC 341-05*, American Institute of Steel Construction, Inc., Chicago, Ill.

AISC. (2005b). "Specification for Structural Steel Buildings." *ANSI/AISC 360-05*, American Institute of Steel Construction, Inc., Chicago, Ill, March 9, 2005.

Astaneh-Asl, A. (2001). "Seismic Behavior of Steel Plate Shear Walls." *Steel Tips Report,* Structural Steel Education Council, Moraga, CA, July 2001.

Behbahanifard, M. R., Grondin, G. Y., and Elwi, A. E. (2003). "Experimental and Numerical Investigation of Steel Plate Shear Wall." *Structural Engineering Report 254,* University of Alberta, Department of Civil and Environmental Engineering, September 2003.

Berman, J. W. and Bruneau, M. (2003a). "Experimental Investigation of Light-Gauge Steel Plate Shear Walls for the Seismic Retrofit Of Buildings." *Technical Report MCEER-03-0001,* Multidisciplinary Center for Earthquake Engineering Research, Buffalo, N.Y., May 2, 2003.

Berman, J. W. and Bruneau, M. (2003b). "Plastic Analysis and Design of Steel Plate Shear Walls." *Journal of Structural Engineering*, ASCE, Vol. 129, No. 11, pp. 1148-1156.

Berman, J. W. and Bruneau, M. (2005). "Experimental Investigation of Light-Gauge Steel Plate Shear Walls." *Journal of Structural Engineering*, ASCE, Vol. 131, No. 2, pp. 259-267.

Brady, W. G. and Drucker, D. C. (1955). "Investigation and Limit Analysis of Net Area in Tension." *Transactions of the American Society of Civil Engineering*, Vol. 120, pp. 1133-1164.

Bruneau, M., Uang, C-M, Whittaker, A.S. (1998). "Ductile Design of Steel Structures." McGraw-Hill, New York.

CSA. (2001). "CAN/CSA–S16–01 – Limit States Design of Steel Structures." Canadian Standards Associations." Mississauga, Ontario, Canada, 146 pages.

Dafalias, Y.F., and Popov, E.P. (1976). "Plastic Internal Variables Formalism of Cyclic Plasticity." *Journal of Applied Mechanics*, ASCE, Vol. 43, pp. 645-651.

Driver, R. G., Kulak, G. L., Kennedy, D. J. L., and Elwi, A. E. (1997). "Seismic Behavior of Steel Plate Shear Walls." *Structural Engineering Report 215,* University of Alberta, Department of Civil and Environmental Engineering, February 1997.

Eatherton, M. and Johnson, K. (2004). "High End Residence using Steel Plate Shear Walls in Woodside, California." SEAOC Convention Proceedings, August 2004.

Eligator, M. H., Chu, S. L., and Occhicone, L. A. (1997). "Tall Buildings." *Structural Engineering Handbook*, Fourth Edition, Gaylord, Edwin H., Gaylord, Charles N., and Stallmeyer, James E., Eds., The McGraw-Hill Companies, Inc., Section 25.

FEMA (2000). "FEMA 350: Recommended Seismic Design Criteria for New Steel Moment-Frame Buildings." SAC Joint Venture for the Federal Emergency Management Agency, Washington, D.C.

FEMA (2004). "FEMA 450: NEHRP Recommended Provisions For Seismic Regulations For New Buildings And Other Structures." Building Seismic Safety Council for the Federal Emergency Management Agency, Washington, D.C.

Gilton, C., Chi, B., and Uang, C-M. (2000). "Cyclic Response of RBS Moment Connections: Weak-Axis Configuration and Deep Column Effects." *Report No. SSRP-00/03*, University of California, San Diego, Department of Structural Engineering, La Jolla, Calif., July 2000.

Hibbitt, Karlsson, and Sorenson, Inc. (HKS) (2002a). "ABAQUS/CAE Users Manual." Version 6.3, Hibbitt, Karlsson, and Sorenson, Inc., Pawtucket, Rhode Island.

Hibbitt, Karlsson, and Sorenson, Inc. (HKS) (2002b). "ABAQUS/Standard Users Manual." Version 6.3, Hibbitt, Karlsson, and Sorenson, Inc., Pawtucket, Rhode Island.

Hitaka, T. and Matsui, C. (2003). "Experimental Study on Steel Shear Wall with Slits." *Journal of Structural Engineering*, ASCE, Vol. 129, No. 5, pp. 586-595.

Hodge, P.G., Jr. (1957). "Discussion of Prager's 'A New Method of Analyzing Stress and Strains in Work-Hardening Solids'." *Journal of Applied Mechanics,* ASME, Vol. 23, pp. 482-484.

Kaufmann, E. J., Metrovich, B., Pense, A. W. (2001). "Characterization of Cyclic Inelastic Strain Behavior On Properties of A572 Gr. 50 and A913 Gr. 50 Rolled Sections." *ATLSS Report No. 01-13,* National Center for Engineering Research on Advanced Technology for Large Structural Systems, Lehigh University, Bethlehem, PA, December 2001.

Kharrazi, M. H. K., Ventura, C. E., Prion, H. G. L., and Sabouri-Ghomi, S. (2004). "Bending and Shear Analysis and Design of Ductile Steel Plate Walls." *Proceedings of the 13th World Conference on Earthquake Engineering*, Vancouver, B.C., Canada, August 1-6, 2004, Paper No. 77.

Krieg, R.D. (1975). "A Practical Two-Surface Plasticity Theory." *Journal of Applied Mechanics*, ASCE, Vol. 42, pp. 641-646.

Kulak, G. L., Kennedy, D. J. L., Driver, R. G., and Medhekar, M. (2001). "Steel Plate Shear Walls – An Overview." *AISC Engineering Journal,* Vol. 38, No. 1. First Quarter 2001.

Lemaitre, J., and J-L. Chaboche. (1990). "Mechanics of Solid Materials." Cambridge University Press.

Lin, Y.C. and Tsai, K.C. (2004). "Seismic Responses of Steel Shear Wall Constructed with Restrainers" (in Chinese) *Technical Report NCREE-04-015,* National Center for Research on Earthquake Engineering, Taipei, Taiwan, R.O.C., September 2004.

Lubell, A., Prion, H., Ventura, C., and Rezai, M. (2000). "Unstiffened steel plate shear wall performance under cyclic loading." *Journal of Structural Engineering*, ASCE, Vol. 126, No. 4, pp. 453-460.

Maeda, Y., Yamaguchi, T., Takeuchi, T., and Ikebe, T. (2001). "Seismic Control Devices Using Low-Yield-Point Steel." *Technical Report MCEER-01-0002, Proceedings of the Second MCEER Workshop on Mitigation of Earthquake Disaster by Advanced Technologies (MEDAT-2).* Multidisciplinary Center for Earthquake Engineering Research, Buffalo, N.Y., July 23, 2001.

NCREE (2002). "Reaction Wall & Strong Floor Test System" NCREE Laboratory Experimental Facilities, <http://www.ncree.gov.tw/eng/3_lab/facility/Facilities2.htm> (February 19, 2003).

Ricles, J. M., Zhang, X., Lu, L-W, Fisher, J. (2004). "Development of Seismic Guidelines for Deep-Column Steel Moment Connections." *ATLSS Report No. 04-13,* National Center for Engineering Research on Advanced Technology for Large Structural Systems, Lehigh University, Bethlehem, PA, June 2004.

Roberts, T. and Sabouri-Ghomi, S. (1991). "Hysteretic characteristics of unstiffened plate shear panels." *Thin Walled Structures*, Vol. 12, No. 2, pp. 145-162.

Roberts, T. and Sabouri-Ghomi, S. (1992). "Hysteretic characteristics of unstiffened perforated steel plate shear panels." *Thin Walled Structures*, Vol. 14, pp. 139-151.

Schumacher, A., Grondin, G.Y., and Kulak, G.L. (1999). "Connection of infill panels in steel plate shear walls." *Canadian Journal of Civil Engineering*, Vol. 26, No. 5, pp. 549-563.

Seaburg, P. A., and Carter, C. J. (1997). "Torsional Analysis of Structural Steel Members." *Steel Design Guide Series 9*, American Institute of Steel Construction, Inc., Chicago, Ill.

Taranath, B. S. (1998). "Steel, Concrete, & Composite Design of Tall Buildings." Second Edition, The McGraw-Hill Companies, Inc, New York.

Thorburn, L. Jane, Kulak, G. L., and Montgomery, C. J. (1983). "Analysis of Steel Plate Shear Walls." *Structural Engineering Report No. 107,* Department of Civil Engineering, The University of Alberta, Edmonton, Alberta, May 1983.

Timler, P. A. and Kulak, G. L. (1983). "Experimental Study of Steel Plate Shear Walls." *Structural Engineering Report No. 114,* Department of Civil Engineering, The University of Alberta, Edmonton, Alberta, November 1983.

Tsai, K.C., Chen, H-W, Hong, C-P, Su, Y-F. (1993). "Design of Steel Triangular Plate Energy Absorbers for Seismic Resistant Construction." *Earthquake Spectra*, Vol. 9, No. 3.

Tsai, K.C. and Huang, Y.C. (2002). "Experimental Responses of Large Scale Buckling Restrained Braced Frames." *Report No. CEER/R91-03,* Center for Earthquake Engineering Research, National Taiwan University. (in Chinese)

Uang, C-M, Nakashima, M. (2003). "Steel Buckling-Restrained Braced Frames." *Earthquake Engineering: Recent Advances and Applications*, Chapter 16, Ed: Bozorgnia, Yousef, and Bertero, Vitelmo, CRC Press.

Uang, C-M. and Fan, C-C. (1999). "Cyclic Instability Of Steel Moment Connections With Reduced Beam Sections." *Report No. SSRP-99/21*, University of California, San Diego, Department of Structural Engineering, La Jolla, Calif., December 1999.

Uang, C-M. and Fan, C-C. (2001). "Cyclic Stability Criteria for Steel Moment Connections with Reduced Beam Sections." *Journal of Structural Engineering*, ASCE, Vol. 127, No. 9, pp. 1021-1027.

Vargas, R. and Bruneau, M. (2004). "Seismic Response of Single Degree (SDOF) Structural Fuse Systems." *Proceedings of the 13th World Conference on Earthquake Engineering*, Vancouver, B.C., Canada, August 1-6, 2004, Paper No. 3277.

Whittaker, A.S., Bertero, V.V., Thompson, C.L., and Alonso, L.J. (1991). "Seismic Testing of Steel Plate Energy Dissipation Devices." *Earthquake Spectra*, Vol. 7, No. 4, pp. 563- 604.

Xue, M. and Lu, L-W. (1994a). "Interaction of Infilled Steel Shear Wall Panels with Surrounding Frame Members." Proceedings, 1994 Annual Task Group Technical Session, Structural Stability Research Council: reports on current research activities: June 20, 1994, Lehigh University, Bethlehem, Pa.

Xue, M. and Lu, L-W. (1994b). "Monotonic and Cyclic Behavior of Infilled Steel Shear Panels." The Seventeenth Czech and Slovak International Conference on Steel Structures and Bridges, Bratislava, Slovakia, September 1994.

Yang, T.Y., and Whittaker, A.S. (2002). "MCEER Demonstration Hospitals – Mathematical Models and Preliminary Results", *Technical Report*, Multidisciplinary Center for Earthquake Engineering Research, University at Buffalo, Buffalo, NY.

Yu, Q. S., Gilton, C., and Uang, C-M. (2000). "Cyclic Response Of RBS Moment Connections: Loading Sequence And Lateral Bracing Effects." *Report No. SSRP-99/13*, University of California, San Diego, Department of Structural Engineering, La Jolla, Calif., July 2000.

Zoruba, S. and Grubb, K. A. (2003). "Do You 992?." *Modern Steel Construction,* American Institute of Steel Construction, Chicago, Ill., January 2003.

APPENDIX A

MIGRATION OF APPROXIMATE COLUMN INFLECTION POINT LOCATIONS FOR FRAME WITH SPSW INFILL PANEL

A.1 General

In section 3.3.1.2, approximate yield drift limits were presented for an SPSW-infilled frame at yield. Assuming that the lateral drift between column inflection points for a bare frame (using the assumptions inherent in the "Portal Method" of moment frame analysis) was equivalent to that of a frame with SPSW infill panels in equations (3-25) and (3-31), respectively, the section below describes that assumed behavior.

A.2 Use of Portal Method with SPSW Infill Panels

In the portal method of moment frame analysis (Taranath 1998, Eligator *et al.* 1997), several assumptions are made in order to calculate internal forces:

1. Column inflection points are at mid-height
2. Beam inflection points are at mid-span
3. Story shears are distributed to column inflection points based on tributary widths

An additional assumption can be made for the relative bending stiffness of the beams and columns in the frame bent, such that simple hand calculations can be used to estimate required member sizes based on the distribution of frame bending moments. This provides good initial member sizes for use in more rigorous computer analysis to complete the frame design using nonlinear static and dynamic techniques.

A.2.1 Method 1 (as used Chapter 3)

In chapter 3, the estimated drift limits assume that the typical cruciform frame bent, as shown in figures 3-9 through 3-12, remains elastic as it displaces and is subjected to the panel yielding forces. The column inflection points are assumed to migrate downward equally from the mid-height locations shown in figure 3-12, for both the upper and lower column stubs. However, the additional column lateral displacement due to this effect is assumed negligible based on the

panel-column loading condition assumed in figure 3-13. From this figure, the column displacement due to this panel effect, Δ_p, at a distance y above the beam is given as:

$$\Delta_p(y) = \frac{\omega \cdot y^2}{24 \cdot E \cdot I_c} \cdot (H - y)^2 \qquad\qquad \text{(A-1)}$$

where all other variables have been presented previously. The top column stub displacement due to frame action, Δ_f, at a distance y above the beam, is given by:

$$\Delta_f(y) = \frac{F_H \cdot y^2}{12 \cdot E \cdot I_c} \cdot [3 \cdot H - 2 \cdot y] \qquad\qquad \text{(A-2)}$$

The displacement of the bottom column stub is given by the same expression, but with "$H - y$" substituted for y. The bottom column stub displacement is also in the opposite direction (i.e. to the left in the figure) as compared with the top column stub. However, the top and bottom column stub displacements due to the panel effect are both positive values. Therefore, assuming the inflection points have migrated the same amount below mid-column height in the top and bottom column beam stubs, to a position y_{inp}, and H - y_{inp}, respectively, the total relative displacement between these inflection points is given by:

$$\Delta_{total}(y_{inp}) = \{\Delta_f(y_{inp}) + \Delta_p(y_{inp})\} - \{-\Delta_f(H - y_{inp}) + \Delta_p(H - y_{inp})\} \qquad \text{(A-3)}$$

which simplifies to:

$$\Delta_{total}(y_{inp}) = \Delta_f(y_{inp}) + \Delta_f(H - y_{inp}) = \frac{F_H \cdot H^3}{12 \cdot E \cdot I_c} \qquad\qquad \text{(A-4)}$$

This is identical to the displacement from column bending as given in (3-20).

A.2.2 Method 2 (for future investigation)

The above development assumed independent kinematic relations for the frame action and the effects of the SPSW infill panel on a moment frame to show that relative lateral displacements between assumed column inflection points above and below a beam within a typical cruciform bent are identical, for elastic frame behavior. However, another means for calculating the effect of panel forces on the migration of column inflection points, based on internal force equilibrium, is presented below for future investigation.

Figure A-1 (a) shows the typical frame bent interior cruciform with panel forces as considered in figure 3-12. Figure A-1 (b) shows how the moment diagram and the location of assumed column inflection points are shifted as a result of panel force effects described section 3.3.1.2, and shown in figure 3-13. The frame action moment diagrams are shown with dashed lines, while the combined moment diagram as a result of the panel force effects is shown with the bold, solid line.

Equilibrium for the revised cruciform is calculated based on the column inflection point locations for "Combined effect", as shown in figure A-1 (a), with a shorter column cantilever stub in the upper section of the cruciform, and a longer column cantilever stub in the lower section, with lengths of y_o above the beam and $H - y_o$ below the beam, respectively. The lateral displacement occurring at the top column stub inflection point, Δ_{top}, is the sum of cantilever displacement due to the inflection point shear (from both frame and panel effects), as well as the distributed panel load acting on the cantilever column stub, as given by:

$$\Delta_{top} = \frac{\left(F_H + \omega \cdot \left(\frac{H}{2} - y_o\right)\right) \cdot y_o^3}{3 \cdot E \cdot I_c} + \frac{\omega \cdot y_o^4}{8 \cdot E \cdot I_c} \tag{A-5}$$

Similarly, the lateral displacement at the bottom inflection point, Δ_{bot}, is given by:

$$\Delta_{bot} = \frac{\omega \cdot (H - y_o)^4}{8 \cdot E \cdot I_c} - \left[\frac{\left(F_H + \omega \cdot \left(\frac{H}{2} - y_o\right)\right) \cdot (H - y_o)^3}{3 \cdot E \cdot I_c}\right] \tag{A-6}$$

Total displacement (due to column bending) between column inflection points is then calculated by subtracting Δ_{bot} from Δ_{top}, giving:

$$\Delta_{c.total} = \Delta_{top} - \Delta_{bot} = \frac{\left(F_H + \omega \cdot \left(\frac{H}{2} - y_o\right)\right)}{3 \cdot E \cdot I_c} \cdot \left[y_o^3 + (H - y_o)^3\right] + \cdots$$
$$\cdots + \frac{\omega}{8 \cdot E \cdot I_c} \cdot \left[y_o^4 - (H - y_o)^4\right] \tag{A-7}$$

In contrast with the assumptions of Method 1 presented in section A.2.1, the displacement at each inflection point due to frame and panel effects is calculated together, since the internal shear from both effects was considered simultaneously. The location of the column inflection points can be calculated by setting the column moment of equation (3-26) equal to zero:

$$M_{tot.c}(y_o) = 0 = M_C \cdot \left[1 - \frac{2 \cdot y_o}{H}\right] + \frac{\omega}{12} \cdot \left[6 \cdot y_o^2 + H^2 - 6 \cdot H \cdot y_o\right] \qquad \text{(A-8)}$$

Solving this expression for upper column stub inflection point distance above the beam:

$$y_o = \frac{1}{2} \cdot \left(\left[H + \frac{4 \cdot M_C}{\omega \cdot H}\right] \pm \sqrt{\left[H + \frac{4 \cdot M_C}{\omega \cdot H}\right]^2 - 4 \cdot \left[\frac{H^2}{6} + \frac{2 \cdot M_C}{\omega}\right]} \right) \qquad \text{(A-9)}$$

Both the expressions for the displacement (and resulting drift) and inflection point using this method are based on having knowledge of the contribution of the frame effect, as observed in the portal method, as compared with the panel tension field effect on boundary frame behavior.

In the displacement expression, (A-7), the lateral force, F_H, acting on the column, is the share of the story shear resisted by the frame. However, since the panel tension field force is related to the frame displacement, the appropriate percent contributions towards story shear resistance by each component should be studied further. In the inflection point expression, (A-9), the column moment due to frame action, M_c, is utilized. Studying the relative contribution between panel and frame action towards this effect would help guide rational design of SPSW systems.
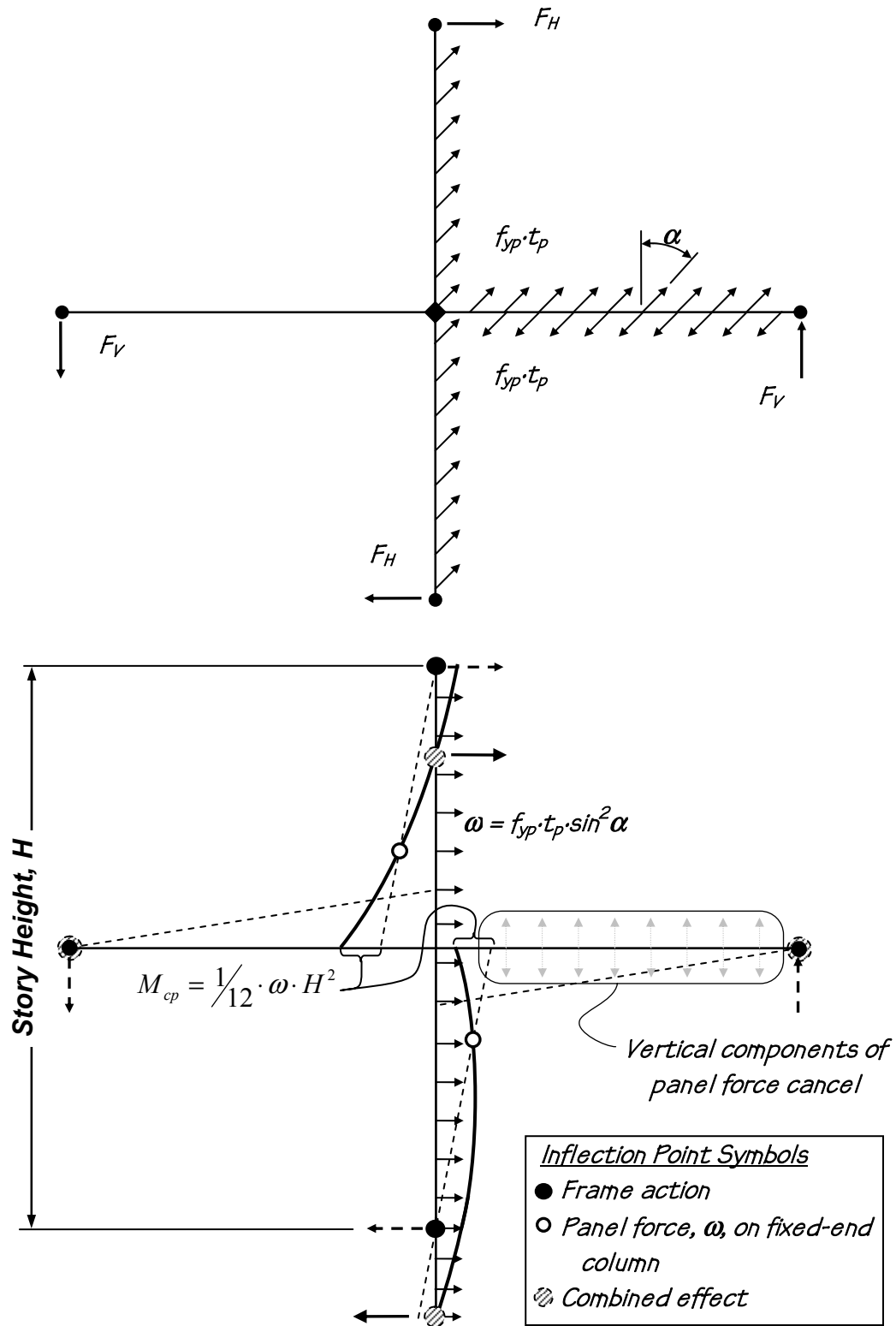
FIGURE A-1 Frame Interior Joint Cruciform with SPSW Infill Panel Forces
(a) Free Body Diagram on Original Frame Cruciform;
(b) Moment Diagram with Adjusted Inflection Point Locations

APPENDIX B

DRIFT LIMITS IN DEFINING SPSW AND
BOUNDARY FRAME DESIGN CONSTRAINTS

B.1   General

This appendix describes how the drift limits presented in chapter 3 can be developed into design equations that limit panel and member sizes by imposing constraints on system behavior. This approach relies on the same portal method assumptions described in chapter 3 and appendix A, and additionally assumes regularity in the framing member sizes between adjacent floor levels and adjacent bays. Therefore, just as the portal method is utilized to aid in selecting preliminary sizes for MRF members, the design equations below may be useful for *initial* design calculations in both retrofit and design situations using SPSW infill panels within a steel MRF.

B.2   Ensuring SPSW Infill Panel as a "Fuse"

The approximate yield drift limits derived in section 3.3.1 for frames with SPSW infill panels could be used in conjunction with expressions for infill panel yield drift to achieve system behavior analogous to the structural fuse concept, using the SPSW infill as a sacrificial element protecting the surrounding frame from damage during and earthquake. The structural fuse concept would require that the sacrificial element exhibit a yielding mechanism without strength and stiffness degradation, so in this case the fuse analogy is imperfect, but the following equations are nonetheless instructive in setting goals to empirically minimize the extent of yielding in the MRF.

For the SPSW strip model (Thorburn and Kulak 1983), the yield displacement for an infill panel is given by:

$$\Delta_{yp} = \frac{2 \cdot H \cdot F_{yp}}{E \cdot \sin 2\alpha} \tag{B-1}$$

which can be expressed in terms of a panel drift:

$$\gamma_{yp} = \frac{\Delta_{yp}}{H} = \frac{2 \cdot F_{yp}}{E \cdot \sin 2\alpha} \tag{B-2}$$

303

To ensure that the frame/panel system behaves in accordance with the structural fuse concept (Vargas and Bruneau 2004), this approximate panel yield drift can be compared against the approximate frame drift limits developed in chapter 3:

$$\gamma_{yp} \le \gamma_y \tag{B-3}$$

Substituting (B-2) and (3-31) into (B-3):

$$\frac{2 \cdot F_{yp}}{E \cdot \sin 2\alpha} \le \frac{1}{6 \cdot E} \cdot \left(\frac{H}{I_c} + \frac{L}{I_b} \right) \cdot \left(S_{xc} \cdot F_{yc} - \tfrac{1}{12} \cdot F_{yp} \cdot t_p \cdot \sin^2 \alpha \cdot H^2 \right) \tag{B-4}$$

This inequality can be solved for the panel thickness, t_p:

$$t_p \le \cdot \left(S_{xc} \cdot F_{yc} - \frac{12 \cdot F_{yp}}{\sin 2\alpha \cdot \left(\dfrac{H}{I_c} + \dfrac{L}{I_b} \right)} \right) \frac{12}{F_{yp} \cdot H^2 \cdot \sin^2 \alpha} \tag{B-5}$$

Note that while (B-5) assumes elastic perfectly plastic material behavior and that frame and panel yield occur simultaneously when the upper limit of the inequality is satisfied, the expression could be modified to account for other considerations. For example, if a target panel ductility, μ_p, is desired at initial frame yield, then this factor would be introduced to multiply both sides of (B-1) and carried through the above derivation so that (B-5) becomes:

$$t_p \le \cdot \left(S_{xc} \cdot F_{yc} - \frac{12 \cdot F_{yp} \cdot \mu_p}{\sin 2\alpha \cdot \left(\dfrac{H}{I_c} + \dfrac{L}{I_b} \right)} \right) \frac{12}{F_{yp} \cdot H^2 \cdot \sin^2 \alpha} \tag{B-6}$$

Note that an additional overstrength factor could be implemented as well, to account for a strain hardening material (instead of elastic perfectly plastic) and other factors that increase the panel strength at the considered drift.

These expressions may be useful in a retrofit situation to determine the maximum panel thickness (given the panel material strength, F_{yp}) for which the surrounding steel frame properties are known.

The inequality of (B-4) could also be solved to obtain the required column section modulus if all other properties are known:

$$S_{xc} \geq \left(\frac{t_p \cdot H^2 \cdot \sin^2 \alpha}{12} + \frac{12}{\sin 2\alpha \cdot \left(\dfrac{H}{I_c} + \dfrac{L}{I_b} \right)} \right) \frac{F_{yp}}{F_{yc}} \qquad \text{(B-7)}$$

By including the target panel ductility at frame yield as in (B-6), (B-7) becomes:

$$S_{xc} \geq \left(\frac{t_p \cdot H^2 \cdot \sin^2 \alpha}{12} + \frac{12 \cdot \mu_p}{\sin 2\alpha \cdot \left(\dfrac{H}{I_c} + \dfrac{L}{I_b} \right)} \right) \frac{F_{yp}}{F_{yc}} \qquad \text{(B-8)}$$

This expression would be appropriate in a new frame design situation to determine the required flexural strength of a boundary column for known panel properties, and, in the case of (B-8), for a target panel ductility at the frame yield drift.

B.3   Design Considerations/Implications

The above equations can be used to initiate SPSW frame design using the portal method. First, the moment frame can be sized to resist a certain percentage of the base shear. This provides a starting point for system design, by preliminarily sizing the moment frame using the equivalent lateral force (ELF) procedure to distribute story shears and the portal method to size beams and columns.

Following the initial moment frame member sizing, the panel can be preliminarily sized for a known material strength, F_{yp}, using equation (B-5) or (B-6), to ensure the frame will not yield when the panel has fully yielded. Then the panel story strength is checked versus the remaining story shear not resisted by the moment frame, using (2-4), or from AISC (2005a):

$$V_{yp} = 0.42 \cdot F_{yp} \cdot t \cdot W_{panel} \cdot \sin 2\alpha \qquad \text{(B-9)}$$

Where the nomenclature of this dissertation (F_{yp}, t, and W_{panel}) has been substituted for panel material strength, F_y; panel thickness, t_w, and width between column flanges, L_{cf}, as used in AISC (2005a). The tension field inclination angle, α, may be taken as 45° for initial calculations.

If the design equations for desired performance are not satisfied, then another iteration is performed in which the portion of the base shear resisted by the moment frame is increased and the panel redesigned as above until the system can resist the total base shear and the design constraints preventing undesirable yielding are satisfied.

Future research should investigate the interaction between the relative stiffness of the moment frame and the SPSWs to determine appropriate percentages of resistance by each system based on stiffness and strength.

Multidisciplinary Center for Earthquake Engineering Research
List of Technical Reports

The Multidisciplinary Center for Earthquake Engineering Research (MCEER) publishes technical reports on a variety of subjects related to earthquake engineering written by authors funded through MCEER. These reports are available from both MCEER Publications and the National Technical Information Service (NTIS). Requests for reports should be directed to MCEER Publications, Multidisciplinary Center for Earthquake Engineering Research, State University of New York at Buffalo, Red Jacket Quadrangle, Buffalo, New York 14261. Reports can also be requested through NTIS, 5285 Port Royal Road, Springfield, Virginia 22161. NTIS accession numbers are shown in parenthesis, if available.

NCEER-87-0001   "First-Year Program in Research, Education and Technology Transfer," 3/5/87, (PB88-134275, A04, MF-A01).

NCEER-87-0002   "Experimental Evaluation of Instantaneous Optimal Algorithms for Structural Control," by R.C. Lin, T.T. Soong and A.M. Reinhorn, 4/20/87, (PB88-134341, A04, MF-A01).

NCEER-87-0003   "Experimentation Using the Earthquake Simulation Facilities at University at Buffalo," by A.M. Reinhorn and R.L. Ketter, to be published.

NCEER-87-0004   "The System Characteristics and Performance of a Shaking Table," by J.S. Hwang, K.C. Chang and G.C. Lee, 6/1/87, (PB88-134259, A03, MF-A01). This report is available only through NTIS (see address given above).

NCEER-87-0005   "A Finite Element Formulation for Nonlinear Viscoplastic Material Using a Q Model," by O. Gyebi and G. Dasgupta, 11/2/87, (PB88-213764, A08, MF-A01).

NCEER-87-0006   "Symbolic Manipulation Program (SMP) - Algebraic Codes for Two and Three Dimensional Finite Element Formulations," by X. Lee and G. Dasgupta, 11/9/87, (PB88-218522, A05, MF-A01).

NCEER-87-0007   "Instantaneous Optimal Control Laws for Tall Buildings Under Seismic Excitations," by J.N. Yang, A. Akbarpour and P. Ghaemmaghami, 6/10/87, (PB88-134333, A06, MF-A01). This report is only available through NTIS (see address given above).

NCEER-87-0008   "IDARC: Inelastic Damage Analysis of Reinforced Concrete Frame - Shear-Wall Structures," by Y.J. Park, A.M. Reinhorn and S.K. Kunnath, 7/20/87, (PB88-134325, A09, MF-A01). This report is only available through NTIS (see address given above).

NCEER-87-0009   "Liquefaction Potential for New York State: A Preliminary Report on Sites in Manhattan and Buffalo," by M. Budhu, V. Vijayakumar, R.F. Giese and L. Baumgras, 8/31/87, (PB88-163704, A03, MF-A01). This report is available only through NTIS (see address given above).

NCEER-87-0010   "Vertical and Torsional Vibration of Foundations in Inhomogeneous Media," by A.S. Veletsos and K.W. Dotson, 6/1/87, (PB88-134291, A03, MF-A01). This report is only available through NTIS (see address given above).

NCEER-87-0011   "Seismic Probabilistic Risk Assessment and Seismic Margins Studies for Nuclear Power Plants," by Howard H.M. Hwang, 6/15/87, (PB88-134267, A03, MF-A01). This report is only available through NTIS (see address given above).

NCEER-87-0012   "Parametric Studies of Frequency Response of Secondary Systems Under Ground-Acceleration Excitations," by Y. Yong and Y.K. Lin, 6/10/87, (PB88-134309, A03, MF-A01). This report is only available through NTIS (see address given above).

NCEER-87-0013   "Frequency Response of Secondary Systems Under Seismic Excitation," by J.A. HoLung, J. Cai and Y.K. Lin, 7/31/87, (PB88-134317, A05, MF-A01). This report is only available through NTIS (see address given above).

NCEER-87-0014   "Modelling Earthquake Ground Motions in Seismically Active Regions Using Parametric Time Series Methods," by G.W. Ellis and A.S. Cakmak, 8/25/87, (PB88-134283, A08, MF-A01). This report is only available through NTIS (see address given above).

NCEER-87-0015   "Detection and Assessment of Seismic Structural Damage," by E. DiPasquale and A.S. Cakmak, 8/25/87, (PB88-163712, A05, MF-A01). This report is only available through NTIS (see address given above).

NCEER-87-0016   "Pipeline Experiment at Parkfield, California," by J. Isenberg and E. Richardson, 9/15/87, (PB88-163720, A03, MF-A01). This report is available only through NTIS (see address given above).

NCEER-87-0017   "Digital Simulation of Seismic Ground Motion," by M. Shinozuka, G. Deodatis and T. Harada, 8/31/87, (PB88-155197, A04, MF-A01). This report is available only through NTIS (see address given above).

NCEER-87-0018   "Practical Considerations for Structural Control: System Uncertainty, System Time Delay and Truncation of Small Control Forces," J.N. Yang and A. Akbarpour, 8/10/87, (PB88-163738, A08, MF-A01). This report is only available through NTIS (see address given above).

NCEER-87-0019   "Modal Analysis of Nonclassically Damped Structural Systems Using Canonical Transformation," by J.N. Yang, S. Sarkani and F.X. Long, 9/27/87, (PB88-187851, A04, MF-A01).

NCEER-87-0020   "A Nonstationary Solution in Random Vibration Theory," by J.R. Red-Horse and P.D. Spanos, 11/3/87, (PB88-163746, A03, MF-A01).

NCEER-87-0021   "Horizontal Impedances for Radially Inhomogeneous Viscoelastic Soil Layers," by A.S. Veletsos and K.W. Dotson, 10/15/87, (PB88-150859, A04, MF-A01).

NCEER-87-0022   "Seismic Damage Assessment of Reinforced Concrete Members," by Y.S. Chung, C. Meyer and M. Shinozuka, 10/9/87, (PB88-150867, A05, MF-A01). This report is available only through NTIS (see address given above).

NCEER-87-0023   "Active Structural Control in Civil Engineering," by T.T. Soong, 11/11/87, (PB88-187778, A03, MF-A01).

NCEER-87-0024   "Vertical and Torsional Impedances for Radially Inhomogeneous Viscoelastic Soil Layers," by K.W. Dotson and A.S. Veletsos, 12/87, (PB88-187786, A03, MF-A01).

NCEER-87-0025   "Proceedings from the Symposium on Seismic Hazards, Ground Motions, Soil-Liquefaction and Engineering Practice in Eastern North America," October 20-22, 1987, edited by K.H. Jacob, 12/87, (PB88-188115, A23, MF-A01). This report is available only through NTIS (see address given above).

NCEER-87-0026   "Report on the Whittier-Narrows, California, Earthquake of October 1, 1987," by J. Pantelic and A. Reinhorn, 11/87, (PB88-187752, A03, MF-A01). This report is available only through NTIS (see address given above).

NCEER-87-0027   "Design of a Modular Program for Transient Nonlinear Analysis of Large 3-D Building Structures," by S. Srivastav and J.F. Abel, 12/30/87, (PB88-187950, A05, MF-A01). This report is only available through NTIS (see address given above).

NCEER-87-0028   "Second-Year Program in Research, Education and Technology Transfer," 3/8/88, (PB88-219480, A04, MF-A01).

NCEER-88-0001   "Workshop on Seismic Computer Analysis and Design of Buildings With Interactive Graphics," by W. McGuire, J.F. Abel and C.H. Conley, 1/18/88, (PB88-187760, A03, MF-A01). This report is only available through NTIS (see address given above).

NCEER-88-0002   "Optimal Control of Nonlinear Flexible Structures," by J.N. Yang, F.X. Long and D. Wong, 1/22/88, (PB88-213772, A06, MF-A01).

NCEER-88-0003   "Substructuring Techniques in the Time Domain for Primary-Secondary Structural Systems," by G.D. Manolis and G. Juhn, 2/10/88, (PB88-213780, A04, MF-A01).

NCEER-88-0004   "Iterative Seismic Analysis of Primary-Secondary Systems," by A. Singhal, L.D. Lutes and P.D. Spanos, 2/23/88, (PB88-213798, A04, MF-A01).

NCEER-88-0005   "Stochastic Finite Element Expansion for Random Media," by P.D. Spanos and R. Ghanem, 3/14/88, (PB88-213806, A03, MF-A01).

NCEER-88-0006   "Combining Structural Optimization and Structural Control," by F.Y. Cheng and C.P. Pantelides, 1/10/88, (PB88-213814, A05, MF-A01).

NCEER-88-0007   "Seismic Performance Assessment of Code-Designed Structures," by H.H-M. Hwang, J-W. Jaw and H-J. Shau, 3/20/88, (PB88-219423, A04, MF-A01). This report is only available through NTIS (see address given above).

NCEER-88-0008   "Reliability Analysis of Code-Designed Structures Under Natural Hazards," by H.H-M. Hwang, H. Ushiba and M. Shinozuka, 2/29/88, (PB88-229471, A07, MF-A01). This report is only available through NTIS (see address given above).

NCEER-88-0009   "Seismic Fragility Analysis of Shear Wall Structures," by J-W Jaw and H.H-M. Hwang, 4/30/88, (PB89-102867, A04, MF-A01).

NCEER-88-0010   "Base Isolation of a Multi-Story Building Under a Harmonic Ground Motion - A Comparison of Performances of Various Systems," by F-G Fan, G. Ahmadi and I.G. Tadjbakhsh, 5/18/88, (PB89-122238, A06, MF-A01). This report is only available through NTIS (see address given above).

NCEER-88-0011   "Seismic Floor Response Spectra for a Combined System by Green's Functions," by F.M. Lavelle, L.A. Bergman and P.D. Spanos, 5/1/88, (PB89-102875, A03, MF-A01).

NCEER-88-0012   "A New Solution Technique for Randomly Excited Hysteretic Structures," by G.Q. Cai and Y.K. Lin, 5/16/88, (PB89-102883, A03, MF-A01).

NCEER-88-0013   "A Study of Radiation Damping and Soil-Structure Interaction Effects in the Centrifuge," by K. Weissman, supervised by J.H. Prevost, 5/24/88, (PB89-144703, A06, MF-A01).

NCEER-88-0014   "Parameter Identification and Implementation of a Kinematic Plasticity Model for Frictional Soils," by J.H. Prevost and D.V. Griffiths, to be published.

NCEER-88-0015   "Two- and Three- Dimensional Dynamic Finite Element Analyses of the Long Valley Dam," by D.V. Griffiths and J.H. Prevost, 6/17/88, (PB89-144711, A04, MF-A01).

NCEER-88-0016   "Damage Assessment of Reinforced Concrete Structures in Eastern United States," by A.M. Reinhorn, M.J. Seidel, S.K. Kunnath and Y.J. Park, 6/15/88, (PB89-122220, A04, MF-A01). This report is only available through NTIS (see address given above).

NCEER-88-0017   "Dynamic Compliance of Vertically Loaded Strip Foundations in Multilayered Viscoelastic Soils," by S. Ahmad and A.S.M. Israil, 6/17/88, (PB89-102891, A04, MF-A01).

NCEER-88-0018   "An Experimental Study of Seismic Structural Response With Added Viscoelastic Dampers," by R.C. Lin, Z. Liang, T.T. Soong and R.H. Zhang, 6/30/88, (PB89-122212, A05, MF-A01). This report is available only through NTIS (see address given above).

NCEER-88-0019   "Experimental Investigation of Primary - Secondary System Interaction," by G.D. Manolis, G. Juhn and A.M. Reinhorn, 5/27/88, (PB89-122204, A04, MF-A01).

NCEER-88-0020   "A Response Spectrum Approach For Analysis of Nonclassically Damped Structures," by J.N. Yang, S. Sarkani and F.X. Long, 4/22/88, (PB89-102909, A04, MF-A01).

NCEER-88-0021   "Seismic Interaction of Structures and Soils: Stochastic Approach," by A.S. Veletsos and A.M. Prasad, 7/21/88, (PB89-122196, A04, MF-A01). This report is only available through NTIS (see address given above).

NCEER-88-0022   "Identification of the Serviceability Limit State and Detection of Seismic Structural Damage," by E. DiPasquale and A.S. Cakmak, 6/15/88, (PB89-122188, A05, MF-A01). This report is available only through NTIS (see address given above).

NCEER-88-0023   "Multi-Hazard Risk Analysis: Case of a Simple Offshore Structure," by B.K. Bhartia and E.H. Vanmarcke, 7/21/88, (PB89-145213, A05, MF-A01).

NCEER-88-0024   "Automated Seismic Design of Reinforced Concrete Buildings," by Y.S. Chung, C. Meyer and M. Shinozuka, 7/5/88, (PB89-122170, A06, MF-A01). This report is available only through NTIS (see address given above).

NCEER-88-0025   "Experimental Study of Active Control of MDOF Structures Under Seismic Excitations," by L.L. Chung, R.C. Lin, T.T. Soong and A.M. Reinhorn, 7/10/88, (PB89-122600, A04, MF-A01).

NCEER-88-0026   "Earthquake Simulation Tests of a Low-Rise Metal Structure," by J.S. Hwang, K.C. Chang, G.C. Lee and R.L. Ketter, 8/1/88, (PB89-102917, A04, MF-A01).

NCEER-88-0027   "Systems Study of Urban Response and Reconstruction Due to Catastrophic Earthquakes," by F. Kozin and H.K. Zhou, 9/22/88, (PB90-162348, A04, MF-A01).

NCEER-88-0028   "Seismic Fragility Analysis of Plane Frame Structures," by H.H-M. Hwang and Y.K. Low, 7/31/88, (PB89-131445, A06, MF-A01).

NCEER-88-0029   "Response Analysis of Stochastic Structures," by A. Kardara, C. Bucher and M. Shinozuka, 9/22/88, (PB89-174429, A04, MF-A01).

NCEER-88-0030   "Nonnormal Accelerations Due to Yielding in a Primary Structure," by D.C.K. Chen and L.D. Lutes, 9/19/88, (PB89-131437, A04, MF-A01).

NCEER-88-0031   "Design Approaches for Soil-Structure Interaction," by A.S. Veletsos, A.M. Prasad and Y. Tang, 12/30/88, (PB89-174437, A03, MF-A01). This report is available only through NTIS (see address given above).

NCEER-88-0032   "A Re-evaluation of Design Spectra for Seismic Damage Control," by C.J. Turkstra and A.G. Tallin, 11/7/88, (PB89-145221, A05, MF-A01).

NCEER-88-0033   "The Behavior and Design of Noncontact Lap Splices Subjected to Repeated Inelastic Tensile Loading," by V.E. Sagan, P. Gergely and R.N. White, 12/8/88, (PB89-163737, A08, MF-A01).

NCEER-88-0034   "Seismic Response of Pile Foundations," by S.M. Mamoon, P.K. Banerjee and S. Ahmad, 11/1/88, (PB89-145239, A04, MF-A01).

NCEER-88-0035   "Modeling of R/C Building Structures With Flexible Floor Diaphragms (IDARC2)," by A.M. Reinhorn, S.K. Kunnath and N. Panahshahi, 9/7/88, (PB89-207153, A07, MF-A01).

NCEER-88-0036   "Solution of the Dam-Reservoir Interaction Problem Using a Combination of FEM, BEM with Particular Integrals, Modal Analysis, and Substructuring," by C-S. Tsai, G.C. Lee and R.L. Ketter, 12/31/88, (PB89-207146, A04, MF-A01).

NCEER-88-0037   "Optimal Placement of Actuators for Structural Control," by F.Y. Cheng and C.P. Pantelides, 8/15/88, (PB89-162846, A05, MF-A01).

NCEER-88-0038   "Teflon Bearings in Aseismic Base Isolation: Experimental Studies and Mathematical Modeling," by A. Mokha, M.C. Constantinou and A.M. Reinhorn, 12/5/88, (PB89-218457, A10, MF-A01). This report is available only through NTIS (see address given above).

NCEER-88-0039   "Seismic Behavior of Flat Slab High-Rise Buildings in the New York City Area," by P. Weidlinger and M. Ettouney, 10/15/88, (PB90-145681, A04, MF-A01).

NCEER-88-0040   "Evaluation of the Earthquake Resistance of Existing Buildings in New York City," by P. Weidlinger and M. Ettouney, 10/15/88, to be published.

NCEER-88-0041   "Small-Scale Modeling Techniques for Reinforced Concrete Structures Subjected to Seismic Loads," by W. Kim, A. El-Attar and R.N. White, 11/22/88, (PB89-189625, A05, MF-A01).

NCEER-88-0042 "Modeling Strong Ground Motion from Multiple Event Earthquakes," by G.W. Ellis and A.S. Cakmak, 10/15/88, (PB89-174445, A03, MF-A01).

NCEER-88-0043 "Nonstationary Models of Seismic Ground Acceleration," by M. Grigoriu, S.E. Ruiz and E. Rosenblueth, 7/15/88, (PB89-189617, A04, MF-A01).

NCEER-88-0044 "SARCF User's Guide: Seismic Analysis of Reinforced Concrete Frames," by Y.S. Chung, C. Meyer and M. Shinozuka, 11/9/88, (PB89-174452, A08, MF-A01).

NCEER-88-0045 "First Expert Panel Meeting on Disaster Research and Planning," edited by J. Pantelic and J. Stoyle, 9/15/88, (PB89-174460, A05, MF-A01).

NCEER-88-0046 "Preliminary Studies of the Effect of Degrading Infill Walls on the Nonlinear Seismic Response of Steel Frames," by C.Z. Chrysostomou, P. Gergely and J.F. Abel, 12/19/88, (PB89-208383, A05, MF-A01).

NCEER-88-0047 "Reinforced Concrete Frame Component Testing Facility - Design, Construction, Instrumentation and Operation," by S.P. Pessiki, C. Conley, T. Bond, P. Gergely and R.N. White, 12/16/88, (PB89-174478, A04, MF-A01).

NCEER-89-0001 "Effects of Protective Cushion and Soil Compliancy on the Response of Equipment Within a Seismically Excited Building," by J.A. HoLung, 2/16/89, (PB89-207179, A04, MF-A01).

NCEER-89-0002 "Statistical Evaluation of Response Modification Factors for Reinforced Concrete Structures," by H.H-M. Hwang and J-W. Jaw, 2/17/89, (PB89-207187, A05, MF-A01).

NCEER-89-0003 "Hysteretic Columns Under Random Excitation," by G-Q. Cai and Y.K. Lin, 1/9/89, (PB89-196513, A03, MF-A01).

NCEER-89-0004 "Experimental Study of `Elephant Foot Bulge' Instability of Thin-Walled Metal Tanks," by Z-H. Jia and R.L. Ketter, 2/22/89, (PB89-207195, A03, MF-A01).

NCEER-89-0005 "Experiment on Performance of Buried Pipelines Across San Andreas Fault," by J. Isenberg, E. Richardson and T.D. O'Rourke, 3/10/89, (PB89-218440, A04, MF-A01). This report is available only through NTIS (see address given above).

NCEER-89-0006 "A Knowledge-Based Approach to Structural Design of Earthquake-Resistant Buildings," by M. Subramani, P. Gergely, C.H. Conley, J.F. Abel and A.H. Zaghw, 1/15/89, (PB89-218465, A06, MF-A01).

NCEER-89-0007 "Liquefaction Hazards and Their Effects on Buried Pipelines," by T.D. O'Rourke and P.A. Lane, 2/1/89, (PB89-218481, A09, MF-A01).

NCEER-89-0008 "Fundamentals of System Identification in Structural Dynamics," by H. Imai, C-B. Yun, O. Maruyama and M. Shinozuka, 1/26/89, (PB89-207211, A04, MF-A01).

NCEER-89-0009 "Effects of the 1985 Michoacan Earthquake on Water Systems and Other Buried Lifelines in Mexico," by A.G. Ayala and M.J. O'Rourke, 3/8/89, (PB89-207229, A06, MF-A01).

NCEER-89-R010 "NCEER Bibliography of Earthquake Education Materials," by K.E.K. Ross, Second Revision, 9/1/89, (PB90-125352, A05, MF-A01). This report is replaced by NCEER-92-0018.

NCEER-89-0011 "Inelastic Three-Dimensional Response Analysis of Reinforced Concrete Building Structures (IDARC-3D), Part I - Modeling," by S.K. Kunnath and A.M. Reinhorn, 4/17/89, (PB90-114612, A07, MF-A01). This report is available only through NTIS (see address given above).

NCEER-89-0012 "Recommended Modifications to ATC-14," by C.D. Poland and J.O. Malley, 4/12/89, (PB90-108648, A15, MF-A01).

NCEER-89-0013 "Repair and Strengthening of Beam-to-Column Connections Subjected to Earthquake Loading," by M. Corazao and A.J. Durrani, 2/28/89, (PB90-109885, A06, MF-A01).

NCEER-89-0014   "Program EXKAL2 for Identification of Structural Dynamic Systems," by O. Maruyama, C-B. Yun, M. Hoshiya and M. Shinozuka, 5/19/89, (PB90-109877, A09, MF-A01).

NCEER-89-0015   "Response of Frames With Bolted Semi-Rigid Connections, Part I - Experimental Study and Analytical Predictions," by P.J. DiCorso, A.M. Reinhorn, J.R. Dickerson, J.B. Radziminski and W.L. Harper, 6/1/89, to be published.

NCEER-89-0016   "ARMA Monte Carlo Simulation in Probabilistic Structural Analysis," by P.D. Spanos and M.P. Mignolet, 7/10/89, (PB90-109893, A03, MF-A01).

NCEER-89-P017   "Preliminary Proceedings from the Conference on Disaster Preparedness - The Place of Earthquake Education in Our Schools," Edited by K.E.K. Ross, 6/23/89, (PB90-108606, A03, MF-A01).

NCEER-89-0017   "Proceedings from the Conference on Disaster Preparedness - The Place of Earthquake Education in Our Schools," Edited by K.E.K. Ross, 12/31/89, (PB90-207895, A012, MF-A02). This report is available only through NTIS (see address given above).

NCEER-89-0018   "Multidimensional Models of Hysteretic Material Behavior for Vibration Analysis of Shape Memory Energy Absorbing Devices, by E.J. Graesser and F.A. Cozzarelli, 6/7/89, (PB90-164146, A04, MF-A01).

NCEER-89-0019   "Nonlinear Dynamic Analysis of Three-Dimensional Base Isolated Structures (3D-BASIS)," by S. Nagarajaiah, A.M. Reinhorn and M.C. Constantinou, 8/3/89, (PB90-161936, A06, MF-A01). This report has been replaced by NCEER-93-0011.

NCEER-89-0020   "Structural Control Considering Time-Rate of Control Forces and Control Rate Constraints," by F.Y. Cheng and C.P. Pantelides, 8/3/89, (PB90-120445, A04, MF-A01).

NCEER-89-0021   "Subsurface Conditions of Memphis and Shelby County," by K.W. Ng, T-S. Chang and H-H.M. Hwang, 7/26/89, (PB90-120437, A03, MF-A01).

NCEER-89-0022   "Seismic Wave Propagation Effects on Straight Jointed Buried Pipelines," by K. Elhmadi and M.J. O'Rourke, 8/24/89, (PB90-162322, A10, MF-A02).

NCEER-89-0023   "Workshop on Serviceability Analysis of Water Delivery Systems," edited by M. Grigoriu, 3/6/89, (PB90-127424, A03, MF-A01).

NCEER-89-0024   "Shaking Table Study of a 1/5 Scale Steel Frame Composed of Tapered Members," by K.C. Chang, J.S. Hwang and G.C. Lee, 9/18/89, (PB90-160169, A04, MF-A01).

NCEER-89-0025   "DYNA1D: A Computer Program for Nonlinear Seismic Site Response Analysis - Technical Documentation," by Jean H. Prevost, 9/14/89, (PB90-161944, A07, MF-A01). This report is available only through NTIS (see address given above).

NCEER-89-0026   "1:4 Scale Model Studies of Active Tendon Systems and Active Mass Dampers for Aseismic Protection," by A.M. Reinhorn, T.T. Soong, R.C. Lin, Y.P. Yang, Y. Fukao, H. Abe and M. Nakai, 9/15/89, (PB90-173246, A10, MF-A02). This report is available only through NTIS (see address given above).

NCEER-89-0027   "Scattering of Waves by Inclusions in a Nonhomogeneous Elastic Half Space Solved by Boundary Element Methods," by P.K. Hadley, A. Askar and A.S. Cakmak, 6/15/89, (PB90-145699, A07, MF-A01).

NCEER-89-0028   "Statistical Evaluation of Deflection Amplification Factors for Reinforced Concrete Structures," by H.H.M. Hwang, J-W. Jaw and A.L. Ch'ng, 8/31/89, (PB90-164633, A05, MF-A01).

NCEER-89-0029   "Bedrock Accelerations in Memphis Area Due to Large New Madrid Earthquakes," by H.H.M. Hwang, C.H.S. Chen and G. Yu, 11/7/89, (PB90-162330, A04, MF-A01).

NCEER-89-0030   "Seismic Behavior and Response Sensitivity of Secondary Structural Systems," by Y.Q. Chen and T.T. Soong, 10/23/89, (PB90-164658, A08, MF-A01).

NCEER-89-0031   "Random Vibration and Reliability Analysis of Primary-Secondary Structural Systems," by Y. Ibrahim, M. Grigoriu and T.T. Soong, 11/10/89, (PB90-161951, A04, MF-A01).

NCEER-89-0032   "Proceedings from the Second U.S. - Japan Workshop on Liquefaction, Large Ground Deformation and Their Effects on Lifelines, September 26-29, 1989," Edited by T.D. O'Rourke and M. Hamada, 12/1/89, (PB90-209388, A22, MF-A03).

NCEER-89-0033   "Deterministic Model for Seismic Damage Evaluation of Reinforced Concrete Structures," by J.M. Bracci, A.M. Reinhorn, J.B. Mander and S.K. Kunnath, 9/27/89, (PB91-108803, A06, MF-A01).

NCEER-89-0034   "On the Relation Between Local and Global Damage Indices," by E. DiPasquale and A.S. Cakmak, 8/15/89, (PB90-173865, A05, MF-A01).

NCEER-89-0035   "Cyclic Undrained Behavior of Nonplastic and Low Plasticity Silts," by A.J. Walker and H.E. Stewart, 7/26/89, (PB90-183518, A10, MF-A01).

NCEER-89-0036   "Liquefaction Potential of Surficial Deposits in the City of Buffalo, New York," by M. Budhu, R. Giese and L. Baumgrass, 1/17/89, (PB90-208455, A04, MF-A01).

NCEER-89-0037   "A Deterministic Assessment of Effects of Ground Motion Incoherence," by A.S. Veletsos and Y. Tang, 7/15/89, (PB90-164294, A03, MF-A01).

NCEER-89-0038   "Workshop on Ground Motion Parameters for Seismic Hazard Mapping," July 17-18, 1989, edited by R.V. Whitman, 12/1/89, (PB90-173923, A04, MF-A01).

NCEER-89-0039   "Seismic Effects on Elevated Transit Lines of the New York City Transit Authority," by C.J. Costantino, C.A. Miller and E. Heymsfield, 12/26/89, (PB90-207887, A06, MF-A01).

NCEER-89-0040   "Centrifugal Modeling of Dynamic Soil-Structure Interaction," by K. Weissman, Supervised by J.H. Prevost, 5/10/89, (PB90-207879, A07, MF-A01).

NCEER-89-0041   "Linearized Identification of Buildings With Cores for Seismic Vulnerability Assessment," by I-K. Ho and A.E. Aktan, 11/1/89, (PB90-251943, A07, MF-A01).

NCEER-90-0001   "Geotechnical and Lifeline Aspects of the October 17, 1989 Loma Prieta Earthquake in San Francisco," by T.D. O'Rourke, H.E. Stewart, F.T. Blackburn and T.S. Dickerman, 1/90, (PB90-208596, A05, MF-A01).

NCEER-90-0002   "Nonnormal Secondary Response Due to Yielding in a Primary Structure," by D.C.K. Chen and L.D. Lutes, 2/28/90, (PB90-251976, A07, MF-A01).

NCEER-90-0003   "Earthquake Education Materials for Grades K-12," by K.E.K. Ross, 4/16/90, (PB91-251984, A05, MF-A05). This report has been replaced by NCEER-92-0018.

NCEER-90-0004   "Catalog of Strong Motion Stations in Eastern North America," by R.W. Busby, 4/3/90, (PB90-251984, A05, MF-A01).

NCEER-90-0005   "NCEER Strong-Motion Data Base: A User Manual for the GeoBase Release (Version 1.0 for the Sun3)," by P. Friberg and K. Jacob, 3/31/90 (PB90-258062, A04, MF-A01).

NCEER-90-0006   "Seismic Hazard Along a Crude Oil Pipeline in the Event of an 1811-1812 Type New Madrid Earthquake," by H.H.M. Hwang and C-H.S. Chen, 4/16/90, (PB90-258054, A04, MF-A01).

NCEER-90-0007   "Site-Specific Response Spectra for Memphis Sheahan Pumping Station," by H.H.M. Hwang and C.S. Lee, 5/15/90, (PB91-108811, A05, MF-A01).

NCEER-90-0008   "Pilot Study on Seismic Vulnerability of Crude Oil Transmission Systems," by T. Ariman, R. Dobry, M. Grigoriu, F. Kozin, M. O'Rourke, T. O'Rourke and M. Shinozuka, 5/25/90, (PB91-108837, A06, MF-A01).

NCEER-90-0009   "A Program to Generate Site Dependent Time Histories: EQGEN," by G.W. Ellis, M. Srinivasan and A.S. Cakmak, 1/30/90, (PB91-108829, A04, MF-A01).

NCEER-90-0010   "Active Isolation for Seismic Protection of Operating Rooms," by M.E. Talbott, Supervised by M. Shinozuka, 6/8/9, (PB91-110205, A05, MF-A01).

NCEER-90-0011   "Program LINEARID for Identification of Linear Structural Dynamic Systems," by C-B. Yun and M. Shinozuka, 6/25/90, (PB91-110312, A08, MF-A01).

NCEER-90-0012   "Two-Dimensional Two-Phase Elasto-Plastic Seismic Response of Earth Dams," by A.N. Yiagos, Supervised by J.H. Prevost, 6/20/90, (PB91-110197, A13, MF-A02).

NCEER-90-0013   "Secondary Systems in Base-Isolated Structures: Experimental Investigation, Stochastic Response and Stochastic Sensitivity," by G.D. Manolis, G. Juhn, M.C. Constantinou and A.M. Reinhorn, 7/1/90, (PB91-110320, A08, MF-A01).

NCEER-90-0014   "Seismic Behavior of Lightly-Reinforced Concrete Column and Beam-Column Joint Details," by S.P. Pessiki, C.H. Conley, P. Gergely and R.N. White, 8/22/90, (PB91-108795, A11, MF-A02).

NCEER-90-0015   "Two Hybrid Control Systems for Building Structures Under Strong Earthquakes," by J.N. Yang and A. Danielians, 6/29/90, (PB91-125393, A04, MF-A01).

NCEER-90-0016   "Instantaneous Optimal Control with Acceleration and Velocity Feedback," by J.N. Yang and Z. Li, 6/29/90, (PB91-125401, A03, MF-A01).

NCEER-90-0017   "Reconnaissance Report on the Northern Iran Earthquake of June 21, 1990," by M. Mehrain, 10/4/90, (PB91-125377, A03, MF-A01).

NCEER-90-0018   "Evaluation of Liquefaction Potential in Memphis and Shelby County," by T.S. Chang, P.S. Tang, C.S. Lee and H. Hwang, 8/10/90, (PB91-125427, A09, MF-A01).

NCEER-90-0019   "Experimental and Analytical Study of a Combined Sliding Disc Bearing and Helical Steel Spring Isolation System," by M.C. Constantinou, A.S. Mokha and A.M. Reinhorn, 10/4/90, (PB91-125385, A06, MF-A01). This report is available only through NTIS (see address given above).

NCEER-90-0020   "Experimental Study and Analytical Prediction of Earthquake Response of a Sliding Isolation System with a Spherical Surface," by A.S. Mokha, M.C. Constantinou and A.M. Reinhorn, 10/11/90, (PB91-125419, A05, MF-A01).

NCEER-90-0021   "Dynamic Interaction Factors for Floating Pile Groups," by G. Gazetas, K. Fan, A. Kaynia and E. Kausel, 9/10/90, (PB91-170381, A05, MF-A01).

NCEER-90-0022   "Evaluation of Seismic Damage Indices for Reinforced Concrete Structures," by S. Rodriguez-Gomez and A.S. Cakmak, 9/30/90, PB91-171322, A06, MF-A01).

NCEER-90-0023   "Study of Site Response at a Selected Memphis Site," by H. Desai, S. Ahmad, E.S. Gazetas and M.R. Oh, 10/11/90, (PB91-196857, A03, MF-A01).

NCEER-90-0024   "A User's Guide to Strongmo: Version 1.0 of NCEER's Strong-Motion Data Access Tool for PCs and Terminals," by P.A. Friberg and C.A.T. Susch, 11/15/90, (PB91-171272, A03, MF-A01).

NCEER-90-0025   "A Three-Dimensional Analytical Study of Spatial Variability of Seismic Ground Motions," by L-L. Hong and A.H.-S. Ang, 10/30/90, (PB91-170399, A09, MF-A01).

NCEER-90-0026   "MUMOID User's Guide - A Program for the Identification of Modal Parameters," by S. Rodriguez-Gomez and E. DiPasquale, 9/30/90, (PB91-171298, A04, MF-A01).

NCEER-90-0027   "SARCF-II User's Guide - Seismic Analysis of Reinforced Concrete Frames," by S. Rodriguez-Gomez, Y.S. Chung and C. Meyer, 9/30/90, (PB91-171280, A05, MF-A01).

NCEER-90-0028   "Viscous Dampers: Testing, Modeling and Application in Vibration and Seismic Isolation," by N. Makris and M.C. Constantinou, 12/20/90 (PB91-190561, A06, MF-A01).

NCEER-90-0029   "Soil Effects on Earthquake Ground Motions in the Memphis Area," by H. Hwang, C.S. Lee, K.W. Ng and T.S. Chang, 8/2/90, (PB91-190751, A05, MF-A01).

NCEER-91-0001 "Proceedings from the Third Japan-U.S. Workshop on Earthquake Resistant Design of Lifeline Facilities and Countermeasures for Soil Liquefaction, December 17-19, 1990," edited by T.D. O'Rourke and M. Hamada, 2/1/91, (PB91-179259, A99, MF-A04).

NCEER-91-0002 "Physical Space Solutions of Non-Proportionally Damped Systems," by M. Tong, Z. Liang and G.C. Lee, 1/15/91, (PB91-179242, A04, MF-A01).

NCEER-91-0003 "Seismic Response of Single Piles and Pile Groups," by K. Fan and G. Gazetas, 1/10/91, (PB92-174994, A04, MF-A01).

NCEER-91-0004 "Damping of Structures: Part 1 - Theory of Complex Damping," by Z. Liang and G. Lee, 10/10/91, (PB92-197235, A12, MF-A03).

NCEER-91-0005 "3D-BASIS - Nonlinear Dynamic Analysis of Three Dimensional Base Isolated Structures: Part II," by S. Nagarajaiah, A.M. Reinhorn and M.C. Constantinou, 2/28/91, (PB91-190553, A07, MF-A01). This report has been replaced by NCEER-93-0011.

NCEER-91-0006 "A Multidimensional Hysteretic Model for Plasticity Deforming Metals in Energy Absorbing Devices," by E.J. Graesser and F.A. Cozzarelli, 4/9/91, (PB92-108364, A04, MF-A01).

NCEER-91-0007 "A Framework for Customizable Knowledge-Based Expert Systems with an Application to a KBES for Evaluating the Seismic Resistance of Existing Buildings," by E.G. Ibarra-Anaya and S.J. Fenves, 4/9/91, (PB91-210930, A08, MF-A01).

NCEER-91-0008 "Nonlinear Analysis of Steel Frames with Semi-Rigid Connections Using the Capacity Spectrum Method," by G.G. Deierlein, S-H. Hsieh, Y-J. Shen and J.F. Abel, 7/2/91, (PB92-113828, A05, MF-A01).

NCEER-91-0009 "Earthquake Education Materials for Grades K-12," by K.E.K. Ross, 4/30/91, (PB91-212142, A06, MF-A01). This report has been replaced by NCEER-92-0018.

NCEER-91-0010 "Phase Wave Velocities and Displacement Phase Differences in a Harmonically Oscillating Pile," by N. Makris and G. Gazetas, 7/8/91, (PB92-108356, A04, MF-A01).

NCEER-91-0011 "Dynamic Characteristics of a Full-Size Five-Story Steel Structure and a 2/5 Scale Model," by K.C. Chang, G.C. Yao, G.C. Lee, D.S. Hao and Y.C. Yeh," 7/2/91, (PB93-116648, A06, MF-A02).

NCEER-91-0012 "Seismic Response of a 2/5 Scale Steel Structure with Added Viscoelastic Dampers," by K.C. Chang, T.T. Soong, S-T. Oh and M.L. Lai, 5/17/91, (PB92-110816, A05, MF-A01).

NCEER-91-0013 "Earthquake Response of Retaining Walls; Full-Scale Testing and Computational Modeling," by S. Alampalli and A-W.M. Elgamal, 6/20/91, to be published.

NCEER-91-0014 "3D-BASIS-M: Nonlinear Dynamic Analysis of Multiple Building Base Isolated Structures," by P.C. Tsopelas, S. Nagarajaiah, M.C. Constantinou and A.M. Reinhorn, 5/28/91, (PB92-113885, A09, MF-A02).

NCEER-91-0015 "Evaluation of SEAOC Design Requirements for Sliding Isolated Structures," by D. Theodossiou and M.C. Constantinou, 6/10/91, (PB92-114602, A11, MF-A03).

NCEER-91-0016 "Closed-Loop Modal Testing of a 27-Story Reinforced Concrete Flat Plate-Core Building," by H.R. Somaprasad, T. Toksoy, H. Yoshiyuki and A.E. Aktan, 7/15/91, (PB92-129980, A07, MF-A02).

NCEER-91-0017 "Shake Table Test of a 1/6 Scale Two-Story Lightly Reinforced Concrete Building," by A.G. El-Attar, R.N. White and P. Gergely, 2/28/91, (PB92-222447, A06, MF-A02).

NCEER-91-0018 "Shake Table Test of a 1/8 Scale Three-Story Lightly Reinforced Concrete Building," by A.G. El-Attar, R.N. White and P. Gergely, 2/28/91, (PB93-116630, A08, MF-A02).

NCEER-91-0019 "Transfer Functions for Rigid Rectangular Foundations," by A.S. Veletsos, A.M. Prasad and W.H. Wu, 7/31/91, to be published.

NCEER-91-0020 "Hybrid Control of Seismic-Excited Nonlinear and Inelastic Structural Systems," by J.N. Yang, Z. Li and A. Danielians, 8/1/91, (PB92-143171, A06, MF-A02).

NCEER-91-0021 "The NCEER-91 Earthquake Catalog: Improved Intensity-Based Magnitudes and Recurrence Relations for U.S. Earthquakes East of New Madrid," by L. Seeber and J.G. Armbruster, 8/28/91, (PB92-176742, A06, MF-A02).

NCEER-91-0022 "Proceedings from the Implementation of Earthquake Planning and Education in Schools: The Need for Change - The Roles of the Changemakers," by K.E.K. Ross and F. Winslow, 7/23/91, (PB92-129998, A12, MF-A03).

NCEER-91-0023 "A Study of Reliability-Based Criteria for Seismic Design of Reinforced Concrete Frame Buildings," by H.H.M. Hwang and H-M. Hsu, 8/10/91, (PB92-140235, A09, MF-A02).

NCEER-91-0024 "Experimental Verification of a Number of Structural System Identification Algorithms," by R.G. Ghanem, H. Gavin and M. Shinozuka, 9/18/91, (PB92-176577, A18, MF-A04).

NCEER-91-0025 "Probabilistic Evaluation of Liquefaction Potential," by H.H.M. Hwang and C.S. Lee," 11/25/91, (PB92-143429, A05, MF-A01).

NCEER-91-0026 "Instantaneous Optimal Control for Linear, Nonlinear and Hysteretic Structures - Stable Controllers," by J.N. Yang and Z. Li, 11/15/91, (PB92-163807, A04, MF-A01).

NCEER-91-0027 "Experimental and Theoretical Study of a Sliding Isolation System for Bridges," by M.C. Constantinou, A. Kartoum, A.M. Reinhorn and P. Bradford, 11/15/91, (PB92-176973, A10, MF-A03).

NCEER-92-0001 "Case Studies of Liquefaction and Lifeline Performance During Past Earthquakes, Volume 1: Japanese Case Studies," Edited by M. Hamada and T. O'Rourke, 2/17/92, (PB92-197243, A18, MF-A04).

NCEER-92-0002 "Case Studies of Liquefaction and Lifeline Performance During Past Earthquakes, Volume 2: United States Case Studies," Edited by T. O'Rourke and M. Hamada, 2/17/92, (PB92-197250, A20, MF-A04).

NCEER-92-0003 "Issues in Earthquake Education," Edited by K. Ross, 2/3/92, (PB92-222389, A07, MF-A02).

NCEER-92-0004 "Proceedings from the First U.S. - Japan Workshop on Earthquake Protective Systems for Bridges," Edited by I.G. Buckle, 2/4/92, (PB94-142239, A99, MF-A06).

NCEER-92-0005 "Seismic Ground Motion from a Haskell-Type Source in a Multiple-Layered Half-Space," A.P. Theoharis, G. Deodatis and M. Shinozuka, 1/2/92, to be published.

NCEER-92-0006 "Proceedings from the Site Effects Workshop," Edited by R. Whitman, 2/29/92, (PB92-197201, A04, MF-A01).

NCEER-92-0007 "Engineering Evaluation of Permanent Ground Deformations Due to Seismically-Induced Liquefaction," by M.H. Baziar, R. Dobry and A-W.M. Elgamal, 3/24/92, (PB92-222421, A13, MF-A03).

NCEER-92-0008 "A Procedure for the Seismic Evaluation of Buildings in the Central and Eastern United States," by C.D. Poland and J.O. Malley, 4/2/92, (PB92-222439, A20, MF-A04).

NCEER-92-0009 "Experimental and Analytical Study of a Hybrid Isolation System Using Friction Controllable Sliding Bearings," by M.Q. Feng, S. Fujii and M. Shinozuka, 5/15/92, (PB93-150282, A06, MF-A02).

NCEER-92-0010 "Seismic Resistance of Slab-Column Connections in Existing Non-Ductile Flat-Plate Buildings," by A.J. Durrani and Y. Du, 5/18/92, (PB93-116812, A06, MF-A02).

NCEER-92-0011 "The Hysteretic and Dynamic Behavior of Brick Masonry Walls Upgraded by Ferrocement Coatings Under Cyclic Loading and Strong Simulated Ground Motion," by H. Lee and S.P. Prawel, 5/11/92, to be published.

NCEER-92-0012 "Study of Wire Rope Systems for Seismic Protection of Equipment in Buildings," by G.F. Demetriades, M.C. Constantinou and A.M. Reinhorn, 5/20/92, (PB93-116655, A08, MF-A02).

NCEER-92-0013   "Shape Memory Structural Dampers: Material Properties, Design and Seismic Testing," by P.R. Witting and F.A. Cozzarelli, 5/26/92, (PB93-116663, A05, MF-A01).

NCEER-92-0014   "Longitudinal Permanent Ground Deformation Effects on Buried Continuous Pipelines," by M.J. O'Rourke, and C. Nordberg, 6/15/92, (PB93-116671, A08, MF-A02).

NCEER-92-0015   "A Simulation Method for Stationary Gaussian Random Functions Based on the Sampling Theorem," by M. Grigoriu and S. Balopoulou, 6/11/92, (PB93-127496, A05, MF-A01).

NCEER-92-0016   "Gravity-Load-Designed Reinforced Concrete Buildings: Seismic Evaluation of Existing Construction and Detailing Strategies for Improved Seismic Resistance," by G.W. Hoffmann, S.K. Kunnath, A.M. Reinhorn and J.B. Mander, 7/15/92, (PB94-142007, A08, MF-A02).

NCEER-92-0017   "Observations on Water System and Pipeline Performance in the Limón Area of Costa Rica Due to the April 22, 1991 Earthquake," by M. O'Rourke and D. Ballantyne, 6/30/92, (PB93-126811, A06, MF-A02).

NCEER-92-0018   "Fourth Edition of Earthquake Education Materials for Grades K-12," Edited by K.E.K. Ross, 8/10/92, (PB93-114023, A07, MF-A02).

NCEER-92-0019   "Proceedings from the Fourth Japan-U.S. Workshop on Earthquake Resistant Design of Lifeline Facilities and Countermeasures for Soil Liquefaction," Edited by M. Hamada and T.D. O'Rourke, 8/12/92, (PB93-163939, A99, MF-E11).

NCEER-92-0020   "Active Bracing System: A Full Scale Implementation of Active Control," by A.M. Reinhorn, T.T. Soong, R.C. Lin, M.A. Riley, Y.P. Wang, S. Aizawa and M. Higashino, 8/14/92, (PB93-127512, A06, MF-A02).

NCEER-92-0021   "Empirical Analysis of Horizontal Ground Displacement Generated by Liquefaction-Induced Lateral Spreads," by S.F. Bartlett and T.L. Youd, 8/17/92, (PB93-188241, A06, MF-A02).

NCEER-92-0022   "IDARC Version 3.0: Inelastic Damage Analysis of Reinforced Concrete Structures," by S.K. Kunnath, A.M. Reinhorn and R.F. Lobo, 8/31/92, (PB93-227502, A07, MF-A02).

NCEER-92-0023   "A Semi-Empirical Analysis of Strong-Motion Peaks in Terms of Seismic Source, Propagation Path and Local Site Conditions, by M. Kamiyama, M.J. O'Rourke and R. Flores-Berrones, 9/9/92, (PB93-150266, A08, MF-A02).

NCEER-92-0024   "Seismic Behavior of Reinforced Concrete Frame Structures with Nonductile Details, Part I: Summary of Experimental Findings of Full Scale Beam-Column Joint Tests," by A. Beres, R.N. White and P. Gergely, 9/30/92, (PB93-227783, A05, MF-A01).

NCEER-92-0025   "Experimental Results of Repaired and Retrofitted Beam-Column Joint Tests in Lightly Reinforced Concrete Frame Buildings," by A. Beres, S. El-Borgi, R.N. White and P. Gergely, 10/29/92, (PB93-227791, A05, MF-A01).

NCEER-92-0026   "A Generalization of Optimal Control Theory: Linear and Nonlinear Structures," by J.N. Yang, Z. Li and S. Vongchavalitkul, 11/2/92, (PB93-188621, A05, MF-A01).

NCEER-92-0027   "Seismic Resistance of Reinforced Concrete Frame Structures Designed Only for Gravity Loads: Part I - Design and Properties of a One-Third Scale Model Structure," by J.M. Bracci, A.M. Reinhorn and J.B. Mander, 12/1/92, (PB94-104502, A08, MF-A02).

NCEER-92-0028   "Seismic Resistance of Reinforced Concrete Frame Structures Designed Only for Gravity Loads: Part II - Experimental Performance of Subassemblages," by L.E. Aycardi, J.B. Mander and A.M. Reinhorn, 12/1/92, (PB94-104510, A08, MF-A02).

NCEER-92-0029   "Seismic Resistance of Reinforced Concrete Frame Structures Designed Only for Gravity Loads: Part III - Experimental Performance and Analytical Study of a Structural Model," by J.M. Bracci, A.M. Reinhorn and J.B. Mander, 12/1/92, (PB93-227528, A09, MF-A01).

NCEER-92-0030   "Evaluation of Seismic Retrofit of Reinforced Concrete Frame Structures: Part I - Experimental Performance of Retrofitted Subassemblages," by D. Choudhuri, J.B. Mander and A.M. Reinhorn, 12/8/92, (PB93-198307, A07, MF-A02).

NCEER-92-0031   "Evaluation of Seismic Retrofit of Reinforced Concrete Frame Structures: Part II - Experimental Performance and Analytical Study of a Retrofitted Structural Model," by J.M. Bracci, A.M. Reinhorn and J.B. Mander, 12/8/92, (PB93-198315, A09, MF-A03).

NCEER-92-0032   "Experimental and Analytical Investigation of Seismic Response of Structures with Supplemental Fluid Viscous Dampers," by M.C. Constantinou and M.D. Symans, 12/21/92, (PB93-191435, A10, MF-A03). This report is available only through NTIS (see address given above).

NCEER-92-0033   "Reconnaissance Report on the Cairo, Egypt Earthquake of October 12, 1992," by M. Khater, 12/23/92, (PB93-188621, A03, MF-A01).

NCEER-92-0034   "Low-Level Dynamic Characteristics of Four Tall Flat-Plate Buildings in New York City," by H. Gavin, S. Yuan, J. Grossman, E. Pekelis and K. Jacob, 12/28/92, (PB93-188217, A07, MF-A02).

NCEER-93-0001   "An Experimental Study on the Seismic Performance of Brick-Infilled Steel Frames With and Without Retrofit," by J.B. Mander, B. Nair, K. Wojtkowski and J. Ma, 1/29/93, (PB93-227510, A07, MF-A02).

NCEER-93-0002   "Social Accounting for Disaster Preparedness and Recovery Planning," by S. Cole, E. Pantoja and V. Razak, 2/22/93, (PB94-142114, A12, MF-A03).

NCEER-93-0003   "Assessment of 1991 NEHRP Provisions for Nonstructural Components and Recommended Revisions," by T.T. Soong, G. Chen, Z. Wu, R-H. Zhang and M. Grigoriu, 3/1/93, (PB93-188639, A06, MF-A02).

NCEER-93-0004   "Evaluation of Static and Response Spectrum Analysis Procedures of SEAOC/UBC for Seismic Isolated Structures," by C.W. Winters and M.C. Constantinou, 3/23/93, (PB93-198299, A10, MF-A03).

NCEER-93-0005   "Earthquakes in the Northeast - Are We Ignoring the Hazard? A Workshop on Earthquake Science and Safety for Educators," edited by K.E.K. Ross, 4/2/93, (PB94-103066, A09, MF-A02).

NCEER-93-0006   "Inelastic Response of Reinforced Concrete Structures with Viscoelastic Braces," by R.F. Lobo, J.M. Bracci, K.L. Shen, A.M. Reinhorn and T.T. Soong, 4/5/93, (PB93-227486, A05, MF-A02).

NCEER-93-0007   "Seismic Testing of Installation Methods for Computers and Data Processing Equipment," by K. Kosar, T.T. Soong, K.L. Shen, J.A. HoLung and Y.K. Lin, 4/12/93, (PB93-198299, A07, MF-A02).

NCEER-93-0008   "Retrofit of Reinforced Concrete Frames Using Added Dampers," by A. Reinhorn, M. Constantinou and C. Li, to be published.

NCEER-93-0009   "Seismic Behavior and Design Guidelines for Steel Frame Structures with Added Viscoelastic Dampers," by K.C. Chang, M.L. Lai, T.T. Soong, D.S. Hao and Y.C. Yeh, 5/1/93, (PB94-141959, A07, MF-A02).

NCEER-93-0010   "Seismic Performance of Shear-Critical Reinforced Concrete Bridge Piers," by J.B. Mander, S.M. Waheed, M.T.A. Chaudhary and S.S. Chen, 5/12/93, (PB93-227494, A08, MF-A02).

NCEER-93-0011   "3D-BASIS-TABS: Computer Program for Nonlinear Dynamic Analysis of Three Dimensional Base Isolated Structures," by S. Nagarajaiah, C. Li, A.M. Reinhorn and M.C. Constantinou, 8/2/93, (PB94-141819, A09, MF-A02).

NCEER-93-0012   "Effects of Hydrocarbon Spills from an Oil Pipeline Break on Ground Water," by O.J. Helweg and H.H.M. Hwang, 8/3/93, (PB94-141942, A06, MF-A02).

NCEER-93-0013   "Simplified Procedures for Seismic Design of Nonstructural Components and Assessment of Current Code Provisions," by M.P. Singh, L.E. Suarez, E.E. Matheu and G.O. Maldonado, 8/4/93, (PB94-141827, A09, MF-A02).

NCEER-93-0014   "An Energy Approach to Seismic Analysis and Design of Secondary Systems," by G. Chen and T.T. Soong, 8/6/93, (PB94-142767, A11, MF-A03).

NCEER-93-0015   "Proceedings from School Sites: Becoming Prepared for Earthquakes - Commemorating the Third Anniversary of the Loma Prieta Earthquake," Edited by F.E. Winslow and K.E.K. Ross, 8/16/93, (PB94-154275, A16, MF-A02).

NCEER-93-0016   "Reconnaissance Report of Damage to Historic Monuments in Cairo, Egypt Following the October 12, 1992 Dahshur Earthquake," by D. Sykora, D. Look, G. Croci, E. Karaesmen and E. Karaesmen, 8/19/93, (PB94-142221, A08, MF-A02).

NCEER-93-0017   "The Island of Guam Earthquake of August 8, 1993," by S.W. Swan and S.K. Harris, 9/30/93, (PB94-141843, A04, MF-A01).

NCEER-93-0018   "Engineering Aspects of the October 12, 1992 Egyptian Earthquake," by A.W. Elgamal, M. Amer, K. Adalier and A. Abul-Fadl, 10/7/93, (PB94-141983, A05, MF-A01).

NCEER-93-0019   "Development of an Earthquake Motion Simulator and its Application in Dynamic Centrifuge Testing," by I. Krstelj, Supervised by J.H. Prevost, 10/23/93, (PB94-181773, A-10, MF-A03).

NCEER-93-0020   "NCEER-Taisei Corporation Research Program on Sliding Seismic Isolation Systems for Bridges: Experimental and Analytical Study of a Friction Pendulum System (FPS)," by M.C. Constantinou, P. Tsopelas, Y-S. Kim and S. Okamoto, 11/1/93, (PB94-142775, A08, MF-A02).

NCEER-93-0021   "Finite Element Modeling of Elastomeric Seismic Isolation Bearings," by L.J. Billings, Supervised by R. Shepherd, 11/8/93, to be published.

NCEER-93-0022   "Seismic Vulnerability of Equipment in Critical Facilities: Life-Safety and Operational Consequences," by K. Porter, G.S. Johnson, M.M. Zadeh, C. Scawthorn and S. Eder, 11/24/93, (PB94-181765, A16, MF-A03).

NCEER-93-0023   "Hokkaido Nansei-oki, Japan Earthquake of July 12, 1993, by P.I. Yanev and C.R. Scawthorn, 12/23/93, (PB94-181500, A07, MF-A01).

NCEER-94-0001   "An Evaluation of Seismic Serviceability of Water Supply Networks with Application to the San Francisco Auxiliary Water Supply System," by I. Markov, Supervised by M. Grigoriu and T. O'Rourke, 1/21/94, (PB94-204013, A07, MF-A02).

NCEER-94-0002   "NCEER-Taisei Corporation Research Program on Sliding Seismic Isolation Systems for Bridges: Experimental and Analytical Study of Systems Consisting of Sliding Bearings, Rubber Restoring Force Devices and Fluid Dampers," Volumes I and II, by P. Tsopelas, S. Okamoto, M.C. Constantinou, D. Ozaki and S. Fujii, 2/4/94, (PB94-181740, A09, MF-A02 and PB94-181757, A12, MF-A03).

NCEER-94-0003   "A Markov Model for Local and Global Damage Indices in Seismic Analysis," by S. Rahman and M. Grigoriu, 2/18/94, (PB94-206000, A12, MF-A03).

NCEER-94-0004   "Proceedings from the NCEER Workshop on Seismic Response of Masonry Infills," edited by D.P. Abrams, 3/1/94, (PB94-180783, A07, MF-A02).

NCEER-94-0005   "The Northridge, California Earthquake of January 17, 1994: General Reconnaissance Report," edited by J.D. Goltz, 3/11/94, (PB94-193943, A10, MF-A03).

NCEER-94-0006   "Seismic Energy Based Fatigue Damage Analysis of Bridge Columns: Part I - Evaluation of Seismic Capacity," by G.A. Chang and J.B. Mander, 3/14/94, (PB94-219185, A11, MF-A03).

NCEER-94-0007   "Seismic Isolation of Multi-Story Frame Structures Using Spherical Sliding Isolation Systems," by T.M. Al-Hussaini, V.A. Zayas and M.C. Constantinou, 3/17/94, (PB94-193745, A09, MF-A02).

NCEER-94-0008   "The Northridge, California Earthquake of January 17, 1994: Performance of Highway Bridges," edited by I.G. Buckle, 3/24/94, (PB94-193851, A06, MF-A02).

NCEER-94-0009   "Proceedings of the Third U.S.-Japan Workshop on Earthquake Protective Systems for Bridges," edited by I.G. Buckle and I. Friedland, 3/31/94, (PB94-195815, A99, MF-A06).

NCEER-94-0010   "3D-BASIS-ME: Computer Program for Nonlinear Dynamic Analysis of Seismically Isolated Single and Multiple Structures and Liquid Storage Tanks," by P.C. Tsopelas, M.C. Constantinou and A.M. Reinhorn, 4/12/94, (PB94-204922, A09, MF-A02).

NCEER-94-0011   "The Northridge, California Earthquake of January 17, 1994: Performance of Gas Transmission Pipelines," by T.D. O'Rourke and M.C. Palmer, 5/16/94, (PB94-204989, A05, MF-A01).

NCEER-94-0012   "Feasibility Study of Replacement Procedures and Earthquake Performance Related to Gas Transmission Pipelines," by T.D. O'Rourke and M.C. Palmer, 5/25/94, (PB94-206638, A09, MF-A02).

NCEER-94-0013   "Seismic Energy Based Fatigue Damage Analysis of Bridge Columns: Part II - Evaluation of Seismic Demand," by G.A. Chang and J.B. Mander, 6/1/94, (PB95-18106, A08, MF-A02).

NCEER-94-0014   "NCEER-Taisei Corporation Research Program on Sliding Seismic Isolation Systems for Bridges: Experimental and Analytical Study of a System Consisting of Sliding Bearings and Fluid Restoring Force/Damping Devices," by P. Tsopelas and M.C. Constantinou, 6/13/94, (PB94-219144, A10, MF-A03).

NCEER-94-0015   "Generation of Hazard-Consistent Fragility Curves for Seismic Loss Estimation Studies," by H. Hwang and J-R. Huo, 6/14/94, (PB95-181996, A09, MF-A02).

NCEER-94-0016   "Seismic Study of Building Frames with Added Energy-Absorbing Devices," by W.S. Pong, C.S. Tsai and G.C. Lee, 6/20/94, (PB94-219136, A10, A03).

NCEER-94-0017   "Sliding Mode Control for Seismic-Excited Linear and Nonlinear Civil Engineering Structures," by J. Yang, J. Wu, A. Agrawal and Z. Li, 6/21/94, (PB95-138483, A06, MF-A02).

NCEER-94-0018   "3D-BASIS-TABS Version 2.0: Computer Program for Nonlinear Dynamic Analysis of Three Dimensional Base Isolated Structures," by A.M. Reinhorn, S. Nagarajaiah, M.C. Constantinou, P. Tsopelas and R. Li, 6/22/94, (PB95-182176, A08, MF-A02).

NCEER-94-0019   "Proceedings of the International Workshop on Civil Infrastructure Systems: Application of Intelligent Systems and Advanced Materials on Bridge Systems," Edited by G.C. Lee and K.C. Chang, 7/18/94, (PB95-252474, A20, MF-A04).

NCEER-94-0020   "Study of Seismic Isolation Systems for Computer Floors," by V. Lambrou and M.C. Constantinou, 7/19/94, (PB95-138533, A10, MF-A03).

NCEER-94-0021   "Proceedings of the U.S.-Italian Workshop on Guidelines for Seismic Evaluation and Rehabilitation of Unreinforced Masonry Buildings," Edited by D.P. Abrams and G.M. Calvi, 7/20/94, (PB95-138749, A13, MF-A03).

NCEER-94-0022   "NCEER-Taisei Corporation Research Program on Sliding Seismic Isolation Systems for Bridges: Experimental and Analytical Study of a System Consisting of Lubricated PTFE Sliding Bearings and Mild Steel Dampers," by P. Tsopelas and M.C. Constantinou, 7/22/94, (PB95-182184, A08, MF-A02).

NCEER-94-0023   "Development of Reliability-Based Design Criteria for Buildings Under Seismic Load," by Y.K. Wen, H. Hwang and M. Shinozuka, 8/1/94, (PB95-211934, A08, MF-A02).

NCEER-94-0024   "Experimental Verification of Acceleration Feedback Control Strategies for an Active Tendon System," by S.J. Dyke, B.F. Spencer, Jr., P. Quast, M.K. Sain, D.C. Kaspari, Jr. and T.T. Soong, 8/29/94, (PB95-212320, A05, MF-A01).

NCEER-94-0025   "Seismic Retrofitting Manual for Highway Bridges," Edited by I.G. Buckle and I.F. Friedland, published by the Federal Highway Administration (PB95-212676, A15, MF-A03).

NCEER-94-0026   "Proceedings from the Fifth U.S.-Japan Workshop on Earthquake Resistant Design of Lifeline Facilities and Countermeasures Against Soil Liquefaction," Edited by T.D. O'Rourke and M. Hamada, 11/7/94, (PB95-220802, A99, MF-E08).

NCEER-95-0001 "Experimental and Analytical Investigation of Seismic Retrofit of Structures with Supplemental Damping: Part 1 - Fluid Viscous Damping Devices," by A.M. Reinhorn, C. Li and M.C. Constantinou, 1/3/95, (PB95-266599, A09, MF-A02).

NCEER-95-0002 "Experimental and Analytical Study of Low-Cycle Fatigue Behavior of Semi-Rigid Top-And-Seat Angle Connections," by G. Pekcan, J.B. Mander and S.S. Chen, 1/5/95, (PB95-220042, A07, MF-A02).

NCEER-95-0003 "NCEER-ATC Joint Study on Fragility of Buildings," by T. Anagnos, C. Rojahn and A.S. Kiremidjian, 1/20/95, (PB95-220026, A06, MF-A02).

NCEER-95-0004 "Nonlinear Control Algorithms for Peak Response Reduction," by Z. Wu, T.T. Soong, V. Gattulli and R.C. Lin, 2/16/95, (PB95-220349, A05, MF-A01).

NCEER-95-0005 "Pipeline Replacement Feasibility Study: A Methodology for Minimizing Seismic and Corrosion Risks to Underground Natural Gas Pipelines," by R.T. Eguchi, H.A. Seligson and D.G. Honegger, 3/2/95, (PB95-252326, A06, MF-A02).

NCEER-95-0006 "Evaluation of Seismic Performance of an 11-Story Frame Building During the 1994 Northridge Earthquake," by F. Naeim, R. DiSulio, K. Benuska, A. Reinhorn and C. Li, to be published.

NCEER-95-0007 "Prioritization of Bridges for Seismic Retrofitting," by N. Basöz and A.S. Kiremidjian, 4/24/95, (PB95-252300, A08, MF-A02).

NCEER-95-0008 "Method for Developing Motion Damage Relationships for Reinforced Concrete Frames," by A. Singhal and A.S. Kiremidjian, 5/11/95, (PB95-266607, A06, MF-A02).

NCEER-95-0009 "Experimental and Analytical Investigation of Seismic Retrofit of Structures with Supplemental Damping: Part II - Friction Devices," by C. Li and A.M. Reinhorn, 7/6/95, (PB96-128087, A11, MF-A03).

NCEER-95-0010 "Experimental Performance and Analytical Study of a Non-Ductile Reinforced Concrete Frame Structure Retrofitted with Elastomeric Spring Dampers," by G. Pekcan, J.B. Mander and S.S. Chen, 7/14/95, (PB96-137161, A08, MF-A02).

NCEER-95-0011 "Development and Experimental Study of Semi-Active Fluid Damping Devices for Seismic Protection of Structures," by M.D. Symans and M.C. Constantinou, 8/3/95, (PB96-136940, A23, MF-A04).

NCEER-95-0012 "Real-Time Structural Parameter Modification (RSPM): Development of Innervated Structures," by Z. Liang, M. Tong and G.C. Lee, 4/11/95, (PB96-137153, A06, MF-A01).

NCEER-95-0013 "Experimental and Analytical Investigation of Seismic Retrofit of Structures with Supplemental Damping: Part III - Viscous Damping Walls," by A.M. Reinhorn and C. Li, 10/1/95, (PB96-176409, A11, MF-A03).

NCEER-95-0014 "Seismic Fragility Analysis of Equipment and Structures in a Memphis Electric Substation," by J-R. Huo and H.H.M. Hwang, 8/10/95, (PB96-128087, A09, MF-A02).

NCEER-95-0015 "The Hanshin-Awaji Earthquake of January 17, 1995: Performance of Lifelines," Edited by M. Shinozuka, 11/3/95, (PB96-176383, A15, MF-A03).

NCEER-95-0016 "Highway Culvert Performance During Earthquakes," by T.L. Youd and C.J. Beckman, available as NCEER-96-0015.

NCEER-95-0017 "The Hanshin-Awaji Earthquake of January 17, 1995: Performance of Highway Bridges," Edited by I.G. Buckle, 12/1/95, to be published.

NCEER-95-0018 "Modeling of Masonry Infill Panels for Structural Analysis," by A.M. Reinhorn, A. Madan, R.E. Valles, Y. Reichmann and J.B. Mander, 12/8/95, (PB97-110886, MF-A01, A06).

NCEER-95-0019 "Optimal Polynomial Control for Linear and Nonlinear Structures," by A.K. Agrawal and J.N. Yang, 12/11/95, (PB96-168737, A07, MF-A02).

NCEER-95-0020   "Retrofit of Non-Ductile Reinforced Concrete Frames Using Friction Dampers," by R.S. Rao, P. Gergely and R.N. White, 12/22/95, (PB97-133508, A10, MF-A02).

NCEER-95-0021   "Parametric Results for Seismic Response of Pile-Supported Bridge Bents," by G. Mylonakis, A. Nikolaou and G. Gazetas, 12/22/95, (PB97-100242, A12, MF-A03).

NCEER-95-0022   "Kinematic Bending Moments in Seismically Stressed Piles," by A. Nikolaou, G. Mylonakis and G. Gazetas, 12/23/95, (PB97-113914, MF-A03, A13).

NCEER-96-0001   "Dynamic Response of Unreinforced Masonry Buildings with Flexible Diaphragms," by A.C. Costley and D.P. Abrams," 10/10/96, (PB97-133573, MF-A03, A15).

NCEER-96-0002   "State of the Art Review: Foundations and Retaining Structures," by I. Po Lam, to be published.

NCEER-96-0003   "Ductility of Rectangular Reinforced Concrete Bridge Columns with Moderate Confinement," by N. Wehbe, M. Saiidi, D. Sanders and B. Douglas, 11/7/96, (PB97-133557, A06, MF-A02).

NCEER-96-0004   "Proceedings of the Long-Span Bridge Seismic Research Workshop," edited by I.G. Buckle and I.M. Friedland, to be published.

NCEER-96-0005   "Establish Representative Pier Types for Comprehensive Study: Eastern United States," by J. Kulicki and Z. Prucz, 5/28/96, (PB98-119217, A07, MF-A02).

NCEER-96-0006   "Establish Representative Pier Types for Comprehensive Study: Western United States," by R. Imbsen, R.A. Schamber and T.A. Osterkamp, 5/28/96, (PB98-118607, A07, MF-A02).

NCEER-96-0007   "Nonlinear Control Techniques for Dynamical Systems with Uncertain Parameters," by R.G. Ghanem and M.I. Bujakov, 5/27/96, (PB97-100259, A17, MF-A03).

NCEER-96-0008   "Seismic Evaluation of a 30-Year Old Non-Ductile Highway Bridge Pier and Its Retrofit," by J.B. Mander, B. Mahmoodzadegan, S. Bhadra and S.S. Chen, 5/31/96, (PB97-110902, MF-A03, A10).

NCEER-96-0009   "Seismic Performance of a Model Reinforced Concrete Bridge Pier Before and After Retrofit," by J.B. Mander, J.H. Kim and C.A. Ligozio, 5/31/96, (PB97-110910, MF-A02, A10).

NCEER-96-0010   "IDARC2D Version 4.0: A Computer Program for the Inelastic Damage Analysis of Buildings," by R.E. Valles, A.M. Reinhorn, S.K. Kunnath, C. Li and A. Madan, 6/3/96, (PB97-100234, A17, MF-A03).

NCEER-96-0011   "Estimation of the Economic Impact of Multiple Lifeline Disruption: Memphis Light, Gas and Water Division Case Study," by S.E. Chang, H.A. Seligson and R.T. Eguchi, 8/16/96, (PB97-133490, A11, MF-A03).

NCEER-96-0012   "Proceedings from the Sixth Japan-U.S. Workshop on Earthquake Resistant Design of Lifeline Facilities and Countermeasures Against Soil Liquefaction, Edited by M. Hamada and T. O'Rourke, 9/11/96, (PB97-133581, A99, MF-A06).

NCEER-96-0013   "Chemical Hazards, Mitigation and Preparedness in Areas of High Seismic Risk: A Methodology for Estimating the Risk of Post-Earthquake Hazardous Materials Release," by H.A. Seligson, R.T. Eguchi, K.J. Tierney and K. Richmond, 11/7/96, (PB97-133565, MF-A02, A08).

NCEER-96-0014   "Response of Steel Bridge Bearings to Reversed Cyclic Loading," by J.B. Mander, D-K. Kim, S.S. Chen and G.J. Premus, 11/13/96, (PB97-140735, A12, MF-A03).

NCEER-96-0015   "Highway Culvert Performance During Past Earthquakes," by T.L. Youd and C.J. Beckman, 11/25/96, (PB97-133532, A06, MF-A01).

NCEER-97-0001   "Evaluation, Prevention and Mitigation of Pounding Effects in Building Structures," by R.E. Valles and A.M. Reinhorn, 2/20/97, (PB97-159552, A14, MF-A03).

NCEER-97-0002   "Seismic Design Criteria for Bridges and Other Highway Structures," by C. Rojahn, R. Mayes, D.G. Anderson, J. Clark, J.H. Hom, R.V. Nutt and M.J. O'Rourke, 4/30/97, (PB97-194658, A06, MF-A03).

NCEER-97-0003   "Proceedings of the U.S.-Italian Workshop on Seismic Evaluation and Retrofit," Edited by D.P. Abrams and G.M. Calvi, 3/19/97, (PB97-194666, A13, MF-A03).

NCEER-97-0004   "Investigation of Seismic Response of Buildings with Linear and Nonlinear Fluid Viscous Dampers," by A.A. Seleemah and M.C. Constantinou, 5/21/97, (PB98-109002, A15, MF-A03).

NCEER-97-0005   "Proceedings of the Workshop on Earthquake Engineering Frontiers in Transportation Facilities," edited by G.C. Lee and I.M. Friedland, 8/29/97, (PB98-128911, A25, MR-A04).

NCEER-97-0006   "Cumulative Seismic Damage of Reinforced Concrete Bridge Piers," by S.K. Kunnath, A. El-Bahy, A. Taylor and W. Stone, 9/2/97, (PB98-108814, A11, MF-A03).

NCEER-97-0007   "Structural Details to Accommodate Seismic Movements of Highway Bridges and Retaining Walls," by R.A. Imbsen, R.A. Schamber, E. Thorkildsen, A. Kartoum, B.T. Martin, T.N. Rosser and J.M. Kulicki, 9/3/97, (PB98-108996, A09, MF-A02).

NCEER-97-0008   "A Method for Earthquake Motion-Damage Relationships with Application to Reinforced Concrete Frames," by A. Singhal and A.S. Kiremidjian, 9/10/97, (PB98-108988, A13, MF-A03).

NCEER-97-0009   "Seismic Analysis and Design of Bridge Abutments Considering Sliding and Rotation," by K. Fishman and R. Richards, Jr., 9/15/97, (PB98-108897, A06, MF-A02).

NCEER-97-0010   "Proceedings of the FHWA/NCEER Workshop on the National Representation of Seismic Ground Motion for New and Existing Highway Facilities," edited by I.M. Friedland, M.S. Power and R.L. Mayes, 9/22/97, (PB98-128903, A21, MF-A04).

NCEER-97-0011   "Seismic Analysis for Design or Retrofit of Gravity Bridge Abutments," by K.L. Fishman, R. Richards, Jr. and R.C. Divito, 10/2/97, (PB98-128937, A08, MF-A02).

NCEER-97-0012   "Evaluation of Simplified Methods of Analysis for Yielding Structures," by P. Tsopelas, M.C. Constantinou, C.A. Kircher and A.S. Whittaker, 10/31/97, (PB98-128929, A10, MF-A03).

NCEER-97-0013   "Seismic Design of Bridge Columns Based on Control and Repairability of Damage," by C-T. Cheng and J.B. Mander, 12/8/97, (PB98-144249, A11, MF-A03).

NCEER-97-0014   "Seismic Resistance of Bridge Piers Based on Damage Avoidance Design," by J.B. Mander and C-T. Cheng, 12/10/97, (PB98-144223, A09, MF-A02).

NCEER-97-0015   "Seismic Response of Nominally Symmetric Systems with Strength Uncertainty," by S. Balopoulou and M. Grigoriu, 12/23/97, (PB98-153422, A11, MF-A03).

NCEER-97-0016   "Evaluation of Seismic Retrofit Methods for Reinforced Concrete Bridge Columns," by T.J. Wipf, F.W. Klaiber and F.M. Russo, 12/28/97, (PB98-144215, A12, MF-A03).

NCEER-97-0017   "Seismic Fragility of Existing Conventional Reinforced Concrete Highway Bridges," by C.L. Mullen and A.S. Cakmak, 12/30/97, (PB98-153406, A08, MF-A02).

NCEER-97-0018   "Loss Asssessment of Memphis Buildings," edited by D.P. Abrams and M. Shinozuka, 12/31/97, (PB98-144231, A13, MF-A03).

NCEER-97-0019   "Seismic Evaluation of Frames with Infill Walls Using Quasi-static Experiments," by K.M. Mosalam, R.N. White and P. Gergely, 12/31/97, (PB98-153455, A07, MF-A02).

NCEER-97-0020   "Seismic Evaluation of Frames with Infill Walls Using Pseudo-dynamic Experiments," by K.M. Mosalam, R.N. White and P. Gergely, 12/31/97, (PB98-153430, A07, MF-A02).

NCEER-97-0021   "Computational Strategies for Frames with Infill Walls: Discrete and Smeared Crack Analyses and Seismic Fragility," by K.M. Mosalam, R.N. White and P. Gergely, 12/31/97, (PB98-153414, A10, MF-A02).

NCEER-97-0022   "Proceedings of the NCEER Workshop on Evaluation of Liquefaction Resistance of Soils," edited by T.L. Youd and I.M. Idriss, 12/31/97, (PB98-155617, A15, MF-A03).

MCEER-98-0001   "Extraction of Nonlinear Hysteretic Properties of Seismically Isolated Bridges from Quick-Release Field Tests," by Q. Chen, B.M. Douglas, E.M. Maragakis and I.G. Buckle, 5/26/98, (PB99-118838, A06, MF-A01).

MCEER-98-0002   "Methodologies for Evaluating the Importance of Highway Bridges," by A. Thomas, S. Eshenaur and J. Kulicki, 5/29/98, (PB99-118846, A10, MF-A02).

MCEER-98-0003   "Capacity Design of Bridge Piers and the Analysis of Overstrength," by J.B. Mander, A. Dutta and P. Goel, 6/1/98, (PB99-118853, A09, MF-A02).

MCEER-98-0004   "Evaluation of Bridge Damage Data from the Loma Prieta and Northridge, California Earthquakes," by N. Basoz and A. Kiremidjian, 6/2/98, (PB99-118861, A15, MF-A03).

MCEER-98-0005   "Screening Guide for Rapid Assessment of Liquefaction Hazard at Highway Bridge Sites," by T. L. Youd, 6/16/98, (PB99-118879, A06, not available on microfiche).

MCEER-98-0006   "Structural Steel and Steel/Concrete Interface Details for Bridges," by P. Ritchie, N. Kauhl and J. Kulicki, 7/13/98, (PB99-118945, A06, MF-A01).

MCEER-98-0007   "Capacity Design and Fatigue Analysis of Confined Concrete Columns," by A. Dutta and J.B. Mander, 7/14/98, (PB99-118960, A14, MF-A03).

MCEER-98-0008   "Proceedings of the Workshop on Performance Criteria for Telecommunication Services Under Earthquake Conditions," edited by A.J. Schiff, 7/15/98, (PB99-118952, A08, MF-A02).

MCEER-98-0009   "Fatigue Analysis of Unconfined Concrete Columns," by J.B. Mander, A. Dutta and J.H. Kim, 9/12/98, (PB99-123655, A10, MF-A02).

MCEER-98-0010   "Centrifuge Modeling of Cyclic Lateral Response of Pile-Cap Systems and Seat-Type Abutments in Dry Sands," by A.D. Gadre and R. Dobry, 10/2/98, (PB99-123606, A13, MF-A03).

MCEER-98-0011   "IDARC-BRIDGE: A Computational Platform for Seismic Damage Assessment of Bridge Structures," by A.M. Reinhorn, V. Simeonov, G. Mylonakis and Y. Reichman, 10/2/98, (PB99-162919, A15, MF-A03).

MCEER-98-0012   "Experimental Investigation of the Dynamic Response of Two Bridges Before and After Retrofitting with Elastomeric Bearings," by D.A. Wendichansky, S.S. Chen and J.B. Mander, 10/2/98, (PB99-162927, A15, MF-A03).

MCEER-98-0013   "Design Procedures for Hinge Restrainers and Hinge Sear Width for Multiple-Frame Bridges," by R. Des Roches and G.L. Fenves, 11/3/98, (PB99-140477, A13, MF-A03).

MCEER-98-0014   "Response Modification Factors for Seismically Isolated Bridges," by M.C. Constantinou and J.K. Quarshie, 11/3/98, (PB99-140485, A14, MF-A03).

MCEER-98-0015   "Proceedings of the U.S.-Italy Workshop on Seismic Protective Systems for Bridges," edited by I.M. Friedland and M.C. Constantinou, 11/3/98, (PB2000-101711, A22, MF-A04).

MCEER-98-0016   "Appropriate Seismic Reliability for Critical Equipment Systems: Recommendations Based on Regional Analysis of Financial and Life Loss," by K. Porter, C. Scawthorn, C. Taylor and N. Blais, 11/10/98, (PB99-157265, A08, MF-A02).

MCEER-98-0017   "Proceedings of the U.S. Japan Joint Seminar on Civil Infrastructure Systems Research," edited by M. Shinozuka and A. Rose, 11/12/98, (PB99-156713, A16, MF-A03).

MCEER-98-0018   "Modeling of Pile Footings and Drilled Shafts for Seismic Design," by I. PoLam, M. Kapuskar and D. Chaudhuri, 12/21/98, (PB99-157257, A09, MF-A02).

MCEER-99-0001 "Seismic Evaluation of a Masonry Infilled Reinforced Concrete Frame by Pseudodynamic Testing," by S.G. Buonopane and R.N. White, 2/16/99, (PB99-162851, A09, MF-A02).

MCEER-99-0002 "Response History Analysis of Structures with Seismic Isolation and Energy Dissipation Systems: Verification Examples for Program SAP2000," by J. Scheller and M.C. Constantinou, 2/22/99, (PB99-162869, A08, MF-A02).

MCEER-99-0003 "Experimental Study on the Seismic Design and Retrofit of Bridge Columns Including Axial Load Effects," by A. Dutta, T. Kokorina and J.B. Mander, 2/22/99, (PB99-162877, A09, MF-A02).

MCEER-99-0004 "Experimental Study of Bridge Elastomeric and Other Isolation and Energy Dissipation Systems with Emphasis on Uplift Prevention and High Velocity Near-source Seismic Excitation," by A. Kasalanati and M. C. Constantinou, 2/26/99, (PB99-162885, A12, MF-A03).

MCEER-99-0005 "Truss Modeling of Reinforced Concrete Shear-flexure Behavior," by J.H. Kim and J.B. Mander, 3/8/99, (PB99-163693, A12, MF-A03).

MCEER-99-0006 "Experimental Investigation and Computational Modeling of Seismic Response of a 1:4 Scale Model Steel Structure with a Load Balancing Supplemental Damping System," by G. Pekcan, J.B. Mander and S.S. Chen, 4/2/99, (PB99-162893, A11, MF-A03).

MCEER-99-0007 "Effect of Vertical Ground Motions on the Structural Response of Highway Bridges," by M.R. Button, C.J. Cronin and R.L. Mayes, 4/10/99, (PB2000-101411, A10, MF-A03).

MCEER-99-0008 "Seismic Reliability Assessment of Critical Facilities: A Handbook, Supporting Documentation, and Model Code Provisions," by G.S. Johnson, R.E. Sheppard, M.D. Quilici, S.J. Eder and C.R. Scawthorn, 4/12/99, (PB2000-101701, A18, MF-A04).

MCEER-99-0009 "Impact Assessment of Selected MCEER Highway Project Research on the Seismic Design of Highway Structures," by C. Rojahn, R. Mayes, D.G. Anderson, J.H. Clark, D'Appolonia Engineering, S. Gloyd and R.V. Nutt, 4/14/99, (PB99-162901, A10, MF-A02).

MCEER-99-0010 "Site Factors and Site Categories in Seismic Codes," by R. Dobry, R. Ramos and M.S. Power, 7/19/99, (PB2000-101705, A08, MF-A02).

MCEER-99-0011 "Restrainer Design Procedures for Multi-Span Simply-Supported Bridges," by M.J. Randall, M. Saiidi, E. Maragakis and T. Isakovic, 7/20/99, (PB2000-101702, A10, MF-A02).

MCEER-99-0012 "Property Modification Factors for Seismic Isolation Bearings," by M.C. Constantinou, P. Tsopelas, A. Kasalanati and E. Wolff, 7/20/99, (PB2000-103387, A11, MF-A03).

MCEER-99-0013 "Critical Seismic Issues for Existing Steel Bridges," by P. Ritchie, N. Kauhl and J. Kulicki, 7/20/99, (PB2000-101697, A09, MF-A02).

MCEER-99-0014 "Nonstructural Damage Database," by A. Kao, T.T. Soong and A. Vender, 7/24/99, (PB2000-101407, A06, MF-A01).

MCEER-99-0015 "Guide to Remedial Measures for Liquefaction Mitigation at Existing Highway Bridge Sites," by H.G. Cooke and J. K. Mitchell, 7/26/99, (PB2000-101703, A11, MF-A03).

MCEER-99-0016 "Proceedings of the MCEER Workshop on Ground Motion Methodologies for the Eastern United States," edited by N. Abrahamson and A. Becker, 8/11/99, (PB2000-103385, A07, MF-A02).

MCEER-99-0017 "Quindío, Colombia Earthquake of January 25, 1999: Reconnaissance Report," by A.P. Asfura and P.J. Flores, 10/4/99, (PB2000-106893, A06, MF-A01).

MCEER-99-0018 "Hysteretic Models for Cyclic Behavior of Deteriorating Inelastic Structures," by M.V. Sivaselvan and A.M. Reinhorn, 11/5/99, (PB2000-103386, A08, MF-A02).

MCEER-99-0019 "Proceedings of the 7th U.S.- Japan Workshop on Earthquake Resistant Design of Lifeline Facilities and Countermeasures Against Soil Liquefaction," edited by T.D. O'Rourke, J.P. Bardet and M. Hamada, 11/19/99, (PB2000-103354, A99, MF-A06).

MCEER-99-0020 "Development of Measurement Capability for Micro-Vibration Evaluations with Application to Chip Fabrication Facilities," by G.C. Lee, Z. Liang, J.W. Song, J.D. Shen and W.C. Liu, 12/1/99, (PB2000-105993, A08, MF-A02).

MCEER-99-0021 "Design and Retrofit Methodology for Building Structures with Supplemental Energy Dissipating Systems," by G. Pekcan, J.B. Mander and S.S. Chen, 12/31/99, (PB2000-105994, A11, MF-A03).

MCEER-00-0001 "The Marmara, Turkey Earthquake of August 17, 1999: Reconnaissance Report," edited by C. Scawthorn; with major contributions by M. Bruneau, R. Eguchi, T. Holzer, G. Johnson, J. Mander, J. Mitchell, W. Mitchell, A. Papageorgiou, C. Scaethorn, and G. Webb, 3/23/00, (PB2000-106200, A11, MF-A03).

MCEER-00-0002 "Proceedings of the MCEER Workshop for Seismic Hazard Mitigation of Health Care Facilities," edited by G.C. Lee, M. Ettouney, M. Grigoriu, J. Hauer and J. Nigg, 3/29/00, (PB2000-106892, A08, MF-A02).

MCEER-00-0003 "The Chi-Chi, Taiwan Earthquake of September 21, 1999: Reconnaissance Report," edited by G.C. Lee and C.H. Loh, with major contributions by G.C. Lee, M. Bruneau, I.G. Buckle, S.E. Chang, P.J. Flores, T.D. O'Rourke, M. Shinozuka, T.T. Soong, C-H. Loh, K-C. Chang, Z-J. Chen, J-S. Hwang, M-L. Lin, G-Y. Liu, K-C. Tsai, G.C. Yao and C-L. Yen, 4/30/00, (PB2001-100980, A10, MF-A02).

MCEER-00-0004 "Seismic Retrofit of End-Sway Frames of Steel Deck-Truss Bridges with a Supplemental Tendon System: Experimental and Analytical Investigation," by G. Pekcan, J.B. Mander and S.S. Chen, 7/1/00, (PB2001-100982, A10, MF-A02).

MCEER-00-0005 "Sliding Fragility of Unrestrained Equipment in Critical Facilities," by W.H. Chong and T.T. Soong, 7/5/00, (PB2001-100983, A08, MF-A02).

MCEER-00-0006 "Seismic Response of Reinforced Concrete Bridge Pier Walls in the Weak Direction," by N. Abo-Shadi, M. Saiidi and D. Sanders, 7/17/00, (PB2001-100981, A17, MF-A03).

MCEER-00-0007 "Low-Cycle Fatigue Behavior of Longitudinal Reinforcement in Reinforced Concrete Bridge Columns," by J. Brown and S.K. Kunnath, 7/23/00, (PB2001-104392, A08, MF-A02).

MCEER-00-0008 "Soil Structure Interaction of Bridges for Seismic Analysis," I. PoLam and H. Law, 9/25/00, (PB2001-105397, A08, MF-A02).

MCEER-00-0009 "Proceedings of the First MCEER Workshop on Mitigation of Earthquake Disaster by Advanced Technologies (MEDAT-1), edited by M. Shinozuka, D.J. Inman and T.D. O'Rourke, 11/10/00, (PB2001-105399, A14, MF-A03).

MCEER-00-0010 "Development and Evaluation of Simplified Procedures for Analysis and Design of Buildings with Passive Energy Dissipation Systems," by O.M. Ramirez, M.C. Constantinou, C.A. Kircher, A.S. Whittaker, M.W. Johnson, J.D. Gomez and C. Chrysostomou, 11/16/01, (PB2001-105523, A23, MF-A04).

MCEER-00-0011 "Dynamic Soil-Foundation-Structure Interaction Analyses of Large Caissons," by C-Y. Chang, C-M. Mok, Z-L. Wang, R. Settgast, F. Waggoner, M.A. Ketchum, H.M. Gonnermann and C-C. Chin, 12/30/00, (PB2001-104373, A07, MF-A02).

MCEER-00-0012 "Experimental Evaluation of Seismic Performance of Bridge Restrainers," by A.G. Vlassis, E.M. Maragakis and M. Saiid Saiidi, 12/30/00, (PB2001-104354, A09, MF-A02).

MCEER-00-0013 "Effect of Spatial Variation of Ground Motion on Highway Structures," by M. Shinozuka, V. Saxena and G. Deodatis, 12/31/00, (PB2001-108755, A13, MF-A03).

MCEER-00-0014 "A Risk-Based Methodology for Assessing the Seismic Performance of Highway Systems," by S.D. Werner, C.E. Taylor, J.E. Moore, II, J.S. Walton and S. Cho, 12/31/00, (PB2001-108756, A14, MF-A03).

MCEER-01-0001 "Experimental Investigation of P-Delta Effects to Collapse During Earthquakes," by D. Vian and M. Bruneau, 6/25/01, (PB2002-100534, A17, MF-A03).

MCEER-01-0002 "Proceedings of the Second MCEER Workshop on Mitigation of Earthquake Disaster by Advanced Technologies (MEDAT-2)," edited by M. Bruneau and D.J. Inman, 7/23/01, (PB2002-100434, A16, MF-A03).

MCEER-01-0003 "Sensitivity Analysis of Dynamic Systems Subjected to Seismic Loads," by C. Roth and M. Grigoriu, 9/18/01, (PB2003-100884, A12, MF-A03).

MCEER-01-0004 "Overcoming Obstacles to Implementing Earthquake Hazard Mitigation Policies: Stage 1 Report," by D.J. Alesch and W.J. Petak, 12/17/01, (PB2002-107949, A07, MF-A02).

MCEER-01-0005 "Updating Real-Time Earthquake Loss Estimates: Methods, Problems and Insights," by C.E. Taylor, S.E. Chang and R.T. Eguchi, 12/17/01, (PB2002-107948, A05, MF-A01).

MCEER-01-0006 "Experimental Investigation and Retrofit of Steel Pile Foundations and Pile Bents Under Cyclic Lateral Loadings," by A. Shama, J. Mander, B. Blabac and S. Chen, 12/31/01, (PB2002-107950, A13, MF-A03).

MCEER-02-0001 "Assessment of Performance of Bolu Viaduct in the 1999 Duzce Earthquake in Turkey" by P.C. Roussis, M.C. Constantinou, M. Erdik, E. Durukal and M. Dicleli, 5/8/02, (PB2003-100883, A08, MF-A02).

MCEER-02-0002 "Seismic Behavior of Rail Counterweight Systems of Elevators in Buildings," by M.P. Singh, Rildova and L.E. Suarez, 5/27/02. (PB2003-100882, A11, MF-A03).

MCEER-02-0003 "Development of Analysis and Design Procedures for Spread Footings," by G. Mylonakis, G. Gazetas, S. Nikolaou and A. Chauncey, 10/02/02, (PB2004-101636, A13, MF-A03, CD-A13).

MCEER-02-0004 "Bare-Earth Algorithms for Use with SAR and LIDAR Digital Elevation Models," by C.K. Huyck, R.T. Eguchi and B. Houshmand, 10/16/02, (PB2004-101637, A07, CD-A07).

MCEER-02-0005 "Review of Energy Dissipation of Compression Members in Concentrically Braced Frames," by K.Lee and M. Bruneau, 10/18/02, (PB2004-101638, A10, CD-A10).

MCEER-03-0001 "Experimental Investigation of Light-Gauge Steel Plate Shear Walls for the Seismic Retrofit of Buildings" by J. Berman and M. Bruneau, 5/2/03, (PB2004-101622, A10, MF-A03, CD-A10).

MCEER-03-0002 "Statistical Analysis of Fragility Curves," by M. Shinozuka, M.Q. Feng, H. Kim, T. Uzawa and T. Ueda, 6/16/03, (PB2004-101849, A09, CD-A09).

MCEER-03-0003 "Proceedings of the Eighth U.S.-Japan Workshop on Earthquake Resistant Design f Lifeline Facilities and Countermeasures Against Liquefaction," edited by M. Hamada, J.P. Bardet and T.D. O'Rourke, 6/30/03, (PB2004-104386, A99, CD-A99).

MCEER-03-0004 "Proceedings of the PRC-US Workshop on Seismic Analysis and Design of Special Bridges," edited by L.C. Fan and G.C. Lee, 7/15/03, (PB2004-104387, A14, CD-A14).

MCEER-03-0005 "Urban Disaster Recovery: A Framework and Simulation Model," by S.B. Miles and S.E. Chang, 7/25/03, (PB2004-104388, A07, CD-A07).

MCEER-03-0006 "Behavior of Underground Piping Joints Due to Static and Dynamic Loading," by R.D. Meis, M. Maragakis and R. Siddharthan, 11/17/03, (PB2005-102194, A13, MF-A03, CD-A00).

MCEER-03-0007 "Seismic Vulnerability of Timber Bridges and Timber Substructures," by A.A. Shama, J.B. Mander, I.M. Friedland and D.R. Allicock, 12/15/03.

MCEER-04-0001 "Experimental Study of Seismic Isolation Systems with Emphasis on Secondary System Response and Verification of Accuracy of Dynamic Response History Analysis Methods," by E. Wolff and M. Constantinou, 1/16/04 (PB2005-102195, A99, MF-E08, CD-A00).

MCEER-04-0002 "Tension, Compression and Cyclic Testing of Engineered Cementitious Composite Materials," by K. Kesner and S.L. Billington, 3/1/04, (PB2005-102196, A08, CD-A08).

MCEER-04-0003 "Cyclic Testing of Braces Laterally Restrained by Steel Studs to Enhance Performance During Earthquakes," by O.C. Celik, J.W. Berman and M. Bruneau, 3/16/04, (PB2005-102197, A13, MF-A03, CD-A00).

MCEER-04-0004 "Methodologies for Post Earthquake Building Damage Detection Using SAR and Optical Remote Sensing: Application to the August 17, 1999 Marmara, Turkey Earthquake," by C.K. Huyck, B.J. Adams, S. Cho, R.T. Eguchi, B. Mansouri and B. Houshmand, 6/15/04, (PB2005-104888, A10, CD-A00).

MCEER-04-0005 "Nonlinear Structural Analysis Towards Collapse Simulation: A Dynamical Systems Approach," by M.V. Sivaselvan and A.M. Reinhorn, 6/16/04, (PB2005-104889, A11, MF-A03, CD-A00).

MCEER-04-0006 "Proceedings of the Second PRC-US Workshop on Seismic Analysis and Design of Special Bridges," edited by G.C. Lee and L.C. Fan, 6/25/04, (PB2005-104890, A16, CD-A00).

MCEER-04-0007 "Seismic Vulnerability Evaluation of Axially Loaded Steel Built-up Laced Members," by K. Lee and M. Bruneau, 6/30/04, (PB2005-104891, A16, CD-A00).

MCEER-04-0008 "Evaluation of Accuracy of Simplified Methods of Analysis and Design of Buildings with Damping Systems for Near-Fault and for Soft-Soil Seismic Motions," by E.A. Pavlou and M.C. Constantinou, 8/16/04, (PB2005-104892, A08, MF-A02, CD-A00).

MCEER-04-0009 "Assessment of Geotechnical Issues in Acute Care Facilities in California," by M. Lew, T.D. O'Rourke, R. Dobry and M. Koch, 9/15/04, (PB2005-104893, A08, CD-A00).

MCEER-04-0010 "Scissor-Jack-Damper Energy Dissipation System," by A.N. Sigaher-Boyle and M.C. Constantinou, 12/1/04.

MCEER-04-0011 "Seismic Retrofit of Bridge Steel Truss Piers Using a Controlled Rocking Approach," by M. Pollino and M. Bruneau, 12/20/04.

MCEER-05-0001 "Experimental and Analytical Studies of Structures Seismically Isolated with an Uplift-Restraint Isolation System," by P.C. Roussis and M.C. Constantinou, 1/10/05.

MCEER-05-0002 "A Versatile Experimentation Model for Study of Structures Near Collapse Applied to Seismic Evaluation of Irregular Structures," by D. Kusumastuti, A.M. Reinhorn and A. Rutenberg, 3/31/05.

MCEER-05-0003 "Proceedings of the Third PRC-US Workshop on Seismic Analysis and Design of Special Bridges," edited by L.C. Fan and G.C. Lee, 4/20/05.

MCEER-05-0004 "Approaches for the Seismic Retrofit of Braced Steel Bridge Piers and Proof-of-Concept Testing of an Eccentrically Braced Frame with Tubular Link," by J.W. Berman and M. Bruneau, 4/21/05.

MCEER-05-0005 "Simulation of Strong Ground Motions for Seismic Fragility Evaluation of Nonstructural Components in Hospitals," by A. Wanitkorkul and A. Filiatrault, 5/26/05.

MCEER-05-0006 "Seismic Safety in California Hospitals: Assessing an Attempt to Accelerate the Replacement or Seismic Retrofit of Older Hospital Facilities," by D.J. Alesch, L.A. Arendt and W.J. Petak, 6/6/05.

MCEER-05-0007 "Development of Seismic Strengthening and Retrofit Strategies for Critical Facilities Using Engineered Cementitious Composite Materials," by K. Kesner and S.L. Billington, 8/29/05.

MCEER-05-0008 "Experimental and Analytical Studies of Base Isolation Systems for Seismic Protection of Power Transformers," by N. Murota, M.Q. Feng and G-Y. Liu, 9/30/05.

MCEER-05-0009 "3D-BASIS-ME-MB: Computer Program for Nonlinear Dynamic Analysis of Seismically Isolated Structures," by P.C. Tsopelas, P.C. Roussis, M.C. Constantinou, R. Buchanan and A.M. Reinhorn, 10/3/05.

MCEER-05-0010 "Steel Plate Shear Walls for Seismic Design and Retrofit of Building Structures," by D. Vian and M. Bruneau, 12/15/05.